Estimation of multiple components and parameters for quantitative MRI

Nagtegaal, M.A.

DOI
10.4233/uuid:8890a4ca-c30a-42e3-9767-a0bf2e16a25a

Publication date
2023

Document Version
Final published version

Citation (APA)
Nagtegaal, M. A. (2023). *Estimation of multiple components and parameters for quantitative MRI*. [Dissertation (TU Delft), Delft University of Technology]. https://doi.org/10.4233/uuid:8890a4ca-c30a-42e3-9767-a0bf2e16a25a

Important note
To cite this publication, please use the final published version (if applicable).
Please check the document version above.

Estimation of multiple components and parameters for quantitative MRI

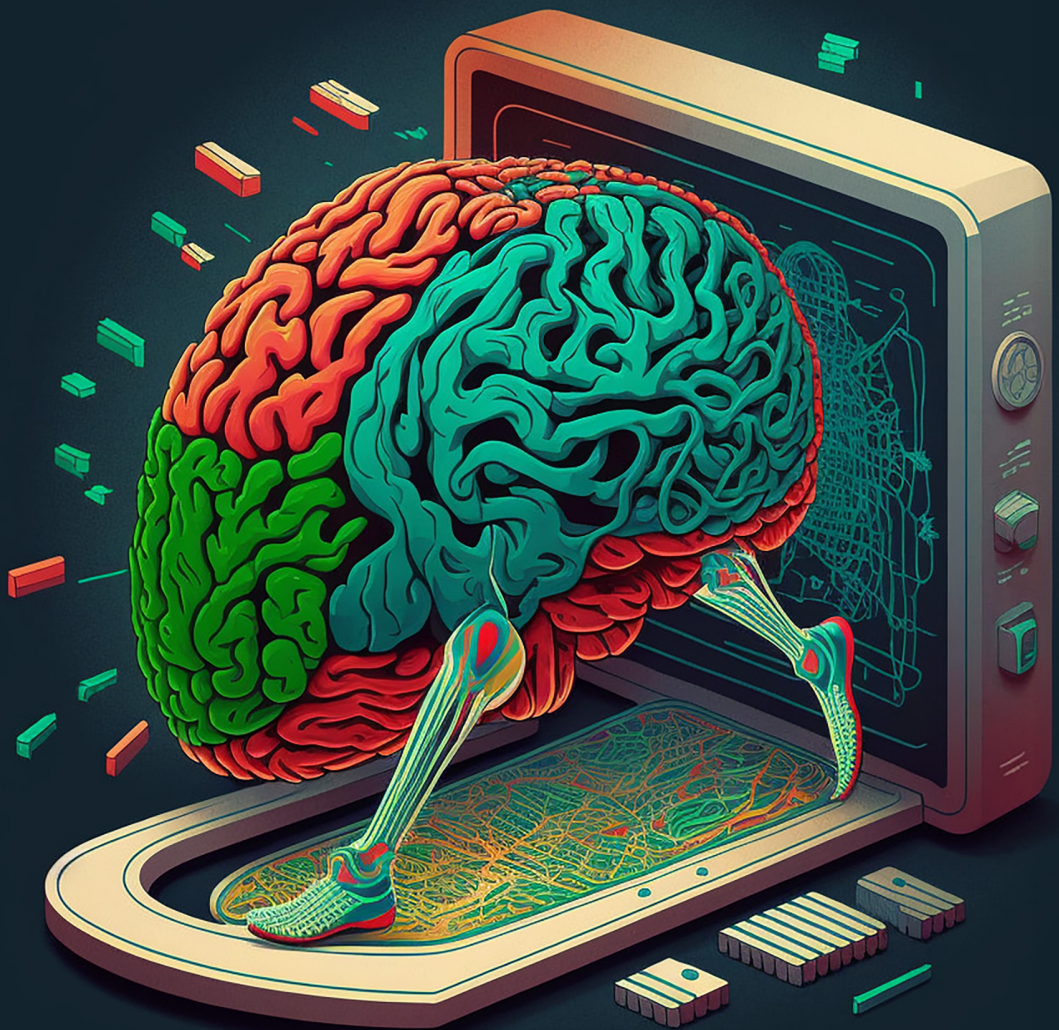

Martijn Nagtegaal

ESTIMATION OF MULTIPLE COMPONENTS AND PARAMETERS FOR QUANTITATIVE MRI

ESTIMATION OF MULTIPLE COMPONENTS AND PARAMETERS FOR QUANTITATIVE MRI

Proefschrift

ter verkrijging van de graad van doctor
aan de Technische Universiteit Delft,
op gezag van de Rector Magnificus prof. dr. ir. T.H.J.J. van der Hagen,
voorzitter van het College voor Promoties,
in het openbaar te verdedigen op woensdag 15 maart 2023 om 12:30 uur

door

Martijn Arie NAGTEGAAL

Ingenieur in Technische Wiskunde,
Technische Universiteit Delft, Delft, Nederland,
Master of Science in Scientific Computing,
Technische Universität Berlin, Berlijn, Duitsland
geboren te Alphen aan den Rijn, Nederland.

Dit proefschrift is goedgekeurd door de

promotoren:	Dr. F. M. Vos
	Prof. dr. ir. M. J. P. van Osch
copromotoren:	Dr. J. H. J. M. de Bresser
	Dr. ir. D. H. J. Poot

Samenstelling promotiecommissie:

Rector Magnificus,	voorzitter
Dr. F. M. Vos,	Technische Universiteit Delft
Prof. dr. ir. M. J. P. van Osch,	Leids Universitair Medisch Centrum
Dr. J. H. J. M. de Bresser,	Leids Universitair Medisch Centrum
Dr. ir. D. H. J. Poot,	Erasmus MC
Onafhankelijke leden:	
Prof. dr. ir. M. B. van Gijzen,	Technische Universiteit Delft
Prof. dr. ir. C. A. T. van der Berg,	UMC Utrecht
Dr. D. Ma,	Case Western Reserve University, USA
Dr. E. E. Bron,	Erasmus MC
Prof. dr. S. Stallinga,	Technische Universiteit Delft, reservelid

This work was performed in the framework of the Medical Delta program Medical Delta Diagnostics 3.0: Dementia and stroke. Medical Delta is gratefully acknowledged for financial support for the printing costs of this thesis.

Keywords:	Quantitative MRI, Multi-component estimations, MR Fingerprinting, Myelin water, Sequence optimization
Printed by:	Gildeprint
Front & Back illustration:	Generated by https://www.midjourney.com/ with prompt `mri, fingerprint, physics, running, brain, cartoon, mathematics seed:41600870`

ISBN 978-94-6384-421-5

An electronic version of this dissertation is available at
http://repository.tudelft.nl/.

CONTENTS

SUMMARY

MAGNETIC Resonance Imaging (MRI) is a flexible medical imaging technique that facilitates measurement of a wide range of contrasts particularly in soft tissue (e.g. brain and heart). Conventionally, qualitative images are acquired in which certain physical tissue properties are emphasized such as the transverse and longitudinal relaxation times. Such images are frequently referred to as "weighted", i.e. T_1-weighted. Quantitative MRI (qMRI) aims at measuring the underlying tissue parameters governing the contrast instead of yielding mere weighted images. These quantitative parameter estimations were proven to be more reproducible than conventional MR images and more sensitive to certain disease processes, enabling enhanced longitudinal comparisons within subjects as well as comparisons between subjects.

MR Fingerprinting (MRF) is an example of such a quantitative technique. MRF uses a combination of transient state acquisitions with varying flip angle patterns, severe undersampling and advanced signal models to allow for fast qMRI acquisitions and accurate estimation of a wide range of parameters. While most qMRI methods assume a single tissue type per voxel, this is almost never a valid assumption. This assumption especially breaks down at tissue boundaries or when tissues consist of multiple, mixed compartments, such as water contained between myelin sheets in the brain, often called myelin water surrounded by extra-cellular water.

The goal of this thesis is to develop enhanced methodology for quantitative MRI by extending traditional signal and image post-processing methods. Specifically, the focus is on MR Fingerprinting in combination with multi-component estimations, in which different compartments are included in a mixed estimation model. This is done to obtain more information from the acquired data and to improve quantification, therefore possibly obtain new clinical insights. Important steps towards clinical use are to enhance estimation accuracy and precision compared to previous methods and reduce the scan time.

In this thesis the Sparsity Promoting Iterative Joint NNLS (SPIJN) algorithm is proposed for obtaining multi-component estimations from MRF data. This enabled subvoxel, fractional estimation of signal components in a region of interest, without making a priori assumptions about tissues expected to be present. The main novelty of this method is to combine a non-negativity with a joint-sparsity constraint that limits the total number of tissues identified in a region of interest. As a result it became possible to obtain magnetization fraction maps of the white matter, gray matter, CSF and a component with shorter relaxation times related to myelin water. The repeatability of the proposed method is studied in 5 subjects that were scanned 8 times with one week in between the scans each time. Comparison of the obtained white matter, gray matter and CSF maps with segmentations from conventional methods shows high repeatability of the estimated relaxation times and more fine structures in the CSF magnetization fraction maps. Additionally, the proposed SPIJN algorithm was applied to data from a more

conventional qMRI sequence, i.e. a multi-echo spin-echo sequence, to obtain estimations of the so-called myelin water fraction in the brain. The resulting images show significantly improved noise robustness compared to the standard multi-component analysis method, improving the usability.

MRF scans can be acquired in a relatively short acquisition time of less than 30 seconds per slice, but this will still result in 15 minutes of total scan-time when full brain coverage is needed. A further reduction in acquisition time is desirable for clinical usage, in which every minute counts. Therefore, improved reconstruction methods for MRF data are proposed, especially tailored to multi-component estimations. In in vivo scans we showed the improved image quality enabled by the proposed methods.

In another study, We applied the SPIJN algorithm to MRF brain scans from MS patients. In the results that we obtained we observe that white matter changes are reflected in a component with prolonged transverse relaxation times which is less pronounced in data of healthy controls. We hypothesize that the observed component reflects an increase in extra-cellular water and allows for early characterization of white matter damage.

In a related project, an adaptation on the SPIJN algorithm was introduced that is more sensitive to small local changes. The adjusted algorithm is applied to imaging data of MS patients and it is shown that it can help to identify small cerebral lesions.

MRF sequences can be chosen rather freely, to further reduce the scan time and reduce the estimation error these sequences can be optimized. A method is proposed in which parameter maps of the brain are used as reference upon which the MRF flip-angle series is optimized, taking into account the used undersampling trajectories. As a result undersampling errors, a major source of estimation errors, are effectively minimized.

Finally, we investigated an adjusted simulation method of MRF sequences that is able to accurately model the effects of through-plane motion, which is a major source of errors in MRF scans. Such a model may support the development of new retrospective correction methods for this type of motion as it enables proper simulation of its effects.

In summary, this thesis proposes new methods for multi-component reconstruction and analysis, sequence optimization and studying the effects of motion in MRF and further investigates the possibilities of multi-component MRF.

SAMENVATTING

MAGNETIC RESONANCE IMAGING (MRI) is een flexibele medische beeldvormingstechniek die het mogelijk maakt afbeeldingen te maken en metingen uit te voeren met een breed scala aan contrasten, voornamelijk in weke weefsels (bijvoorbeeld de hersenen of het hart). Van oudsher worden kwalitatieve beelden geacquireerd waarin bepaalde fysische weefseleigenschappen extra naar voren komen, zoals de transversale of longitudinale relaxatietijden. Naar zulke beelden verwijzen we doorgaans als "gewogen", bijvoorbeeld T_1-gewogen. Kwantitatieve MRI (qMRI) heeft als doel de onderliggende weefseleigenschappen te meten in plaats van slechts gewogen afbeeldingen te verkrijgen. Deze kwantitatieve parameterschattingen zijn meer reproduceerbaar dan conventionele MRI scans en gevoeliger voor bepaalde ziekteprocessen, waardoor het mogelijk wordt scans beter te vergelijken over langere tijd en tussen personen.

MR Fingerprinting (MRF) is een voorbeeld van een dergelijke kwantitatieve techniek. MRF gebruikt een combinatie van een acquisitie waarbij het signaal langzaam veranderd door variërende fliphoek-patronen, sterke onderbemonstering (undersampling) en geavanceerde signaalmodellen om het mogelijke te maken meerdere qMRI parameters in een korte tijd te schatten. De meeste qMRI methoden nemen aan dat er een enkel weefseltype per voxel (3D pixel) aanwezig is, maar dit is haast nooit het geval. Deze aanname klopt zeker niet langs de grens van twee weefsels of wanneer weefsels bestaan uit meerdere, gemengde componenten, zoals het geval is in de witte stof bij het water tussen de myelineschede in de hersenen, ook wel myelinewater genoemd, dat omringd wordt door extra-cellulair water.

Het doel van dit proefschrift is het ontwikkelen van verbeterde methodes voor kwantitatieve MRI door het verbeteren van signaalverwerkings- en acquisitietechnieken. Hierbij ligt de nadruk op MR Fingerprinting in combinatie met meerdere componenten schattingen, waarin we deze componenten meenemen in de signaalverwerking. Dit doen we om meer informatie te verkrijgen uit het gemeten signaal wat nieuwe klinische inzichten en betere kwantificatie kan bieden. Belangrijke stappen om klinisch gebruik mogelijk te maken zijn het verhogen van de nauwkeurigheid en precisie en het verkorten van de benodigde scantijd.

In dit proefschrift wordt een algoritme (SPIJN) geïntroduceerd voor het verkrijgen van schattingen van meerdere signaalcomponenten uit MRF data. Dit maakt het mogelijk sub-voxel fractieschattingen van de componenten in een gebied van interesse te verkrijgen zonder van tevoren aannames te doen over de aanwezige weefsels. De voornaamste noviteit in deze methode is het combineren van een niet-negativiteitsaanname per voxel met een aanname dat slechts enkele componenten gebruikt worden, dit beperkt het totaal aantal weefsel in het gebied van interesse. Als gevolg hiervan wordt het mogelijk fractieschattingen van de witte stof, grijze stof, hersenvocht en een component met kortere relaxatietijden, gerelateerd aan myelinewater, te verkrijgen. De herhaalbaarheid van de voorgestelde methode bestuderen we aan de hand van 5 personen die acht-

maal gescand zijn met steeds een week tussen de herhaalde scans. Vergelijking van de verkregen componentmappen van witte stof, grijze stof en hersenvocht met segmentaties verkregen via standaard methoden laat zien dat de geschatte relaxatietijden zeer goed reproduceren en meer fijne structuren van hersenvocht zichtbaar zijn in de fractiebeelden. In aanvullend onderzoek is het geïntroduceerde SPIJN-algoritme toegepast op data van een meer conventionele qMRI sequentie, een multi-echo-spin-echo sequentie om myelinewater fractie schattingen in de hersenen te verkrijgen. De resulterende afbeeldingen laten een significante afname in ruis zien vergeleken met de standaard meerdere componenten analyse, waardoor ze beter bruikbaar zijn.

MRF scans kunnen verkregen worden in een relatief korte scantijd van minder dan 30 seconden per plak, maar dit resulteert nog steeds in een scantijd van 15 minuten wanneer de hele hersenen gescand worden. Voor klinisch gebruik, waar elke minuut telt, zijn kortere scantijden zeer wenselijk. Daarom worden verbeterde reconstructiemethoden voorgesteld, toegesneden op het afschatten van meerdere componenten. In in vivo scans laten we zien dat dit resulteert in een verbeterde beeldkwaliteit bij korte scantijden.

Het SPIJN-algoritme passen we toe om meerdere componenten schattingen te krijgen uit MRF-hersenbeelden verkregen bij MS patiënten. In de verkregen resultaten zien we dat witte stof veranderingen gekenmerkt worden door componenten met een langere transversale relaxatietijd, die minder aanwezig zijn bij gezonde personen. We veronderstellen dat dit veroorzaakt wordt door een toename in extracellulair water en wellicht het mogelijk maakt om witte stofschade eerder te karakteriseren.

In een gerelateerd project is een aanpassing van het SPIJN-algoritme geïntroduceerd dat gevoeliger is voor kleine lokale afwijkingen. Het algoritme is toegepast op data van MS-patiënten en laat zien dat het kan helpen in het eerder detecteren van kleine hersenlaesies.

Er zijn veel parameters te kiezen in een MRF-sequentie, dus om de scantijd verder terug te brengen en fouten te reduceren, willen we de gebruikte sequenties optimaliseren. Een methode wordt geïntroduceerd die het mogelijk maakt de parameterwaarden zoals we die afbeelden in de hersenen te gebruiken als referentie, waarna de MRF-sequentie geoptimaliseerd wordt, terwijl het undersampling patroon daarin wordt meegenomen. Als resultaat kunnen de soms grote fouten veroorzaakt door undersampling effectief verminderd worden.

Tot slot bestuderen we een aangepaste simulatiemethode van MRF-acquisities die het mogelijk maakt om accuraat de effecten van beweging loodrecht op het afgebeelde volume mee te schatten. Deze *through plane motion* kan grote fouten veroorzaken in MRF schattingen. Dit model kan mogelijk gebruikt worden in retrospectieve correctie methoden voor deze vorm van bewegingsartifacten aangezien deze nu beter gesimuleerd kunnen worden.

Resumerend, introduceert dit proefschrift nieuwe reconstructie en analyse methoden voor meerdere componenten schattingen, sequentie optimalisatie en beweging in MRF en gaat het verder in op de mogelijkheden van meerdere componenten schattingen in MRF.

1

GENERAL INTRODUCTION

ABSTRACT

In this chapter I give a general introduction into MRI and the concepts required to understand the research as performed in the rest of this thesis. Afterwards I summarize research challenges that can be identified in the field of quantitative MRI, which are reflected in the research goals. I finish with an outline of the rest of the thesis.

1

A fascinating property of Magnetic Resonance Imaging (MRI) is the flexibility it offers in measurement approaches resulting in the possibility of many different imaging contrasts. As such, a wide variety of information can be obtained, including properties of tissues related to spin relaxivity, diffusion and perfusion. For instance in brain imaging, which is the main application of this thesis, a typical MRI protocol consists of a T_1-weighted scan, a T_2-weighted scan, a Fluid Attenuated Inversion Recovery (FLAIR) scan, a diffusion weighted scan (DWI), perhaps a proton density (PD) weighted scan and somtetimes more specialized sequences such as arterial spin labeling (ASL), or susceptibility weighted scans.

This example brain MRI protocol results in so-called weighted images that stress particular tissue properties (e.g. degree of T_1 relaxation). These images provide contrast between the different tissues types, like white matter (WM), gray matter (GM), cerebrospinal fluid (CSF) as well as potential abnormalities. For instance, in Alzheimer's disease brain atrophy has been demonstrated as an important marker of disease progression [1], which can be derived from weighted scans by determining volume estimates of the different tissues. Another example are white matter hyper-intensities (WMHs), that show a brighter signal on T_2-weighted scans and are a sign of disease progression.. Moreover, pathologies such as WMHs often have different relaxometry properties compared to physiological WM and GM, resulting in a different imaging signal. Effectively, this enables their identification in such weighted brain images.

Unfortunately, the signal values in weighted scans only 'qualitatively' reflect tissue properties since they are susceptible to a range of confounding factors like field inhomogeneities and specific choice of sequence parameters. Therefore, the resulting pixel values can only be compared relative to other pixels in the same image, but the exact values do not harbor more information. As a result, the weighted images have two main limitations: (1) possibilities are restricted to relate measurements to biophysical models and processes and (2) inter-patient analyses and longitudinal comparison of tissue properties like water content are not directly possible.

Additionally, while its versatility makes MRI a valuable diagnostic tool, a large number of scans also results in prolonged imaging times (potentially in the range of an hour or longer), making it also a relatively slow and therefore expensive imaging modality.

1.1. QUANTITATIVE MRI (QMRI)

ALTHOUGH MRI has mainly developed as a qualitative imaging technique relying on weighted images in the past 30 years, MRI *can* be used for quantitative imaging as well. However, this requires combining a set of qualitative measurements with well-chosen scan parameters and subsequent post-processing to relate signal models and tissue properties to the measured signals. In this thesis, my main interest lies in the relaxometry properties of water hydrogen atoms (often referred to as protons), i.e. the T_1, T_2 relaxation times and tissue magnetizations M_0 (or equivalently magnetization fractions) as these are the primary tissue properties underlying clinically used weighted scans.

The T_1 and T_2 relaxation times are measures of the time it takes for the magnetization of a perturbed ensemble of water protons to return to the original state after an excitation radio-frequency (RF) pulse [2]. In particular, T_1 relaxation time refers to the longitudinal magnetization and is mainly determined by an exchange of magnetization

between water protons and other protons in the surrounding area. Complementary, T_2 relaxation is a process that is primarily determined by the interaction between the water protons, leading to a variable degree of dephasing between spins and associated decrease in transverse magnetization, causing the transverse magnetization to disappear over time. In addition to this, inhomogeneities in the main magnetic field and/or susceptibility effects can be an extra source of dephasing, resulting in an even shorter effective transverse relaxation time that is generally denoted as T_2^*. In most qMRI sequences used in this thesis this effect is corrected for, so that the focus is on measuring the T_2 value.

Compared to relaxation times, proton density or tissue magnetization is a conceptually simpler property, though difficult to measure quantitatively. It relates to the amount of water protons affected by the MR experiment and therefore causes a linear scaling in signal strength, resulting in no signal in regions with air and higher signal in regions rich with water.

It has been shown that brain pathologies, such as Multiple Sclerosis (MS) lesions and tumors, often lead to prolonged T_1 and T_2 relaxation times compared to healthy tissue [3]. What is more, the use of relaxometry also allows to identify different sub-types of pathology and identify more subtle changes in the surrounding tissue, e.g. in relation to different brain tumor types [4].

Over the last decades, much progress was made regarding the amount of information that can be extracted from MRI scans using computational methods. Conventional qMRI, as briefly discussed in Section 1.2, focuses on determining single tissue parameters through fitting to analytical models. The modern-day computing potential and advances in MR acquisition and multi-parametric modeling, however, has paved the way to entirely new qMRI paradigms. As such, qMRI techniques can be broadly categorized in traditional, single tissue parameter approaches, and those methods developed in the last decade, making use of new computational possibilities and multi-parametric estimations, of which MR Fingerprinting (MRF) is a main component, as introduced in Section 1.3.

1.2. CONVENTIONAL QUANTITATIVE MRI SEQUENCES

CONVENTIONAL qMRI sequences can be considered a natural extension of weighted MR imaging to acquire a quantitative map. Often multiple weighted images are separately acquired, while one or more acquisition parameter are varied. From these image data a single tissue parameter is estimated based on an assumed relation between the acquired MR signal and tissue parameters. For T_1-mapping the quantitative protocol is often an inversion recovery (IR) sequence, in which the exponential T_1-recovery is sampled by acquiring images with varying inversion times (TI). For T_2-mapping, multi turbo spin echo (MSE) or multi-echo spin-echo (MESE) sequences are chosen that sample the exponential T_2-decay of the transverse magnetization by varying the echo times (TE). In an MSE sequence, each echo is separately acquired as a single acquisition, whereas in a MESE sequence multiple echos are acquired in one scan. The latter approach, however, goes at the cost of increased sensitivity to a homogeneous RF transmit field (i.e. so-called B_1^+-inhomogeneities).

Based on the acquired images a voxel-wise fit can be performed, using an explicit

1

TECHNICAL CONCEPTS: LOCALIZATION AND UNDERSAMPLING IN MRI

Magnetic field gradients An MR scanner can only measure the total transverse magnetization of an object of interest placed in the scanner. As such, the scanner cannot directly probe the signal emanating from individual locations. To encode spatial information extra magnetic fields are therefore superposed on the main magnetic field (B_0). These so-called gradient fields change the resonance frequency and phase-offset of the hydrogen protons as a function of spatial location [5].

Slice selection To restrict the MR imaging procedure to a 2D slice, a slice selection gradient can be used. This changes the resonance frequency in the slice encoding (z) direction to make only a part of the region of interest sensitive to an applied RF pulse with a specific frequency. In effect only the magnetization in this slice is perturbed and will be measurable.

Fourier encoding To encode spatial information within a slice, additional gradients are used. Over time, each gradient induces a phase accumulation to the complex valued MR-signal. Essentially, this phase accumulation is linearly dependent on the position since the gradients have an approximately linear profile. This holds both in the x- and y-direction. The relation thereby imposed is mathematically equivalent to the well known Fourier transform and therefore it is often said that MRI measures the Fourier transform of an image, or the so-called *k-space*.

k-space trajectories By sampling the MRI-signal while gradients are switched on, part of the k-space is being sampled. The possible image quality and field of view is determined by how and which points in k-space are sampled. For a 2D acquisition, k-space can be conceived as a 2-dimensional array, with the same number of elements as the reconstructed image. In most MRI sequences it is not desired to acquire the full k-space after a single excitation pulse due to the long sampling time that would be required. Such long sampling times can result in unwanted measurement errors (e.g. blurring), as the magnetization will change during the acquisition due to signal decay and eventually decay to zero for very long readouts. Therefore MRI sequences often consist of repeated elements to acquire the k-space data sequentially. In most conventional implementations k-space is filled line by line, but other trajectories can be more efficient e.g. sampling multiple lines per readout or spiral trajectories through k-space.

Undersampling When only part of k-space is acquired, we call the k-space or the data *undersampled*. A Fourier transform performed based on undersampled data is equivalent to filling the non-sampled locations in k-space with zeros. Therefore we call this a zero-filled reconstruction. If the acquisition is strongly undersampled, there is insufficient data to accurately solve the inverse problem resulting in undersampling artifacts. The size, shape and severity of these artifacts highly depend on the used k-space trajectory and severity of the undersampling.

Parallel imaging When multiple receive coils are used, each coil will have a varying reception profile field, making the recorded information per coil different. Techniques such as GRAPPA [6] and SENSE [7] allow to use this information in the reconstruction and make the inverse problem less ill-posed.

model equation and standard fitting algorithms. In the previous two examples this would boil down to fitting an exponential function. Beside IR and MSE/MESE, other qMRI sequences have been proposed, e.g. variable flip angle (VFA or DESPOT) sequences [8], Look-Locker sequences and T_2-prepared sequences. In all these sequences multiple images are acquired, and in most of them the number of images linearly increases the total scan time. Simultaneously, the acquisition of more images can lead to an increased noise robustness and higher risk of motion. One could argue, however, that the acquisition of very similar images with comparable acquisition settings is not information efficient. The long scan time has been an important argument that kept qMRI techniques from being excluded in clinical protocols.

1.3. MAGNETIC RESONANCE FINGERPRINTING

MAGNETIC Resonance Fingerprinting (MRF) [9] was introduced in 2013 as a new qMRI framework for multi-parameter estimation (T_1 and T_2) based on three key concepts:

1. A complicated signal evolution over time is induced by applying a (randomly or well-chosen) train of RF-pulses with varying flip angles and (short) waiting times. Typically the number of RF-pulses and corresponding k-space readouts are between 400 to 5000. Where conventional methods acquire a steady-state signal, MRF acquires a so-called *transient state* signal;

2. The parameter estimation is not based on model-based fits, but on matching to a *signal dictionary* precalculated using Bloch simulations, allowing for large freedom in the used acquisition scheme;

3. The k-space measurements or readouts after each RF-pulse are highly undersampled and often involve *non-Cartesian trajectories* such as spirals that rotate over time, to achieve full k-space coverage when the total data is considered.

The combination of these ideas led to a (flexible) framework which allows for efficient acquisition of data that contains enough information to estimate multiple tissue property maps in a limited amount of time. MRF implementations can vary in many ways. A first distinguishing element is the used sequence building block. Amongst others, this can be a balanced steady state free processing (bSSFP) sequence, which is typically sensitive to T_1, T_2 as well as inhomogeneities in the main magnetic field (B_0^+) [9], a gradient spoiled SSFP sequence with sensitivity to T_1 and T_2 (and potentially B_1^+) [10] or a gradient echo sequence sensitive to T_1 and T_2^* [11] relaxation times. In such sequences preparation pulses can be used, of which an inversion pulse at the start is the main example which is employed to improve T_1 sensitivity, but T_2 or $T_{1\rho}$ preparation is also possible [12].

A next distinguishing element between MRF sequences is the used k-space sampling pattern. First of all, the sequence can be based on 2D or 3D acquisitions, where a 2D acquisition acquires different slices sequentially and a 3D acquisition traverses through a 3D k-space. In this thesis 2D acquisitions are used with spiral undersampling patterns, but many other options are available, such as Cartesian patterns, radial spokes,

c.q. stars, or music-based patterns [13, Fig. 3]. Compared to Cartesian patterns, most other trajectories provide less coherent undersampling artifacts and especially spirals provide a more efficient sampling of k-space.

As these sequence elements are selected, the exact train of RF flip angle pulses and repetition times (TR) and the length of this train have to be defined. The influence on the estimated results will be discussed in Chapter 8.

The acquired k-space data contains information about the tissue properties, but image reconstruction is needed to derive this information. Often (time-compressed) time frame images are reconstructed first, and different reconstruction pipelines can be employed in this step [12, Table 1]. Subsequently, the images can be matched to a dictionary with simulated MRF signals for different tissue properties. This leads to the estimation of T_1 and T_2 parameter maps with a single set of T_1, T_2 values per voxel, thus assuming a single tissue component per voxel.

1.4. MULTI-COMPONENT ESTIMATIONS

DUE to the typical voxel size of 1mm × 1mm × 3mm MRI measurements, the assumption that a voxel consists of a single tissue type and thus can be represented with a single T_1, T_2 combination is almost never valid. This becomes especially problematic for estimations at tissue boundaries, as there sometimes is a smooth transition from one tissue to another or a hard transition that does not align with voxel boundaries. Also, such partial volume effects occur with diffusely mixed tissues and more gradual or diffuse transition from one tissue to the other.

Neglecting partial volume effects will therefore be a simplification and can be a source of error, since a single value representing the full voxel is inaccurate. Moreover, small structures can be missed. Segmentation methods based on T_1-weighted scans such as FSL [14] and SPM [15] therefore often include a partial volume estimation.

A main clinical application of multi-component models that assume multiple tissues per voxel lies in the study of the myelination of the axons in the brain. Myelin is a lipid-rich substance surrounding axons that accelerates the communication between nerve cells. The axons are surrounded by layers of myelin (approximately 10 nm thick), with water in between the layers. The presence of this water in close proximity to the myelin results in a signal that is in itself measurable with MR. Also, the myelin water is expected to have shorter relaxation times compared to the surrounding intra- and extracellular water. However, as the signal from the myelin water is mixed with that from surrounding tissues, multi-component methods are needed for measuring the myelin water content [16, 17]. This complicates the estimation problem compared to a single component estimation in which less parameters need to be estimated, i.e. a single combination of T_1, T_2 and M_0. To overcome this difficulty either more acquired information and therefore longer acquisitions than for a single component estimation is required or improved estimation and reconstruction methods are needed that make it possible to include prior information.

Myelin water fraction (MWF) imaging has until recently mainly been done with MESE sequences to identify different T_2-compartments [18]. This conventional qMRI sequence is, however, relatively slow, hindering clinical use. Specifically, while a noise robust single T_2 estimate could be obtained with mere eight echo times, a multi-component estimate

would require a high image quality and 32 echos or more.

To obtain multi-component estimations from a MESE measurement consisting of 32 echo, conventionally, a voxel-wise method is used [19]. In this algorithm a non-negative least squares solution is obtained that estimates the relative weight of a discretized set of possible T_2 values. Typically more than 40 T_2 values are modeled to contribute to the measured signal, making this problem under-determined. This can partly be addressed by regularization and thereby imposing preliminary knowledge about the expected T_2 distribution, but it leaves the method noise-sensitive.

Other methods for myelin water imaging have been proposed as described in several review papers [16, 17, 20, 21]. Examples of such methods are (1) multi-component driven-equilibrium single-pulse observation of T_1 and T_2 (MCDESPOT) [22], using a variable flip angle approach both estimating T_1 and T_2 , and (2) multi-gradient echo methods [16], estimating the T_2^* components. In all of these methods the number of tissues has been fixed to three to allow for easier modeling, and inhomogeneities or magnetization exchange need to be corrected for or might lead to a bias in estimated fractions.

1.5. RESEARCH CHALLENGES

1.5.1. MULTI-COMPONENT MRF

MRF enables simultaneous encoding of spatial information and tissue properties, such as the T_1 and T_2 parameters, in a time efficient manner. Conventionally it is asserted that there is a single tissue type per voxel, ignoring potential multi-component signal contributions. Ma et al. [9, 23], proposed to assume a total of three tissues in the brain, specifically white matter, gray matter and CSF to estimate the respective magnetization fractions for each of these tissues. They report that this results in additional findings in epilepsy patients [23]. The corresponding relaxation times were based on literature values [9] or k-means clustering of the single component results [23, 24]. However, this requires a-priori assumptions on the exact tissues being present or at least the number of components.

An alternative to these a-priori assumptions is an unconstrained multi-component estimation. However, this problem is a strongly ill-posed, since the number of unknowns is often larger than the number of data points. Accordingly, McGivney et al. [25] proposed a Bayesian method to obtain partial volume estimates per voxel. Effectively, a weighted ℓ_2-norm regularization was performed on the estimated T_1-T_2 distribution. However, this still leaves the problem highly ill-posed, resulting in T_1-T_2 distributions that differ strongly for neighboring voxels and are sensitive to undersampling artifacts. To cope with this, relatively long acquisitions with longer readout durations would be required leading to longer acquisition times, making standard MRF sequences less suitable for MC approximations.

1.5.2. MYELIN WATER IMAGING IN T_2 RELAXOMETRY

For myelin water imaging based on MESE T_2-relaxometry, the clinical applicability is hindered by long acquisition and reconstruction times as well as noise-like effects in the estimated MW fraction maps. Simultaneously, biased estimation was observed when

acquisition times were shortened [21].

1.5.3. MRF SEQUENCE OPTIMIZATION

While a multi-component model allows to characterize more complicated tissue structures, single component estimations provide an easier glimpse of tissue properties and are therefore broadly used. As described above, MRF uses a flip angle train to create a transient state magnetization over time. The choice of flip angle train has a strong effect on the accuracy of the estimated T_1, T_2 maps. Previous work [26, 27] has used the Cramér Rao lower bound to optimize MRF sequences such that the theoretically smallest possible variance of the estimated parameters is obtained. However this work does not include the effects of undersampling in the optimization, making it sensitive to imaging artifacts. Other studies used more heuristic and brute force methods [28, 29] or were limited to a selected number of tissues [30] when optimizing the MRF sequences.

1.5.4. MOTION SENSITIVITY

Although quantitative MRI holds many promises, an important challenge in any MRI acquisition protocol is motion. While healthy subjects are generally able to lie still for a long time, motion is more likely when patients are scanned and this is an issue affecting the quality of a substantial portion of clinical scans, sometimes even resulting in asking the patient to return for a repeated MRI-examination. This is an important reason to push for shorter scans times and create efficient, optimized MRF scans and effective reconstruction methods. However, motion can not always be avoided and can cause spatial, blurry artifacts in the reconstructed parameter maps or over- or underestimation of parameters [31]. In-plane motion in MRF can often be corrected with improved reconstruction methods since enough information to estimate the motion pattern and the original image is contained in the k-space signal [32]. However, the effects of through plane motion are generally more severe and less predictable since the region of interest moves out of view so that information is lost and the spin history changes along the slice.

1.6. RESEARCH GOALS

THE overall goal of this thesis is to develop methodology for quantitative MRI addressing the challenges as described in the previous section and as subsequent goal to make steps towards clinical use of these methods where possible. Specifically, the focus is on MR Fingerprinting and multi-component estimations, to obtain more information, enhance estimation accuracy and precision, and reduce scan time.

The first goal is to create a method for improved multi-component estimation method without making a priori assumptions about the exact number of tissues present and work towards clinical use of the created method. Therefore, a first associated goal is to study the repeatability and accuracy of the proposed method and compare to segmentations as obtained with conventional methods based on qualitative images. Another associated goal is to improve the reconstruction that is used in the MRF pipeline and make this more suitable for the performed multi-component analysis.

We also aim to work towards clinical use of the created method. Therefore we study the application of the proposed method on MESE data for myelin water imaging, apply

the proposed multi-component MRF method in brain scans of Multiple Sclerosis (MS) patients and study whether this method is sensitive to subtle white matter changes.

A next goal is to develop a flexible method to design efficient MRF sequences. Such a sequence design method should take into account the undersampling as performed in MRF and be designed for tissue parameter maps as realistic as possible in an in vivo scan.

The effects of in-plane motion in MRF have been studied before and solutions from other acquisitions (often designed for 3D readouts) can potentially be used. However, the effects of through plane motion are more unpredictable due to the relatively long acquisition time per slice (order of seconds) in which the magnetization and spin history changes over time. The final goal of this thesis will therefore be a study into the effects of through plane motion on an MRF experiment and possibilities to model these effects.

1.7. OUTLINE

In Chapter 2 we describe the multi-component estimation problem in MRF and propose to use a new joint-sparsity constraint (the SPIJN algorithm) on the tissue components in the optimization problem. We use this form of regularization to overcome the ill-posedness of the multi-component estimation, by introducing the prior information that only a small number of tissues is to be expected in the imaged region. The introduced regularization term therefore reduces the number of estimated components over the imaged region and make the multi-component minimization problem more stable. In Chapter 3 we further validate the accuracy and reproducibility of the estimated relaxation times. Also the accuracy and precision of the MW, WM, GM and CSF fraction maps obtained with the SPIJN-MRF method are studied in simulations and numerical experiments.

In Chapter 4 we will apply the SPIJN algorithm to MESE data, performing a T_2-multi-component analysis to obtain MWF maps. The proposed SPIJN algorithm uses reconstructed (compressed) images as input to perform the multi-component analysis, since the inverse multi-component problem and the proposed algorithm are more sensitive to noise and undersampling artifacts than single-component MRF. We will propose two new reconstruction algorithms in Chapter 5 that include the multi-component model *in the reconstruction* to allow for further regularization of the inverse problem. One reconstruction method, k-SPIJN, is tailored to the SPIJN algorithm, the other algorithm (Multi-component ADMM) does not include the joint-sparsity constraint and can therefore be used more generally. Both reconstruction methods allow for shorter acquisitions and can result in improved image quality compared to state-of-the-art reconstruction methods followed by a SPIJN estimation.

In Chapter 6 we apply the SPIJN algorithm on EPI-MRF data from MS patients and healthy controls. A distinct component is identified that relates to affected white matter tissue such as MS lesions and Dirty Appearing White Matter (DAWM). In Chapter 7 the SPIJN algorithm will be adapted to be more sensitive to small, local changes by applying a local joint sparsity constraint. We will show that this makes the method more sensitive to small changes such as lesions in EPI-MRF data as studied in the previous chapter.

In Chapter 8 we propose an method to optimize the MRF flip angle pattern in order to mitigate the effects of a standard, zero-filled reconstruction when a highly under-

sampled acquisition is performed. We will do this by using a perturbation theory based method that allows for efficient estimations of the undersampling error without time intensive calculations of complete MRF signal dictionaries.

In Chapter 9 we study the effects of through-plane motion and include those effects in the simulation of an MRF dictionary. We will verify these simulations and test the effect of parameter estimation with a motion-corrected dictionary.

Finally, in Chapter 10 I will discuss the open and future challenges of multi-component MR estimations and MRF in general.

2

FAST MULTI-COMPONENT ANALYSIS USING A JOINT SPARSITY CONSTRAINT FOR MR FINGERPRINTING

Martijn A. Nagtegaal
Peter Koken
Thomas Amthor
Mariya Doneva

Magnetic Resonance in Medicine 83.2 (2020), pp. 521534. ISSN: 1522-2594.
DOI: 10.1002/mrm.27947

ABSTRACT

Purpose: To develop an efficient algorithm for multi-component analysis of Magnetic Resonance Fingerprinting (MRF) data without making a-priori assumptions about the exact number of tissues or their relaxation properties.

Methods: Different tissues or components within a voxel are potentially separable in MRF because of their distinct signal evolutions. The observed signal evolution in each voxel can be described as a linear combination of the signals for each component with a non-negative weight. An assumption that only a small number of components are present in the measured field of view is usually imposed in the interpretation of multi-component data. In this work, a joint sparsity constraint is introduced to utilize this additional prior knowledge in the multi-component analysis of MRF data.

A new algorithm combining joint sparsity and non-negativity constraints is proposed and compared to state-of-the-art multi-component MRF approaches in simulations and brain MRF scans of 11 healthy volunteers.

Results: Simulations and in vivo measurements show reduced noise in the estimated tissue fraction maps compared to previously proposed methods. Applying the proposed algorithm to the brain data resulted in 4 or 5 components, which could be attributed to different brain structures, consistent with previous multi-component MRF publications.

Conclusion: The proposed algorithm is faster than previously proposed methods for multi-component MRF and the simulations suggest improved accuracy and precision of the estimated weights. The results are easier to interpret compared to voxel-wise methods, which combined with the improved speed is an important step towards clinical evaluation of multi-component MRF.

2.1. INTRODUCTION

MAGNETIC resonance fingerprinting (MRF) [9] is a novel technique for simultaneous mapping of multiple quantitative parameters. MRF has been mainly applied for single-component matching of a set of system and tissue parameters, e.g. T_1, T_2, and B_1^+, to each voxel. The standard method matches the measured signal to a pre-calculated dictionary with a pattern recognition algorithm based on the inner product similarity measure. However, single-component matching only considers the average signal produced by multiple tissues in a voxel. Multiple tissues can be present in a voxel either in the boundary region between two tissues or simply as a mixture of multiple components because of the complex structure of tissue. In the brain, the first effect occurs in the boundary region between white and gray matter, the second example is the case for myelin in the white matter. This partial volume effect [33] can lead to blurring artifacts or averaged tissue parameters in the maps obtained by single component matching.

Multi-component analysis takes into account that a voxel can consist of several tissues and assumes that the measured signal is composed of a weighted sum of signals corresponding to the individual tissues present in the voxel. Multi-component analysis can be performed for standard relaxometry scans like multi-echo spin echo (MESE) T_2 mapping by a multi-exponential fit. The standard method for multi-component analysis is the T2 Non-Negative Least Squares (T2NNLS) algorithm introduced by Whittall and MacKay [34], based on the Non-Negative Least Squares (NNLS) algorithm by Lawson and Hanson [35]. With this algorithm a smooth T_2 spectrum is obtained and the Myelin Water Fraction (MWF) is determined by integrating over all weights in the spectrum with $T_2 < 40\,\text{ms}$. Besides myelin water, another peak can be recognized which belongs to intra-extracellular water [18].

Multi-component analysis applied to MRF has the potential to distinguish more tissues than multi-exponential T_2 methods because multiple tissue parameters are taken into account. A first approach to Multi-Component MRF (MC-MRF), where each voxel is modelled as a composition of only three possible tissues with predefined relaxation times, was proposed in the supplemental material of the original MRF publication [9]. A dictionary containing only three T_1,T_2 combinations was used with a least-squares algorithm to determine the weights for the three possible components. This approach imposes a very strong constraint, namely that the number and relaxation times of the individual components are known. This may not always be the case and the resulting solution is very sensitive to the choice of tissue parameters. Deshmane et al. [24] expanded this approach by estimating the main tissues based on the single component matching combined with k-means clustering, where the number of components is selected on forehand. This partial volume model assumes that most voxels contain a single component and partial volume effects are only present at the boundaries of tissues (See Supporting Information Figure S2.1).

A first MC-MRF method using a large dictionary of T_1 and T_2 combinations was proposed in [25], which applies a Bayesian estimation method to obtain a MC-MRF matching. This method considers each voxel independently and is able to distinguish different components within a voxel without explicitly including prior knowledge about the number of components or their corresponding relaxation times. This approach applies a sparsity constraint, but the coefficient weights are complex and the absolute value of

the complex weights is returned as the final solution. Computation times of 12 seconds per voxel were reported in this work, corresponding to several days for the processing of a single slice. Another voxel-wise approach was recently proposed in [36], which applies both sparsity and non-negativity constraints to the component weights within an iteratively reweighted ℓ_1-norm regularized least squares algorithm. Computation times between 0.1 s and 1 s for a single voxel are reported for this algorithm when executed on a computer cluster.

Besides the long processing times reported in these approaches, another difficulty is the interpretation and visualization of the results. When the complete MRF measurement is considered, the matched components in each voxel can correspond to different relaxation times, and need further processing to visualize the results. This can be done with a simple grouping based on T_1 or T_2 ranges as done for the MWF from T2NNLS or with a more sophisticated method e.g. Bayesian grouping strategies [25]. This interpretation step requires additional assumptions about the tissues present in the region of interest (ROI), the number of components or voxels in which a pure tissue can be found.

Two works are currently published in arXiv, in which the multi-component analysis includes dependencies between different voxels. The greedy-approximate projection algorithm (GAP-MRF) [37] approximates the main tissues present in the ROI and determines MC-MRF maps based on these components. This method results in 5-6 components in the brain, assuming that most voxels contain single tissue. Relaxation-Relaxation Correlation Spectroscopic Imaging (RR-CSI) [38] is a related approach, which uses an inversion recovery multi-echo spin-echo (IR-MESE) acquisition sequence simultaneously encoding T_1 and T_2 relaxation times. The corresponding multi-component analysis assumes smoothness in the T_1, T_2 parameter space and spatial smoothness to determine T_1, T_2 distributions for all voxels. This method can be seen as an extension on T2NNLS methods where spatial smoothness is applied [39–41] and multiple relaxation parameters are simultaneously encoded. Six main peaks are detected in the reconstructed spectrum, which are interpreted as six different components. This algorithm was not demonstrated on MRF-data, but is related because it performs multi-component analysis from a sequence simultaneously encoding T_1 and T_2 relaxation times. Another work by the same authors proposes a set of greedy algorithms for non-negativity constraining simultaneous sparse recovery [42], related to the GAP-MRF algorithm [37].

In this study, we investigate different approaches for MC-MRF with the aim to obtain an accurate and robust result in a shorter time than the previously proposed MC-MRF approaches. Several different approaches were implemented and compared, including the NNLS algorithm as used for T2NNLS, the fixed 3 component approach presented in the original MRF publication [9], the Bayesian algorithm [25] and reweighted-ℓ_1-norm regularized algorithm [36]. Furthermore, we propose a new algorithm that applies joint sparsity and non-negativity constraints for the component weights, which can reduce the noise amplification in MC-MRF keeping the reconstruction time tractable. The main premise of this approach is that only a small number of "basis" tissues is present throughout the ROI and the tissue in each voxel is a mixture of these basis tissues. The method is theoretically described and compared with the previously mentioned methods. The evaluation was performed in numerical simulations and in brain

data of 11 healthy volunteers.

2.2. METHODS

2.2.1. THEORY

Voxel-wise problem setting In a multi-component signal model, the MRF signal $\mathbf{x}_j$ of a voxel $j \in \{1,2,...J\}$, where J is the number of voxels, can be written as

$$\mathbf{x}_j = D\mathbf{c}_j + \mathbf{e}_j, \tag{2.1}$$

where D is the MRF dictionary, $\mathbf{c}_j$ the vector containing the weights for the different components and $\mathbf{e}_j$ the noise term. The measured MRF signal is generally complex, however, if the phase is known, the signal can be rotated to the real axis resulting in a real vector $\mathbf{x}_j \in \mathbb{R}^M$ of length M, where M is the number of time points of the fingerprinting sequence or the length of the signal after SVD compression [43].

The dictionary $D \in \mathbb{R}^{M\times N}$ contains the signal evolutions for N different components. The measured signal is modeled as a non-negative linear combination of the dictionary signals. The weights of these different components are contained in the vector $\mathbf{c}_j \in \mathbb{R}^N_{\geq 0}$. Besides the non-negativity constraint, it can be assumed that the weight vector $\mathbf{c}_j$ is sparse, thus the measured signal can be represented by a small number of components, representing a small number of tissue types. The weights for each component in Eq. (2.1) can be obtained by least squares minimization. When we include the requirement that $\mathbf{c}$ is non-negative, we obtain the following NNLS problem for each voxel j:

$$\min_{\mathbf{c}_j \in \mathbb{R}^N_{\geq 0}} \|\mathbf{x}_j - D\mathbf{c}_j\|_2^2. \tag{2.2}$$

For a dictionary with a large number of components, this problem is highly under-determined and has infinitely many solutions. This formulation is very similar to a compressed sensing problem. Therefore, if the solution vector is sparse, there are some theoretical guarantees that it can be recovered using a sparsity constraint. However, due to the high coherence of MRF dictionaries a unique solution only exists for very sparse solutions.

One sparsity promoting approach to solve this problem is the active set NNLS algorithm as proposed by Lawson and Hanson [35, Chapter 23]. The NNLS algorithm shows similarities to the orthogonal matching pursuit (OMP) algorithm [44] with its active set principle and results in sparse solutions.

Another approach to restrict the solution is in the form of regularization. A typical choice for sparsity promoting regularization is the ℓ_1-norm. The non-negativity constraint makes it possible to use the ℓ_1^2-non-negative regularization instead, which can be used with computationally more efficient algorithms [45]:

$$\min_{\mathbf{c}_j \in \mathbb{R}^N_{\geq 0}} \|\mathbf{x}_j - D\mathbf{c}_j\|_2^2 + \lambda^2 \|\mathbf{c}_j\|_1^2, \tag{2.3}$$

where $\lambda > 0$ is the regularization parameter. This problem can be recast to the equivalent non-negative least squares problem of the form

$$\min_{\mathbf{c}_j \in \mathbb{R}^N_{\geq 0}} \|\bar{\mathbf{x}}_j - \bar{D}\mathbf{c}_j\|_2^2, \tag{2.4}$$

where $\bar{D} \in \mathbb{R}^{M+1 \times N}$ and $\bar{\mathbf{x}}_j \in \mathbb{R}^{M+1}$ are given by:

$$\bar{D} = \begin{bmatrix} & D & \\ \lambda & \dots & \lambda \end{bmatrix} \text{ and } \bar{\mathbf{x}}_j = \begin{bmatrix} \mathbf{x}_j \\ 0 \end{bmatrix}, \tag{2.5}$$

which can still be solved using the NNLS algorithm from [35]. In this setting, an independent (sparse) solution is obtained for each voxel.

Joint sparsity constraint The voxel-wise approach can lead to different components for each voxel, even for a small region of interest that has uniform intensity in a contrast weighted image. This is most likely due to noise and not due to actual large variability in the tissue composition. The main premise in this work is that the tissue in the measured volume is composed of a small number of "basis tissues", or components, which are shared for all voxels in the region of interest. In other words, we assume that there is a small number of dictionary signals (atoms), which form a basis for the measured MRF signal for the whole region of interest. The measured MRF signals can be represented by a linear combination of this shared set of dictionary signals. This assumption is similar to the fixed basis approach [9], however, we don't assume that the number of components and their T_1 and T_2 values are known in advance. To include this requirement in the reconstruction, we introduce the joint sparsity constraint.

The joint forward model can be written as

$$X = DC + E, \tag{2.6}$$

where $X = [\mathbf{x}_1, \dots \mathbf{x}_J] \in \mathbb{R}^{M \times J}$ contains the measured signals and $C = [\mathbf{c}_1, \dots \mathbf{c}_J] \in \mathbb{R}^{N \times J}$ contains the weights for all the voxels and E contains the noise terms. Each row $\mathbf{c}^i$ of the weight matrix contains the weights of a single component i for all voxels in the region of interest. The joint inverse problem can be written as a NNLS minimization problem:

$$\min_{C \in \mathbb{R}^{N \times J}_{\geq 0}} \|X - DC\|_F^2, \tag{2.7}$$

where $\|\cdot\|_F$ denotes the Frobenius norm.

The requirement that the measured signals can be represented by a small number of shared signals, can be summarized as the constraint that $\sum_{i=1}^{N} \|\mathbf{c}^i\|_0$ must be small. This joint sparsity constraint has been considered with different names and in different problem settings [46–50] and has only been combined with a non-negativity constraint in a Greedy algorithm in [42].
The non-negativity and joint sparsity constraints can be combined in the minimization problem

$$\min_{C \in \mathbb{R}^{N \times J}_{\geq 0}} \left[\|X - DC\|_F^2 + \mu \sum_{i}^{N} \|\mathbf{c}^i\|_0 \right], \tag{2.8}$$

where μ is a regularization parameter that balances sparsity and reconstruction error.

Sparsity Promoting Iterative Joint Non-negative least squares (SPIJN) algorithm To solve the optimization problem 2.8, we propose a new iteratively reweighted non-negative least squares algorithm, called Sparsity Promoting Iterative Joint NNLS (SPIJN), which is summarized in Algorithm 2.1 to which we will refer in the rest of this section. In the spirit of reproducible research, the source code of the proposed algorithm including the later discussed numerical phantom is available at `https://github.com/MNagtegaal/SPIJN`.

The algorithm uses the NNLS algorithm to solve the joint NNLS problem, with a reweighting in each iteration. The weights promote a jointly sparse solution, finding a small number of atoms that serve as a common basis for all voxels. Both the measured signals X and the dictionary D are normalized such that $\|\mathbf{x}\|_2 = \|\mathbf{d}\|_2 = 1$. The normalization of the dictionary prevents a bias caused by high signal intensity, the normalization of the signals makes sure that all voxels have an equal influence on the joint sparsity.

The core of the algorithm is formed by lines 9-14. In each iteration, the NNLS algorithm is used to solve the reweighted problem in line 13. The weights

$$w_{k+1,i} \leftarrow \|\mathbf{c}_k^i\|_2 + \epsilon, \forall i \in \{1, ..., N\} \tag{2.9}$$

are used, where ϵ is a small parameter to improve the stability. To make the reweighting more effective, the ℓ_1^2 regularization from Eq. (2.5) is used in lines 11 and 12 of the algorithm. The regularization parameter λ is scaled with $\log_{10} J$, to make the values of the regularization parameter less sensitive to the number of voxels. The scaled regularization parameter $\bar{\lambda}$ determines the sparsity of the solution, similar to μ in Eq.(2.8).

The algorithm is stopped after T iterations or when convergence is reached, according to

$$\frac{\|C_{k+1} - C_k\|_F}{\|C_k\|_F} < \delta, \tag{2.10}$$

where δ is the convergence threshold, as calculated in line 15.

Most of the dictionary elements are not used after a small number of iterations and remain unused for the rest of the process. These dictionary elements can therefore be removed from the dictionary (line 7) to speed up the computations. This pruning is performed in iteration p, where rows with an ℓ_1 norm smaller than $\tilde{\delta} \cdot J$ are pruned. In the final solution, the weights corresponding to the pruned dictionary atoms are set to 0.

2.2.2. EXPERIMENTS

Simulated data To test the proposed method, simulations were performed with a fully sampled numerical phantom containing three different components. The relaxation times for the simulated components were chosen according to a three tissue brain model, where the measured MR signal is a combination of myelin water (MW), intra- and extracellular water (IEW) and free water (FW). The first component is in the range of MW with relaxation times (T_1 =67 ms and T_2 =13 ms) [51], the second component in the range IEW (T_1 =1 s and T_2 = 100 ms) and the third component in the range of FW (T_1 = 2000 ms and T_2 = 50 ms) [52]. 10 multi-component compositions were simulated, the first component had a weight of 10 % in each composition, the other two components vary from 0 % to 90 %. For each combination, the signal evolution was calculated and Gaussian

Algorithm 2.1 The Sparsity Promoting Iterative Joint NNLS (SPIJN) algorithm to perform a multi-component analysis for an MRF measurement.

INPUT:

$X = [\mathbf{x}_1, ...\mathbf{x}_J]$	-	J real valued, normalized signals (size $M \times J$)
D	-	a real valued, normalized dictionary (size $M \times N$)
λ	-	regularization parameter
T	-	maximum number of iterations (default 20)
$p, \tilde{\delta}$	-	pruning takes place at this iteration, using this threshold (defaults $2, 10^{-10}$)
δ	-	convergence threshold (default 10^{-4})
ϵ	-	parameter for the reweighting (default 10^{-4})

OUTPUT:

C - non-negative, jointly sparse solution for optimization problem 2.8.

$k \leftarrow 1$ ▷ Counter for the number of iterations
$C_1 \leftarrow \arg\min_{C \in \mathbb{R}^{N \times J}_{\geq 0}} \|X - DC\|_F^2$ ▷ Initial solution
$d \leftarrow 1$ ▷ Initial convergence threshold
$\bar{\lambda} \leftarrow \lambda \cdot \log_{10} J$ ▷ Scale the regularization parameter with the number of voxels
while $k \leq T$ and $d > \delta$ **do**
  if $k = p$ **then**
    Prune D and C according to $\frac{\|\mathbf{c}_k^i\|_1}{J} < \tilde{\delta}$ ▷ Pruning of the dictionary
  end if
  $w_{k+1,i} \leftarrow \|\mathbf{c}_k^i\|_2 + \epsilon, \ \forall i \in \{1, ..., N\}$ ▷ Calculation of the weights
  $W_{k+1} \leftarrow \text{diag}\left(\mathbf{w}_{k+1}^{1/2}\right)$
  $\tilde{D}_{k+1} \leftarrow \begin{bmatrix} DW_{k+1} \\ \bar{\lambda}\mathbf{1}^T \end{bmatrix}$ ▷ Weighting and ℓ_1^2 regularization, $\mathbf{1}$ is a vector of all ones with length N
  $\tilde{X} \leftarrow \begin{bmatrix} X \\ \mathbf{0}^T \end{bmatrix}$ ▷ ℓ_1^2 regularization
  $\tilde{C}_{k+1} \leftarrow \arg\min_{C \in \mathbb{R}^{N \times J}_{\geq 0}} \|\tilde{X} - \tilde{D}C\|_F^2$ ▷ Solve step using the NNLS algorithm
  $C_{k+1} \leftarrow W_{k+1}\tilde{C}_{k+1}$ ▷ Compensate for the weighting
  $d \leftarrow \frac{\|C_{k+1} - C_k\|_F}{\|C_k\|_F}$ ▷ Convergence threshold
  $k \leftarrow k + 1$
end while
if $k > p$ **then**
  Fill C_k with zeros at pruned dictionary atoms. ▷ To return a matrix with weights for all the components
end if
$C \leftarrow C_k$ ▷ Only return the last iteration

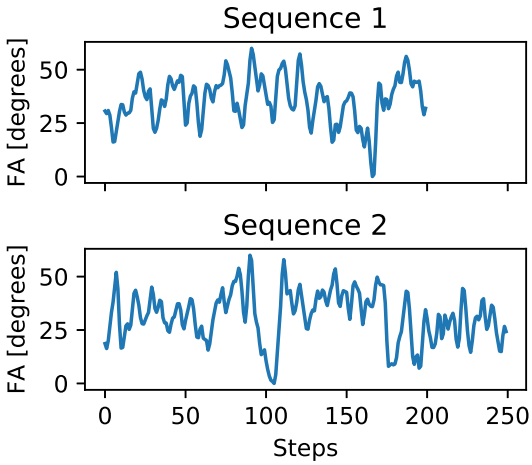

Figure 2.1: The two flip angle (FA) sequences used in this work. Both sequences have a repetition time of 15 ms. Sequence 1 has a $TE = 4$ ms and repetition delay of 500 ms. Sequence 2 has a $TE = 5$ ms and repetition delay of 3 s. The maximal flip angle in both sequences is 60ř.

noise was added, resulting in a total of 10×10 simulated voxels with a signal to noise ratio of 50.

A gradient-spoiled MRF sequence [10] of 200 time points was used for the simulations. The sequence had a flip angle variation as shown in Figure 2.1 (Sequence 1) and a constant repetition time of $TR = 10$ ms. A logarithmically spaced dictionary with 3240 atoms consisting of 80 T_1 values from 10 msto 5 s and 80 T_2 values from 10 ms to 5 s with the restriction $T_2 \leq T_1$ was computed with the extended phase graph algorithm (EPG) [53].

In vivo data To demonstrate the feasibility of the proposed method in vivo, fully sampled MRF brain data were acquired for 11 healthy volunteers with informed consent obtained. The scans were performed with different MRF sequences on two different field strengths in order to test the approach in different settings. The measured signals were corrected with a phase term to obtain real-valued vectors. In a pre-processing step, the lipid tissue and skin were removed to keep only the region containing the brain.

One volunteer scan was performed on a 1.5 T Philips Achieva scanner with Sequence 1 as given in Figure 2.1 using an 8 channel head coil and a spiral acquisition pattern, a FOV of 240 mm×240 mm, 1 mm× 1 mm in plane resolution and 5 mm slice thickness. Three slices were acquired with an acquisition time of 359 ms. A logarithmically spaced dictionary was computed with T_1 ranging from 10 ms to 4 s in 100 steps and T_2 from 4 ms to 2 s in 80 steps, with the restriction $T_2 \leq T_1$, consisting of 4974 dictionary atoms.

Ten volunteers were scanned on a 3 T Philips Ingenia scanner with Sequence 2 as given in Figure 2.1 with a Cartesian sampling pattern, a FOV of 240 mm×240 mm, in plane resolution of 1.25 mm×1.25 mm and 10 mm slice thickness. The acquisition time

for one slice was 337 s. For the dictionary the same T_1 and T_2 combinations were used as in the numerical experiments and included different relative B_1^+-inhomogeneity values, ranging from 0.75 to 1.26 with step size 0.003, leading to a dictionary size of 845580.

Comparison to other algorithms The proposed SPIJN algorithm was compared in simulations to three voxel-wise algorithms, the NNLS algorithm [35], the MC-MRF reweighted-ℓ_1-norm regularized algorithm [36] and the MC-MRF Bayesian approach [25]. The NNLS forms the basis of our algorithm and a comparison is included in order to estimate the effects of the joint sparsity constraint. The 1.5 T measurement was used to compare the SPIJN algorithm to the three voxel-wise algorithms and MC-MRF analysis using two different subdictionaries containing only three fixed components. The first set (set A) of components of the subdictionaries is based on literature values from a work applying this approach for MC-MRF [54] and the (T_1, T_2) values are (127 ms, 21 ms), (1267 ms, 127 ms) and (2056 ms, 485 ms). The second set B is based on components as matched by SPIJN with (T_1, T_2) relaxation times (10 ms, 10 ms), (781 ms, 58 ms) and (1821 ms, 842 ms). The comparison with the two different sets of fixed components was performed to evaluate the sensitivity to the choice of the components.

The normalized root mean squared error (NRMSE) is used to evaluate the data consistency between the estimated signal from the multi-component matching and the measured signal. The NRMSE is calculated as $\frac{\|X-DC\|_F}{\|X\|_F}$.

For the Bayesian algorithm three parameters had to be chosen, for the shape parameters $\alpha = 2$ and $\beta = 0.1$ were used. Regularization parameter $\mu = 6$ was used for the in vivo measurement and $\mu = 0.01$ for the simulations. For the reweighted-ℓ_1-norm regularized algorithm $\lambda = 0.01$ was used for the in vivo data and $\lambda = 0.001$ for the simulations. For the SPIJN algorithm $\lambda = 3.5$ was used for the 1.5 T in vivo measurements and $\lambda = 0.03$ in the simulations.

All algorithms were implemented in Python. SVD compression [43] to a dimension of 25 was used for all the measurements and simulations. The NNLS algorithm uses the FORTRAN implementation as included in the SciPy package. For the subdictionaries the NNLS algorithm was used to find the corresponding weights for the fixed components.

The single-voxel algorithms require grouping to relate similar components found in different voxels to each other and to known tissue types. Components in the range $T_1 \leq 200$ ms and $T_2 \leq 40$ ms are considered to belong to the MW component, in the range 200 ms $\leq T_1 \leq$ 1800 ms and 30 ms $\leq T_2 \leq$ 200 ms to the IEW and in the range $T_1 \geq 850$ ms and $T_2 \geq 200$ ms to the FW. Components outside these ranges are considered as outliers and not grouped to any of the three water types. These ranges are based on a combination of the following; relaxation times as expected from literature [55], ranges as used for T_2 relaxometry MWF mapping and the visually distinguishable clusters in the MC-MRF decompositions from the different algorithms.

Repeatability of the SPIJN algorithm The 10 MRF measurements at 3 T were used to evaluate the repeatability of the multi-component matching from the SPIJN algorithm on multiple healthy volunteers with the same MRF sequence. Single component matching was first used to obtain the B_1^+ map. Then for each voxel the corresponding subdictionary with fixed B_1^+, was selected for the MC-MRF analysis. The SPIJN algorithm was

then used to obtain a decomposition for each of the measurements. The regularization parameter was selected in a way that the number of components was as small as possible but without increasing the NRMSE compared to regularized voxel-wise methods. This resulted in λ values of either 12 or 15 for these measurements. From these decompositions, the components corresponding to white and gray matter were selected for the evaluation.

The relaxation times matched to the white and gray matter are determined as an indication of the repeatability of the SPIJN decomposition over multiple scans. An overview of relaxation times from [52, 55] for white and gray matter at 3 T from different studies is given in Table 2.1 as a reference.

Table 2.1: An overview of relaxation times (ms) from [52, 55] for white and gray matter at 3 T. The tables include the number of studies resulting in the list of literature values used to determine the average values, standard deviations and minimal and maximal values .

T_1	Average (ms)	Std (ms)	Min (ms)	Max (ms)	# Studies
Gray matter	1459	192.3	968	1815	20
White matter	974	210	728	1735	26
T_2	Average (ms)	Std (ms)	Min (ms)	Max (ms)	# studies
Gray matter	92.6	16.9	65	110	5
White matter	60.8	13.1	49.5	79.6	4

2.3. RESULTS

2.3.1. COMPARISON TO OTHER ALGORITHMS

Simulated data The results of the multi-component analysis for the simulated data are shown in Figs. 2.2 and 2.3. Figure 2.2 shows the ground truth of the three different components and the component weights obtained by the four different algorithms. The root mean squared error (RMSE) is given above each of the grouped components. The results of the NNLS and the reweighted-ℓ_1-norm-regularized algorithm are very similar, while the Bayesian approach results in larger errors than the other two voxel-wise methods. The SPIJN algorithm results in a smaller error and less variance in the solution.

Figure 2.3 shows the distribution of the T_1 and T_2 values of the matched components for the different algorithms, the grouping boxes and the true relaxation times of the simulated components. The matched components are spread around the true relaxation times and for all the algorithms the component with the shortest T_1 and T_2 is the most difficult to estimate. Although the T_1 and T_2 values of the shortest component are biased, the corresponding component weights are still accurate.

The reweighted-ℓ_1-norm regularized algorithm shows a smaller spread in the relaxation times of the matched components compared to the other voxel-wise methods, but the differences with the NNLS algorithm are small. The SPIJN algorithm matches three components with T_1, T_2 relaxation times (52.17 ms, 10 ms), (1036.78 ms, 105.91 ms) and (1945.36 ms, 510.75 ms). The computations for 100 voxels took 0.935 s for the NNLS algorithm, 56.49 s for the ℓ_1 algorithm, 82.60 s for the Bayesian method and 1.658 s for the SPIJN algorithm. The computations were performed on a standard laptop (IntelCore

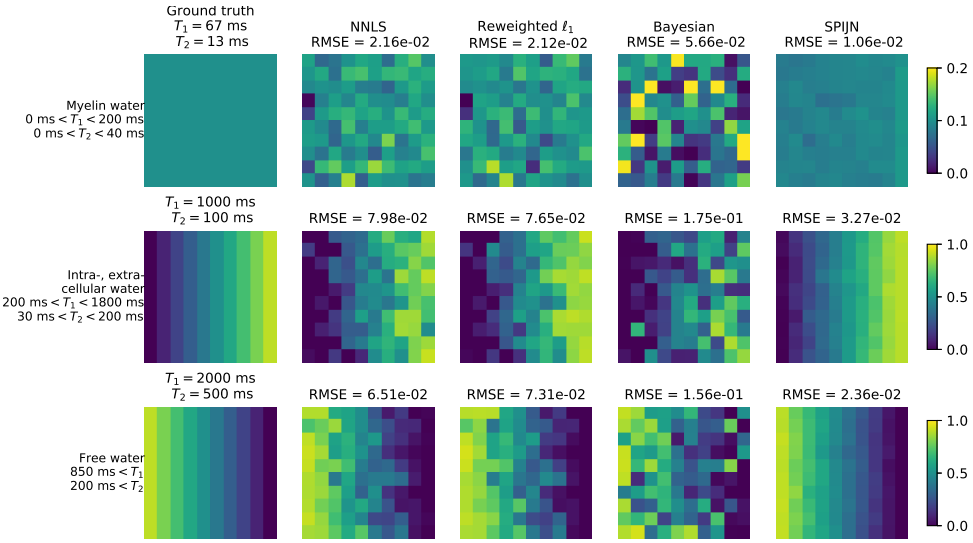

Figure 2.2: The results of the simulations with three components comparing the four different MC-MRF algorithms. Sequence 1 as shown in Figure 1 was used in the simulation. A numerical phantom containing three different components was simulated with an SNR of 50. The numerical phantom consists of 100 pixels, the first component is present in each pixel with ten percent and the other two components vary in the horizontal direction from 0 % to 90 % in 10 steps. The first column shows the ground truth for the distribution of the weights for the different components and the other columns show the retrieved component weights with the different algorithms and the corresponding root mean squared error (RMSE) to the ground truth.

i5-6300U CPU @2.4 GHz 2 cores, 4 threads).

In vivo data The 1.5 T measurement was used for in vivo comparison of the SPIJN algorithm to previously proposed MC-MRF methods. Figure 2.4 shows the T_1 and T_2 values of the matched components for the different algorithms and how they are grouped to a MW component, IEW and free water. Figure 2.5 shows the component weights for the different methods, grouped in the same manner as for the simulated data, including the NRMSE values. The processing time for the NNLS algorithm was 123 s, for the reweighted-ℓ_1-norm regularized algorithm 169 min, for the Bayesian algorithm 89 min and for the SPIJN algorithm 171 s. The matrix size was 240 × 240, of which a ROI consisting of 32 % of the voxels with signal above the noise threshold was selected, resulting in 18546 voxels.

The results of the NNLS and the reweighted-ℓ_1-norm regularized algorithm are very similar just as for the simulations, but visibly differ from the results of the Bayesian approach. The SPIJN algorithm shows similar structures for the IEW and FW components, but the estimated weights are less noisy compared to the voxel-wise methods. Although the NRMSE of the NNLS, reweighted-ℓ_1-norm regularized and SPIJN algorithm are similar, the introduction of the joint sparsity constraint results in less noise and more clear anatomical structures in the estimated weights.

The results of the two MC-MRF decompositions with three fixed components are

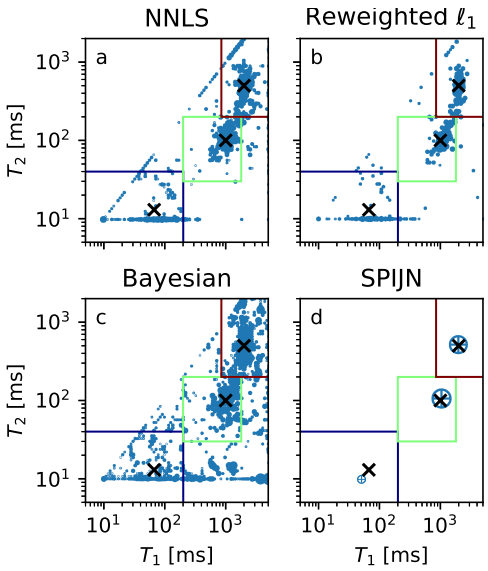

Figure 2.3: The distribution of the matched components for the numerical phantom with the different algorithms. The boxes indicate how the components are grouped. The blue box is the short component, the green box the middle component and the red box the long component. The size of the circles corresponds to the relative abundance of the components. The three crosses give the locations of the true components.

very different, depending on the chosen combination of relaxation times. Just as the SPIJN algorithm, they show less noise in the estimated weights compared to the voxel-wise methods. The results of the first set are consistent with the results from [54], but the higher NRMSE indicates a lower consistency with the measured data. The second set of fixed components was based on the results from the SPIJN algorithm and the resulting weights are very similar to the results from the SPIJN algorithm.

The SPIJN algorithm resulted in five components, which are shown in Figure 2.6. These components were grouped to three components in Figure 2.5, which was necessary in order to compare the results of SPIJN to the voxel-wise algorithms.

2.3.2. REPEATABILITY OF THE SPIJN MULTI-COMPONENT ANALYSIS

The ten 3 T measurements are used to test the repeatability over multiple healthy volunteers. The estimated T_1 and T_2 relaxation times for the components related to white and gray matter are listed in Table 2.2. The results for the different measurements are similar and in general within one or two steps of the dictionary resolution away from the mean value. Except for the T_2 relaxation time of the gray matter, the matched values are consistent with literature values [52] as tabulated in Table 2.1. While a single component is reconstructed for white matter with our decomposition, the voxels corresponding to gray matter also had a contribution from a component with longer relaxation times.

Only four components were matched by the SPIJN algorithm in the 3 T brain measurements. These estimated component weights are shown for one volunteer in Figure 2.7. Component *a* and *b* are assumed to be related to white and gray matter respectively, where as the other two components can be attributed to CSF.

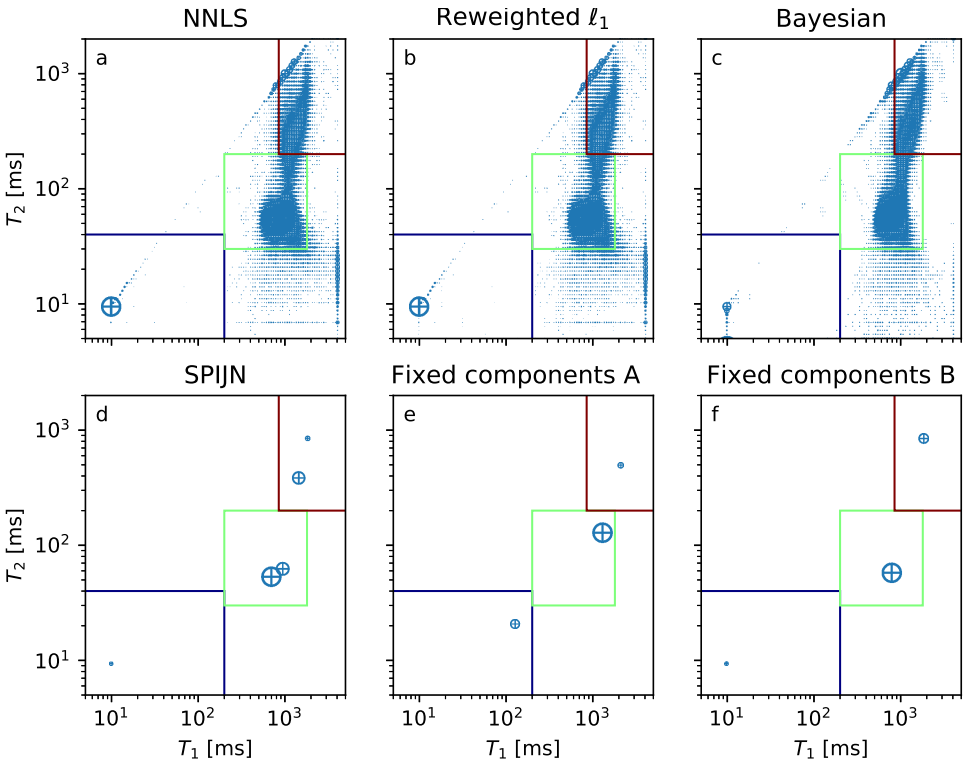

Figure 2.4: The distribution of the matched components for the 1.5 T in vivo measurement from the four different algorithms and an approach with two different subdictionaries. The blue box is the short component (myelin water), the green box the middle component (white and gray matter) and the red box the long component (CSF). The size of the circles corresponds to the relative abundance of the components. The subdictionaries contain pre-fixed components, the first set is based on [24] , the second set on results from the SPIJN algorithm.

2.4. DISCUSSION

A new algorithm with joint sparsity constraint was proposed to perform a MC-MRF analysis. The SPIJN algorithm was theoretically described and its basic feasibility was demonstrated in simulations and in vivo brain measurements. The proposed algorithm was compared to other recently proposed algorithms for MC-MRF analysis as well as to the NNLS algorithm, and the repeatability of the results was demonstrated in 10 healthy volunteers.

A first, general observation from the performed experiments is that the NNLS and the reweighted-ℓ_1-norm regularized algorithm give very similar results. Both algorithms try to solve the same mathematical problem, but the NNLS algorithm is much faster without the need for regularization. Secondly, the results from the Bayesian approach were significantly different compared to the other algorithms. This can be explained by the absence of the non-negativity constraint during the iterations of the algorithm.

To compare the voxel-wise algorithms to the SPIJN algorithm, the results were grou-

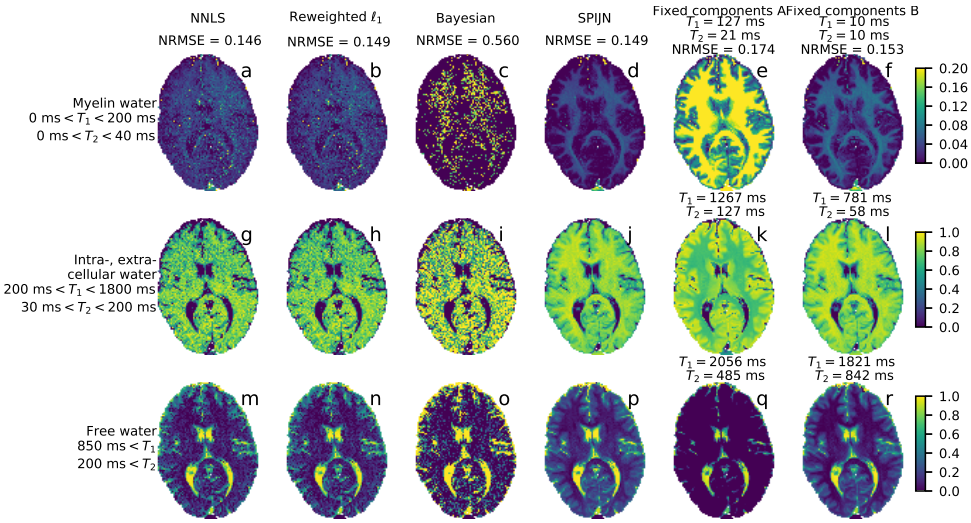

Figure 2.5: The results of different MC-MRF algorithms for a brain MRF measurement at 1.5 T. The rows correspond to the different grouped components and the columns to the different algorithms. The last two columns contain the results using dictionaries using only 3 components. The color indicates the relative weight of the (grouped) component in each voxel. The first row has a different color scale than the lower two rows.

ped based on T_1, T_2 ranges. Using larger grouping regions enables including all matched components, generally leading to smoother fraction maps, but the grouped relaxation times are less related. When using smaller regions, it is more likely to miss components, leading to noisier tissue fraction maps. Thus, the visualization of voxel-wise methods is a difficult problem and the provided visualization may not be optimal for each of the individual algorithms, but nevertheless provides some basis of comparison between the results of different algorithms.

The numerical simulations showed that the proposed SPIJN algorithm can separate 3 components with improved accuracy and precision compared to voxel-by-voxel MC-MRF approaches, with a FOV of 100 voxels and 10 voxels per component weight combination. This indicates that the joint sparsity constraint can improve the stability of the ill-posed inverse problem of MC-MRF already with a small number of voxels. Therefore, a patch-based approach, in which the joint sparsity is applied on small local neighbourhoods is feasible, and could be an alternative to the global joint sparsity investigated in this work.

The results from the in vivo data in Figure 2.5 show that the SPIJN algorithm finds a small number of components that form a common basis for the measured MRF signal of the entire ROI, without significantly increasing the representation error compared to voxel-by-voxel MC-MRF approaches. The relaxation times of these components are centered withing clusters formed by the relaxation times obtained by the voxel-by-voxel algorithms on the (T_1-T_2) plane. The SPIJN algorithm results in a similar noise level in the component weights as the approach with 3 fixed, a priori chosen components,

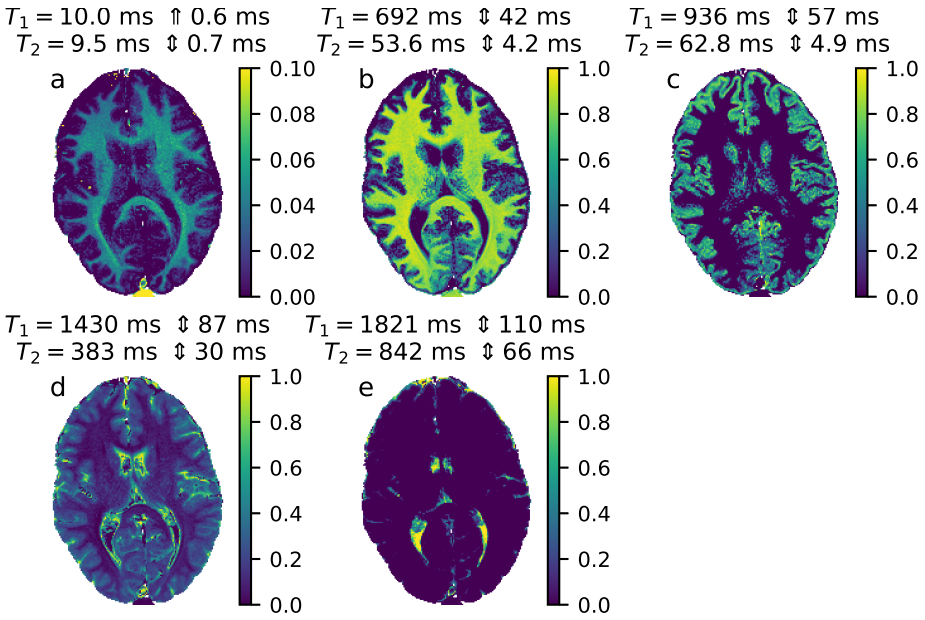

Figure 2.6: The five components matched by the SPIJN algorithm for a measurement at 1.5 T. The color indicates the relative weight of the component in each voxel. The relaxation times for the different components are given. To indicate the grid spacing at a certain point the symbol ⇕ is used, indicating the average distance to the next lower and next higher relaxation time for the matched T_1, T_2 combination. The relaxation times of component *a* are related to myelin water, the relaxation times of component *b* to white mater, the relaxation times of component *c* to gray matter and the relaxation times of components *d* and *e* to CSF.

but it additionally has the freedom to better adapt the chosen components to the data. The components obtained by the SPIJN algorithm can be interpreted as basis tissues that compose the tissue within each voxel and form the mixed signal measured in MRF. These components are recovered merely with the assumption of sparsity and don't necessarily need to correspond to known physical tissues. Depending on the coherence of the dictionary and the selected regularization parameters, it is possible that multiple components would be recovered as a single mixed component or a single component is split into multiple in the decomposition. While the ability of the algorithm to accurately separate multiple components was confirmed in simulations, in-vivo validation is more difficult since the number of components is unknown.

Nevertheless, in the performed experiments, the resulting MC-MRF decompositions showed similarities to decompositions presented in previous works [37, 38, 56] and can be related to known anatomical structures. With the proposed algorithm, five components were observed for the 1.5 T measurement: one component that could be related to a MW component, two components related to white matter and gray matter that were grouped to IEW for the comparison, and two more components can be interpreted as free water. The weight of the MW component of 5% is lower than the MWF as known from T_2 relaxation measurements (typically 10%). Although the results were much nois-

Table 2.2: The matched relaxation times for the white matter and gray matter component for measurements at 10 volunteers at 3T.

	White matter T_1 (mean 898 ms)				**Gray matter T_1** (mean 1241 ms)				
Relaxation time [ms]	830	881	936	994	1056	1192	1267	1346	
Grid step size [ms]	50	53	57	60	64	72	77	81	
Count	1	6	2	1	2	1	4	3	
	White matter T_2 (mean 53.2 ms)				**Gray matter T_2** (mean 58.8 ms)				
Relaxation time [ms]	50	54	58		50	54	58	63	68
Grid step size [ms]	4	4	5		4	4	5	5	5
Count	4	4	2		1	1	5	2	1

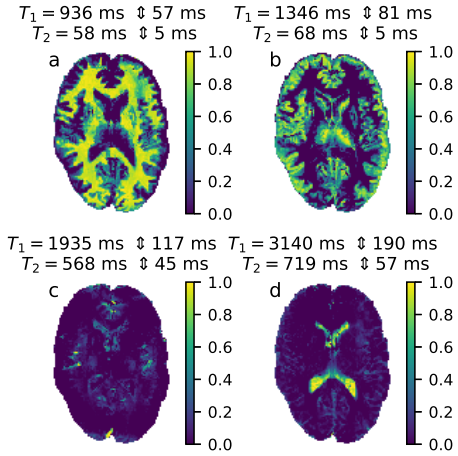

Figure 2.7: The four components matched by the SPIJN algorithm for a measurement at 3 T. The color indicates the relative weight of the component in each voxel. The relaxation times for the different components are given. To indicate the grid spacing at a certain point the symbol ⇕ is used, indicating the average distance to the next lower and next higher relaxation time for the matched T_1, T_2 combination. The relaxation times of component *a* are related to white mater, the relaxation times of component *b* to gray matter and the relaxation times of components *c* and *d* to CSF.

ier, all algorithms were able to recover the MW component in the simulations, and the NNLS and reweighted-ℓ_1-norm regularized algorithm also resulted in a MW component of about 5% in the in vivo data.

For the 3 T measurements, using a different MRF sequence, four components were recovered. These are similar to the last four components found in the 1.5 T experiment and can be related to white matter, gray matter and CSF, for which two components were found. Similar to [25, 37], no short T_2 component that can be attributed to MW was recovered for these data.

These results suggest that the number of components and the corresponding weights depend on the MRF sequence. Different sequences may have different sensitivity to shorter T_2 components. Differences in estimated MWF were also reported between MESE and DESPOT measurements, supporting the possible dependence on the acquisition method [57]. By showing these different results for the two similar sequences we want to stress the influence of the sequence on the recovered components and the relevance of this as a topic of future research.

In addition, data inconsistencies due to an incomplete model used for the computation of the dictionary may bias the estimation of the component weights. B_1^+ compensation was included for the 3 T data, however, further effects like diffusion or magnetization transfer that were not considered may introduce potential bias. It would be interesting to investigate how more parameters can be efficiently included in the multi-component analysis and their effect on the component estimation.

The proposed algorithm gives consistent results over repeated measurement in 10 volunteers as shown in Table 2.2. Direct comparison with literature values is difficult, since these studies do not take in to account the multi-component effects. Furthermore the literature values from different studies are not very consistent (see Table 2.1), probably because of differences in the parameter mapping sequences and fitting procedures, different segmentation tools, and potentially certain natural variation between volunteers. However, even a rough comparison can be useful in order to better understand the results from the multi-component analysis. Performing such a comparison, we see that most relaxation times are in the range of literature values, only the T_2 of gray matter (mean 58.8 ms) is slightly shorter than the shortest value (65 ms) reported in literature, which was from an Gradient-spoiled MRF measurement [10], but within the uncertainty range. Most parts of the gray matter are not matched as one component, but as a combination of component b and d (see Figure 2.7, where the latter has long relaxation times, which will lead to longer relaxation times for single component matching.

As already reported in [36, 37], MC-MRF is more sensitive to noise and the signal perturbations from undersampling can cause significant noise amplification in the estimated weights. One can use very long sequences with few thousand time points in order to gain back the SNR lost by undersampling. In this work, we chose to use a relatively short fully sampled MRF sequence instead, in order to ensure practical processing times for the computationally demanding approaches [25, 36] used in the comparisons. It is known that advanced reconstruction methods [58–61] can be applied to reconstruct artifact free image series from the undersampled MRF data, which enables the application of multi-component analysis on undersampled data with short MRF sequences (see Supporting Information Figure S2.2). The optimal choice of the MRF sequence and the reconstruction method are out of the scope of this study, but will be interesting topics for future research.

In this study, the regularization parameter was selected such that it minimizes the number of components without increasing the NRMSE compared to regularized voxel-wise methods, which was used as quality measure of the fit. Alternatively, the regularization parameter can be chosen in a way that specific number of components are recovered, or estimated with methods similar to the χ^2 misfit used for T2NNLS [34].

A requirement from the non-negativity constraint is that the signal and dictionary are real valued. For the FISP MRF sequence with constant TE it is possible to make this required transformation from a complex to a real signal, since the phase is constant for all time points. When a different MRF acquisition is used, resulting in temporal phase evolution, the phase difference between dictionary and signal may be more challenging to determine. When this phase is determined, the real and imaginary part of the signal can be concatenated to a real signal to perform the MC-MRF analysis.

This initial technical feasibility study was performed on healthy volunteers only. The

ability to capture different tissues or pathology depends on the sensitivity of the used MRF sequence for the tissue of interest. Based on the results from Badve et al. [62], we think brain tumors would result in one or two extra components. Investigating the proposed algorithm, the effects of the regularization parameter and influence of the MRF sequence for MC-MRF in patients would be an important step towards the validation of the approach.

2.5. CONCLUSION

THE sparsity promoting iterative joint NNLS (SPIJN) algorithm was proposed to solve the multi-component MRF problem through the introduction of a joint sparsity constraint. The introduction of the joint sparsity constraint leads to a higher robustness to noise compared to existing methods and results in a small number of components matched throughout the ROI. This makes the results directly interpretable without further assumptions or complex regrouping strategies. The proposed algorithm finds a small number of components in MRF brain measurements, that can be attributed to known anatomical structures and requires a minimum of further processing of the results. The proposed algorithm is over 10 times faster than previously proposed algorithms for multi-component MR fingerprinting analysis, which facilitates the potential application of the method in a clinical setting.

2.6. SUPPORTING INFORMATION

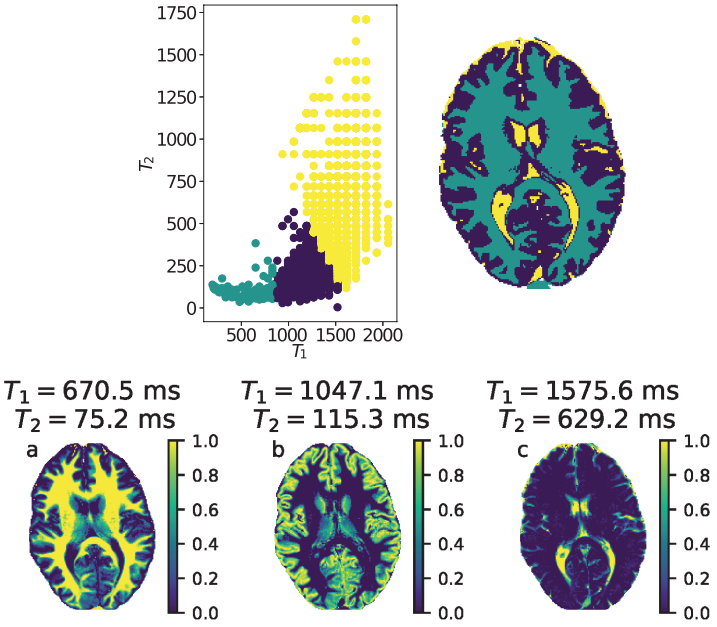

Figure S2.1: Results from partial volume estimation based on k-means clustering as proposed by [24] applied to the 1.5T MC-MRF measurement as used for Figure 2.4. MRF-mapped relaxation times from a single component matching are used for a k-means clustering method to determine the k=3 main tissue components. The NNLS algorithm is used to find a multi-component solution with the subdictionary containing these three components. The k-means clustering method, with a fixed number of components, results in pure tissues in most of the voxels, in contrast to the SPIJN algorithm.

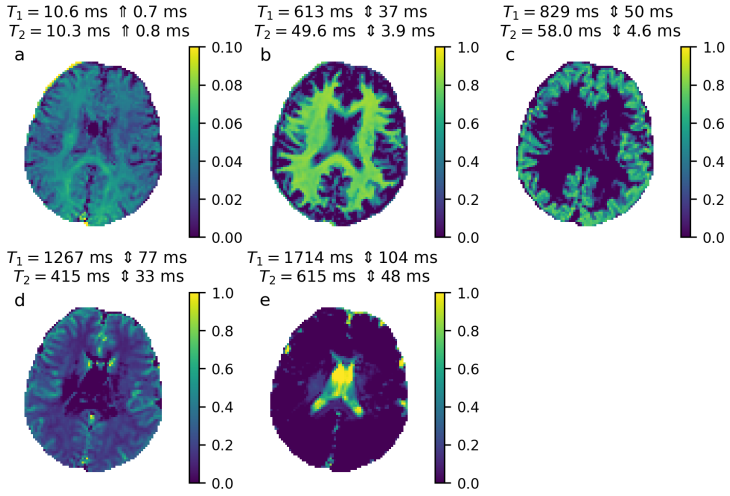

(a) Fully sampled data

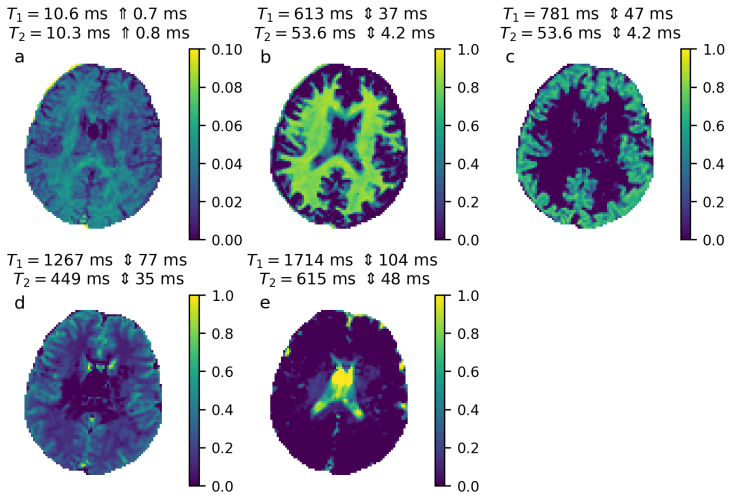

(b) Retrospectively undersampled data iteratively reconstructed [60]

Figure S2.2: The effect of undersampling on the MC-MRF decomposition using the SPIJN algorithm. Fully sampled data from an MRF acquisition with Sequence 1 was retrospectively undersampled with an undersampling factor of 12. This dataset was iteratively reconstructed with matrix-completion [60]. Figure (a) shows the results of the SPIJN algorithm for fully sampled data, Figure (b) shows the results for the iteratively reconstructed undersampled data. The matched components are at most one grid step apart and the resulting fraction maps are almost identical.

3

ACCURACY AND REPEATABILITY OF JOINT SPARSITY MULTI-COMPONENT ESTIMATION IN MR FINGERPRINTING

Laura Nunez Gonzalez & Martijn A. Nagtegaal[1]
Dirk Poot
Jeroen de Bresser
Matthias J.P. van Osch
Juan A. Hernandez Tamames
Frans M. Vos

NeuroImage 263 (Nov. 1, 2022), p. 119638. ISSN: 1053-8119.
DOI: 10.1016/j.neuroimage.2022.119638

[1] Authors contributed equally

ABSTRACT

MR fingerprinting (MRF) is a promising method for quantitative characterization of tissues. Often, voxel-wise measurements are made, assuming a single tissue-type per voxel. Alternatively, the Sparsity Promoting Iterative Joint Non-negative least squares Multi-Component MRF method (SPIJN-MRF) facilitates tissue parameter estimation for identified components as well as partial volume segmentations.

The aim of this paper was to evaluate the accuracy and repeatability of the SPIJN-MRF parameter estimations and partial volume segmentations. This was done (1) through numerical simulations based on the BrainWeb phantoms and (2) using in vivo acquired MRF data from 5 subjects that were scanned on the same week-day for 8 consecutive weeks. The partial volume segmentations of the SPIJN-MRF method were compared to those obtained by two conventional methods: SPM12 and FSL.

SPIJN-MRF showed higher accuracy in simulations in comparison to FSL- and SPM12-based segmentations: Fuzzy Tanimoto Coefficients (FTC) comparing these segmentations and Brainweb references were higher than 0.95 for SPIJN-MRF in all the tissues and between 0.6 and 0.7 for SPM12 and FSL in white and gray matter and between 0.5 and 0.6 in CSF. For the in vivo MRF data, the estimated relaxation times were in line with literature and minimal variation was observed. Furthermore, the coefficient of variation (CoV) for estimated tissue volumes with SPIJN-MRF were 10.5 % for the myelin water, 6.0 % for the white matter, 5.6 % for the gray matter, 4.6 % for the CSF and 1.1 % for the total brain volume. CoVs for CSF and total brain volume measured on the scanned data for SPIJN-MRF were in line with those obtained with SPM12 and FSL. The CoVs for white and gray matter volumes were distinctively higher for SPIJN-MRF than those measured with SPM12 and FSL.

In conclusion, the use of SPIJN-MRF provides accurate and precise tissue relaxation parameter estimations taking into account intrinsic partial volume effects. It facilitates obtaining tissue fraction maps of prevalent tissues including myelin water which can be relevant for evaluating diseases affecting the white matter.

3.1. INTRODUCTION

QUANTITATIVE magnetic resonance imaging is getting increasingly more attention since several fast, multiparametric quantitative methods have emerged, e.g. MR-Fingerprinting (MRF) [9] and QRAPMASTER [63]. The reduced scan-time of these acquisitions has facilitated their usefulness in research and clinical protocols [62, 64–66].

While these approaches can have a rich sensitivity to a wide range of tissue properties, the measurements are typically made voxel-wise, assuming a single tissue-type per voxel. However, partial volume effects are known to hinder this so-called single component approach [67–70]. Several methods were proposed facilitating multi-parameter estimates for a range of tissue components in a voxel. Examples of such multi-component techniques for MRF are modeling the signal with 3 a priori defined tissues [9, 24], a Bayesian approach [25], a reweighted-L_1-norm regularized algorithm [36], and a region-wise Greedy approximation method [71] . Following the principles of MRF, other techniques modeled bi-compartment voxels to distinguish between water and fat in cardiac MRF [72], to separate tissue from blood in arterial-spin-labeling MRF [73] or estimated T_1-T_2 spectra per voxel [74]. However these methods are limited by long computation times, a restricted number of predefined tissues within a voxel, and assume predominantly single compartment voxels or concern very different types of multi-parameter acquisitions.

Another recently published method for coping with different tissue types within a voxel is the Sparsity Promoting Iterative Joint Non-negative least squares algorithm that was applied to MRF data [75] (SPIJN-MRF). This approach asserted joint sparsity of the number of tissue components in a region of interest, i.e. in a voxel as well as spatially. A priori no assumptions are made about the number of tissues and relaxation times while the method still proved faster than previously proposed techniques. As such it yields tissue parameters for each identified tissue component as well as tissue volume fraction maps. The SPIJN-MRF algorithm estimated brain tissue fraction maps from fully sampled MRF data with promising accuracy and precision. These maps particularly showed components representing myelin water, white matter (WM), gray matter (GM) and cerebrospinal fluid (CSF) components. To be able to distinguish myelin water is specially relevant in the diagnosis and evaluation of multiple sclerosis (MS), since it has been shown that patients have reduced myelin water content [19, 76–78]. Also, imaging the increasing myelin content of the developing brain has been done in several initial studies [79, 80].

Although the initial results with the SPIJN-MRF method were encouraging, an extensive study into the accuracy and precision of the method has not yet been performed. Additionally, it is unknown how the obtained brain tissue fraction maps relate to existing methods for tissue segmentations.

The aim of this work is to evaluate the accuracy and repeatability of the SPIJN-MRF parameter estimations from highly undersampled MRF acquisitions. The accuracy of the method will be assessed through estimation of the relaxation times and tissue fractions on simulated data from the BrainWeb numerical phantom environment, including a comparison to conventional techniques: the Functional Magnetic Resonance Imaging of the Brain Software Library (FSL) and the Statistical Parametric Mapping Software (SPM12). Furthermore, the repeatability will be assessed through the parameter esti-

mates in eight weekly repeated scan sessions in 5 healthy volunteers. As in the simulations, tissue fraction maps will be compared to the SPM12 and FSL segmentations.

3.2. METHODS

3.2.1. SIMULATIONS

Numerical simulations using the 20 BrainWeb phantoms [81] were performed to test the accuracy and precision of the segmentations obtained with SPIJN-MRF and T_1-weighted based methods (FSL,SPM12). The BrainWeb phantoms were based on multiple high resolution conventional weighted scans from 20 different healthy subjects. Simulations were performed with resolution 1 mm × 1 mm × 5 mm. T_2 values were as defined in the BrainWeb database, but for white and gray matter T_1=930 ms and 1300 ms were used instead of 500 ms and 830 ms as these are more realistic relaxation times for 3 T [82, 83].

The MRF data was created by simulating a gradient-spoiled MRF sequence with a train of 1000 radiofrequency pulses as in [10]. This was done by performing extended phase graph signal generation [53, 84] for each tissue after which a weighted combination of the signals based on the BrainWeb partial volume fractions yielded the MRF images. Subsequently, independent random complex Gaussian noise with standard deviation $\sigma = \max(|X|)/100$ was added to each MRF image X_i, to yield the same noise level for all voxels and time points. No undersampling was performed in these simulations, as in [75].

The T_1-weighted images were also simulated by the BrainWeb simulator, using a spoiled FLASH sequence (TR=18 ms, TE=10 ms, FA=30 deg), after which Rician noise was added with noise level parameter $\sigma = \max(|X|)/100$. The input tissue parameters and partial volume segmentations from the BrainWeb database served as ground truth values.

3.2.2. IN VIVO DATA ACQUISITION

In vivo acquisitions were performed on a 3 T GE MR750 MRI scanner (General Electric, Milwaukee, WI, USA). A Head, Neck and Spine array coil was used from which the 12 channels dedicated to the head were used for imaging.

Five healthy volunteers (3 females and 2 males, between 18-25 years) participated in this Institutional Review Board-approved study. All volunteers gave written informed consent to usage of their data prior to the first scan session.

MRF imaging was performed on the same day and time (± 15 min) of the week for 8 consecutive weeks. As such the same gradient-spoiled MRF sequence as in the simulations was applied, varying the flip angle and the TR along a train of 1000 radiofrequency pulses [10]. The acquisition was performed with a FOV of 31 cm and slice thickness of 5 mm and slice gap of 1 mm (voxel size 1.2 mm × 1.2 mm × 5 mm). Total number of slices was 27, consisting of 256 × 256 voxels. The total scan time was 5 minutes and 54 seconds.

In each session, a READYBrain sequence was applied to align the MRF acquisitions to the anterior-posterior commissure (AC-PC) plane. READYBrain automatically detects the AC-PC plane for each subject and exploits this to plan the MRF with comparable imaging orientation across time and subjects.

Motion during 2D-MRF acquisitions is known to result in artifacts and errors in es-

timated T_1 and T_2 maps. Especially through-plane motion can lead to blurring and underestimation in T_2 [31, 32, 85, 86]. Slices showing such through-plane motion artifacts were visually identified in single component T_1 and T_2 maps by notably deviating values compared to neighboring slices before performing the multi-component analysis and excluded from further analysis unless explicitly stated otherwise. T_2 underestimation can also be caused by e.g. B_1^+ inhomogeneity. However, we assert that B_1^+ variation cannot cause abrupt changes in T_2 from slice to slice.

3.2.3. IMAGE RECONSTRUCTION

The acquired MRF data was reconstructed using an in-house implemented low-rank (LR) reconstruction algorithm in which the LR images were obtained while a compression matrix was iteratively updated. The spatial L_1 norm of the L_2 norm across the component images was applied for regularization purposes. A complete description of the used method can be found in Appendix Section 3.6.

3.2.4. SINGLE AND MULTI-COMPONENT PARAMETER ESTIMATION

A dictionary was precomputed with the extended phase graph algorithm [53, 84]. This dictionary was created for T_1 values ranging from 100 ms to 3042 ms and T_2 values from 10 ms to 1030 ms, sampled with increasing step sizes by 5 % (chosen as a compromise between dictionary size and resolution).

Synthetic T_1-weighted images were calculated based on the T_1, T_2 and M_0 maps estimated by single-component dictionary matching with the same settings as for the BrainWeb simulations. We chose to generate synthetic T_1-weighted images from the same data to have perfect spatial correspondence of the MRF and T_1-weighted data. As such differences in imaged volume were avoided. Based on the synthetic T_1-weighted images a brain mask was created using FSL-BET [14].

Subsequently, the SPIJN-MRF algorithm [75] (Chapter 2) was applied to the MRF data, to obtain multi-component estimations for the tissues present in the brain mask region. A regularization value λ of 0.03 was used in the multi-component analysis. This regularization level was manually determined for one in vivo dataset and kept constant with all subsequent numerical and in vivo analyses.

3.2.5. SPM12 AND FSL SEGMENTATIONS

The conventional methods were applied to the synthetic T_1-weighted images (created as described above). FSL-FAST [14, 87] was applied after brain extraction (through FSL-BET) to obtain tissue segmentations while using default settings. SPM12 segmentation [88, 89] was also used with default settings, but the sampling distance was set to 1 instead of 3 to produce the most accurate segmentations (at the cost of consuming more time and memory resources). Tissue volumes in a voxel were calculated by multiplying obtained tissue probabilities in a voxel from SPM12 and FSL with the voxel size.

3.2.6. ATLAS REGISTRATION

To facilitate assessment of particular brain regions, all imaging data was aligned to the ICBM 152 Nonlinear atlases version 2009 [90, 91]. This alignment was based on the synthetic T_1-weighted images using the Diffeomorphic Anatomical Registration through Ex-

ponentiated Lie algebra (DARTEL) algorithm [15] as implemented in SPM12 [89]. Subsequently, the obtained deformations were applied to all SPIJN-MRF, SPM12 and FSL partial volume segmentations to achieve voxel-wise alignment to the atlas. All subsequent analyses focused on a common brain region, specifically: the region for which the mean intracranial volume fraction per voxel (WM+GM+CSF) was at least 75 % with all segmentation methods.

3.2.7. ANALYSIS

TISSUE DISCRIMINATION

From the SPIJN-MRF parameter estimations, different components were identified based on the relaxation times, see Table 3.1 [19, 55, 82, 83, 92]: myelin water, white matter (excluding myelin water), gray matter, CSF and veins and arteries. CSF was partitioned into a short and long T_2 component after inspection of first results, as was observed in [75]. Simultaneously, components with T_1 and T_2 relaxation times around 1 s were identified, which we associated with veins and arteries. Total tissue volumes were calculated by summing the tissue fraction estimates multiplied by the voxel size (using an effective slice thickness of 6 mm to correct for slice gap).

Table 3.1: Ranges used to categorize SPIJN-MRF tissue/material components [19, 55, 82, 83, 92].

Name	T_1 range (ms)	T_2 range (ms)
White matter (without myelin water)	800 - 1050	50 - 100
Gray matter	1050 - 1500	50 - 100
CSF short T_2	2000 - 4000	9 - 300
CSF long T_2	2000 - 4000	300 - 2000
Myelin water	99 - 500	9 - 20
Veins and arteries	500 - 2000	200 - 1200

ANALYSIS OF ACCURACY

The accuracy, i.e. systematic error, of the obtained SPIJN-MRF, and SPM12 and FSL segmentations was evaluated using the simulated data. The agreement between estimated total white matter (including myelin water), gray matter and CSF volumes and the reference volumes was evaluated through Bland-Altman style plots. These showed the deviation from the reference as a function of reference value. Furthermore, the voxel-wise similarity between estimated partial volume and reference was assessed using the Fuzzy Tanimoto Coefficient (FTC) [93], which expresses the similarity of paired data as

$$\mathrm{FTC}(A,B) = \frac{\sum_{i\in\Omega_{ROI}} \mathrm{MIN}(A_i,B_i)}{\sum_{i\in\Omega_{ROI}} \mathrm{MAX}(A_i,B_i)} \tag{3.1}$$

where A, B is a pair of tissue fraction maps of a complete volume, specific region or slice; subscript i represents a spatial index of the concerned voxels. The FTC is an adaptation of the Jaccard index or Tanimoto coefficient for non-binary segmentations.

ANALYSIS OF REPEATABILITY

The repeatability of the SPIJN-MRF method was determined for the tissue parameter estimations and partial volume segmentations on the in vivo imaging data.

First, the mean and standard deviation of the SPIJN-MRF relaxation times were calculated per subject and tissue over the eight different time points. Subsequently, the repeatability was evaluated based on the range of standard deviations across the subjects per tissue.

Second, the repeatability of tissue volume estimation of the SPIJN-MRF and conventional methods over the time points was evaluated voxel-wise, in different brain regions and for the entire brain per tissue. In each case the mean value and corresponding standard deviation was determined per subject across the time points. The repeatability was quantified using the Coefficients of Variation (CoV $=\frac{\sigma}{\mu}$, where is the standard deviation and is the mean of the tissue volume over the 8 scan sessions) and the Combined Fuzzy Tanimoto Coefficient (CFTC) [93] for each subject and tissue

$$\text{CTFC(A)} = \frac{\sum_{k=1}^{\#\text{days}-1}\sum_{j=k+1}^{\#\text{days}}\sum_{i\in\Omega_{ROI}}\text{MIN}(A_{ki},A_{ji})}{\sum_{k=1}^{\#\text{days}-1}\sum_{j=k+1}^{\#\text{days}}\sum_{i\in\Omega_{ROI}}\text{MAX}(A_{ki},A_{ji})}, \tag{3.2}$$

where A_{ki} denotes the volume fraction of voxel i at day k for a subject and tissue of interest.

COMPARISON WITH CONVENTIONAL METHODS

Initially, comparison of the methods was performed by visual assessment of the segmentation maps. Subsequently, estimated total tissue volumes for the entire brain and per region were compared across the methods. While doing so, the volume fractions obtained with SPIJN-MRF for white matter and myelin water were summed into a single white matter tissue. Similarly, the SPIJN-MRF CSF fractions of long and short T_2 times were summed to yield the total CSF partial volumes. CoVs and CFTCs for total brain tissue volumes were calculated including and excluding the slices with motion artifacts to evaluate the effect of these artifacts on the repeatability.

3.3. RESULTS

3.3.1. SIMULATIONS

SPIJN-MRF yielded exact estimates of underlying T_1 and T_2 tissue parameters in all 20 datasets. Figure 3.1 shows representative partial volume segmentations obtained with SPIJN-MRF, SPM12 and FSL. Observe that the SPIJN-MRF images closely resemble the ground truth with soft transitions between tissue and background, while these transitions are sharper in the SPM12 and FSL segmentations.

Figure 3.2 shows Bland-Altman style plots, for each subject, method and the three tissues of interest, with the deviation from the true total tissue volume (vertically) as a function of the true value (horizontally). The mean deviations from the true value are indicated by solid lines. Limits of agreement are delineated by the light blue regions.

It can be observed that SPIJN-MRF and FSL showed little bias (defined as only a small deviation from the true value), whereas marked bias was found with SPM12. All three

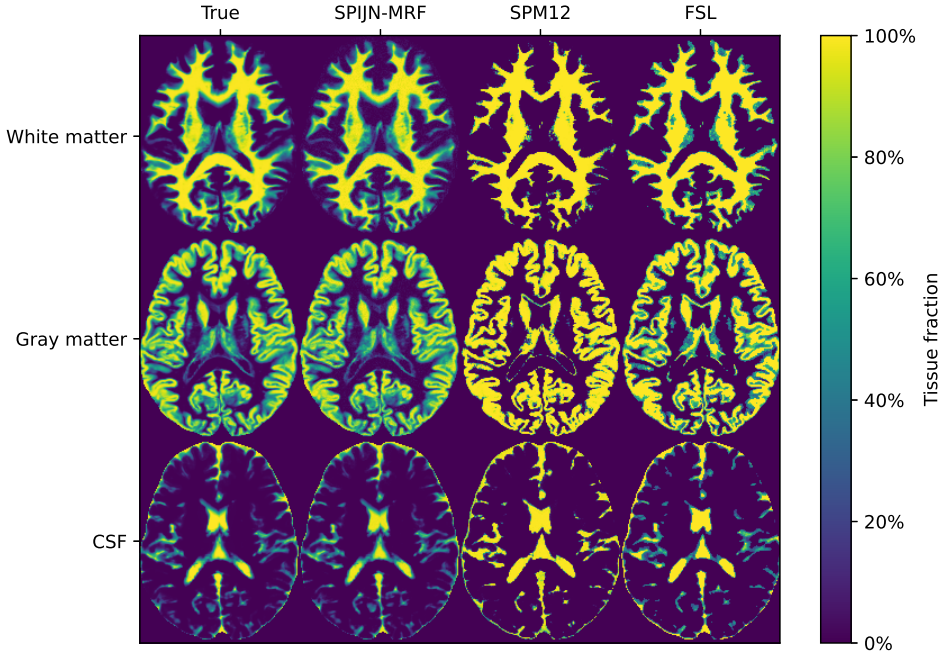

Figure 3.1: Example of partial volume segmentations obtained with multi-component SPIJN-MRF, SPM12 and FSL in simulations based on the central slice of a BrainWeb phantom (first column).

methods had the lowest bias in gray matter compared to the other tissues (max3.3 cm^3 for SPM12). SPM12 had the largest bias for white matter (mean deviation $-78.4\,cm^3$).

The limits of agreements between the estimated volumes and the reference values were smaller for SPIJN-MRF than for SPM12 and FSL, indicating that the differences between SPIJN-MRF estimations and the true values vary less than for SPM12 and FSL. SPM12 had the largest spread in the limits of agreements, which indicates a lower precision.

Figure 3.3 shows the distribution of FTCs obtained with SPIJN-MRF, SPM12 and FSL. In all the tissues, the segmentations performed by SPIJN-MRF were the most similar to the true segmentations, with FTCs around 0.97. SPM12 and FSL had lower FTCs: between 0.6 and 0.7 for white and gray matter and between 0.5 and 0.6 for CSF, respectively. Segmentations made with FSL had slightly higher FTCs than segmentations with SPM12. FTCs varied across slices, following a similar trend as the total amount of tissue per slice (see Supplementary Figure S3.1). A fixed SNR level (100) was used in the shown results, in additional experiments different noise levels led to similar findings as shown in Supplementary Figures S3.2-S3.4.

3.3.2. IN VIVO DATA ANALYSES

A total of 10 MRF acquisitions (out of 40) were affected by motion artifacts in one or more slices. It concerned 3 % of the total number of slices. Computation times were

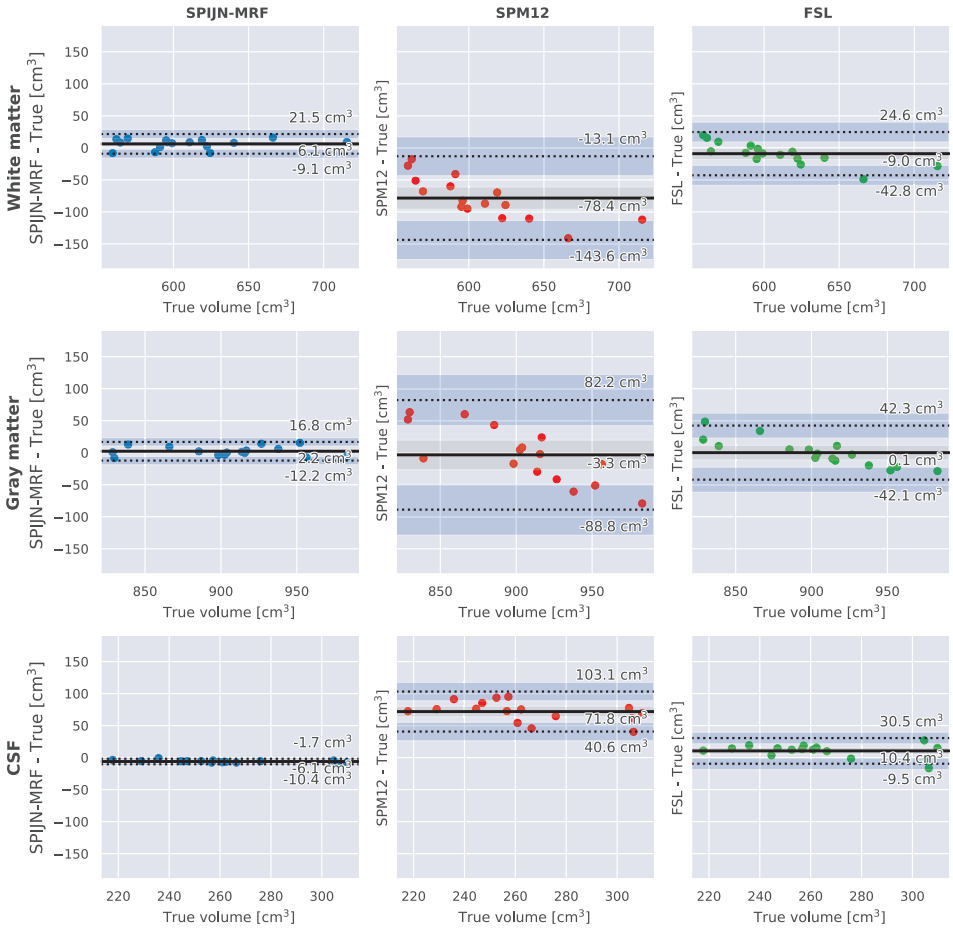

Figure 3.2: Bland-Altman style plots showing the deviation (vertically) from the true volume in the 20 BrainWeb phantom volumes obtained with the SPIJN-MRF (left), SPM12 (middle), and FSL (right) methods. The solid lines indicate the mean deviation in each plot (i.e. the bias), the exact value of which is indicated next to each line. Dotted lines reflect the limits of agreement (1.96 times the standard deviation of the bias). Shadowed areas in gray and blue delineate the 95 % confidence interval of the mean and the limits of agreement respectively.

approximately 50 minutes for SPIJN-MRF estimations on a standard desktop pc (Intel i7-8650U CPU 1.9GHz, 8GB RAM).

TISSUE DISCRIMINATION

Figure 3.4 shows all components resulting from the MRF data of a single acquisition across several slices from one representative subject. The leftmost column shows the T_1 and T_2 values for each of 9 identified components while the images depict corresponding estimated tissue fractions.

In Figure 3.5, the main component maps and standard deviation (std) maps (after registration) obtained after grouping as per Table 3.1 for a central slice from the same

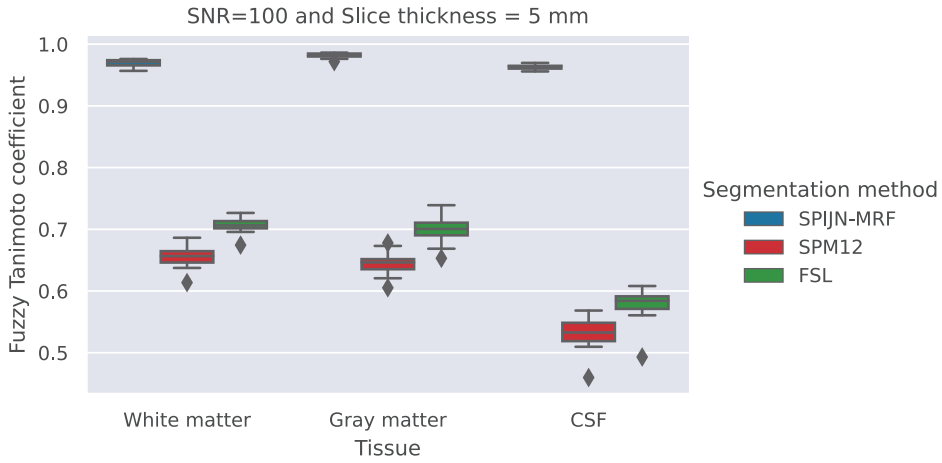

Figure 3.3: Box plots showing distributions of the Fuzzy Tanimoto Coefficient (FTC) for white matter (left), gray matter (middle), and CSF (right) comparing the 20 BrainWeb phantoms and the tissue segmentations using SPIJN-MRF(blue), SPM12 (red), and FSL (green).

subject are depicted for each acquisition day. Observe that there are minimal differences over time (as reflected in the std maps in the right column). Global intensity variations can be observed in the myelin water map (in particular concerning scans 5 and 6 seem to yield higher tissue fractions). However, for the other tissues the variability is similar across the brain.

Table 3.2 collates the means and standard deviations of T_1 and T_2 relaxation times across all subjects and scans per tissue as well as the mean intra-subject standard deviations per tissue. On average 8.3 components were identified over all acquisitions (26 times 8 components, 13 times 9 and 1 time 10). No components were outside the predefined ranges (Table 3.1). The mean intrasubject standard deviations of myelin water and *veins and arteries* for T_1 estimation and of short CSF for T_2 estimation was larger than 10 % percent of the reported mean value. For all other tissues the intrasubject standard deviations of T_1 and T_2 relaxation times showed small variation. After changing the dictionary ranges the observed clipping to the dictionary boundaries appeared persistent and visually did not appear to affect the estimated partial volume maps. Supplementary Figure S3.5 shows scatter plots of the estimated T_1 and T_2 values across subjects and scans.

REPEATABILITY

Table 3.3 presents the CoVs of the total volume estimates of myelin water, white matter (including myelin water), gray matter, CSF and the total brain volume (WM + GM) across subjects. Total brain volume showed minor variation (mean CoV = 1.1 %); the volume estimates of CSF, GM and WM (including MW) were slightly more variable, with mean CoV of 4.6 %, 5.6 % and 6.0 %, respectively, while MW by itself had higher mean CoV (10.5 %).

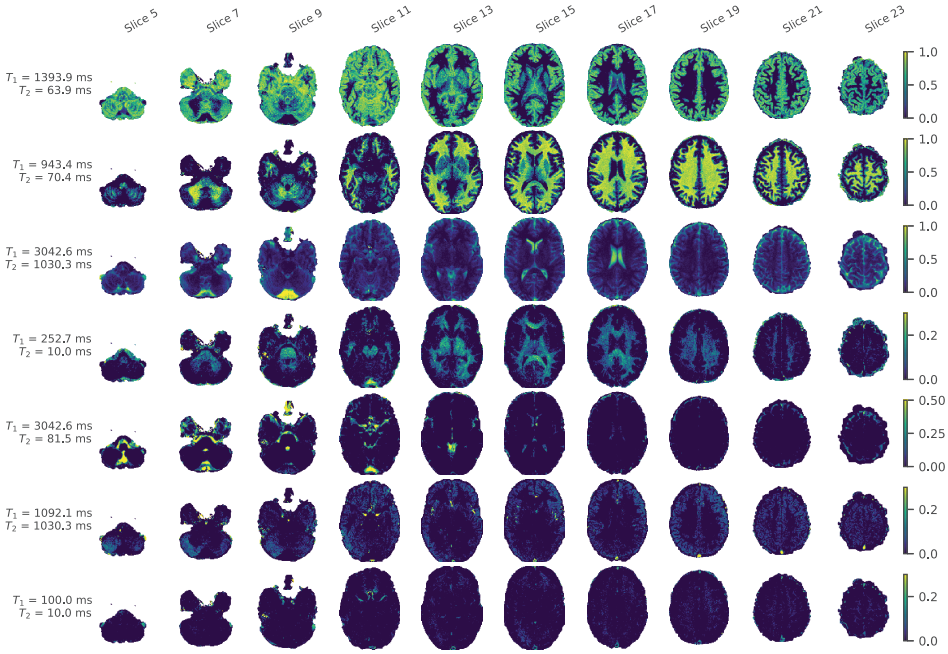

Figure 3.4: Multi-component tissue fraction maps for one MRF dataset of a single subject. Obtained T_1 and T_2 relaxation times are shown in the left column. Note that the component maps are only estimated inside the brain mask. For illustration purposes only the ten central odd slices are shown instead of the total 28 slices and components with a relative volume fraction of less than 1 % were not shown.

COMPARISON WITH BRAIN VOLUME MEASUREMENT METHODS

Figure 3.6 illustrates that the SPIJN-MRF tissue maps from the in vivo data contained more gradual transitions between brain tissues than the conventional methods, similar to simulated data. For instance, the SPIJN-MRF CSF map shows small details not observed in the other maps (green circle) whereas parts are more confined in the SPM12 and FSL segmentations (red circle). Furthermore, the GM SPIJN-MRF component was almost always identified as a mixture of GM and CSF or WM components (maximal GM fraction around 90 %). This highlights the ability of SPIJN-MRF to approximate brain tissue content of partial volume voxels.

The distributions of total volumes for each subject with SPIJN-MRF, SPM12 and FSL are collated in Figure 3.7. It can be observed that SPM12 estimates are lower in white matter than FSL estimates, and consequently, the opposite is noticeable for gray matter and CSF as the sum of tissue percentages is 100 % by definition. In general, the estimated volumes with SPIJN-MRF appear between the estimated volumes of SPM12 and FSL. Furthermore, the SPIJN-MRF volume distributions show a larger spread than those of SPM12 and FSL.

In Figure 3.8, the estimated relative volumes per anatomical region for each tissue, method and subject are summarized (see Supplementary Figure S3.6 for absolute volumes per region). In general, the three methods had relatively similar relative volumes

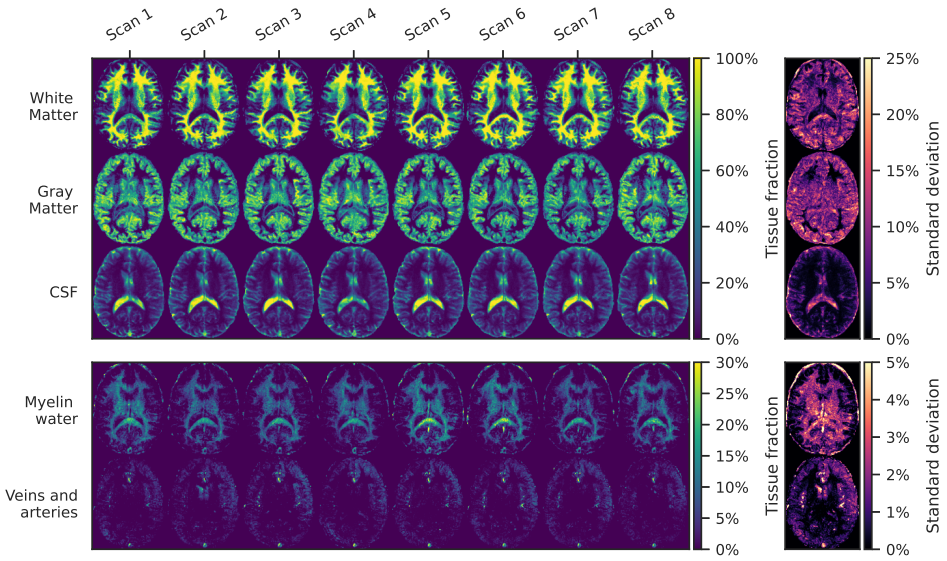

Figure 3.5: SPIJN-MRF maps across days and tissue types are for a central slice for one subject after grouping based on relaxation time. Note that the lower two rows use a different color range for illustration purposes. Standard deviation maps are shown in the column on the right.

per region. However, for the cerebellum and for the deep gray matter FSL gave higher white matter volume than SPIJN-MRF and SPM12 in all subjects. As a consequence, FSL yielded lower gray matter volumes.

Figure 3.9 shows CFTCs (upper row) and CoVs (lower row) for the motion-artifact-free data and the full dataset across the subjects and the tissues. The SPM12 yielded slightly higher CFTC than SPIJN-MRF in white and gray matter in all subjects. SPIJN-MRF gave higher CFTCs compared to both SPM12 and FSL in CSF, which was observed consistently across slices (see Supplementary Figure S3.7). Also, the CoVs of SPM12 and FSL were distinctly lower than those of SPIJN-MRF for white and gray matter, whereas differences were smaller for CSF and total brain volume.

The CoVs for SPIJN-MRF were lower using the data without motion artifacts than with all data in all tissues but one in subjects C and D, and E. The only exception was in subject E, in which the white matter score was barely affected.

We did not observe a particular trend in the CFTCs nor in the CoVs of the motion-artifact-free data related to anatomical region nor any specific differences between left and right brain regions (see Supplementary Figure S3.8).

3.4. DISCUSSION

THIS paper aimed at evaluating the accuracy and repeatability of the joint sparsity based SPIJN-MRF estimations [75]. The results show that it yields accurate brain tissue voxel fraction estimation in simulated data (mean systematic errors between 2 cm^3 and 6 cm^3 and Fuzzy Tanimoto Coefficient above 0.95) and gives good repeatability in

Table 3.2: Means and corresponding standard deviations (std) of estimated T_1 and T_2 relaxation times across all 5 subjects and 8 repeated scans per tissue as well as the means of 5 intrasubject standard deviations per tissue. *T_1 or T_2 values are the minimum/maximum value represented in the dictionary, which also occured with extended boundaries.

	T_1 (ms)		T_2 (ms)	
Tissue	Mean ± Std across all subjects and scans	Mean intra-subject Std	Mean ± Std across all subjects and scans	Mean intra-subject Std
White matter excluding myelin water	943.4 ± 0.0	0	69.2 ± 1.2	2.5
Gray matter	1383.9 ± 10.8	17.7	62.3 ± 1.2	1.7
CSF longer T_2	3042.6 ± 0.0*	0	1030.3 ± 0.0*	0
CSF shorter T_2	3042.6 ± 0.0*	0	149.3 ± 9.4	18.3
Myelin water	230.7 ± 20.1	34	10.0 ± 0.0*	0
Veins and arteries	876.2 ± 93.9	106.7	1030.3 ± 0.0*	0

Table 3.3: CoVs of the estimated total myelin water volume, white matter volume (including myelin water), gray matter volume, CSF volume and total brain volume. The last column reports the mean of the CoVs over all subjects.

	Subject					Mean
Tissue	A	B	C	D	E	
Myelin water (MW)	13.70 %	13.30 %	4.40 %	13.30 %	7.60 %	10.50 %
White matter (including MW)	3.80 %	6.40 %	7.00 %	4.70 %	8.20 %	6.00 %
Gray matter	3.40 %	5.50 %	8.70 %	3.70 %	6.60 %	5.60 %
CSF	6.40 %	6.50 %	6.40 %	2.10 %	1.70 %	4.60 %
Brain volume	1.00 %	1.70 %	1.80 %	0.50 %	0.70 %	1.10 %

in vivo data (Fuzzy Tanimoto Coefficient above 0.7 and mean (across subjects) CoVs between 5.7 % and 6.1 %).

In simulations, we observed that the white matter, gray matter and CSF fraction maps obtained with SPIJN-MRF had smaller systematic errors than those obtained with SPM12 and FSL in both total volume estimation as voxel-wise similarity.

The T_1 and T_2 values obtained by SPIJN-MRF from the in vivo data for each component were very stable for all the acquisitions and in the range of previous quantitative studies [16, 19, 55, 94, 95]. The observed standard deviation of zero for WM derives from the dictionary resolution (which is 5 % for T_1 values) and resulted from repeated selection of the same dictionary atom. Previous studies have reported variations in T_1 below 5 % [64, 83]. Unexpectedly and contrary to the single-component estimations, we found that the T_2 value from the white matter component was slightly longer than the T_2 value found for the gray matter (see table 3.2). This can be partly due to the attribution of myelin water (having a very short T_2 time) to a separate component independently of

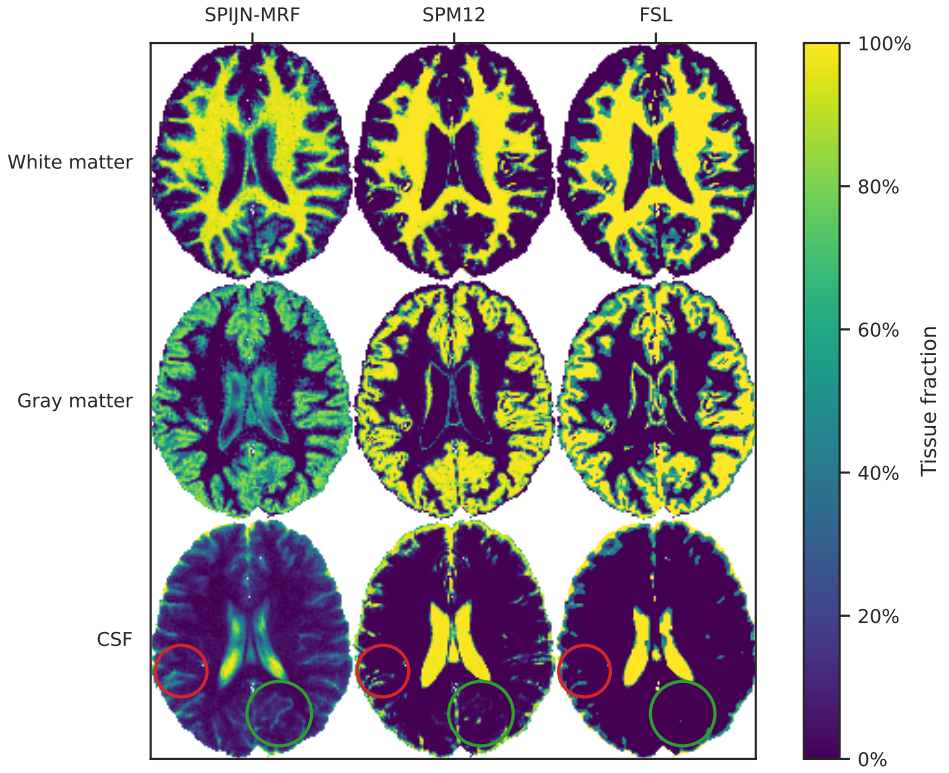

Figure 3.6: A representative slice showing the white matter (top), gray matter (middle) and CSF (bottom) fraction maps obtained using SPIJN-MRF (left), SPM12 (middle), and FSL (right) for one single acquisition of one subject (subject B, day 5). Red and green circles point out notable differences in CSF between methods.

white matter, whereas values reported in the literature for white matter commonly include myelin water In effect, this will lead to longer relaxation values for the pure white matter component, merely as a shorter time component is left out. Previously, a thorough study of the T_2 distributions in the brain indeed demonstrated that T_2 distributions are affected by properties of the spaces between myelin sheaths [18].

Furthermore, CSF was consistently represented by two different components, one with longer T_2 (around 1 s) and one with shorter T_2 (around 150 ms). This separation could be caused by the choroid plexus within the ventricles or by flow effects. The identification of the veins and arteries component as shown in Figure 3.4 was not observed before in multi-component relaxometry to our knowledge. This component had high T_1 and T_2 times (both around 1 s) and consistently appeared in all subjects and scans. Further research into physiologically understanding of this fluid-like component would be an interesting direction for future work.

Estimated T_1 relaxation times showed a very high repeatability, but for some components the maximum T_1 value of the dictionary was selected. The use of a maximum

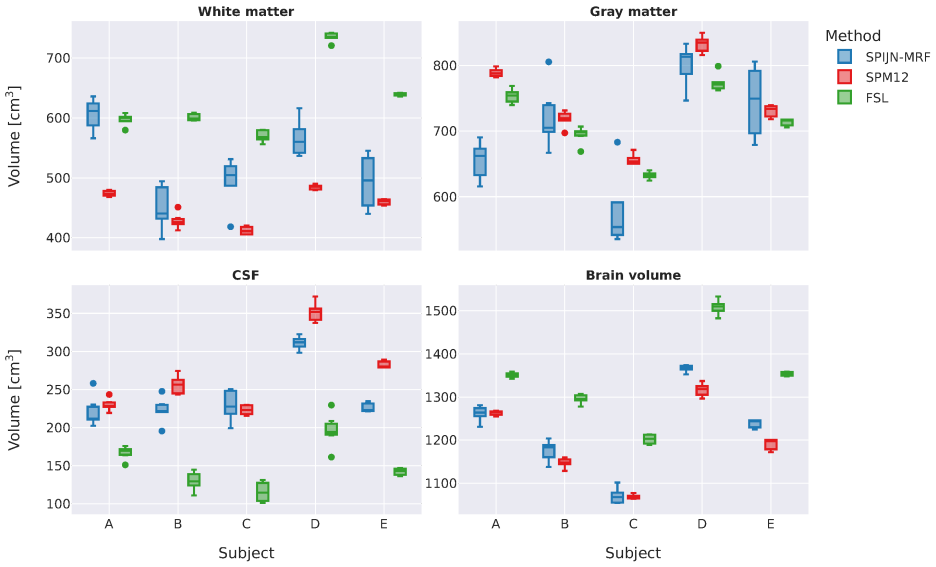

Figure 3.7: Box plots showing for each subject the total volume of the white matter (top-left), the gray matter (top-right), the CSF (bottom-left), and the total brain (bottom-right) estimated using SPIJN-MRF (blue), SPM12 (red) and FSL (green).

T_1 value of 6 s instead of 3 s did not affect this biasing effect (data not shown here) and was therefore not used any further. For better estimation of T_1 relaxation times in CSF a different MRF sequence and dictionary range would probably be required to improve discrimination between long T_1 components.

The consistent estimation of a separate myelin water fraction (MWF) map with the SPIJN-MRF approach could be useful, e.g. for assessment of multiple sclerosis as well as other white matter diseases [19]. A comparison to other MWF estimation methods [21] would be needed to further validate our technique, although differences between methods are known [96, 97].

A SPIJN regularization of 0.03 was used in the analysis resulting in reproducible estimates. We observed that changes from 0.025 to 0.035 led to only small changes in MW and veins/arteries component relaxation times and volume fractions, while WM, GM and CSF were less affected by the regularization. The required regularization will be affected by the SNR level and might therefore require adaptation for different scanners, sequences, or reconstructions.

The study on the repeatability of the SPIJN-MRF yielded CoVs < 10 % for the total white matter volume (including myelin water), the gray matter volume and the CSF volume for all subjects. This variation of the estimated volumes with the SPIJN-MRF is similar to the variation found previously with commonly accepted methods, such as SPM12 and FSL [98, 99]. The estimation of the myelin water volume showed more variation

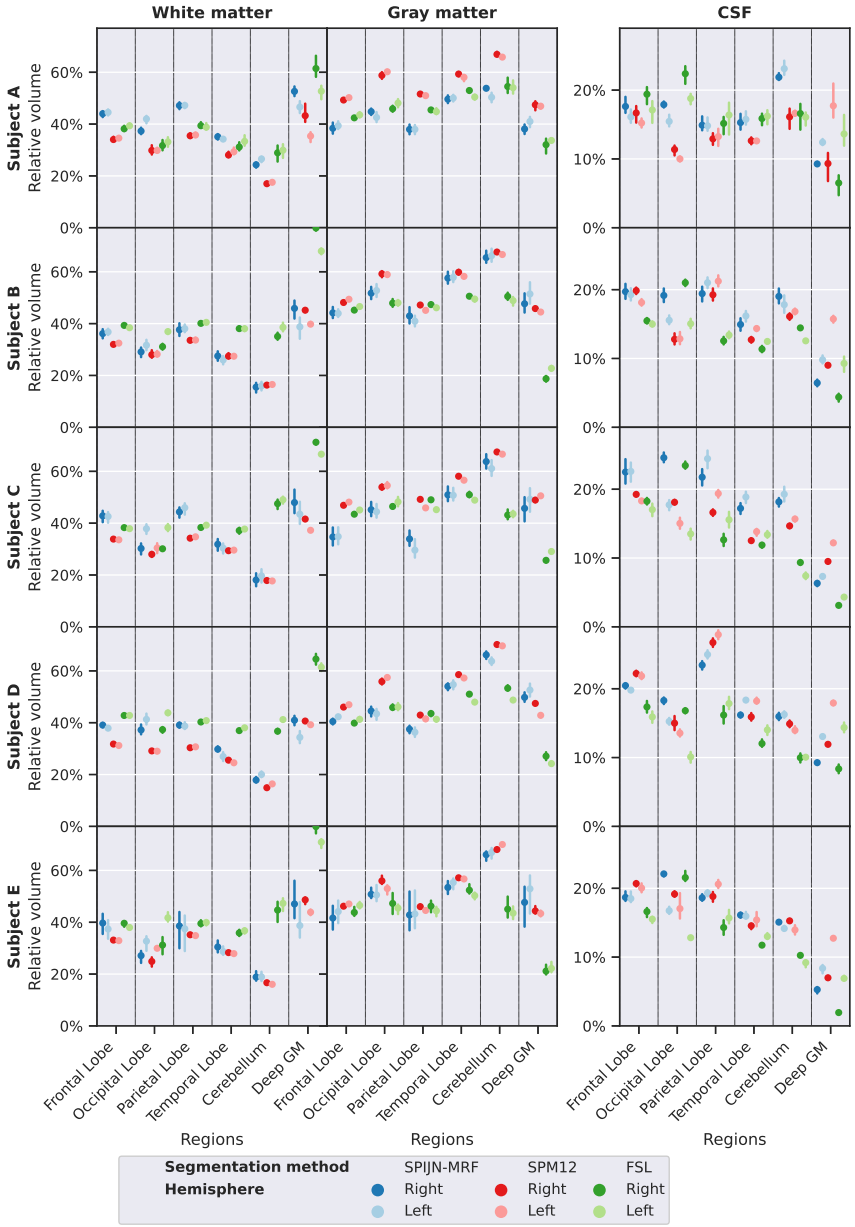

Figure 3.8: Mean relative volume for each subject over time (dots) and associated standard deviation (vertical lines) for different anatomical regions of the white matter (left), the gray matter (middle), the CSF (right) estimated using SPIJN-MRF (blue), SPM12 (red) and FSL (green).

(average CoV = 10 %) than other tissues. The repeatability was similar across the whole

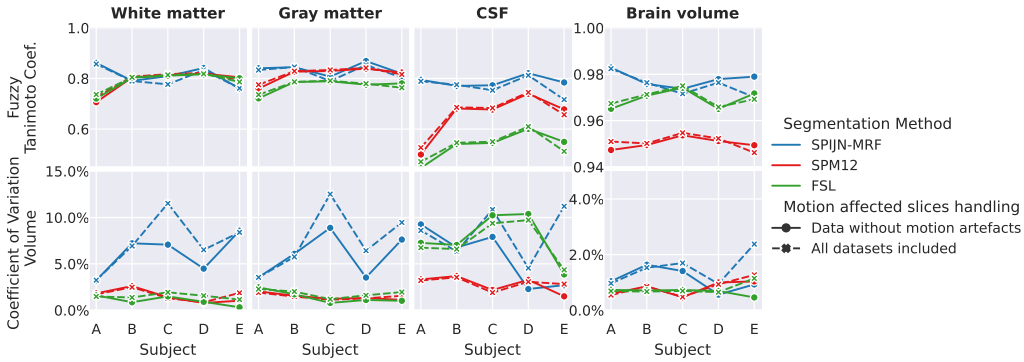

Figure 3.9: Combined Fuzzy Tanimoto Coefficient and CoV of estimated total volumes for each subject for white matter (including myelin), gray matter, CSF and total brain (white matter plus gray matter) obtained with SPIJN-MRF (blue), SPM12 (red), and FSL (green). Results from the data without motion artifacts are depicted using circles and solid lines, results obtained using all data are depicted with squares and dashed lines.

brain, even though we applied a rather large slice thickness.This signifies the robustness of the method also in regions with large susceptibility variations such as in areas with air (frontal part) or areas with more iron (deep gray matter).

The closer resemblance of the SPIJN-MRF maps to the reference in the simulations was reflected in higher FTC values with smaller standard deviations compared to the conventional methods. Especially in the CSF maps (both in simulation and in vivo), more details of the anatomy were visible with the SPIJN-MRF method than with SPM12 and FSL. These results could indicate that SPIJN-MRF improves measuring partial volume properties of smaller brain structures. Furthermore, compared to SPM12 and FSL it may provide new information, such as the myelin water fraction. To validate the high accuracy in simulations, further investigation into the in vivo accuracy should be performed. Currently we considered this outside the scope of our in vivo study, which mainly focused on the repeatability of SPIJN-MRF. Post-hoc, we performed as a preliminary approach to an accuracy evaluation, a small follow-up study one of the subjects that was rescaneed four times indicating similar performance in volume estimation of SPIJN-MRF compared to conventional SPM12 and FSL segmentation using conventional, high resolution T_1-weighted acquisitions (see Supplementary Figure S3.9). Furthermore, FSL and SPM12 recommend using T_1-weighted MPRAGE for segmentation, while our simulated images were created based on a spoiled FLASH sequence as was used for the BrainWeb simulations. Although the resulting images have a very similar contrast (see Figure S3.10), the set of parameters for the synthetic T_1-weighted images can be optimized further and the reported accuracy might be slightly affected by the generated contrast.

SPM12 uses a probability atlas with anatomical information to segment the brain tissues, which could enhance the repeatability of results but potentially also introduces a bias. FSL uses a hidden Markov random field model and an expectation-maximization algorithm to obtain robust results with improved denoising, but this might lead to removing small brain structures. Instead, the joint sparsity multi-component MRF model does not incorporate explicit *spatial* regularization or anatomical a priori knowledge.

Differences in estimated brain tissue volumes between SPM12 and FSL were already previously reported [98]. Our estimated volumes for FSL are higher in white and gray matter and lower in CSF compared to SPM12 with the simulated data just as in [99]. Contrary to the simulated data, the estimated total brain volumes for the in vivo data by SPIJN-MRF are closer to the estimated volumes from SPM12 than those from FSL. Also, the relative volume per region calculated by SPIJN-MRF is closer to the relative volume calculated by SPM12 than FSL for the in vivo data. This could be caused by intrinsic differences between the T_1-weighted brainweb images (used in the simulations) and the MRF based T_1-weighted images (used in the in vivo experiments). The differences in the contrast could result in slightly different classification of the voxels and affect the local partial volume estimates.

In contrast to the simulations, the CoVs of SPIJN-MRF for in vivo data reflected higher variability than those of SPM12 and FSL for almost all subjects and tissues. The low variability of SPM12 and FSL, also in comparison with previous studies [98, 99], could be due to the use of synthetic images. This is because the quantitative parameters (M_0, T_1 and T_2) from MRF were highly repeatable, differing only between 0 and 2 % among all the acquisitions. As a consequence the resulting synthetic T_1-weighted images are also highly similar. This likely biases the repeatability of the SPM12 and FSL segmentations. We chose to create synthetic T_1-weighted images in order to have perfect spatial correspondence of the data. As such differences in imaged volume were avoided.

SPM12 and FSL demonstrated to be slightly more robust against motion artifacts than SPIJN-MRF, resulting in minimal differences in CoV and FTC when using data without and with motion artifacts. Although motion effects were observed in a relatively small number of slices, it did affect the volume estimates. Simultaneously, however, estimated T_1 and T_2 relaxation times were not affected by motion affected slices. Nevertheless, our results show that efforts to minimize the impact of subject-motion in the MRF data may enhance in particular the repeatability, e.g. by applying motion-correction [32] or 3D-acquisitions with possible use of navigators [100] or self-navigations [86].

A limitation of this work is that the evaluation of accuracy was mostly done on simulated data (see Figure 3.1, 3.3 and Supplementary Figure S3.9). Further validation of segmentation accuracy could be performed, for example by assessment of the segmentations through expert neuroradiologists. Future work could also take into account other potentially relevant aspects in the simulations, such as: reconstructions from undersampled data, modeling of B_0 or B_1^+ inhomogeneities, representation of the presence of myelin water or inclusion of other biological phenomena such as magnetization transfer or flow.

Another limitation could be that we did not include B_1^+ field inhomogeneity as a parameter in our SPIJN-MRF estimation. B_1^+ inhomogeneity might affect the SPIJN-MRF parameter estimation and especially MWF estimation. However, we did not observe particular spatial variations in the obtained fraction maps that appear to resemble smoothly varying B_1^+ inhomogeneities. Further research (including an acquired B_1^+ map) would be needed to explicitly study the effect of B_1^+ and to analyze the potential benefits of accounting for B_1^+ variation in the estimation of the tissue fraction maps.

Furthermore, optimizing the MRF sequence for multi-component MRF estimations [101] to make it more sensitive to myelin water or to improve the distinction between

gray and white matter could lead to further improvement of estimations, reduced scan times or the possibility to use a reduced slice-thickness. However, we consider the implementation of such optimization beyond the scope of our current paper.

3.5. CONCLUSION

We studied the accuracy and repeatability of the SPIJN-MRF method in simulations and in vivo brain MRI scans. SPIJN-MRF showed more accuracy and higher repeatability in simulated data than conventional methods (SPM12 and FSL). In the in vivo data, SPIJN-MRF consistently identified the same brain tissue components and gave highly repeatable relaxation times related to these tissues. SPIJN-MRF partial volume maps showed small details, also in CSF. The repeatability of the estimated brain tissue volumes of SPIJN-MRF was somewhat lower compared to SPM12 and FSL, possibly due to simulation bias . A further advantage of using SPIJN-MRF is the additional simultaneous estimation of MWF maps, which is not obtainable with single compartment-based methods.

3.6. APPENDIX

The acquired MRF data was reconstructed using an in-house created low-rank reconstruction algorithm, solving

$$P, U = \underset{P,U}{\arg\min} \sum_{c,j} \| S_{j,c} - F_j C_c P U_j \|_2^2 + R(P), \tag{3.3}$$

where $P \in \mathbb{C}^{|\Omega_X| \times N}$ is a matrix containing the N low-rank component images of spatial dimension $|\Omega_X|$, which the compressed representation of the MRF series; $P \in \Omega^{N \times 1000}$ contains the N time components based on which the MRF signal is compressed, i.e. the time compression matrix and $U_j \in \mathbb{C}^N$ is a particular column for this matrix for contrast weighting j (thus $x = PU_j$ is the reconstructed contrast image j from the MRF series); $S_{j,c} \in \mathbb{C}^{|\Omega_j|}$ is the acquired undersampled data of MRF contrast weighting j of coil c; $C_c \in \mathbb{C}^{|\Omega_X| \times |\Omega_X|}$ is a diagonal matrix specifying the sensitivity of coil c; $F_j \in |\Omega| \times |\Omega_{\mathbb{X}}|$ represents the non-uniform Fast Fourier transform [102] for contrast weighting j. Furthermore $R(P) = \sum_X \sqrt{\sum_i P_{x,i}^2}$, i.e. the spatial L_1 norm of the L_2 norm acreoss the component images is applied for regularization purposes.

The equation was solved by three iterations of a block coordinate descent optimization, alternating the optimization between U and P. The initial time compression matrix U was constructed from the first 6 singular vectors obtained through SVD of a dictionary precomputed as described in Section 3.2.4. After this, initial-images were created by subsequently applying to S_j: a density compensation, an adjoint non-uniform Fourier transformation, and a projection to the subspace with the initial U. Then, using the first subspace component derived from the initial-images, the cross-correlation matrix among the 12 acquired channels was computed for each voxel. The output was a matrix of 12 by 12 images which were filtered using a box blur filter of size 5, resulting in a modified correlation-among-channels matrix for each voxel. Each voxel of the coil sensitivity maps (C_c) was created from the first singular vector of its modified correlation-among-channels matrix. The initial P was created by the projection of the initial-images on

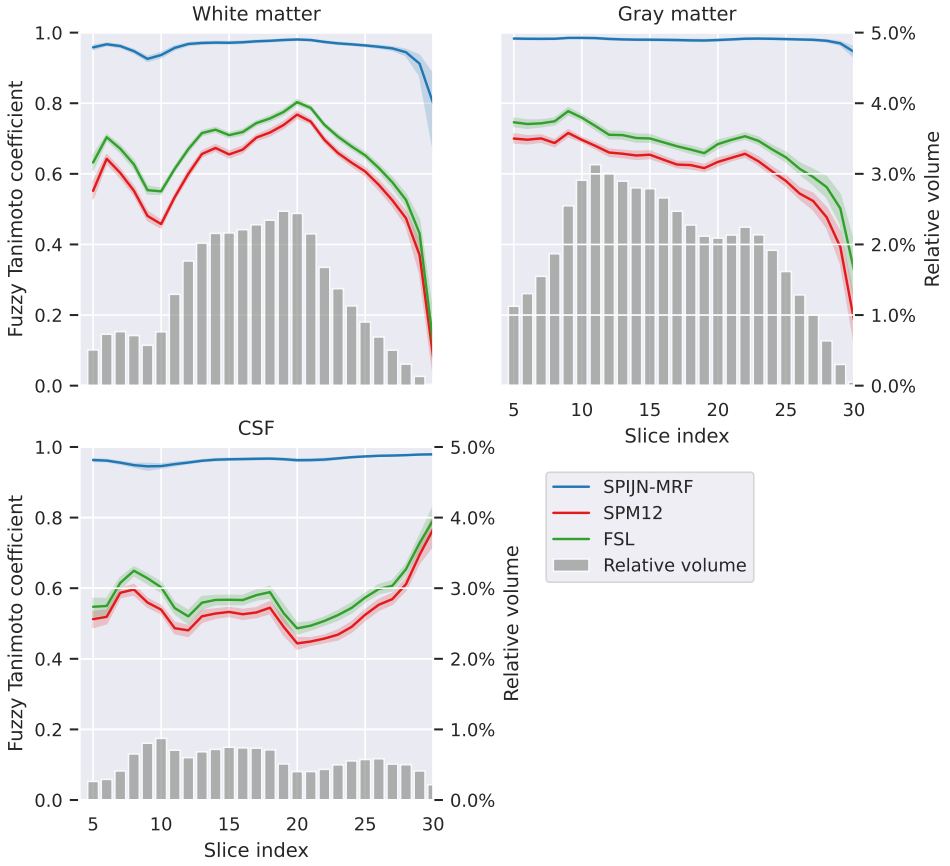

Figure S3.1: Line plots showing the averaged Fuzzy Tanimoto Coefficient (and the 95 % confidence interval as the shaded region) over the 20 BrainWeb phantoms between tissue fraction maps estimated with SPIJN-MRF (blue), SPM12 (orange), and FSL (green) and the Brainweb partial volume maps across all the slices. Gray bars indicate the relative tissue volume compared to the total brain volume for each slice.

C_c. In subsequent iterations the explicit least squares solution for U_j was computed followed by ortho-normalization. Subsequently, the subproblem for P was solved by the conjugate gradient algorithm, where $R(P)$ was approximated by its tight quadratic overbound [103].

3.7. SUPPORTING INFORMATION

3.7.1. SUPPLEMENTARY EXPERIMENT

Two follow-up acquisition sessions were performed for subject B to compare SPIJN-MRF total volume estimations and FSL and SPM12 segmentations based on high resolution T_1-weighted acquisitions.

In these sessions, a total of four 3D-high resolution T_1-weighted were acquired using

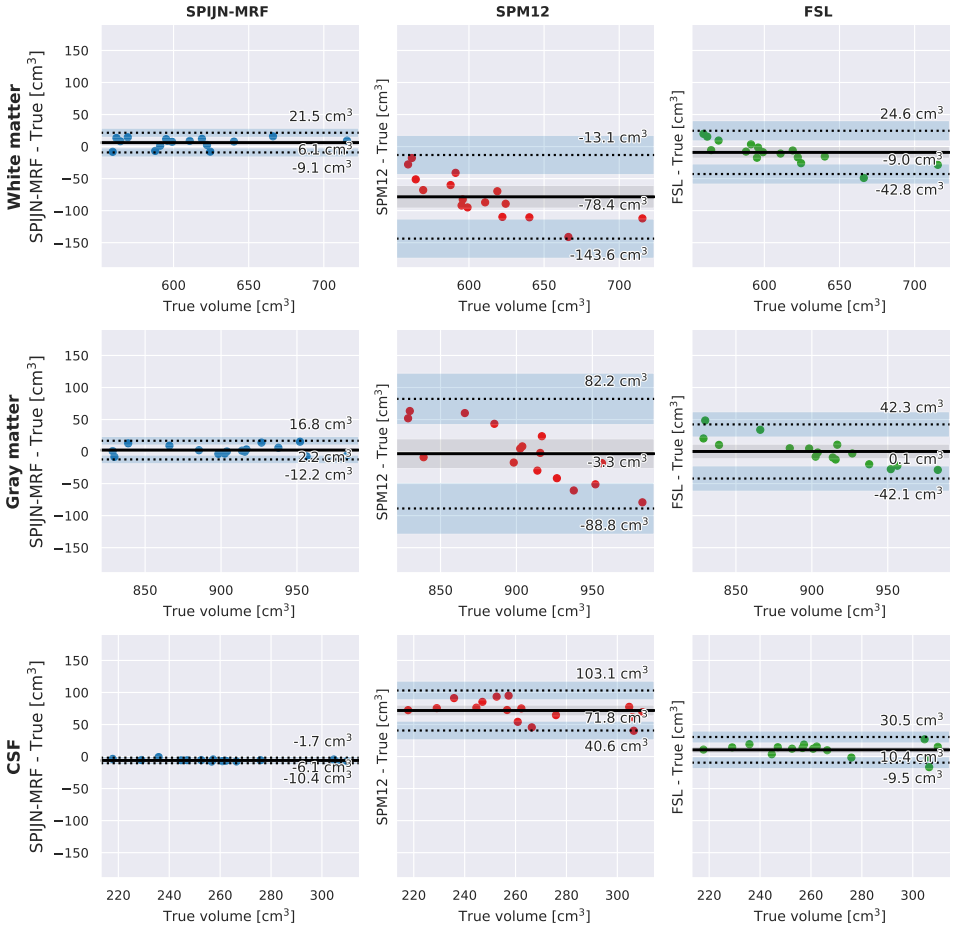

Figure S3.2: Replica of Figure 3.2 with different SNR(33 instead of SNR= 100). Bland-Altman style plots showing the deviation (vertically) from the true volume in the 20 BrainWeb phantom volumes obtained with the SPIJN-MRF (left), SPM12 (middle), and FSL (right) methods. The solid lines indicate the mean deviation in each plot (i.e. the bias), the exact value of which is indicated next to each line. Dotted lines reflect the limits of agreement (1.96 times the standard deviation of the bias). Shadowed areas in gray and blue delineate the 95 % confidence interval of the mean and the limits of agreement respectively.

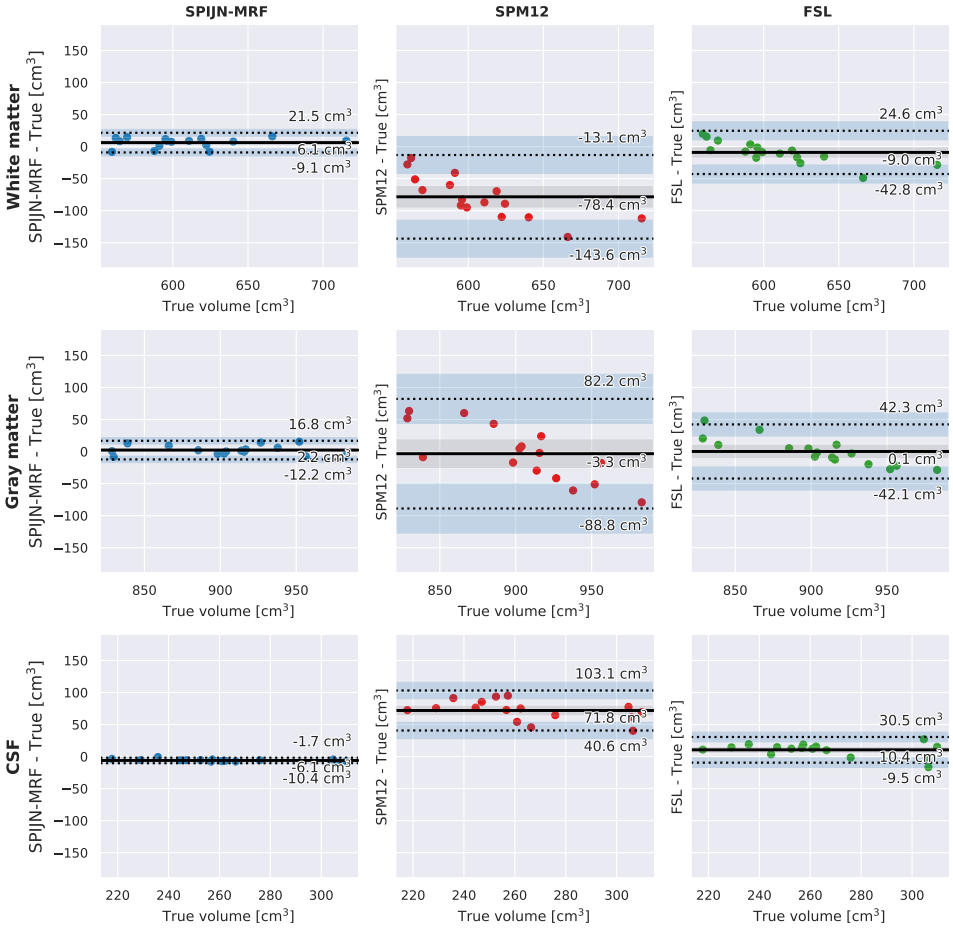

Figure S3.3: Replica of Figure 3.2 with no noise(instead of SNR= 100). Bland-Altman style plots showing the deviation (vertically) from the true volume in the 20 BrainWeb phantom volumes obtained with the SPIJN-MRF (left), SPM12 (middle), and FSL (right) methods. The solid lines indicate the mean deviation in each plot (i.e. the bias), the exact value of which is indicated next to each line. Dotted lines reflect the limits of agreement (1.96 times the standard deviation of the bias). Shadowed areas in gray and blue delineate the 95 % confidence interval of the mean and the limits of agreement respectively.

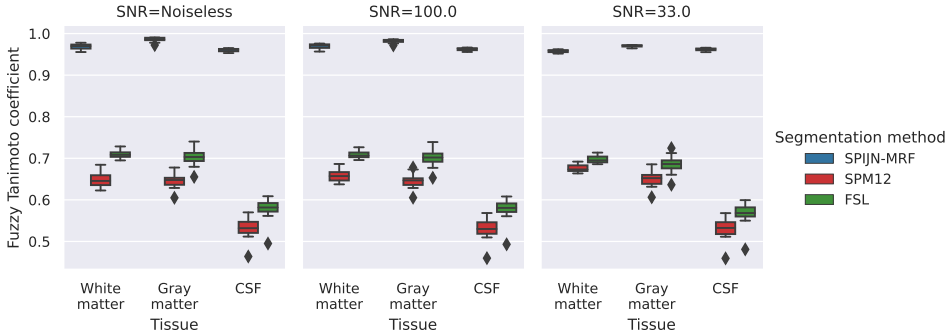

Figure S3.4: Replica of Figure 3.3 with different SNR levels (33 and no noise added). Box plots showing distributions of the Fuzzy Tanimoto Coefficient (FTC) for white matter (left), gray matter (middle), and CSF (right) comparing the 20 BrainWeb phantoms and the tissue segmentations using SPIJN-MRF(blue), SPM12 (red), and FSL (green).

a gradient-echo sequence with inversion recovery preparation. Three of these were acquired with an isotropic resolution of 0.5 mm. One of the T_1-weighted acquisitions was performed with the same resolution in-plane as previous MRF acquisitions (1.2 mm) and slice thickness of 0.5 mm. On every occasion, the subject was completely removed from the scanner and re-positioned again between sequences.

Figure S3.9 shows the estimated volumes using SPM12 (red) and FSL (green) for these the T_1-weighted acquisitions together with the previously estimated volumes using SPIJN-MRF (blue). The difference in estimated volumes for SPM12 and FSL has been observed before in literature [98, 99] and the performed simulations. The estimated volumes using SPIJN-MRF are within the range of the estimated volumes using the conventional methods SPM12 and FSL, with small differences between methods. This is indicative of the capability of SPIJN-MRF for estimating volumes accurately on in vivo subjects. However, to validate the accuracy of SPIJN-MRF a larger and more thorough study would be required.

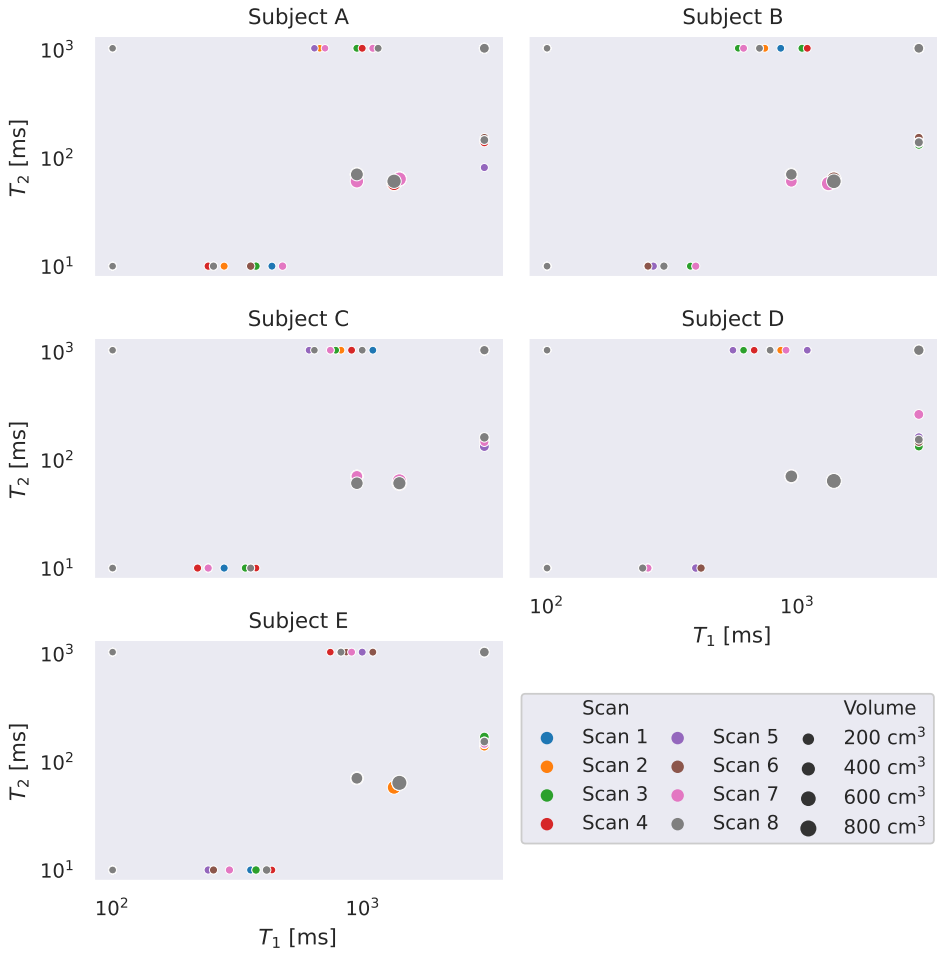

Figure S3.5: Estimated T_1 and T_2 relaxation times for the different acquisitions (represented with different color). The estimated volume of each component is reflected in the size of the spheres.

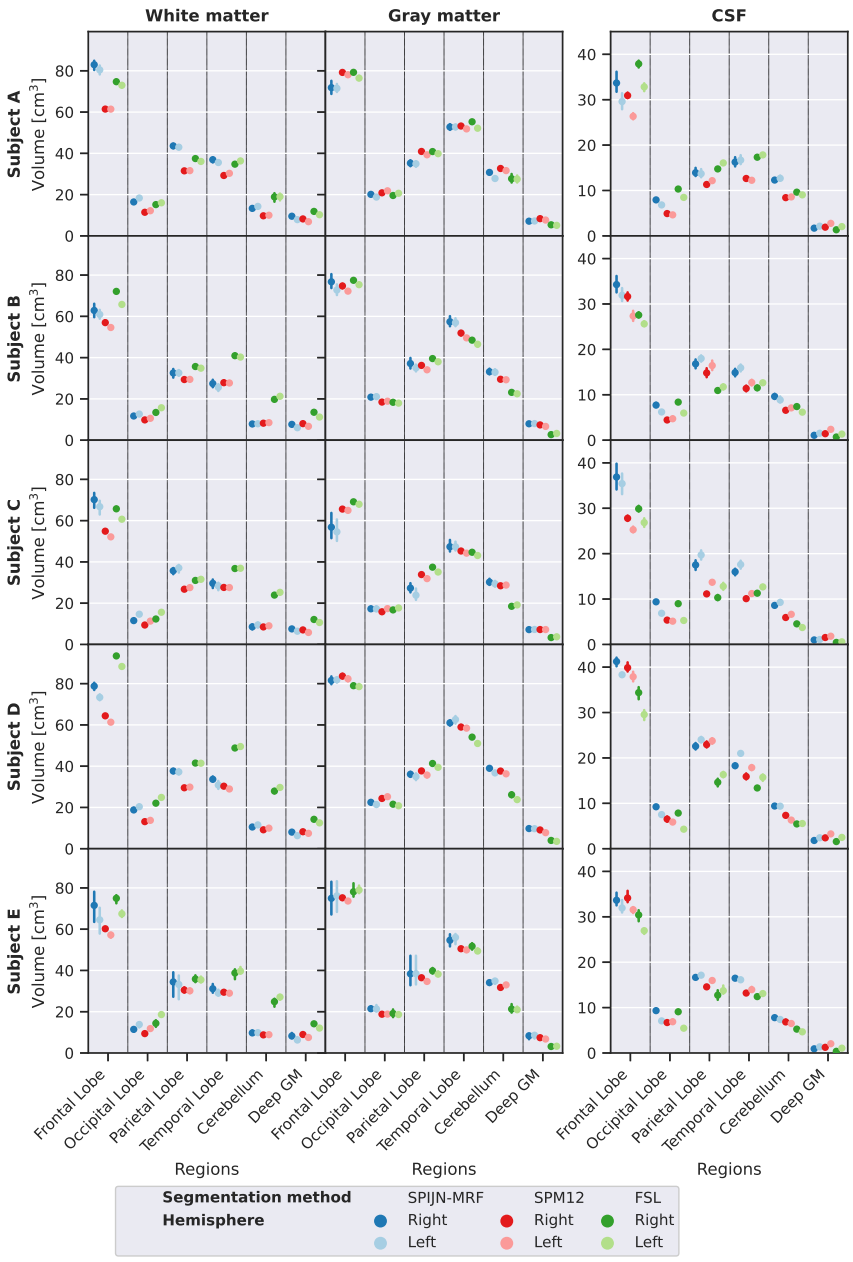

Figure S3.6: Mean absolute volumes for each subject over time (dots) and associated standard deviation (vertical lines) for different anatomical regions of the white matter (left), the gray matter (middle), the CSF (right) estimated using SPIJN-MRF (blue), SPM12 (red) and FSL (green).

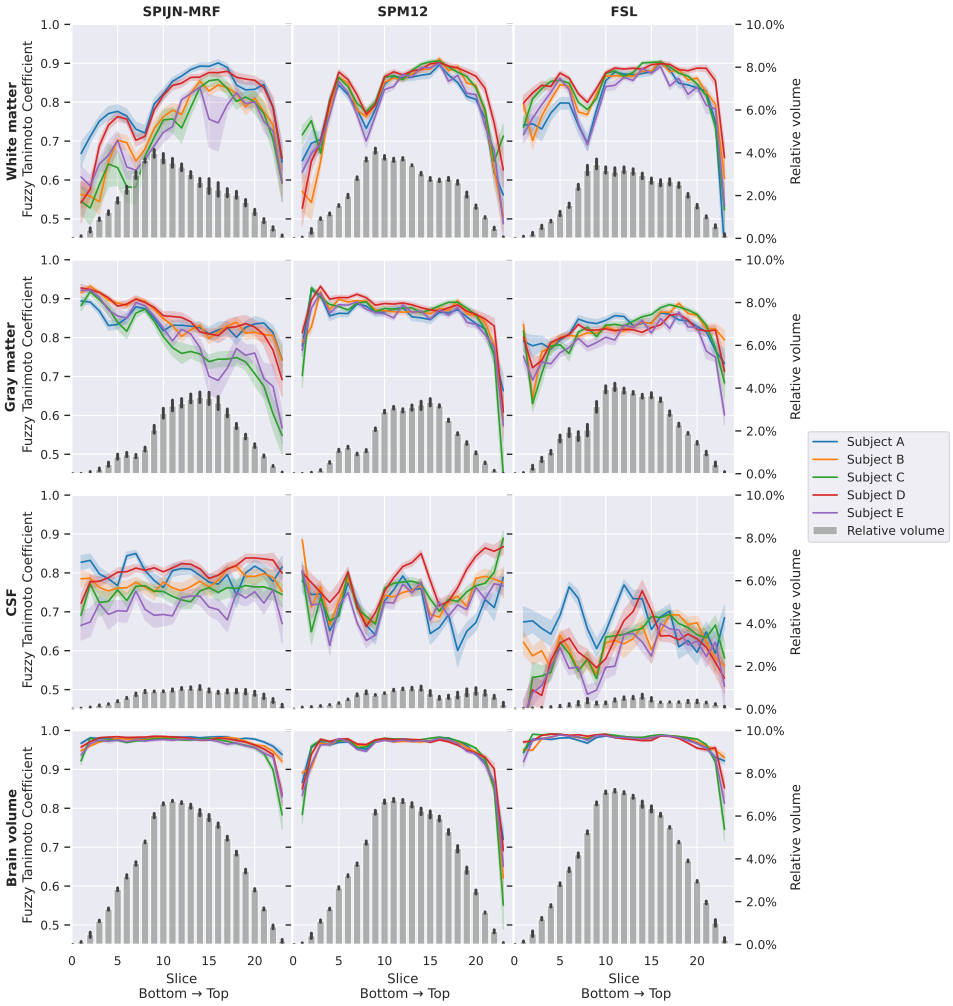

Figure S3.7: Line plots showing averaged pair-wise Fuzzy Tanimoto Coefficient (and the 95 % confidence interval shadowed) for each subject with SPIJN-MRF , SPM12, and FSL for each slice. Gray bars indicate the averaged across the subjects relative tissue volume compared to the total brain volume for each slice. Vertical line on top of the bars indicates the standard deviation.

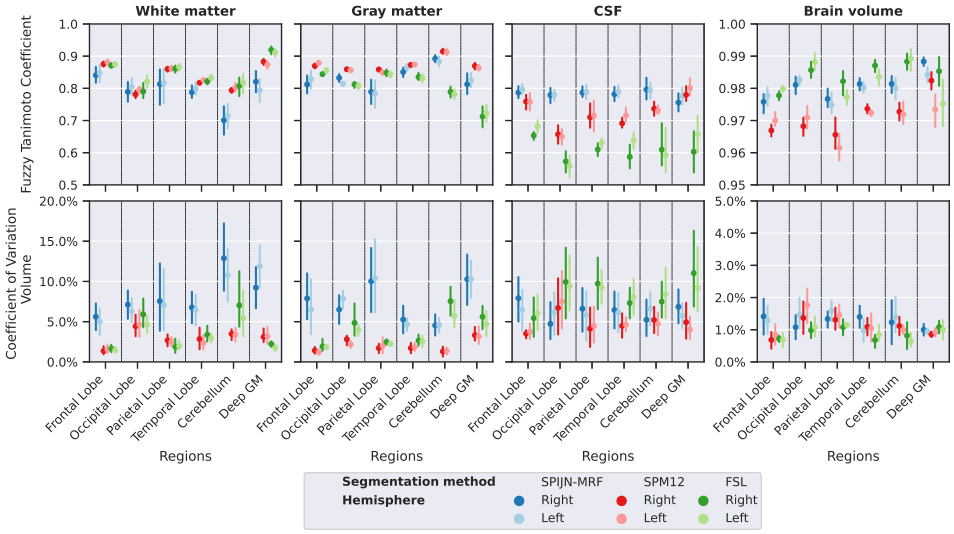

Figure S3.8: Mean Combined Fuzzy Tanimoto Coefficient and CoV in different brain regions for white matter (including myelin), gray matter, CSF and total brain volumes (white matter, gray matter plus CSF) obtained with SPIJN-MRF (blue), SPM12 (red), and FSL (green). Darker colors represent values for the right side of the brain, lighter colors reflect values for the left side of the brain.

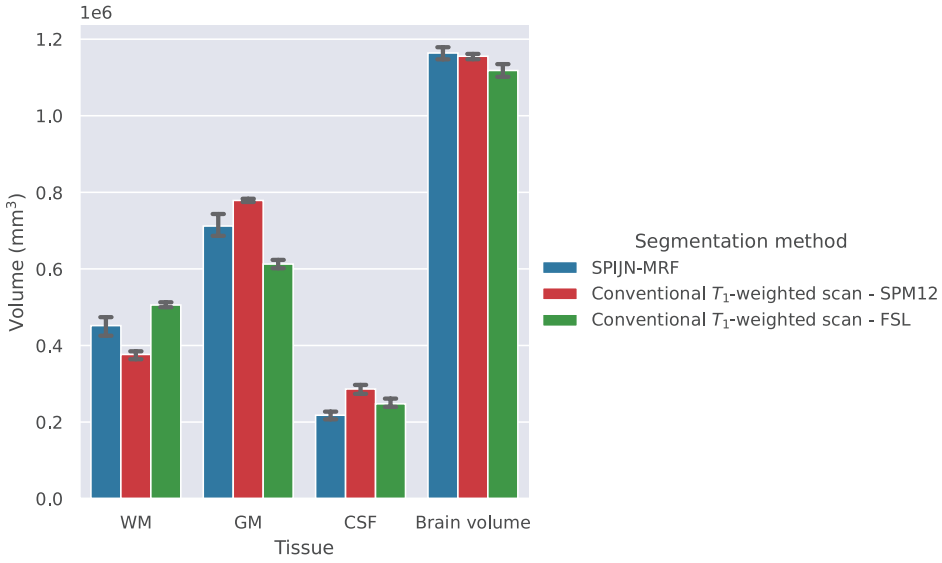

Figure S3.9: Estimated volumes using SPM12 (red) and FSL (green) for four high resolution T_1-weighted acquisitions together with the previously estimated volumes using SPIJN-MRF (blue).

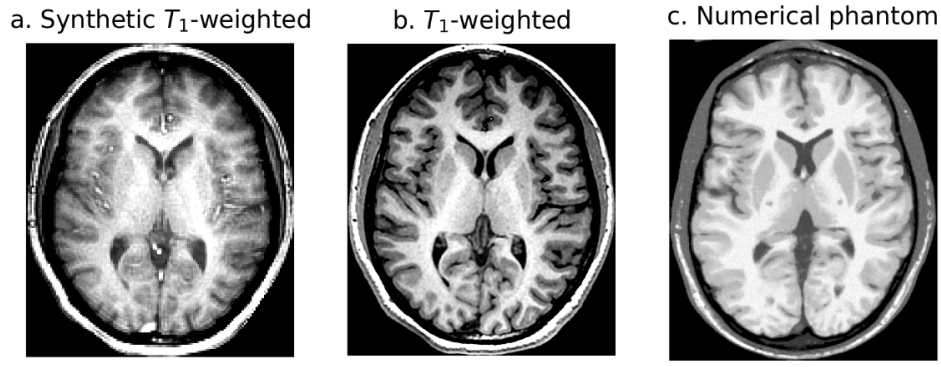

Figure S3.10: Example T_1-weighted images. A) Synthetic T_1-weighted image generated using the quantitative maps from MRF. B) Conventional 3D high-resolution MPRAGE sequence. C) T_1-weighted image simulated with BrainWeb as a spoiled FLASH sequence with the standard settings.

4

MYELIN WATER IMAGING FROM MULTI-ECHO T_2 MR RELAXOMETRY DATA USING A JOINT SPARSITY CONSTRAINT

Martijn A. Nagtegaal
Peter Koken
Thomas Amthor
Jeroen de Bresser
Burkhard Mädler
Frans M. Vos
Mariya Doneva

NeuroImage 219 (Oct. 1, 2020), p. 117014. ISSN: 1053-8119.
DOI: 10.1016/j.neuroimage.2020.117014

ABSTRACT

Demyelination is the key pathological process in multiple sclerosis (MS). The extent of demyelination can be quantified with magnetic resonance imaging by assessing the myelin water fraction (MWF). However, long computation times and high noise sensitivity hinder the translation of MWF imaging to clinical practice. In this work, we introduce a more efficient and noise robust method to determine the MWF using a joint sparsity constraint and a pre-computed B_1^+-T_2 dictionary.

A single component analysis with this dictionary is used in an initial step to obtain a B_1^+ map. The T_2 distribution is then determined from a reduced dictionary corresponding to the estimated B_1^+ map using a combination of a non-negativity and a joint sparsity constraint.

The non-negativity constraint ensures that a feasible solution with non-negative contribution of each T_2 component is obtained. The joint sparsity constraint restricts the T_2 distribution to a small set of T_2 relaxation times shared between all voxels and reduces the noise sensitivity.

The applied Sparsity Promoting Iterative Joint NNLS (SPIJN) algorithm can be implemented efficiently, reducing the computation time by a factor of 50 compared to the commonly used regularized non-negative least squares algorithm. The proposed method was validated in simulations and in 8 healthy subjects with a 3D multi-echo gradient- and spin echo scan at 3T. In simulations, the absolute error in the MWF decreased from 0.031 to 0.013 compared to the regularized NNLS algorithm for SNR=250. The in vivo results were consistent with values reported in literature and improved MWF-quantification was obtained especially in the frontal white matter. The maximum standard deviation in mean MWF in different regions of interest between subjects was smaller for the proposed method (0.0193) compared to the regularized NNLS algorithm (0.0266). In conclusion, the proposed method for MWF estimation is less computationally expensive and less susceptible to noise compared to state of the art methods. These improvements might be an important step towards clinical translation of MWF measurements.

4.1. INTRODUCTION

MYELINATION is a crucial aspect of brain development and is essential for the functioning of the nervous system. Demyelination, on the other hand, is a pathological process that plays an important role in certain diseases such as multiple sclerosis [104, 105]. Accurate measurement of myelin content has the potential to increase our insights into several disease processes. Magnetic resonance imaging (MRI) enables imaging of features related to (de-)myelination in vivo. Methods to do so include ultra-short echo time imaging, diffusion tensor imaging, magnetization transfer imaging and multi-echo T_2 (MET_2) or T_2^* relaxometry methods [17, 106]. In MET_2 relaxometry [19, 34, 107], a T_2 distribution is determined from a multi-echo spin-echo (MESE) acquisition. The analysis of this distribution is normally limited to the white matter, in which the short T_2 relaxation times (10-40 ms) are considered as myelin water (MW), intermediate T_2 relaxation times (40-200 ms) as intra- and extracellular water (IECW) and longer T_2 relaxation times (>1 s) as free water [106]. The myelin water fraction (MWF) is calculated as the ratio between the signal contribution from MW to the total sum of signal contributions. It was shown that the method results in reproducible MWF maps, but these maps are dependent on methodological variability [108, 109].

A Gradient- and Spin-Echo (GRASE) acquisition pattern was introduced in the field of MET_2 relaxometry to obtain whole brain images with shorter acquisition times compared to a regular MESE acquisition [110]. The outcomes of regular MESE and multi-echo GRASE imaging are known to be highly similar [41, 111].

However, MESE and multi-echo GRASE signals are sensitive to inhomogeneities in the B_1 transmit field (B_1^+). In particular, these inhomogeneities can cause refocusing pulses with flip angles very different from 180°, leading to secondary and stimulated echos [112]. As a result, deviations from mere exponential decays can occur. To account for B_1 inhomogeneity effects, the signal for each T_2 component may be calculated based on the extended phase graph (EPG) formalism [53] using the corrected flip angle. Such flip angle inhomogeneity (FAI) correction is especially important at high field strength ($B_0 \geq 3T$), since in that case the B_1^+ field becomes less homogeneous.

In addition, the inverse problem of computing a T_2 distribution from MET_2 data is highly underdetermined and therefore very sensitive to noise [113]. Therefore, it is crucial to acquire data with a high signal to noise ratio (SNR) and apply regularization in order to obtain a stable solution. A common approach [34] is to solve the problem for every voxel independently assuming that the T_2 distribution is smooth. This smoothness is enforced by including the first-order derivative of the T_2 distribution as a penalty term in the objective function. The resulting problem can be solved by the regularized non-negative least squares (regNNLS) algorithm [35]. To include FAI correction, Prasloski et al. [114] proposed an EPG approach using regNNLS fitting, which was solved for different FAI. This makes it possible to find the optimal FAI value to calculate the final T_2 distribution in a voxel-wise manner. However, including this correction increases the computational complexity leading to very long processing times. Yoo et al. [115] were able to reduce the computation time by a factor 4 using CPU and GPU parallelization leading to 10 minutes computation time for a dataset with matrix size $256 \times 256 \times 7$ and 32 echos. Although it has been shown that this method gives reproducible results [116, 117], it remains sensitive to noise, leading to relatively large coefficients of variation.

As such, the method can benefit from improved regularization or other techniques that better control the noise amplification.

Several other regularization approaches were proposed, either leading to simplifications of the signal model or to increased computation times. Hwang and Du [39] proposed to include additional (2D) spatial regularization in the regNNLS algorithm, leading to smoother MWF maps. Similarly, 2D spatially regularized MWF mapping with B_1^+ inhomogeneity correction was proposed by Kumar et al. [40] and later extended to include spatial smoothness of the FAI map and 3D spatial regularization [41]. Due to the complexity of the problem, the computation time was reported to take approximately 15-16 hours for MET_2 data of size $80 \times 80 \times 64$ with 32 echoes.

While the above mentioned methods allow for a large number of T_2 components (up to 50 or 100), [118–120] proposed a two or three compartment model, assuming that the distribution can be described by Gaussian peaks representing MW, intra- and extracellular water (IEW) and free water, respectively. Constraining these components to a predefined T_2 range combined with the restriction of having a fixed, small number of components drastically reduces the flexibility of the model, but yields improved noise robustness. In a similar way, Akhondi-Asl et al. [121] used an inverse Gaussian distribution for a three compartment model, which prevents a distribution with a tail reaching to negative T_2 values.

Recently, several methods were introduced that used a T_2 distribution consisting of delta peaks. Björk et al. showed that the distribution does not necessarily need to be smooth, since a Gaussian distribution or combination of delta peaks essentially lead to the same measurement. For exponential signals, this makes it possible to estimate the MWF in a parameter-free manner, without a pre-defined T_2 grid through a system identification approach (EASI-SM algorithm) [123]. However, since this algorithm is specifically designed for exponential signals, it does not allow the correction for FAI using EPG simulations. Drenthen et al. recently proposed to use orthogonal matching pursuit (OMP) instead of the regNNLS algorithm. They applied the non-negative OMP algorithm proposed by Yaghoobi, Wu, and Davies and Nguyen et al. , which implicitly includes a non-negativity constraint. The NNLS and NNOMP algorithm show great similarities, but Drenthen et al. demonstrated that applying temporal regularization in the NNLS algorithm leads to a bias in the estimated MWF. Recently, Does et al. [126] proposed a method based on principle component analysis to distinguish the components contributing to the signal from those characterizing the noise. In this manner the method provides a way to pre-process noisy relaxometry data.

In most of these studies, the proposed algorithms were compared to the state of the art regNNLS algorithm. In these comparisons, several methods showed a higher MWF in the sub-cortical white matter and major white matter tract regions, which was confirmed by the signal in T_2 weighted scans.

Most recently, dictionary-based methods have gained increased interest for quantitative MR parameter mapping. Popular examples include applying a dictionary as a signal representation for compressed sensing image reconstruction [127, 128], a grid search for fast parameter estimation [129–131], and MR Fingerprinting (MRF) in which multiple tissue parameters and system parameters are estimated simultaneously [9]. In these methods, a pre-computed dictionary containing simulated signal evolutions is used for

tissue and/or system parameter mapping. Specifically, the inner product is applied to identify the best matching dictionary atom and in effect the corresponding parameters from a measured signal. The dictionary depends on the pulse sequence and the expected range of tissue and system parameters that need to be estimated. This dictionary is computed once for a given pulse sequence and can be reused for all subsequent acquisitions.

Recently, several algorithms were proposed to perform a multi-component analysis of MR Fingerprinting data [25, 36], where components are distinguished based on T_1 and T_2 values. Similarly to multi-component T_2 approaches, these methods perform the multi-component MRF (MC-MRF) analysis for each voxel separately applying a sparsity constraint to limit the number of components per voxel. Following on these methods, we recently proposed a new method for MC-MRF based on the NNLS algorithm that applies a spatial joint-sparsity constraint leading to a small number of components across the region of interest [75]. This additional constraint enables further noise resilience of the estimated component weights and implementation in a computationally efficient algorithm. Consequently, it leads to significantly reduced computation time compared to the Bayesian and reweighted ℓ_1-norm approaches.

In this work, we propose a new multi-component approach to MWF mapping, based on our previously proposed algorithm for MC-MRF, which is extended to include FAI correction. The FAI map is initiated by performing a voxel-by-voxel, dictionary based, single-component parameter estimation. Subsequently, a multi-component analysis is performed with an algorithm combining a joint-sparsity constraint with non-negativity, in which the correction for FAI effects is included. We assume that the T_2 distribution is sparse and all voxels within a region of interest share the same T_2 components.

This is a crucial difference with the common assumption that the T_2 distribution is temporally, and (optionally) spatially smooth. We hypothesize that our approach will reduce noise amplification in the MWF maps and allow for a computationally efficient algorithm. The proposed method is evaluated in numerical simulations and in vivo measurements and compared to the regNNLS algorithm.

4.2. METHODS

4.2.1. DATA MODEL

To describe the used data model we will start with the model for a single voxel and expand this to the complete set of voxels in the region of interest. The multi-component signal $\mathbf{x}_j \in \mathbb{R}^M$ measured in voxel j at M time points for a MESE sequence is modeled as

$$\mathbf{x}_j = \int_0^\infty \mathbf{S}(a_j, T_2) c_j(T_2) dT_2 + \mathbf{e}_j \tag{4.1}$$

where $\mathbf{S}(a_j, T_2) \in \mathbb{R}^M$ is the signal for relaxation time T_2 at FAI value a_j, $c_j(\cdot)$ is the T_2 distribution, and $\mathbf{e}_j$ a Gaussian noise vector. The value of $c_j(T_2)$ can be considered the signal contribution of a tissue with a certain T_2 time in voxel j.

The MESE signal decay $\mathbf{S}(a_j, T_2)$ for non-ideal refocusing pulse flip angles can be calculated using the EPG formalism [53]. The applied sequence consists of an $a_j \cdot 90^\circ$ pulse followed by M $a_j \cdot 180^\circ$ pulses.

The integral of Equation (4.1) might be discretized by taking N_{T_2} T_2-values and N_{FAI}

FAI values assuming that there are $N = N_{T_2} \cdot N_{FAI}$ possible signal realizations. These signals will be stored in a matrix $D \in \mathbb{R}^{M \times N}$, to which we will refer as the dictionary. A sub-dictionary containing the signals for a specific FAI value a is indicated as $D_a \in \mathbb{R}^{M \times N_{T_2}}$. In this matrix the rows correspond to the simulated signal and each column to a particular T_2 time.

Assuming that there is only a single FAI-value in voxel j, Equation (4.1) can be written as a linear combination of N_{T_2} signals with weights $\mathbf{c}_j$, corresponding to the discretized T_2 distribution values and the FAI value a_j for the given voxel:

$$\mathbf{x}_j = D_{a_j}\mathbf{c}_j + \mathbf{e}_j, \tag{4.2}$$

The weights of the T_2 distribution are assumed to be non-negative. Given a measured signal $\mathbf{x}_j \in \mathbb{R}^M$ the weights of the T_2 components can then be estimated by solving the non-negative least squares problem:

$$\mathbf{c}_j = \underset{\tilde{\mathbf{c}}_j \in \mathbb{R}^N_{\geq 0}}{\arg\min} \left\| \mathbf{x}_j - D_{a_j}\tilde{\mathbf{c}}_j \right\|_2^2. \tag{4.3}$$

Conventional methods for solving this minimization problem assume that the vector $\mathbf{c}$ is either smooth or sparse. In the smooth model it is usually assumed that the T_2 spectrum has a small number of peaks, which in the discrete delta peak model means that the vector c is sparse. Very recently, we introduced a different approach by imposing a joint sparsity constraint [75]. Our premise was that the measured signals in a region of interest (ROI) could be described by a small set of T_2 relaxation times, common for all voxels in the ROI. To formalize this, let $C = \begin{bmatrix} \mathbf{c}_1 & \dots & \mathbf{c}_J \end{bmatrix}$ be the $N_{T_2} \times J$ sized matrix containing the contributions for all J voxels. Furthermore, $\mathbf{c}^i$ is taken to represent a row from this matrix, corresponding to the contributions of a particular T_2 signal to all voxels, so that at the same time $C = \begin{bmatrix} \mathbf{c}^{1T} & \dots & \mathbf{c}^{N_{T_2}T} \end{bmatrix}^T$.

This leads to the joint sparsity minimization problem:

$$\begin{aligned} \min_{C \in \mathbb{R}^{N_{T_2} \times J}_{\geq 0}} \quad & \sum_{j=1}^{J} \|\mathbf{x}_j - D_{a_j}\mathbf{c}_j\|_2^2 \\ \text{s.t.} \quad & \sum_{i=1}^{N_{T_2}} \left\| \mathbf{c}^i \right\|_0 \text{ is small.} \end{aligned} \tag{4.4}$$

The term $\sum_{i=1}^{N_{T_2}} \left\| \mathbf{c}^i \right\|_0$ counts the number of used components, but does not restrict this to a prescribed maximum. The joint sparsity problem including the non-negativity constraint can be solved with different algorithms. We applied the Sparsity Promoting Iterative Joint NNLS (SPIJN) algorithm [75] for MC-MRF involving highly-coherent signals. This approach enabled a higher noise robustness compared to voxel by voxel methods and leads to easy interpretable results because of the small number of components. In this work we extend the SPIJN algorithm to include FAI correction and investigate its application to multi-component T_2 analysis.

4.2.2. FITTING PROCEDURE

We propose a two-step approach to perform multi-component T_2 analysis of MET_2 data: (1) a FAI map is computed assuming that the measured signal is dominated by a main component, and thus can be modeled as a single component in each voxel; (2) a multi-component T_2 analysis is performed using the estimated FAI map and applying the joint sparsity constraint as stated in Eq. (4.4). The algorithm is schematically described in Algorithm 4.1.

Using the EPG formalism a dictionary D was computed containing combinations of FAI and T_2-values. A fixed $T_1 = 1$ s was used in the EPG simulations similarly to [41, 114]. FAIs were simulated as a multiplicative factor modifying the prescribed flip angle. The FAI values are modeled as $a = \frac{\alpha_{\text{effective}}}{\alpha_{\text{intended}}}$, for a CPMG sequence the effective signals are symmetric around $a = 1$. The modeled FAIs ranged from 0.75 to 1 in 140 linear steps, while T_2 relaxation times were chosen on a logarithmic scale from 10 ms to 5 s with 141 steps. The total computation time for the dictionary was 81 seconds.

The dictionary was first used to perform a single component matching. For each voxel, the inner product between measured signal and (normalized) dictionary signals was used to determine the FAI-T_2 combination that best described the measured signal.

Subsequently, the same dictionary was applied in the SPIJN algorithm for multi-component estimation and while doing so the FAI was restricted by the value obtained through single component matching. The SPIJN algorithm was based on the NNLS algorithm and used an iterative reweighting scheme to couple the non-negative sparse solutions of the different voxels. By applying this reweighting the solution converged to a jointly sparse solution.

The proposed method was implemented in Python. More details on the used convergence thresholds, the used reweighting and regularization can be found in [75]. The regularized NNLS algorithm including FAI correction [114] was used as a reference method. 101 T_2 values logarithmically spaced from 10 ms to 5 s and a fixed T_1 of 1 s were used. The regNNLS computations were performed with MATLAB 2018b.

4.2.3. NUMERICAL SIMULATION EXPERIMENTS

Two numerical experiments were performed to analyze the proposed method. Both experiments were performed for $M = 48$ echoes with a spacing of $\Delta TE = 10$ ms (first echo at 10 ms). These settings were also applied in the in vivo experiment (see below).

First, the behavior of the proposed FAI estimation was analyzed and compared to FAI estimation with the regNNLS algorithm. Simulations were performed based on a signal composed as the weighted sum of two components: a short water (SW) relaxation component, with T_2=20 ms, and a long water (LW) relaxation component with T_2 times from 25 ms to 3 s with 41 steps on a logarithmic scale. The SW fraction (SWF) ranged from 0 to 1 with step size 0.05 (while LWF = 1 - SWF). The FAI level varied between 0.75 and 1 in 5 steps. Furthermore, 100 real valued Gaussian noise realizations were added to each simulated signal, to yield 100 noisy signal versions at each setting. The Gaussian noise had a standard deviation defined as s_0/SNR, in which s_0 was the signal intensity of the first echo. A fixed SNR of 250 was used, which was comparable to the SNR of the in vivo experiment (see below). The absolute value of the noisy signal was then analyzed with the proposed FAI estimation.

Algorithm 4.1 The Sparsity Promoting Iterative Joint NNLS (SPIJN) algorithm to perform a multi-component analysis for MET_2 data with correction for flip angle inhomogeneities.

INPUT:

$X = [\mathbf{x}_1, ...\mathbf{x}_J]$	-	real valued, normalized signals (size $M \times J$)
D	-	real valued, normalized dictionary for a range of FAI and T_2 combinations (size $M \times N$)
$\mathbf{f}$	-	supporting look-up table of FAI values of length N
λ	-	regularization parameter
ϵ	-	parameter for reweighting (default 10^{-4})

OUTPUT:

C	-	non-negative, jointly sparse solution for Eq. (4.4).

a $\leftarrow \mathbf{1} \in \mathbb{R}^J$ ▷ Initialize FAI values as vector of length J
for $j \in \{1, ..., J\}$ **do** ▷ For all voxels j determine the FAI
  $i \leftarrow \underset{i \in \{1,...,N\}}{\arg\max}(D^T \cdot \mathbf{x}_j)_i$ ▷ Find dictionary atom with max inner product
  $a_j \leftarrow f_i$ ▷ Determine FAI value for voxel
end for
$k \leftarrow 1$ ▷ Counter for the number of iterations
$C_1 \leftarrow \frac{1}{M}\mathbf{1} \in \mathbb{R}^{N \times J}$ ▷ Initial solution: equal component weights
$\bar{\lambda} \leftarrow \lambda \cdot \log_{10} J$ ▷ Scale the regularization parameter
while not converged **do**
  $w_{k+1,i} \leftarrow \|\mathbf{c}_k^i\|_2 + \epsilon, \ \forall i \in \{1, ..., N_{T_2}\}$ ▷ Calculation of the weights based on rows $\mathbf{c}_k^i$ of C_k
  $W_{k+1} \leftarrow \mathrm{diag}\left(\mathbf{w}_{k+1}^{1/2}\right)$
  for $j \in \{1, ...J\}$ **do** ▷ Calculate solution for each voxel
    $\tilde{D}_{k+1} \leftarrow \begin{bmatrix} D_{a_j} W_{k+1} \\ \bar{\lambda}\mathbf{1}^T \end{bmatrix}; \tilde{\mathbf{x}}_j \leftarrow \begin{bmatrix} \mathbf{x}_j \\ 0 \end{bmatrix}$ ▷ Weighting and ℓ_1^2 regularization
    $\mathbf{c}_j \leftarrow \arg\min_{c \in \mathbb{R}^N_{\geq 0}} \|\tilde{\mathbf{x}}_j - \tilde{D}\mathbf{c}\|_F^2$ ▷ Solve using NNLS algorithm
  end for
  $C_{k+1} \leftarrow W_{k+1} \cdot [\mathbf{c}_1, ..., \mathbf{c}_j]$ ▷ Compensate for the weighting
  $k \leftarrow k + 1$
end while
$C \leftarrow C_k$ ▷ Only return the last iteration

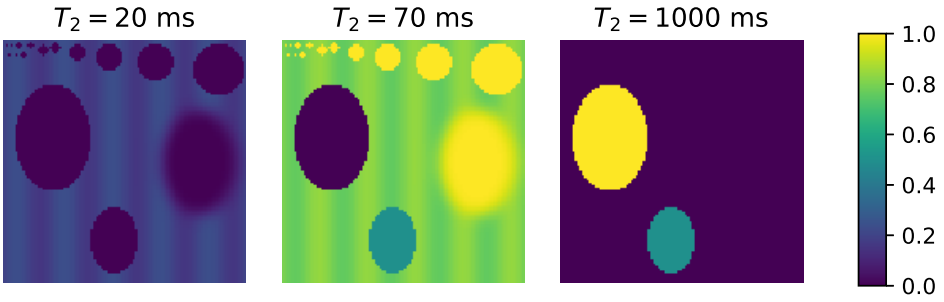

Figure 4.1: The ground truth fraction maps of the three components simulated in numerical experiments. The first component with mean $T_2 = 20$ ms resembles MW and shows a smoothly varying fraction oscillating around 0.2 and is absent at certain locations. The second component with $T_2 = 70$ ms resembles IECW and is the main component present in the simulated image. The third component with $T_2 = 1000$ ms resembles cerebrospinal fluid and is present in two regions for 100 % and 50 %.

The mean residual signal error as well as the mean FAI error were calculated for each parameter combination (SWF/FAI/LW-T_2). The mean residual signal error was computed as $\frac{1}{100}\sum_{i=1}^{100}\|\mathbf{s}-\mathbf{d}_i\|_2/\|\mathbf{s}\|_2$ where $\mathbf{s}$ is the ground truth noise free signal and $\mathbf{d}_i$ is the matched dictionary signal for noise realization i.

Second, the precision and accuracy of the calculated MWF with the proposed method was compared to outcomes of NNLS and regNNLS algorithms. Therefore, an image was simulated consisting of 100×100 pixels with a mixture of three components. These components had T_2 relaxation times of 20 ms, 70 ms and 1000 ms roughly corresponding to MW, IECW and FW, respectively. The map with the signal fractions (summing to one) of the components is shown in Figure 4.1.

The simulations were performed with two different, constant FAI levels of 1.0 (i.e. no offset in B_1^+ field) and 0.9. The simulations were performed with different noise realizations, applying SNRs of 500, 250 and 100.

The MWF was computed with the unregularized NNLS and SPIJN algorithms using the FAI map estimated in an initial single component analysis step as described above. For the SPIJN algorithm $\lambda = 0.02$ was used. These MWF maps were compared to the MWF from the regNNLS algorithm and to the ground truth. Relaxation times below 40 ms were considered to correspond to the MW component.

4.2.4. IN VIVO IMAGING EXPERIMENTS

To study the practical feasibility of the proposed method, brain scans were performed in 8 healthy subjects. Informed consent was obtained from all subjects. Imaging was performed on a 3 T Ingenia scanner (Philips, Best, The Netherlands) based on a 3D multi echo GRASE acquisition scheme using a 13 channel head coil. The sequence parameters were: 48 echoes with echo spacing of $\Delta TE = 10$ ms; EPI factor of 3; field of view 240 mm × 205 mm × 72 mm; voxel sizes 1.25 mm × 1.25 mm × 8 mm ; repetition time $TR =$ 1.2 s, resulting in a total acquisition time of 6 minutes and 14 seconds.

A multi-component analysis of the acquired brain data was performed using the pro-

posed method. The proposed method was applied to all slices simultaneously. Skull and air were masked based on their signal intensity and other tissues not connected to the brain were also discarded as such. Additionally, the regNNLS algorithm was applied for myelin water mapping. For the SPIJN algorithm, the regularization parameter λ was set to 30 for the in vivo data (see Supplementary material Figure S4.1 for a range of λ values). The part of the T_2 distribution with a relaxation time shorter than a preset threshold value $\tilde{T}_2$ was attributed to MW. The MWF was calculated as $MWF = \sum_{i:T_2^i \leq \tilde{T}_2} c_i / \sum_{i=1}^{N_{T_2}} c_i$ for both methods. Experimentally, we studied two different thresholds: $\tilde{T}_2 = 30$ ms and $\tilde{T}_2 = 40$ ms. Regions of interest (ROIs) were manually annotated: splenium, thalamus and genu of the corpus callosum and parts of the frontal, occipital and temporal white matter lobes.

The SNR of the in vivo data was calculated from the results of the regNNLS algorithm as the ratio between the signal intensity in the white matter structures in the first echo and the standard deviation of the residual.

For each method, subject and ROI the mean MWF and coefficient of variation (CoV) were calculated. A paired two-sample t-test was used to determine the significance of the differences in MWF values and CoV per region.

4.3. RESULTS

4.3.1. NUMERICAL SIMULATION EXPERIMENTS

Figure 4.2 summarizes the outcomes of the first, FAI estimation experiment. It shows the absolute mean error of the estimated FAI and the single component signal approximation error for varying FAI, SWF and LW-T_2 relaxation times (averaged over 100 noise realizations) for the SPIJN and regNNLS algorithm. The signal approximation error is not shown for the regNNLS, since it was negligible (max. $5 \cdot 10^{-4}$). The middle row demonstrates that the error in the proposed method is largest for a combination of a SWF between approximately 0.5 and 0.9, large LW-T_2 relaxation times and more severe flip angle inhomogeneity level (FAI toward 0.75). Furthermore, the bottom images show that when the SWF and LW-T_2 increase, the signal estimation error increases as well because the signal model becomes less accurate. A LW-$T_2 < 160$ ms and SWF ≤ 0.2 is a realistic range for a mixture of MW and IECW, see e.g. [106]. In this range, demarcated by the dotted line in the figure, the maximum mean absolute error in the estimated FAI is 0.0266.

Compared to the regNNLS algorithm (first row) the proposed method shows similar errors in the range of interest, but not for more extreme combinations. The overall mean FAI error using the regNNLS algorithm was lower (0.0158) compared to the proposed method (0.0460). However, the maximum error in the realistic range was 0.0301 with the regNNLS method, which is higher than the error of the proposed method (0.0266). Also, the mean error in this range was higher: 0.0146 compared to 0.0133, for regNNLS and proposed approach, respectively.

In Figure 4.3 the absolute mean MWF error maps (over 100 noise realizations) are shown for a FAI values of 1 and 0.9, summarizing the second MWF estimation experiment. Above each map, the root mean square error (RMSE) is indicated. Estimates were calculated with the NNLS, SPIJN, and regNNLS algorithms, at SNR values of 500, 250 and 100.

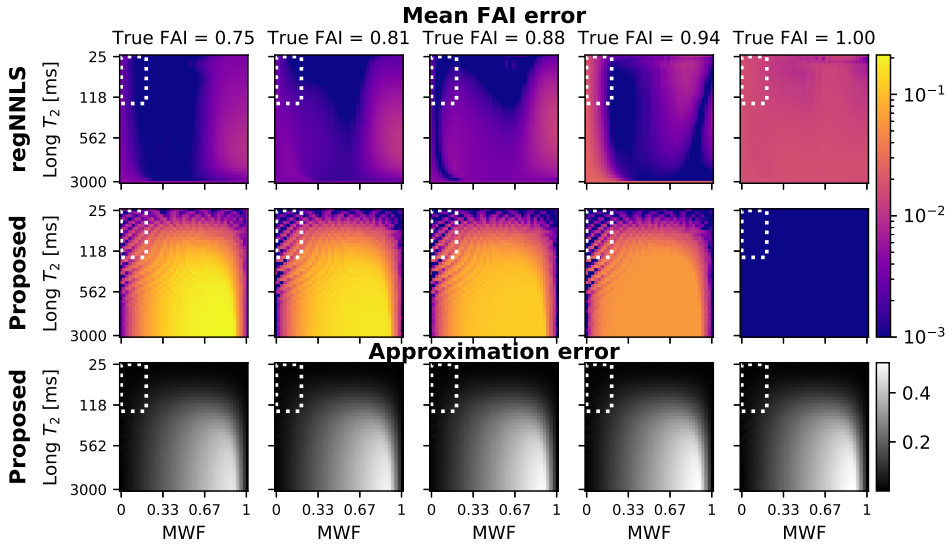

Figure 4.2: Absolute mean error of the estimated FAI (top 2 rows) and mean signal approximation error (bottom row) in simulations for varying FAI values, MWF values and T_2 relaxation times for the long component. FAI errors are shown for the proposed and regNNLS algorithm, signal approximation errors for the proposed method. The MW component has a fixed relaxation time of T_2=20 ms. The white box indicates the range for realistic IECW T_2 relaxation times and plausible (short) MW fractions.

The SPIJN algorithm resulted in lower MWF RMSE for all SNR values compared to the NNLS and regNNLS algorithms. Observe that especially for FAI=1 the RMSE were markedly lower. Particularly for SNR=250 the SPIJN algorithm achieved a 58 % lower error compared to the regNNLS algorithm.

4.3.2. IN VIVO IMAGING EXPERIMENTS

The mean SNR of the in vivo MET_2 data sets, as defined in Section 4.2.4, was 320 (maximum: 436; minimum: 254). Application of the SPIJN algorithm led to 5 to 7 components. The distribution of T_2-values across identified components in the subjects is shown in Figure 4.4. In general, it can be seen that components are matched to the lower and upper bound of T_2 values in the dictionary (10 ms and 5 s respectively). In between these bounds, components are matched to T_2 values around 35, 75 and 250 ms. The fraction maps for the different components for a representative subject (subject 2) are shown in Figure 4.5.

Figure 4.6 shows representative T_2 weighted images, estimated FAI maps and MWF maps ($\tilde{T}_2$ = 40 ms) for the same subject. FAI and MWF maps were obtained with the SPIJN algorithm and the reference regNNLS algorithm. The FAI maps of the two methods show good agreement. The main difference between the regNNLS and SPIJN MWF maps can be seen in the frontal white matter (red circle). Here, the T_2 weighted images show evidence that there is myelin present, signified by the white- gray matter contrast. However, the regNNLS algorithm estimates very low MWF in these regions. Figure 4.5

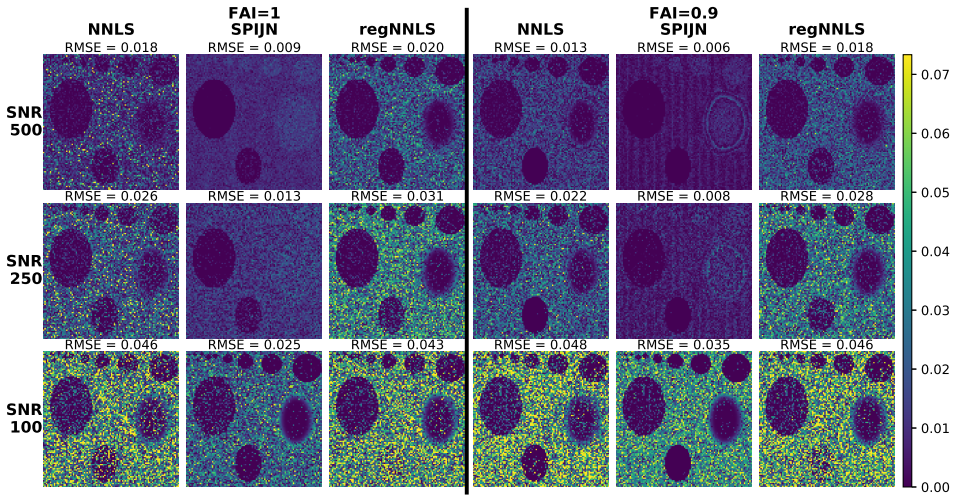

Figure 4.3: Absolute error maps of estimated MWF with the NNLS, SPIJN and regNNLS [114] algorithms for FAI values of 0.9 and 1 in simulations with different SNR. Underlying ground truth fraction maps are shown in Figure 4.1. The maps of the NNLS and SPIJN algorithms were computed using FAI estimations from the proposed single component dictionary matching. The root mean square error (RMSE) for each map is indicated on top.

Table 4.1: MWF values for different structures with the reference method reg NNLS and proposed SPIJN algorithm for different T_2 boundary values. The mean value of the ROI averaged MWFs among 8 different volunteers is given, with the standard deviation among the ROI averaged MWFs. Significant differences between the two methods ($p < 0.05$) are indicated by *.

$\tilde{T}_2$ [ms]	30		40	
Method	**reg NNLS**	**SPIJN**	**reg NNLS**	**SPIJN**
Frontal lobe	0.0610 (± 0.0187)	0.0625 (± 0.0169)	0.0683 (± 0.0189)	0.1371 (± 0.0141)*
Genu of the corpus callosum	0.0808 (± 0.0270)	0.0798 (± 0.0222)	0.0863 (± 0.0266)	0.1725 (± 0.0120)*
Occipital lobe	0.0684 (± 0.0132)	0.0799 (± 0.0078)	0.0847 (± 0.0172)	0.1119 (± 0.0193)*
Splenium of the corpus callosum	0.1287 (± 0.0156)	0.1267 (± 0.0167)	0.1295 (± 0.0153)	0.1315 (± 0.0147)
Temporal lobe	0.0838 (± 0.0229)	0.0919 (± 0.0179)	0.0886 (± 0.0207)	0.1186 (± 0.0168)*
Thalamus	0.1248 (± 0.0235)	0.1264 (± 0.0158)	0.1467 (± 0.0139)	0.1711 (± 0.0178)*

shows that the T_2 component of 36.2 ms is in particular responsible for the higher MWF detected by the SPIJN algorithm.

The mean MWF values across the ROIs and the subjects for the regNNLS and SPIJN with $\tilde{T}_2 = 30$ ms and 40 ms are summarized in Table 4.1. Furthermore, CoVs are collated in Table 4.2. For reference, literature values as measured with different algorithms are shown in Table 4.3. Observe that for $\tilde{T}_2 = 30$ ms differences between the methods are not significant. However, they are significant in most structures for $\tilde{T}_2 = 40$ ms. Only for the splenium the outcomes of the two methods are not significantly different at this threshold. Simultaneously, note that for $\tilde{T}_2 = 40$ ms the CoVs are significantly smaller for the proposed method compared to the regNNLS method.

The distribution of the differences between the two methods across the regions for $\tilde{T}_2 = 30$ ms are plotted in Figure 4.7. In most subjects the differences are not significant; only in subjects 7 and 8 significant differences were found at this setting. Notably, these

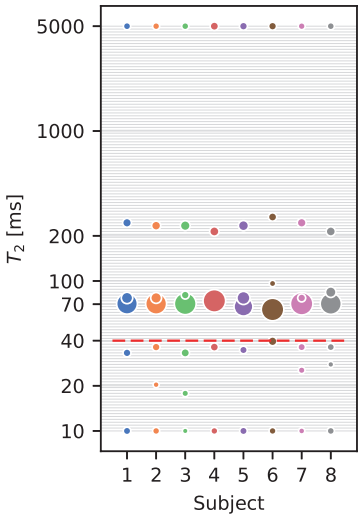

Figure 4.4: T_2 value distribution of components identified by the SPIJN algorithm for 8 subjects. The typical threshold value for MW detection ($\tilde{T}_2$ = 40 ms) is marked by a red line. The distance between the light gray grid lines reflects the dictionary step size. The size of the dots shows the relative abundance of the different components.

Table 4.2: Coefficient of variation of the MWF values for different structures with the reference method reg NNLS and proposed SPIJN algorithm for different T_2 boundary values. Significant differences ($p < 0.05$) between the two methods are indicated by *.

$\tilde{T}_2$ (ms)	30		40	
Method	**reg NNLS**	**SPIJN**	**reg NNLS**	**SPIJN**
Frontal lobe	0.488	0.513	0.406	0.221*
Genu of the corpus callosum	0.450	0.497	0.401	0.208*
Occipital lobe	0.556	0.439*	0.451	0.239*
Splenium of the corpus callosum	0.254	0.239	0.251	0.222*
Temporal lobe	0.462	0.400	0.432	0.230*
Thalamus	0.396	0.410	0.341	0.216*

two subjects yield components with T_2 = 25 ms (see also Figure 4.4), which adds to the MWF at $\tilde{T}_2$ = 30 ms.

The average computation time per slice was 1.19 s for the single component matching and 7.00 s for the multi component matching with the SPIJN algorithm. The average computation time per slice for the regNNLS was 48 s.

4.4. DISCUSSION

IN this study the SPIJN algorithm was introduced as a new, fast method to determine the MWF from MET_2 relaxometry data through a multi-component analysis with a correction for flip angle inhomogeneity. The method was compared to the NNLS and state of the art regNNLS algorithms in numerical simulations and on data from 8 subjects acquired at 3T.

The first simulation experiment showed that a FAI map can be accurately estimated, especially in a realistic range of IECW relaxation times and MWFs. The FAI-mapping

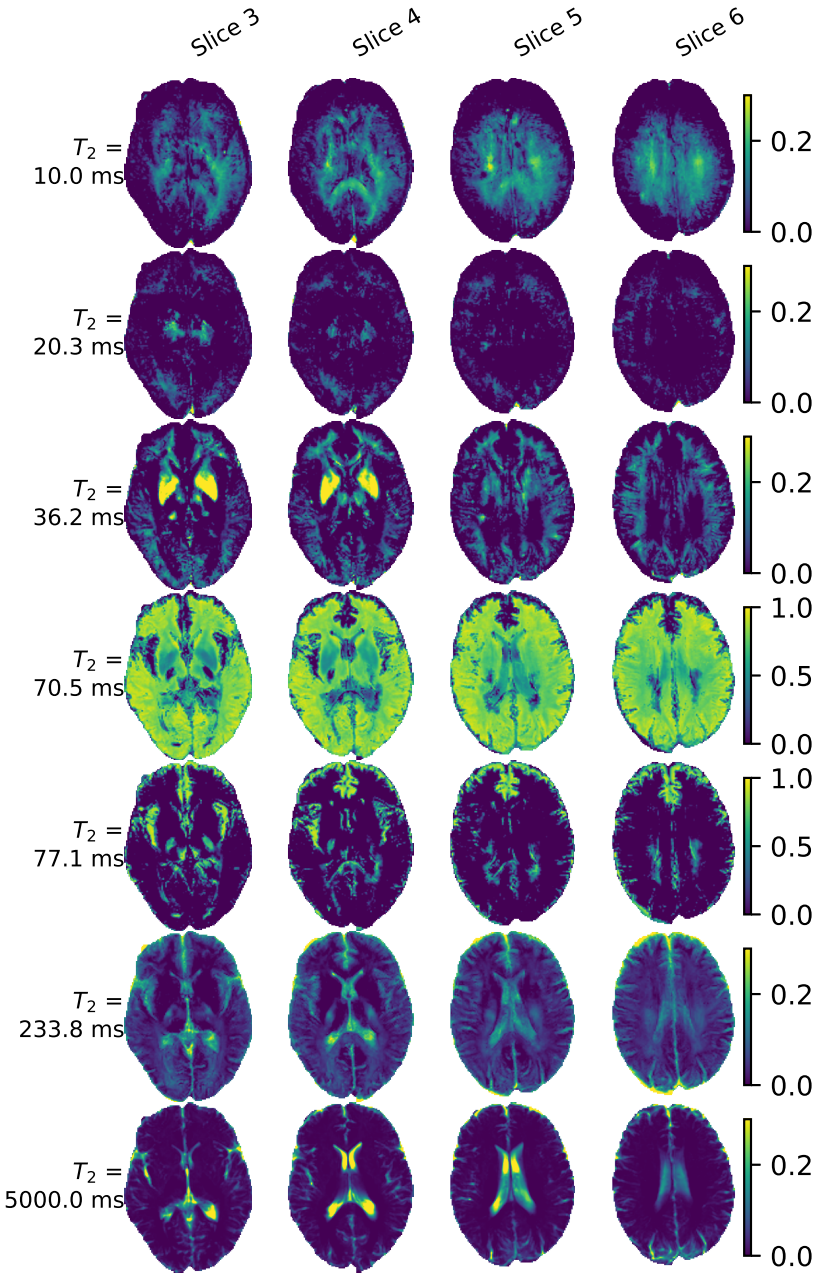

Figure 4.5: Fraction maps of matched components by the SPIJN algorithm for a representative subject. Across the columns is a selection of slices; rows show fraction maps for different components. Matched relaxation times are given on the left.

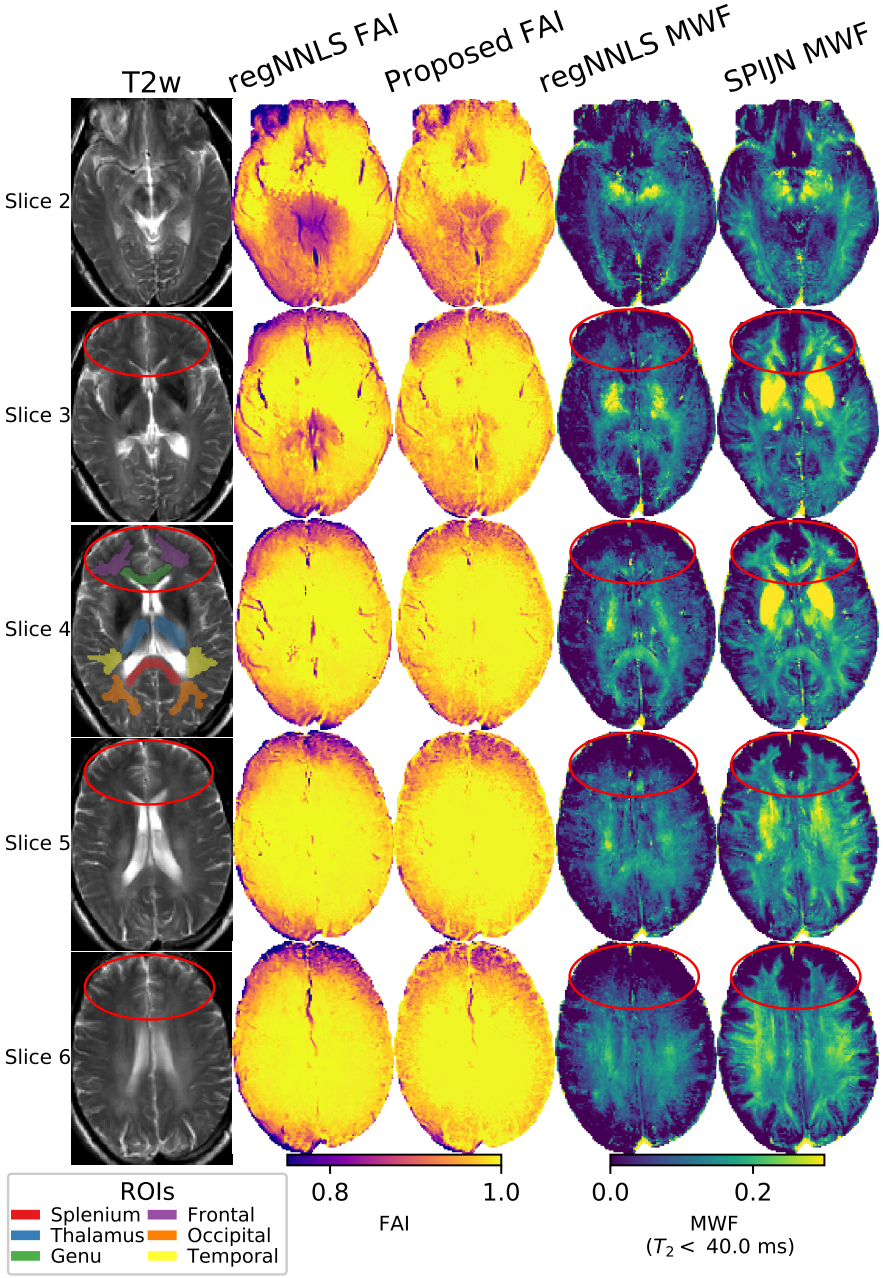

Figure 4.6: T_2-weighted images, FAI and MWF maps for the regNNLS and SPIJN algorithm for a representative subject. $T_2 \leq 40$ ms was considered to correspond to MW. Frontal white matter regions with increased white-gray matter contrast are annotated with red ellipses. In slice 4 an example of the manually annotated ROIs is shown.

Table 4.3: MWF values across several brain structures as reported in literature. All methods used $\bar{T}_2 = 40$ ms. Studies with * were performed at 1.5T, other studies were performed at 3T as the results shows in this paper.

Brain structure	[18]*	[108] *	[41]	[117]
Frontal lobe			0.14425 ± 0.00995	
Genu of the corpus callosum	0.0986 ± 0.0096	0.102 ± 0.048	0.1154 ± 0.0106	0.132 ± 0.053
Occipital lobe			0.10765 ± 0.0086	
Splenium of the corpus callosum	0.1305 ± 0.0096	0.149 ± 0.076	0.1533 ± 0.0292	0.211 ± 0.056
Thalamus	0.0579 ± 0.0054			0.170 ± 0.039

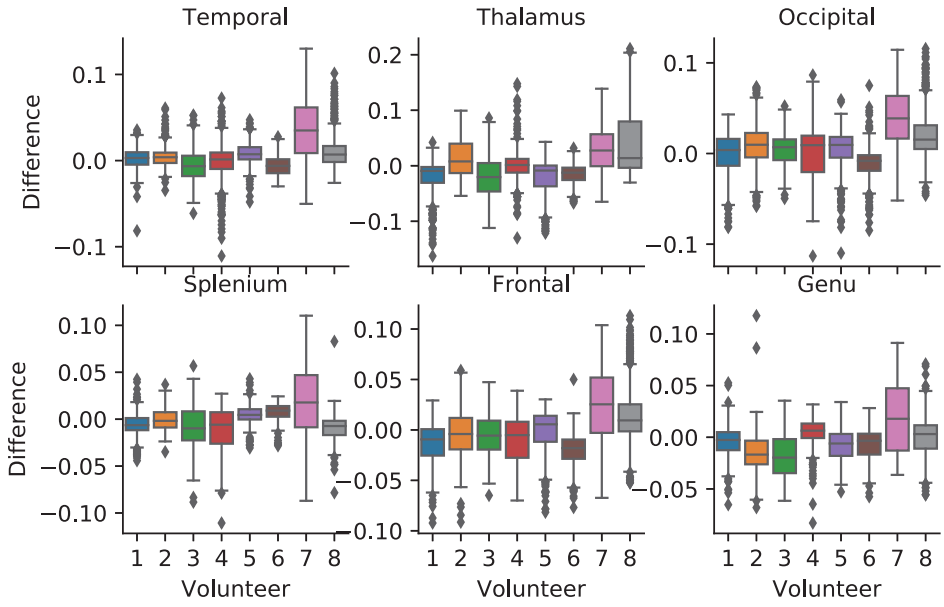

Figure 4.7: Box plots of difference between the MWF obtained for the SPIJN and regNNLS algorithms in 7 anatomical structures across the eight subjects. $T_2 \leq 30$ ms was considered to correspond to MW.

method is proposed as a computationally efficient technique and relies on the presence of a dominant tissue or small differences in T_2 between different components. The regNNLS approach [114] provides a more generally applicable method, but is computationally much more expensive. The mean error of the estimated FAI increases (order of 20 %) with increasing FAI, MWF (> 0.4) and increased T_2 of the non-MW component (> 400 ms). This could result in a biased FAI estimation e.g. in partial volume voxels with mainly myelin and cerebrospinal fluid. However, this setting represents a non-realistic configuration in myelinated tissue.

The second simulation experiment as shown in Figure 4.3 demonstrated that the SPIJN algorithm yields lower RMSE for MWF estimation than the NNLS and regNNLS algorithms. The shown simulations used a signal model with a sparse distribution of T_2 values, possibly favoring SPIJN over the regNNLS algorithm, which assumes a smooth distribution. As such, the difference between SPIJN and NNLS, in which a sparse distri-

bution is the only assumption, particularly shows the benefit of the joint sparsity constraint. The assumption of a jointly sparse T_2 distribution makes it possible to benefit from shared information in different regions and large numbers of voxels. As a consequence, improved noise resilience could be observed, especially at SNR=100. In-vivo measurements this may be important for balancing the trade-off between resolution and SNR. Reduced SNR caused by higher resolutions are expected to have smaller effects on accuracy with the proposed SPIJN algorithm compared to voxel-wise methods.

The number of resulting components enforced by the joint sparsity constraint may be difficult to predict a priori due to the complexity of tissue microstructure and potential natural variation. The number of retained components is influenced by the T_2 values of tissues present in the region of interest, the sensitivity of the used MET_2 sequence to these tissue parameters and the used level of regularization. As shown in Figure 4.4 the in vivo experiments yield small variations in the number of estimated components and associated T_2 relaxation times, which is probably due to natural diversity.

In general the T_2 values of the main groups of components are in agreement with the myelin water, intra- extracellular water and free water, as observed on a voxel basis by e.g. [18]. Three components with $T_2 < 40$ ms were identified in 4/8 subjects, while only two such components were obtained in the other 4/8 subjects. Figure 4.5 illustrated that the additional component ($T_2 = 20.3$ ms in this case) typically was associated with small signal fractions. In addition to these MW components, all subjects yielded a component with T_2 around 70 ms, which forms the main component in most voxels and is attributed to intra and/or extra cellular water. The identification of two further components with longer relaxation times is consistent with our earlier findings with MC-MRF [75]. The longest T_2 component ($T_2 = 5$ s) can be contributed to free water and is mainly present in the locations where free water is expected. The component around $T_2 = 250$ ms is rather small (typically 10 %), but is in confirmation with earlier observations [18, 132] and was interpreted as extra-axonal water [17]. A dominant component with comparable relaxation times was observed in patients with MS [133]. This component is not often reported in healthy subjects. The appearance of this component could be caused by increased sensitivity of the proposed algorithm to components with a low presence and thus contain useful information. It could also be caused by the proposed analysis method and then it has to be considered as an artifact. The information contained by this component would be of interest in further clinical studies or in an analysis of already acquired data.

Underlying biological principles could also cause a slight variation of T_2 values of the same component. This would conflict with the assumption of group sparsity, which determines a small basis to represent all measured signals. Since small differences in T_2 only cause a small difference in the exponential decay the effect of a slight variation on the T_2-components are minor. This was further assessed in an experiment as described in Supplementary material Figure S4.2.

The focus of the rest of the paper is on the accuracy with which a MWF map could be obtained from components reflecting low T_2 times. The values obtained with the SPIJN algorithm at $\tilde{T}_2 = 40$ ms are in agreement with the literature values as given in Table 4.3. Only the mean MWF in the genu of the corpus callosum shows a large difference with the values as reported by Kumar et al. On the other hand, they are in line with the results

as reported by Drenthen et al. The MWF values for the regNNLS algorithm are consistent with the values as reported in [110]. The MWF maps obtained by the SPIJN algorithm showed higher fractions compared to those computed with the regNNLS approach. This difference might be due to the smoothness constraint on the T_2 distribution imposed by regNNLS. In effect, myelin water with a T_2 around 35 ms could be smoothed into the larger IECW pool, so that it is not identified as MW.

Notably, the shown T_2 weighted images indicated that higher levels of myelin might be expected than reflected in the regNNLS maps. Moreover, the MWF maps obtained by the SPIJN algorithm are very similar to MWF maps presented by Kumar et al. The main difference compared to the regNNLS algorithm can be seen in the frontal white matter. A possible lack of sensitivity in this region was reported by Wiggermann et al. as well, where it was hypothesized that this insensitivity was caused by the increased flip angle inhomogeneities in this region. The estimation of FAI presented by us is slightly different and combined with the improved noise resilience this could result in an improved MWF estimation in these regions.

The work by Kumar et al. also reported MWF values in several regions of interest that are comparable to those found with the SPIJN algorithm. Unfortunately, only a small number of studies reported MWFs for different structures, making a reliable comparison difficult. Possibly the limited number of studies reporting this is because of large natural variation in subjects. When values were reported (see e.g. [41, 110, 117]), this was done as part of the introduction of new acquisition methods or algorithms, using only a small number of subjects in a similar way as was done here.

The regularization parameter in the SPIJN algorithm (λ, see Algorithm 4.1) was experimentally determined, but showed to be robust across different scans from the same scanner, once the same λ was used for processing of all scans after the value was set. Variations in the regularization parameter (from 20 to 60; observe that 30 was used in the results) only had very small effects on the resulting MWF maps (less than 1 %, see Supplementary material Figure S4.1). In the simulations a different regularization parameter was used compared to the in vivo data. This was necessary because the simulations were based on a different number of tissue types and associated T_2 times.
The regularization level mainly determines the number of components and only indirectly the fractions of the different components. This makes the SPIJN method less sensitive to the exact regularization value. Essentially, setting λ smaller will lead to a reduced fit error, but simultaneously to a larger number of components. Consequently, the regularization parameter might for example be automatically selected by requiring that a certain minimal fit error is achieved. However, performing such optimization for every scan will go at the expense of increased computation time.

We propose to use a jointly reweighted NNLS scheme to approximate the multi-component problem from (4.4). Other optimization schemes could be considered e.g. group LASSO [135] as well. However, we experienced that the highly coherent T_2 dictionary atoms strongly affect the convergence properties of some of these methods. This confirms findings by others that FISTA or LASSO based methods are not always suitable choices [36, 136].

Very recently two papers were published on the use of deep learning networks for the calculation of MW fractions based on the regNNLS algorithm [137, 138]. These net-

works are trained based on the regNNLS algorithm and are therefore able to reproduce these maps very well and therefore show the same level of noise sensitivity as the regNNLS algorithm. Both papers applied this in a voxel-by-voxel manner, where the here proposed method aims to improve the model through the addition of the joint sparsity assumption.

The proposed method was here applied on MET_2 relaxometry data. The use of a joint-sparsity constraint could also be beneficial for other T_1, T_2 or T_2^* relaxometry methods, as long as a similar multi-component model is applicable. The here proposed method was only evaluated in simulations and healthy subjects with GRASE acquisitions, focusing on the differences in the normally expected signals and MWF maps. We consider the evaluation of the method in patients a very important topic for future research.

4.5. CONCLUSION

THE SPIJN algorithm facilitates estimation of MW fractions through a joint sparsity promoting fit of multiple T_2 components to T_2 relaxometry data. The method yielded enhanced accuracy in simulations compared to the state-of-art regularized NNLS algorithm. Furthermore, the MWF maps from healthy subjects showed visual improvements over the regNNLS approach. The method was also 50 times faster than the regNNLS algorithm: the average computation time per slice was 8.19 s on a standard desktop PC.

The faster computation of MWF maps combined with improved accuracy can help to increase our insights into (de)myelination and enables reconstruction of MWF maps directly after data acquisition

4.6. SUPPORTING INFORMATION

4.6.1. EXPERIMENT S1

To assess the effect of the regularization parameter on the resulting MWF maps the regularization was varied from 0 (no joint sparsity) to 60 (factor 2) for the dataset as shown in the manuscript. The used regularization value in the manuscript was 30. For λ between 20 and 50 the differences compared to $\lambda = 30$ between the MWF maps are less than 1 % as shown in Figure S4.1.

4.6.2. EXPERIMENT S2

In a small numerical simulation, as shown in Figure S4.2 the error on the MWF caused by small variations in T_2 values was assessed. The numerical phantom of the second experiment was used, but for every voxel the T_2 values of the MW, IEW and FW component were drawn from a Gaussian distribution around the T_2 values as used in the preceding numerical experiment (20 ms, 70 ms, 1 s). The standard deviation of the Gaussian distribution was scaled with respect to the T_2 value. This was repeated 25 times per std, which ranged from 0 to 5 ms.

With increasing range of T_2 values used per water component the number of components as determined by the SPIJN algorithm increases. The error in the estimated MWF first rapidly increases, but soon stabilizes around 1 percent and only increases again for the larger standard deviations when the MW and IEW distribution start to mix.

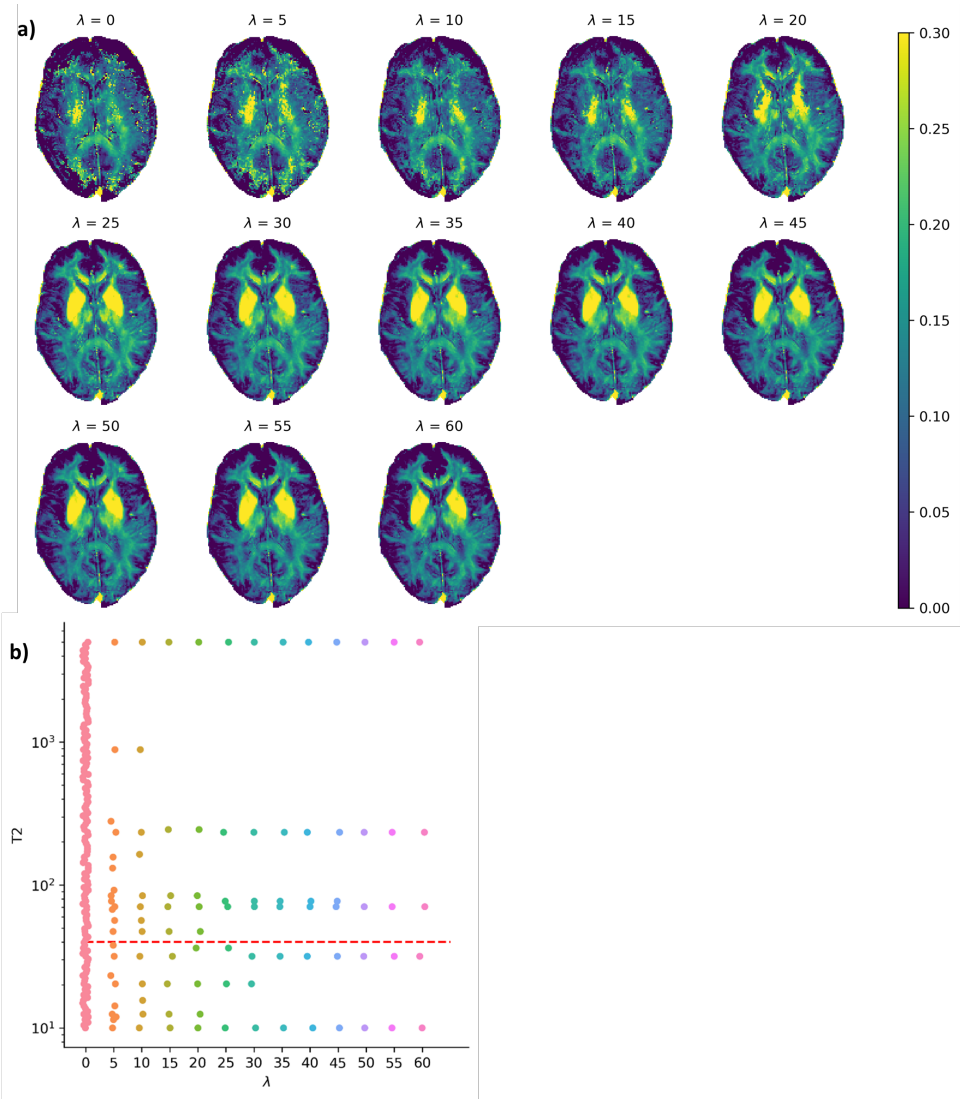

Figure S4.1: **a)** Estimated MWF for varying values of regularization parameter λ for a single slice. $\lambda = 30$ was used in the manuscript. **b)** Estimated T_2 components as function of regularization parameter λ. The plot shows the distribution of the matched components. Increasing λ results in less components, but the main components remain, therefore resulting in only minor changes in the MWF map.

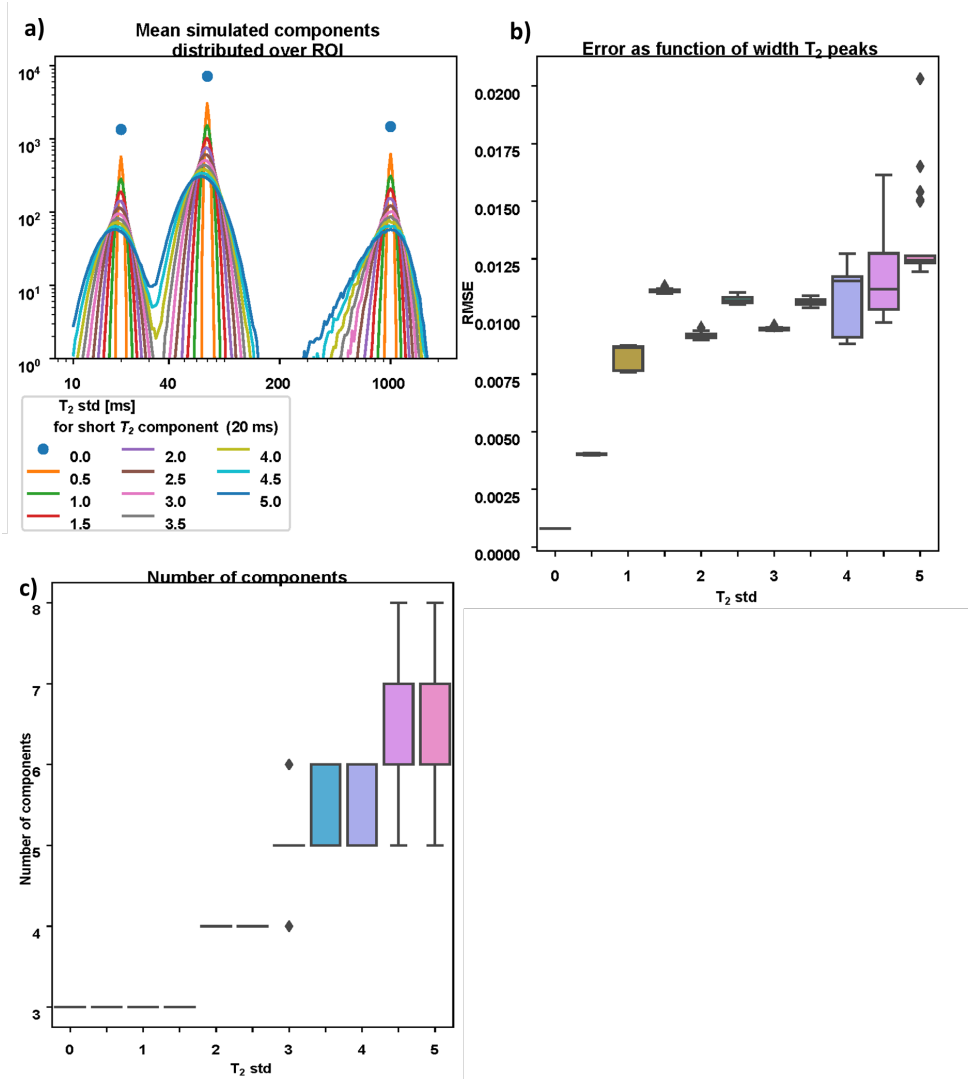

Figure S4.2: **a)** Distributions of T_2 values over the ROI for varying T_2 std values. **b)** The error in the estimated MWF. **c)** The estimated number of components for different std values.

5

MULTI-COMPONENT MR FINGERPRINTING RECONSTRUCTION USING JOINT SPARSITY AND LOW RANK CONSTRAINTS

Martijn A. Nagtegaal & Emiel Hartsema[1]
Kirsten Koolstra
Frans M. Vos

Magnetic Resonance in Medicine 89.1 (2023). ISSN: 1522-2594.
DOI: 10.1002/mrm.29442

[1] Authors contributed equally

ABSTRACT

Purpose: To develop an efficient algorithm for multi-component MR fingerprinting (MC-MRF) reconstructions directly from highly undersampled data without making prior assumptions about tissue relaxation times and expected number of tissues.

Methods: The proposed method reconstructs MC-MRF maps from highly undersampled data by iteratively applying a joint-sparsity constraint to the estimated tissue components. Intermediate component maps are obtained by a low rank multi-component alternating direction method of multipliers (MC-ADMM) including the non-negativity of tissue weights as extra regularization term. Over iterations the used dictionary compression is adjusted. The proposed method (k-SPIJN) is compared to a two-step approach in which image reconstruction and multi-component estimations are performed sequentially and tested in numerical simulations and in vivo applying different undersampling factors in eight healthy volunteers. In the latter case fully sampled data serves as the reference.

Results: The proposed method shows improved precision and accuracy in simulations compared to a state-of-art sequential approach. Obtained in vivo magnetization fraction maps for different tissue types show reduced systematic errors and reduced noise-like effects. Root mean square errors in estimated magnetization fraction maps significantly reduce from 13.0 %± 5.8 % with the conventional, two step approach to 9.6 %± 3.9 % and 9.6 %± 3.2 % with the proposed MC-ADMM and k-SPIJN methods respectively. Mean standard deviation in homogeneous white matter regions reduced significantly from 8.6 % to 2.9 % (two step vs. k-SPIJN).

Conclusion: The proposed MC-ADMM and k-SPIJN reconstruction methods estimate MC-MRF maps from highly undersampled data resulting in improved image quality compared to the existing method.

5.1. INTRODUCTION

MR Fingerprinting (MRF) [9] enables the estimation of tissue and system properties by sampling the MR signal in transient states. Conventionally, undersampled images are acquired from which single-component estimates of specific tissue and system parameters are obtained in each voxel, e.g. T_1, T_2, M_0, B_1^+. These parameters are usually estimated by retrieving the best match of a measured time series with a pre-calculated set of reference signals: the so-called dictionary. However, partial volume effects at tissue boundaries as well as diffuse combinations of tissue structures can lead to mixing of different underlying components. Myelin water imaging (MWI) [21] is a main research application in which estimating these different tissue components is relevant. MWI is used to detect demyelination caused by multiple sclerosis [104] or myelination in the developing human brain [79, 80]. MWI methods such as T_2-sensitive multi-echo spin echo, GRASE or T_2-prep [18, 110, 139], T_2^* multi-echo gradient echo [140], T_1,T_2 mcDESPOT [22] result in scan times of more than 10 minutes when full brain coverage is required [21]. MWI based on highly undersampled MRF data would make it possible to obtain this clinically relevant information in feasible scan times.

To model such multi-component effects the measured MRF signal in a voxel can be represented as a linear combination of the dictionary signals [9]. By definition, however, this multi-component MRF (MC-MRF) problem is underdetermined due to the large number of possible T_1, T_2 values, even with different forms of voxel-by-voxel regularization [25, 36], leading to large numbers of components and non-unique solutions. Recently, we proposed a spatial form of regularization to reduce the number of used tissue components. This Sparsity Promoting Iterative Joint NNLS (SPIJN) algorithm was shown to render improved noise resilience in estimated magnetization fraction maps and a small number of identified tissues [75].

Whereas the conventional single component dictionary matching is relatively robust to the effects of severe undersampling, MC-MRF generally is not. However, advanced reconstruction schemes can be used to enhance the image quality, exploiting either spatial or temporal similarities of the signals or applying other model-based knowledge. Assuming spatial similarity of signals, a multi-scale method was proposed [59] in which MRF time-series images were reconstructed in an iterative fashion while reducing blurring during iterations. Alternatively, temporal similarities were exploited (asserting a certain smoothness of the signal) in sliding window methods in image space [141] as well as in key-hole methods [142] in k-space.

Most of the recently proposed MRF-reconstruction methods rely on low-rank properties in the temporal dimension to regularize the inverse problem. For instance, a low-rank space from a central, fully sampled calibration region has been identified [60]. Other methods determined the low rank SVD space from the simulated signals [43, 61, 127, 143, 144]. While these methods focus on low-rank assumptions in the temporal direction, additional spatial regularization can be included as a locally low-rank constraint [144–147].

To further regularize the problem, Zhao et al. [148] proposed a maximum likelihood framework to estimate parameter maps of interest during the reconstruction. Likewise, Assländer et al. [61] introduced an Alternating Direction Method of Multipliers (ADMM) combining low rank image reconstruction and dictionary matching, which resulted in

improved parameter estimations. However, these methods assumed a single tissue component per voxel, ignoring multi-component effects.

In this study, we propose a new reconstruction method for obtaining multi-component parameter estimates directly from MRF k-space data continuing on the previously proposed SPIJN algorithm to obtain SPIJN-MRF estimates from highly undersampled data. The underlying multi-component inverse problem is solved using a multi-component alternating direction method of multipliers (MC-ADMM). Since the inverse problem is ill-conditioned, intermediate image reconstruction is performed in a low-rank space. During iterations the used low rank compression is updated based on the intermediate results. The proposed method is validated and compared to a more standard approach in simulations and in vivo brain data.

5.2. METHODS

5.2.1. RECONSTRUCTION METHODS

FRAME-BY-FRAME RECONSTRUCTION

The MRF image reconstruction problem per time point (excluding regularization or matching) can be mathematically modeled as

$$\hat{x} = \underset{x \in \mathbb{C}^{N_t \times N_n}}{\arg\min} \left\| G F_{N_t} S_{N_t} x - k \right\|_2^2, \tag{5.1}$$

in which $x \in \mathbb{C}^{N_t \times N_n}$ denotes the MRF (time) series of N_t images consisting of N_n voxels; $k \in \mathbb{C}^{N_t N_k N_s}$ is the acquired k-space data consisting of N_k points per image and N_s represents the number of (virtual) coils. The linear operators G, F and S correspond to the non-Cartesian undersampling (interpolation and gridding), Fourier transform and coil sensitivity encodings, respectively. Essentially, F_{N_t} (F_r) and S_{N_t} (S_r) represent the repetitively applied versions of F and S along the (compressed) time dimension, respectively (see below). However, this problem is highly under-determined and without further forms of regularization this will result in strong artifacts in the reconstructed images.

LOW RANK INVERSION (LRI)

The MRF time signal is often modeled based on a low-rank approximation of the MRF-dictionary obtained through a singular value decomposition (SVD). Let $D \in \mathbb{C}^{N_t \times N_d}$ represent a dictionary consisting of N_d dictionary atoms, such that the SVD yields $D = U\Sigma V^H$. Here, U, V contain the left and right singular vectors, Σ is a diagonal matrix with singular values, while H denotes Hermitian conjugation [43]. Essentially, $U_r \in \mathbb{C}^{N_t \times r}$, harboring the first r column vectors from U, is applied in MRF as a compression operator, such that $D_r := U_r^H D$ and $x_r := U_r^H x$. As proposed by McGivney et al. [43] and Assländer et al. [61] (in the appendix) the compression matrix and Fourier and coil sensitivity operators can be interchanged. After interchanging these operators, the low rank inversion (LRI) problem can be written as

$$\hat{x}_r = \underset{x_r \in \mathbb{C}^{r \times N_n}}{\arg\min} \left\| G U_r F_r S_r x_r - k \right\|_2^2, \tag{5.2}$$

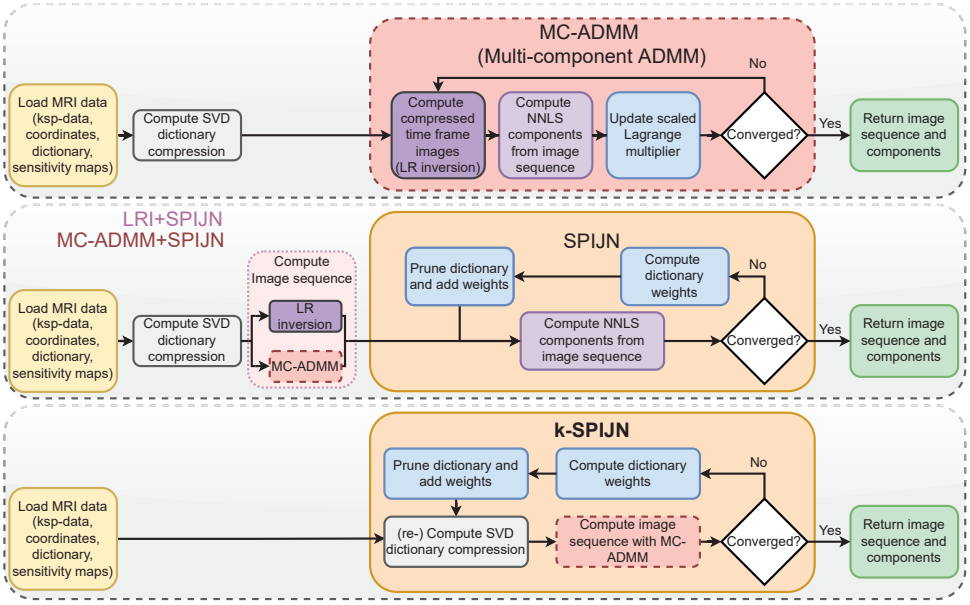

Figure 5.1: Schematic description of the proposed reconstruction schemes. The upper row visualizes the proposed multi-component ADMM, including the non-negativity constraint on the component weights, that is integrated in the performed MRF reconstruction. MC-ADMM reconstruction (red box) is used as part of the second and third reconstruction scheme. The center row shows the combination of the previously proposed SPIJN [75] method applied to LR inversion images (LRI+SPIJN) and MC-ADMM reconstructed images (MC-ADMM+SPIJN). The last flow chart (k-SPIJN) combines the joint-sparsity constraint from SPIJN with the MC-ADMM solver to obtain multi-component magnetization maps.

which can be efficiently solved. Optionally, a wavelet regularization term can be included in this step

$$\hat{x}_r = \underset{x_r \in \mathbb{C}^{r \times Nn}}{\arg\min} \|GU_r F_r S_r x_r - k\|_2^2 + \sum_{i=1}^{r} |\tilde{v}_i| \left\| W(x_{r,i}) \right\|_1, \tag{5.3}$$

where W is a wavelet operator and $\tilde{v}_i$ the used regularization parameter per time-compressed image $x_{r,i}$. The intensity of these time-compressed images decreases sharply with i and the regularization parameter was adjusted accordingly. As such, the image-wise regularization is based on the intensity over time as $\tilde{\mathbf{v}} = v \times U_r^H \mathbf{k}_{\mathbf{0},\mathbf{0}}$, where $\mathbf{k}_{\mathbf{0},\mathbf{0}} \in \mathbb{C}^{N_t}$ are the central positions in k-space of the first virtual coil along time. Effectively, $v \in \mathbb{R}_{\geq 0}$ is used as an overall wavelet regularization parameter.

In effect, (5.3) results in r reconstructed low rank images instead of the original N_t time frame images.

MULTI-COMPONENT ADMM RECONSTRUCTION

We assert that any mixing effects, e.g. emanating from partial voluming, can be modeled as a linearly weighted combination of dictionary items. Given certain low-rank images x_r, the weights of the dictionary items can be obtained by solving a non-negative least

squares problem:

$$\hat{c} = \underset{c \in \mathbb{R}_{\geq 0}^{N_d \times N_n}}{\arg\min} \|P_r(D_r c) - x_r\|_2^2, \tag{5.4}$$

in which $c \in \mathbb{R}_{\geq 0}^{N_d \times N_n}$ are estimated magnetization weights per voxel and dictionary atom, and P_r is applied to represent spatial phase variations. Observe that a single phase is asserted per voxel, independent of the (real-valued) component weights. In our approach $P \in \mathbb{C}^{N_n}$ was directly calculated based on the LR-solution of (5.2), using $r = 1$, as

$$P = \frac{x_1}{\text{abs}(x_1)} \tag{5.5}$$

(in which the division is done element-wise). Subsequently, P is is used to form a linear operator $P_r : \mathbb{R}^{N_r \times N_n} \rightarrow \mathbb{C}^{N_r \times N_n}$. Essentially, P_r sustains a multiplication with P along the temporal dimension.

The full, inverse multi-component reconstruction problem is defined by combining (5.2) and (5.4), leading to:

$$\hat{c} = \underset{c \in \mathbb{R}_{\geq 0}^{N_d \times N_n}}{\arg\min} \|GU_r F_r S_r P_r D_r c - k\|_2^2. \tag{5.6}$$

Since most efficient non negative least squares solvers, e.g. the NNLS algorithm by Lawson and Hanson [35], require full matrix expressions, and non-uniform FFT operations can only efficiently be used as a linear operator, this problem can not be solved directly in an efficient manner.

In order to efficiently solve this non-negative least squares (NNLS) problem, we performed variable splitting similar to Reference [61], in which such splitting was applied for single component MRF. Accordingly, we rewrote the MC-MRF reconstruction as an augmented Lagrangian minimization problem, in which low rank images x_r are reconstructed as intermediate step to split the operators $(GU_r F_r S_r)(P_r D_r)$, and included the wavelet regularization term:

$$\begin{aligned} \hat{x}_r, \hat{c}, \hat{u} = \underset{x_r, u \in \mathbb{C}^{r \times N_n}, c \in \mathbb{R}_{\geq 0}^{N_d \times N_n}}{\arg\min} \Big(& \frac{1}{2} \|GU_r F_r S_r x_r - k\|_2^2 + \\ & \frac{1}{2} \sum_{i=1}^{r} |\tilde{v}_i| \left\| W(x_{r,i}) \right\|_1 + \\ & \frac{\mu}{2} \|P_r D_r c - x_r + u\|_2^2 - \frac{\mu}{2} \|u\|_2^2 \Big), \end{aligned} \tag{5.7}$$

in which u is the scaled Lagrange multiplier and μ is the coupling parameter balancing the data and MC-MRF-model consistency.

Subsequently, an Alternating Directions of Multipliers Method (ADMM) [149] was

used to solve (5.7), alternating between:

$$\hat{x}_r = \underset{x_r \in \mathbb{C}^{r \times N_n}}{\arg\min} \frac{1}{2} \|GU_r F_r S_r x_r - k\|_2^2 + \tag{5.8a}$$

$$\frac{\mu}{2} \|P_r D_r \hat{c} - \hat{x}_r + \hat{u}\|_2^2 + \sum_{i=1}^{r} |v_i| \left\| W(x_{r,i}) \right\|_1,$$

$$\hat{c} = \underset{c \in \mathbb{R}_{\geq 0}^{N_d \times N_n}}{\arg\min} \frac{\mu}{2} \left\| D_r c - P_r^H (\hat{x}_r + \hat{u}) \right\|_2^2, \tag{5.8b}$$

$$\hat{u} = u + \hat{x}_r - P_r D_r \hat{c}, \tag{5.8c}$$

until convergence was reached. Specifically, we solved (5.8a) using a preconditioned Primal Dual Hybrid Gradient solver [150, 151] with a relative convergence tolerance of 0.5 %. Eq. (5.8b) was solved using the NNLS algorithm [35]. Essentially, the here proposed Low-Rank Multi-Component ADMM (MC-ADMM) estimates the MRF image sequence as non-negative linear combination of dictionary atoms and corresponding weights (magnetization maps). The steps of the algorithm are depicted in Figure 5.1, top. Henceforth we will refer to this basic building block as the Low-Rank Multi-Component Alternating Directions of Multipliers Method (MC-ADMM). As opposed to the algorithm discussed in the next paragraph (SPIJN), this method does not constrain the component weights other than by imposing non-negativity.

In the next subsection we will detail the underlying steps of the SPIJN algorithm. Subsequently, we describe how the SPIJN steps can be applied for simultaneous image series reconstruction and multi-component estimation using mere k-space data as input.

JOINT-SPARSITY CONSTRAINT IMPLEMENTATION (SPIJN)

To further restrict the solution space we introduce the joint-sparsity constraint that was previously implemented in the Sparsity Promoting Iterative Joint NNLS (SPIJN) algorithm [75]. The SPIJN algorithm was originally developed for multi-component estimation taking *reconstructed*, presumed artifact-free MRF images as its input.

The joint (component) sparsity constraint limits the number of tissue components, i.e. in a voxel as well as spatially, resulting in a small number of non-zero magnetization fraction maps. The sparsity term was implemented by combining dictionary reweighting [48] and ℓ_1^2-regularization [45] in an iterative process to reduce the number of used dictionary atoms. SPIJN repeatedly solves a modified version of equation (5.4):

$$\hat{c} = \underset{c \in \mathbb{R}_{\geq 0}^{N_c \times N_n}}{\arg\min} \left\| \tilde{D}_r c - P_r^H \tilde{x}_r \right\|_2^2, \tag{5.9}$$

during which $N_c = \sum_{i=1}^{N} \|c_i\|_0$ reduces over iterations while the variables $\tilde{D}_r$ and $\tilde{x}_r$ are

updated according to

$$w_i = \|\mathbf{c}^i\|_2 + \epsilon,\ \forall i \in \{1,...,N_c\}, \tag{5.10a}$$

$$W = \mathrm{diag}\left(\mathbf{w}^{1/2}\right), \tag{5.10b}$$

$$\tilde{D}_r = \begin{bmatrix} D_r W \\ \lambda \mathbf{1}^T \end{bmatrix}, \tag{5.10c}$$

$$\tilde{x}_r = \begin{bmatrix} P_r^H(x_r) \\ \mathbf{0}^T \end{bmatrix}, \tag{5.10d}$$

in which λ and $\epsilon = 10^{-4}$ are the SPIJN and reweighting regularization parameters respectively. Note that in equation 5.10c,d, the tilde symbol is used to to indicate intermediate representations of concerned variables, that are updated during iterations. While doing so, the ℓ_1^2 regularization is imposed by adding a row of λ's to the reweighted dictionary $D_r W$ and zeros to $P_r^H(x_r)$. Not used dictionary atoms will be assigned a zero weight. However, computationally it is more efficient to remove these atoms from the dictionary and further calculations, a processing step we refer to as pruning.

We applied this algorithm to image series reconstructed by LRI and the MC-ADMM, referred to as LRI+SPIJN and MC-ADMM+SPIJN reconstructions, which is graphically depicted in Figure 5.1, center flow-chart. In our previous work, we performed the multi-component estimation only after image reconstruction of fully sampled data or under-sampled data from longer acquisitions, involving markedly longer scan times.

SIMULTANEOUS IMAGE RECONSTRUCTION AND JOINT SPARSITY MULTI-COMPONENT PARAMETER ESTIMATION

Isolating the dictionary reweighting and pruning steps facilitates to integrate them in a new iterative algorithm in which image reconstruction and joint-sparsity multi-component parameter estimation directly uses the k-space data as input. Specifically, the restricted dictionary $D_{\mathscr{S}}$ was used to update the SVD-compression matrix U_r for improved compression efficiency of the remaining dictionary signals. Effectively we are solving the following minimization problem:

$$\hat{c}, \hat{U}_r = \underset{c \in \mathbb{R}_{\geq 0}^{N_d \times N_n}, U_r \in \mathbb{C}^{N_t \times r}}{\arg\min} \|G U_r F_r S_r P_r D_r c - k\|_2^2 + \lambda \sum_{i=1}^{N} \|c_i\|_1, \tag{5.11}$$

where λ is the joint sparsity regularization parameter. As such, the MC-ADMM was employed to obtain multi-component estimates in an inner loop, while dictionary reweighting and compression were performed in the outer loop of our algorithm. This novel approach will be referred to as k-SPIJN and is summarized in Figure 5.1, bottom flow-chart. A step-by-step description of the proposed reconstruction method can be found in the supplementary material, Algorithm 1.

5.2.2. EXPERIMENTAL SETUP

All the methods were programmed in Python using main parts of the SigPy library [152]. Computations were performed on an Intel E5-2683 CPU based on a single core implementation and using a NVIDIA GTX 1080 Ti GPU.

All experiments were performed with a gradient spoiled SSFP MRF acquisition [10] using a flip angle train of length 400 (see Supplementary Figure S5.1) [153] with fixed TR=15 ms. Dictionary signals were simulated with extended phase graphs [53] using a T_1 ranging from 100 ms to 5 s and T_2 from 10 ms to 3 s, applying a logarithmic stepsize of 5 %.

Data was normalized with respect to the ℓ_2-norm of the k-space data. All experiments were performed with an initial rank of $r = 10$. Visible effects of wavelet regularization were kept to a minimum while reducing noise like artifacts using an experimentally determined value of $\nu = 5 \times 10^{-6}$.

NUMERICAL EXPERIMENTS

Numerical experiments were performed with the BrainWeb phantom as ground truth [154] making use of the provided partial volume segmentations of white matter (WM), gray matter (GM) and CSF. Time frame images were computed after which simulated coil sensitivity maps were applied and noise was added (SNR=$\frac{\text{image mean}}{\text{standard deviation}} = 70$). Subsequently, k-space data was generated by performing a Fourier transform which was then undersampled with a constant density spiral at an undersampling factor of 1/32.

Experiments were performed with different ADMM-coupling parameter values μ, while the root mean square error (RMSE) in estimated mean T_1, T_2 and M_0 (as defined below) and signal residual were evaluated during iterations.

IN VIVO EXPERIMENTS

After obtaining informed consent and with approval of the local Ethics board, eight volunteers were scanned on a 3 T Philips Ingenia (Philips, Best, The Netherlands) scanner with a 32 channel head coil, SVD-compressed to 5 virtual coils [155] after ESPIRiT coil estimation [156]. A constant density spiral sampling pattern, FOV of 240 mm × 240 mm, in plane resolution of 1 mm × 1 mm and 5 mm slice thickness were used. A single brain slice was imaged. Data were acquired using spiral sampling of 1/32 of the fully sampled k-space per spiral arm, having a readout duration of 6.5 ms; incremental rotations of 360°/32 were applied with each flip angle. Furthermore, acquisitions were performed with 1, 5 and 32 flip angle train repetitions, resulting in acquisition times of 6 s, 42 s and 4:48 minutes.

Undersampled data was reconstructed with LRI+SPIJN, MC-ADMM+SPIJN and k-SPIJN with SPIJN-regularization $\lambda = 0.05$. Additionally, fully sampled time frame images were reconstructed with a SENSE reconstruction [7] and a SPIJN segmentation was obtained serving as a reference. For all estimations tissue types were identified based on the following relaxation times: myelin water (MW): $T_1 < 800$ ms, $T_2 < 40$ ms; white matter (WM): 800 ms $< T_1 <$ 1200 ms, 40 ms $< T_2 <$ 100 ms; gray matter (GM):1200 ms $< T_1 <$ 1700 ms, 45 ms $< T_2 <$ 100 ms; CSF: $T_1 > 1750$ ms. When multiple components were estimated for one tissue type, magnetization fractions were summed and a weighted average of relaxation times was computed.

To assess structural differences, fully sampled (partial volume) segmentations (A) and segmentations from undersampled data (B) were compared using the Fuzzy Tani-

moto coefficient [93]:

$$\mathrm{TC_F} = \frac{\sum_{i=1}^{N_v} \mathrm{MIN}(A_i, B_i)}{\sum_{i=1}^{N_v} \mathrm{MAX}(A_i, B_i)}, \tag{5.12}$$

in which N_v is the number of non-zero voxels. Additionally the Root Mean Square Error measure was calculated:

$$\mathrm{RMSE} = \sqrt{\frac{\sum_{i=1}^{N_v} (A_i - B_i)^2}{N_v}} \tag{5.13}$$

across the brain per tissue type. To quantify the image quality of segmentations, the standard deviation (std) in a homogeneous frontal white matter region (size 10×20 voxels) was also calculated for MW, GM and WM. A Wilcoxon signed rank test was performed to statistically assess the differences between error measures, while a p-value < 0.05 was considered significant.

5

5.3. RESULTS

5.3.1. NUMERICAL EXPERIMENTS

Results of numerical simulations showing the effect of the ADMM-coupling parameter μ are depicted in Supplementary Figure S5.2. A high μ reduces the convergence speed. Simultaneously, the individual RMSE in mean T_1 and T_2 increases for too small or large coupling parameters and do not exhibit a monotonic relation. Based on these finding we chose to use $\mu = 2 \cdot 10^{-3}$ in further experiments.

In Figure 5.2 relative error maps are shown comparing the segmentations obtained from LRI+SPIJN, MC-ADMM+SPIJN and k-SPIJN reconstructions. Only small effects are observable in CSF segmentations (RMSE ranging from 1.7-2.7 %), but larger differences are noticeable for WM and GM (RMSE up to 29.9 %). Additionally, LRI+SPIJN yields highly deviating relaxation times, while the proposed methods result in smaller errors of the relaxation times.

5.3.2. IN VIVO EXPERIMENTS

The computation time for the LRI+SPIJN was 4:34 minutes (maximum memory usage: 5GB), for MC-ADMM+SPIJN 45:49 minutes (11GB) and for k-SPIJN 1:42:51 hours (16GB).

Figure 5.3 shows estimated multi-component estimations for one subject. Figure 5.4 shows similar difference maps for a second subject. From these maps it can be observed that differences between Fully sampled and undersampled scans are reduced with k-SPIJN and MC-ADMM+SPIJN. However, small structural biases can still be observed.

A further quantitative comparison between reconstruction methods is collated in Figure 5.5, showing the $\mathrm{TC_F}$ and RMSE across the component images, the standard deviation in a homogeneous, frontal WM region with different undersampling factors and estimated T_1 and T_2 relaxation times for the different methods and undersampling factors.

The proposed MC-ADMM+SPIJN and k-SPIJN method accurately estimated fraction maps from 1/32 undersampled data: mean RMSE of 9.6 %±3.9 % and 9.6 %±3.2 %. This is a significant improvement compared to the conventional LRI+SPIJN approach: mean

RMSE 13.0 %±5.8 %. For an undersampling of 5/32 the respective mean RMSE were 9.9 %±5.4 %, 7.3 %±2.5 % and 7.8 %±2.4 % for LRI+SPIJN, MC-ADMM+SPIJN and k-SPIJN, again showing a significant difference between LRI+SPIJN and the two proposed methods. An overview of performed tests and results is given in Table S2 in the supplementary material.

Differences between k-SPIJN and MC-ADMM were mostly not significant with respect to the FT_C and RMSE, but significant differences were observed with respect to the standard deviation in white matter regions, both for 1/32 and 5/32 undersampling.

Estimated relaxation times for MC-ADMM+SPIJN and k-SPIJN were highly similar irrespective of the used undersampling factor and in line with reference values [55]. For LRI+SPIJN extra components between WM-GM and GM-CSF relaxation times were identified, resulting in 12 components on average, in which cases MC-ADMM and k-SPIJN estimated 9 and 8 components on average. The largest spread in estimated relaxation times was observed for CSF, which did not seem to effect the estimated magnetization fraction maps.

5.4. DISCUSSION

We proposed two new reconstruction methods for MRF data, tailored to the estimation of multi-component magnetization maps. The proposed MC-ADMM and k-SPIJN methods were assessed in simulations and in vivo data. As reference we used numerical ground truth data in the simulations and conventional multi-component estimations after traditional image reconstruction with the fully sampled in vivo data.

We found in the numerical simulations that the MC-ADMM-SPIJN and k-SPIJN facilitated accurate magnetization fraction estimation for a short (200 readouts) MRF sequence, while the state-of-art LRI+SPIJN yielded markedly poorer outcomes (see Figure 5.2). In in vivo experiments this shorter sequence of length 200 was not used (sequence length 400 was used), as the improved image quality in all reconstruction was preferred over the reduced scan time.

The proposed methods yielded MW, WM, GM and CSF maps from in vivo data for single spiral readouts (1/32) that closely resembled the reference. The LRI+SPIJN method showed larger deviations in this respect. Furthermore, we observed that the main improvement from MC-ADMM+SPIJN to k-SPIJN is a reduction in noise-like patterns (See Figure 5.3 and Figure 5.5; std. estimates). This came at the cost of increased computation times for both the MC-ADMM+SPIJN and k-SPIJN method compared to the LRI+SPIJN reconstruction. These increased computation times are mainly caused by the many NNLS optimizations that are performed. Notably, these optimizations were not performed in parallel in the current implementation. Obviously, doing so could drastically reduce the calculation times [157, 158].

The main novelty in the MC-ADMM reconstruction essentially lies in imposing a voxel-wise temporal constraint, while reconstructing LR-images from the k-space data in an iterative process. This constrains the reconstructed LR-images to a non-negative combination of dictionary atoms, which is more restrictive than standard LR-reconstruction [144, 147], in which only the dimension of the solution space is reduced. At the same time such a constraint still allows for multi-component estimations, with or without a joint-sparsity constraint [25, 36, 159], which is not possible with methods that

benefit from a dictionary matching based constraint [59, 61, 148, 160], assuming a single tissue per voxel. By regularizing the total number of T_1, T_2-components used, the proposed k-SPIJN reconstruction adds a spatial constraint leading to a further improvement in image quality.

A wavelet regularization term with a relatively small regularization value was used in all the reconstructions to suppress small spiral artifacts in the low rank images. The low rank image reconstruction (eq. (5.3)) can be easily expanded to 3D-acquisitions or to include other regularization terms [144, 146] and spiral blurring correction methods [161–163].

Some limitations of the performed work can be identified. A limitation of the SPIJN and k-SPIJN algorithms is that potentially important components could be discarded in early iterations. This risk is limited by not rejecting too many components and only refute those ones that have very small weight. Incidentally, we have not observed in any of our experiments that key components (e.g. reflecting WM/GM or myelin water) were discarded at an early stage.

In the performed experiments no corrections for B_1^+ inhomogeneities were included since B_1^+ was rather homogeneous. However, in the multi-component estimation a (separately acquired) B_1^+-map could be included to fixate B_1^+ per voxel. Modeling B_1^+ in the dictionary may require applying a higher rank in the compression.

Although relaxation times and visual appearance of identified myelin water like components are in agreement with literature [21], comprehensive validation with conventional MWI methods is a subject of further study and is required to study potential biases, caused by e.g. the proposed algorithm, magnetization transfer effects or MRF sequence choice. Observe that such a study is increasingly feasible due to the achieved reduction in scan time and reconstruction quality. Further research should therefore also look in the sensitivity of different flip angle patterns to multi-component effects and how this can improve myelin water imaging, for example by using multiple inversion pulses [164] or model-based sequence optimization [26, 165].

5.5. CONCLUSION

NEW MC-ADMM+SPIJN and k-SPIJN algorithms facilitate accurate estimation of magnetization fraction maps from highly undersampled MRF k-space data. The generated in vivo maps show close resemblance to fully sampled reference data, while scan times of less than 10 s per slice can be achieved.

DATA AVAILABILITY STATEMENT

The full implementation of the proposed MC-ADMM and k-SPIJN methods can be found at `https://github.com/imphys/MC-MRF_reconstruction` [166].

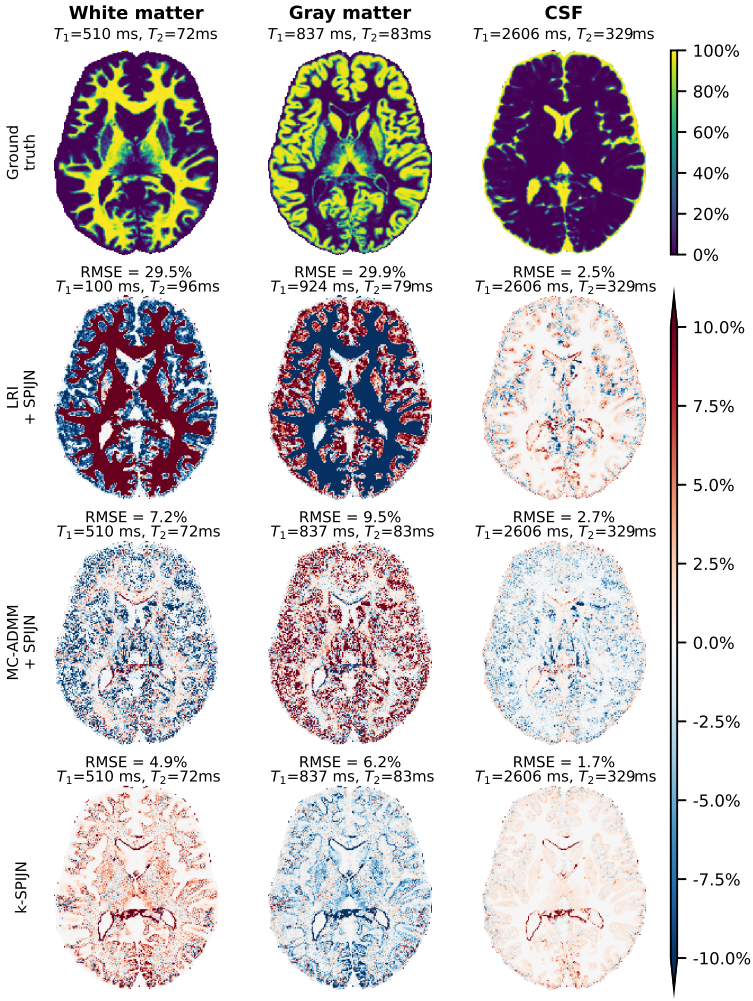

Figure 5.2: Error maps for obtained multi-component tissue segmentations using different reconstruction methods (bottom 3 rows). A numerical BrainWeb phantom was used as ground truth (upper row) for which an MRF sequence of length 200 was generated. Root mean square error (RMSE) is reported over the whole brain. Ground truth (top row) and estimated relaxation times are reported above each map.

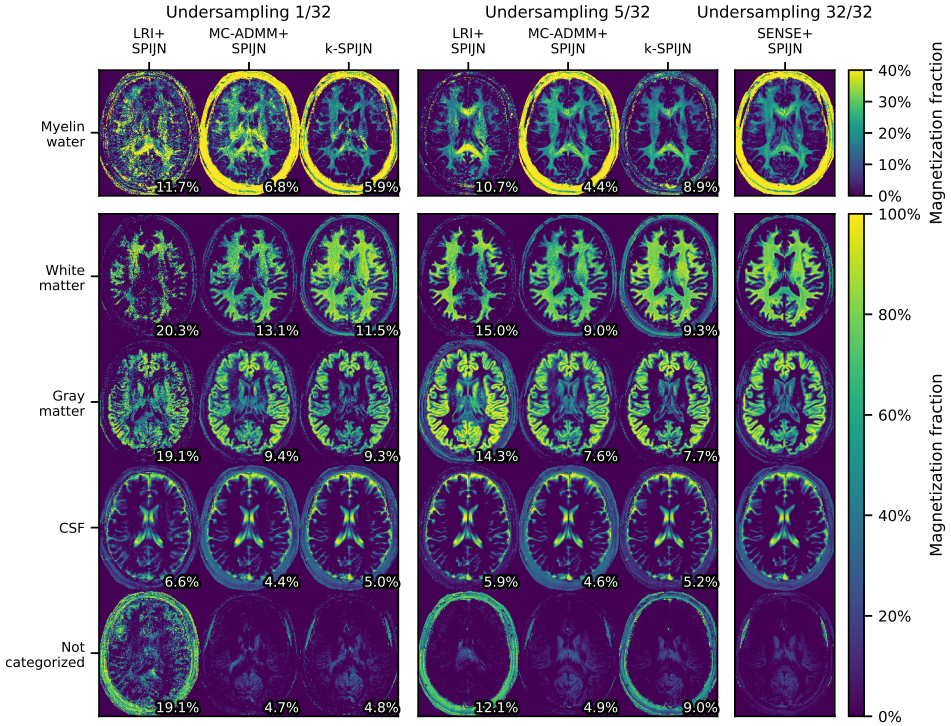

Figure 5.3: Estimated magnetization fraction maps from single slice data of one volunteer acquired with different undersampling factors applying different reconstruction methods. Estimated SPIJN-MRF maps with undersampling factors 1/32 and 5/32 are shown for the LRI+SPIJN, the proposed MC-ADMM+SPIJN and k-SPIJN reconstructions. Fully sampled MRF data with SENSE reconstruction and SPIJN-MRF estimation shown on the right serve as a reference. On the lower right side of each image the RMSE compared to the fully sampled data is given.

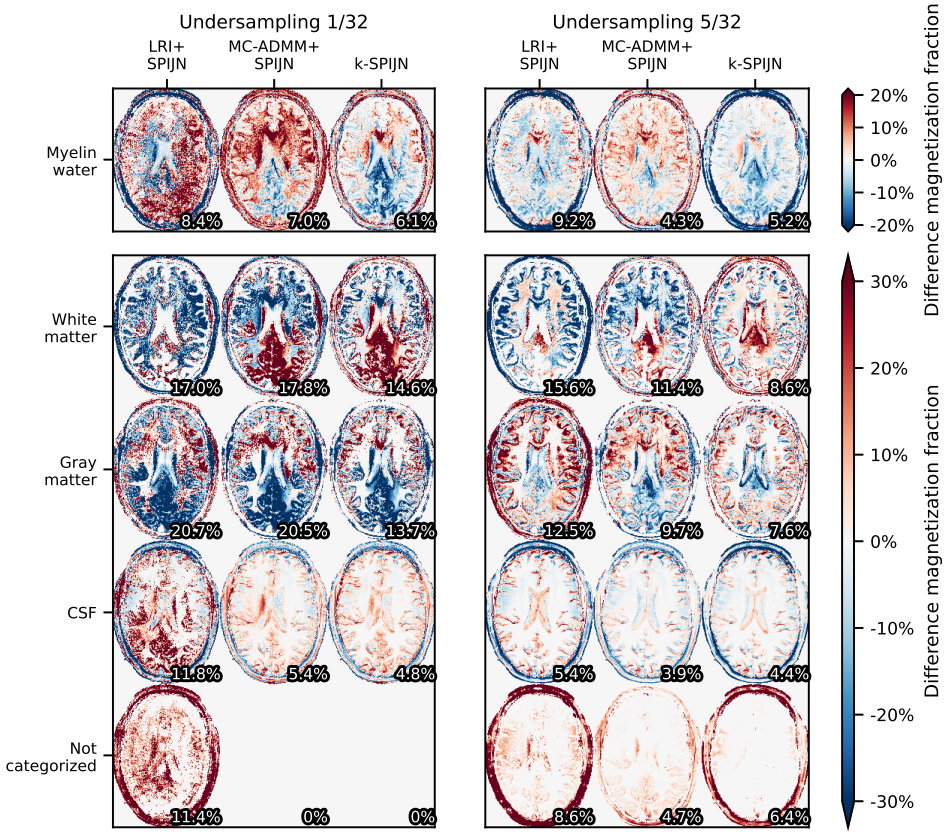

Figure 5.4: Differences in estimated magnetization fraction maps from single slice data of a second volunteer acquired with different undersampling factors applying different reconstruction methods. Difference maps for estimated SPIJN-MRF maps with undersampling factors 1/32 and 5/32 are shown for the LRI+SPIJN, the proposed MC-ADMM+SPIJN and k-SPIJN reconstructions. On the lower right of each image the RMSE compared to the fully sampled data is indicated.

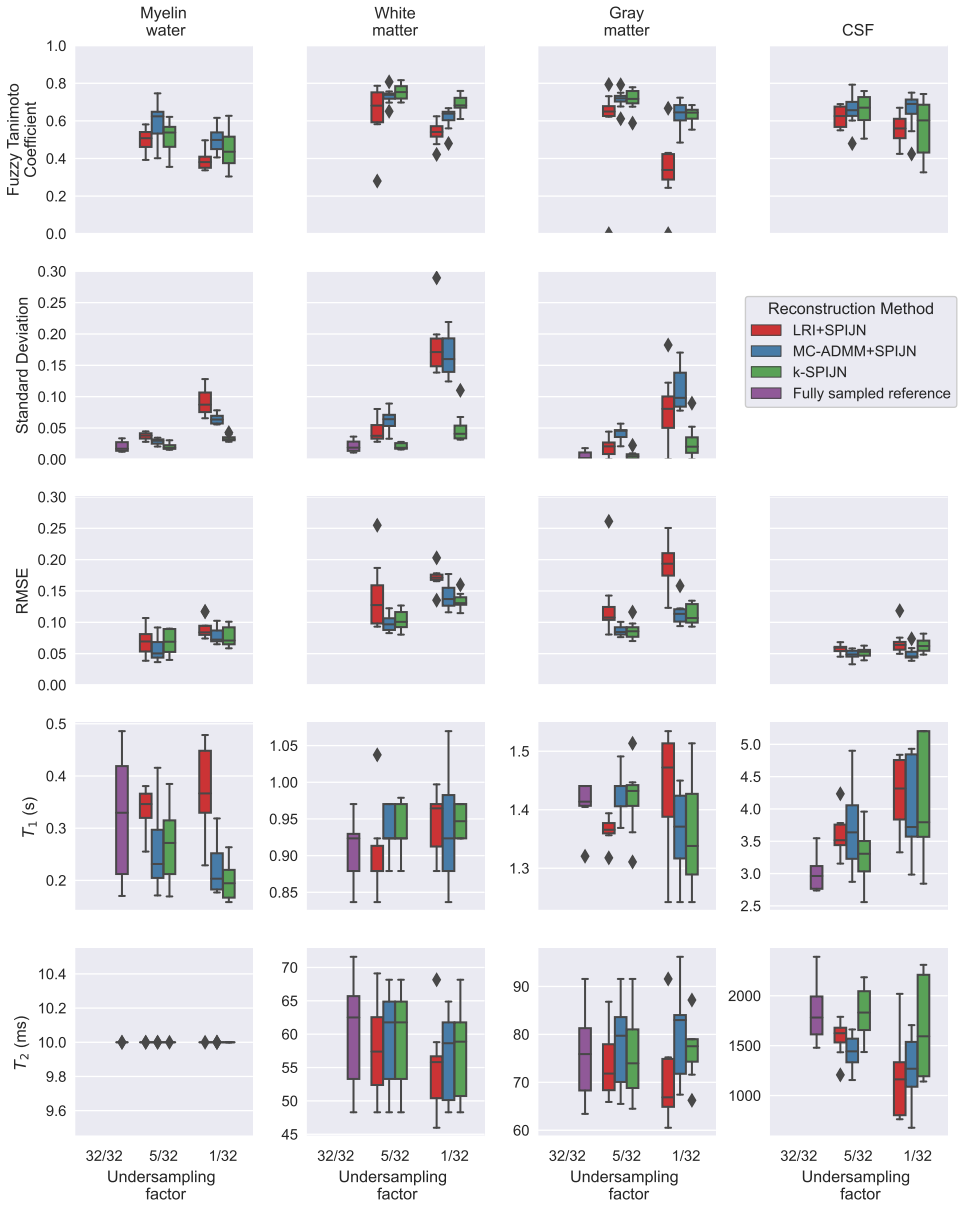

Figure 5.5: Comparison of different reconstructions based on undersampled data of 8 in vivo scans. The Fuzzy Tanimoto coefficient and Root Mean Square Error (RMSE) were calculated over the complete components with respect to the fully sampled (32/32) SENSE+SPIJN reconstruction. The standard deviation of the magnetization fraction was calculated in a frontal white matter region for all acquisitions, including the fully sampled data. As no CSF was identified in the frontal WM region, the graph showing the standard deviation of this component is left out. The distribution of estimated T_1 and T_2 relaxation times per tissue are shown in the lower two rows. Mean values and standard deviations can be found in Table S1 of the Supplementary material.

5.6. SUPPORTING INFORMATION

		Error measure	FTC		RMSE		Std		T_1 (s)		T_2 (ms)	
			mean	std	mean	std	mean	std	mean	std	mean	std
Tissue	Undersampling	Method										
CSF	1	LRI+SPIJN	0.555	0.083	0.069	0.022	0.016	0.011	4.209	0.621	1181.572	426.330
		MC-ADMM+SPIJN	0.650	0.110	0.050	0.011	0.004	0.002	4.017	0.764	1249.072	361.483
		k-SPIJN	0.565	0.154	0.063	0.012	0.003	0.003	4.130	0.942	1678.750	506.142
	5	LRI+SPIJN	0.623	0.061	0.058	0.007	0.000	0.000	3.600	0.325	1578.757	183.476
		MC-ADMM+SPIJN	0.658	0.096	0.048	0.008	0.001	0.001	3.737	0.698	1437.366	168.653
		k-SPIJN	0.660	0.087	0.052	0.007	0.000	0.000	3.291	0.482	1836.606	260.654
	32	Fully sampled reference					0.001	0.003	3.017	0.301	1834.004	297.569
Gray matter	1	LRI+SPIJN	0.343	0.189	0.191	0.037	0.081	0.055	1.436	0.105	71.212	10.446
		MC-ADMM+SPIJN	0.630	0.079	0.115	0.020	0.111	0.035	1.365	0.072	80.371	9.546
		k-SPIJN	0.633	0.046	0.112	0.017	0.029	0.029	1.355	0.098	76.657	6.105
	5	LRI+SPIJN	0.592	0.246	0.128	0.056	0.020	0.014	1.364	0.024	73.875	8.014
		MC-ADMM+SPIJN	0.714	0.053	0.086	0.009	0.041	0.013	1.426	0.040	78.030	9.169
		k-SPIJN	0.713	0.062	0.088	0.015	0.006	0.007	1.420	0.061	75.700	9.917
	32	Fully sampled reference					0.006	0.007	1.410	0.039	75.871	9.423
Myelin water	1	LRI+SPIJN	0.392	0.058	0.090	0.017	0.092	0.024	0.376	0.086	10.000	0.000
		MC-ADMM+SPIJN	0.497	0.071	0.078	0.013	0.064	0.008	0.223	0.053	10.000	0.000
		k-SPIJN	0.447	0.106	0.077	0.017	0.034	0.005	0.198	0.038	10.000	0.000
	5	LRI+SPIJN	0.498	0.061	0.069	0.023	0.037	0.006	0.335	0.044	10.000	0.000
		MC-ADMM+SPIJN	0.591	0.112	0.058	0.021	0.028	0.005	0.261	0.086	10.000	0.000
		k-SPIJN	0.510	0.100	0.069	0.020	0.020	0.005	0.269	0.074	10.000	0.000
	32	Fully sampled reference					0.021	0.009	0.322	0.116	10.000	0.000
White matter	1	LRI+SPIJN	0.537	0.065	0.171	0.019	0.182	0.049	0.943	0.045	54.866	7.075
		MC-ADMM+SPIJN	0.613	0.063	0.142	0.024	0.166	0.034	0.938	0.078	56.628	6.729
		k-SPIJN	0.690	0.045	0.134	0.014	0.051	0.027	0.947	0.025	57.399	7.039
	5	LRI+SPIJN	0.639	0.163	0.142	0.056	0.046	0.020	0.903	0.060	57.812	7.191
		MC-ADMM+SPIJN	0.732	0.045	0.099	0.014	0.061	0.019	0.935	0.033	59.542	7.029
		k-SPIJN	0.755	0.045	0.103	0.016	0.021	0.005	0.937	0.034	59.542	7.029
	32	Fully sampled reference					0.021	0.010	0.910	0.043	60.565	8.132

Table S5.1: Descriptive statistic from the box plots as shown in Figure 5.5

.

Algorithm 5.1 The proposed MC-MRF reconstruction algorithm k-SPIJN with joint-sparsity and low rank constraints

INPUT:
- $k \in \mathbb{C}^{N_t N_k N_s}$ - k-space data
- D - a real valued, normalized dictionary (size $M \times N$)
- λ - SPIJN regularization parameter
- μ - ADMM coupling parameter
- T - maximum number of iterations (default 20)
- ν - Wavelet regularization parameter
- $\delta, \tilde{\delta}$ - convergence and pruning threshold (def 10^{-4}, 10^{-10})
- ϵ - parameter for the reweighting (default 10^{-4})
- r_0 - Compression rank

OUTPUT:
- $\hat{c}^k$ - non-negative, jointly sparse multi-component maps.
- $\hat{x}_r^k$ - compressed time-frame images
- $\bar{U}_r^k$ - - compression matrix

$k \leftarrow 0$, ▷ Counter for the number of iterations

Calculate SVD-compression matrix $\bar{U}_r^0$ from D, calculate wavelet regularization parameters ν

$\hat{x}_{r_0}^0, \hat{u}, \hat{c}^0 \leftarrow \underset{x_{r_0}, u; c \in \mathbb{R}_{\geq 0}^{N_d \times N_n}}{\arg\min} + \frac{1}{2} \left\| G U_{r_0} F_{r_0} S_{r_0} x_{r_0} - k \right\|_2^2 + \frac{1}{2} \sum_{i=1}^{r} |\tilde{v}_i| \left\| V(x_{r,i}) \right\|_1 + \frac{\mu}{2} \left\| P_{r_0} D_{r_0} c - x_{r_0} + u \right\|_2^2 - \frac{\mu}{2} \|u\|_2^2$ ▷ Initial solution

$\bar{\lambda} \leftarrow \lambda \cdot \log_{10} N_n$ ▷ Scale the regularization parameter with the number of voxels

while $k < T$ and $\frac{\|c^{k+1} - c^k\|_F}{\|c^k\|_F} > \delta$ **do**

  $\mathcal{S} \leftarrow \{i : \|c_i^k\|_1 > N_n \cdot \tilde{\delta}\}$ ▷ Active set of dictionary atoms

  $r \leftarrow \min(r_0, |\mathcal{S}|)$ ▷ Compression rank can not be larger than number of atoms

  Calculate SVD-compression matrix $\bar{U}_r^k$ from $D_{\mathcal{S}}$

  $D_{\mathcal{S},r} \leftarrow \bar{U}_r^{kH} D$ ▷ Compressed, pruned dictionary

  $w^{k+1,i} \leftarrow \|\mathbf{c}_k^i\|_2 + \epsilon, \ \forall i \in \mathcal{S}$ ▷ Calculation of the weights

  $W_{k+1} \leftarrow \operatorname{diag}\left(\mathbf{w}_{k+1}^{1/2}\right)$

  $\tilde{D}^{k+1} \leftarrow \begin{bmatrix} D_{\mathcal{S},r} W_{k+1} \\ \bar{\lambda} \mathbf{1}^T \end{bmatrix}$ ▷ Weighting and ℓ_1^2 regularization, $\mathbf{1}$ is a vector of all ones with length $|\mathcal{S}|$

  $\hat{x}_r^k, \hat{u}, \tilde{c}_{\mathcal{S}}^k \leftarrow \underset{x_r, u \in \mathbb{C}^{r \times |\mathcal{S}|}; c \in \mathbb{R}_{\geq 0}^{N_d \times N_n}}{\arg\min} \frac{1}{2} \left\| G \bar{U}_r^k F_r S_r x_r - k \right\|_2^2 + \frac{1}{2} \sum_{i=1}^{r} |\tilde{v}_i| \left\| V(x_{r,i}) \right\|_1 + \frac{\mu}{2} \left\| P_r \tilde{D}^{k+1} c - \begin{bmatrix} x_r + u \\ \mathbf{0}^T \end{bmatrix} \right\|_2^2 - \frac{\mu}{2} \|u\|_2^2$ ▷ Solve step using ADMM Eq. 8

  $\hat{c}_{\mathcal{S}}^{k+1} \leftarrow W_{k+1} \tilde{c}_{\mathcal{S}}^{k+1}$ ▷ Compensate for the weighting

  $k \leftarrow k + 1$

end while

A	B	mean(A)	std(A)	mean(B)	std(B)	W-val	p-unc	hedges	Und.	Measure
LRI+SPIJN	MC-ADMM+SPIJN	0.457	0.141	0.598	0.099	1.000	0.0%	-1.141	1	FTC
LRI+SPIJN	k-SPIJN	0.457	0.141	0.584	0.131	75.000	0.0%	-0.919	1	FTC
MC-ADMM+SPIJN	k-SPIJN	0.598	0.099	0.584	0.131	243.000	70.1%	0.119	1	FTC
LRI+SPIJN	MC-ADMM+SPIJN	0.093	0.071	0.086	0.065	189.000	16.4%	0.098	1	Std
LRI+SPIJN	k-SPIJN	0.093	0.071	0.029	0.026	20.000	0.0%	1.186	1	Std
MC-ADMM+SPIJN	k-SPIJN	0.086	0.065	0.029	0.026	18.000	0.0%	1.140	1	Std
LRI+SPIJN	MC-ADMM+SPIJN	0.130	0.058	0.096	0.040	35.000	0.0%	0.677	1	RMSE
LRI+SPIJN	k-SPIJN	0.130	0.058	0.097	0.032	69.000	0.0%	0.716	1	RMSE
MC-ADMM+SPIJN	k-SPIJN	0.096	0.040	0.097	0.032	256.000	88.8%	-0.001	1	RMSE
LRI+SPIJN	MC-ADMM+SPIJN	1.751	1.551	1.644	1.527	133.000	4.2%	0.069	1	T_1
LRI+SPIJN	k-SPIJN	1.751	1.551	1.669	1.601	148.500	8.6%	0.051	1	T_1
MC-ADMM+SPIJN	k-SPIJN	1.644	1.527	1.669	1.601	190.000	55.9%	-0.016	1	T_1
LRI+SPIJN	MC-ADMM+SPIJN	337.741	546.701	357.173	563.063	115.500	7.9%	-0.035	1	T_2
LRI+SPIJN	k-SPIJN	337.741	546.701	467.871	766.409	76.000	0.7%	-0.193	1	T_2
MC-ADMM+SPIJN	k-SPIJN	357.173	563.063	467.871	766.409	104.000	11.9%	-0.163	1	T_2
LRI+SPIJN	MC-ADMM+SPIJN	0.588	0.156	0.673	0.095	94.000	0.2%	-0.652	5	FTC
LRI+SPIJN	k-SPIJN	0.588	0.156	0.660	0.119	125.000	1.0%	-0.509	5	FTC
MC-ADMM+SPIJN	k-SPIJN	0.673	0.095	0.660	0.119	187.000	15.3%	0.127	5	FTC
LRI+SPIJN	MC-ADMM+SPIJN	0.026	0.022	0.033	0.025	135.000	2.7%	-0.299	5	Std
LRI+SPIJN	k-SPIJN	0.026	0.022	0.012	0.010	13.000	0.0%	0.809	5	Std
MC-ADMM+SPIJN	k-SPIJN	0.033	0.025	0.012	0.010	4.000	0.0%	1.091	5	Std
LRI+SPIJN	MC-ADMM+SPIJN	0.099	0.054	0.073	0.025	32.000	0.0%	0.617	5	RMSE
LRI+SPIJN	k-SPIJN	0.099	0.054	0.078	0.024	122.000	0.8%	0.507	5	RMSE
MC-ADMM+SPIJN	k-SPIJN	0.073	0.025	0.078	0.024	133.000	1.5%	-0.190	5	RMSE
LRI+SPIJN	MC-ADMM+SPIJN	1.557	1.288	1.595	1.392	218.000	56.3%	-0.028	5	T_1
LRI+SPIJN	k-SPIJN	1.557	1.288	1.481	1.184	183.000	31.4%	0.061	5	T_1
MC-ADMM+SPIJN	k-SPIJN	1.595	1.392	1.481	1.184	158.000	31.1%	0.087	5	T_1
LRI+SPIJN	MC-ADMM+SPIJN	441.602	687.908	406.339	623.985	156.500	63.8%	0.053	5	T_2
LRI+SPIJN	k-SPIJN	441.602	687.908	508.491	806.489	114.000	31.0%	-0.088	5	T_2
MC-ADMM+SPIJN	k-SPIJN	406.339	623.985	508.491	806.489	85.000	46.6%	-0.140	5	T_2

Table S5.2: Results as obtained from Wilcoxon signed rank tests to compare the different methods for different undersampling factors and error measures. Gray rows show significant results. FTC: Fuzzy Tanimoto Coefficient.

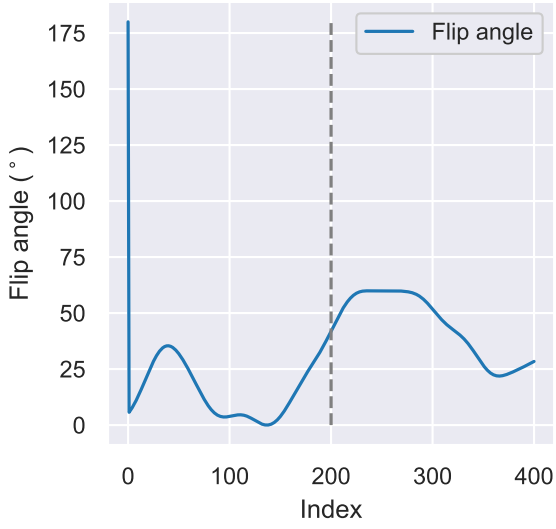

Figure S5.1: The used flip angle pattern [153] of length 400. For the simulations a shortened version of length 200 (dashed line) was used.

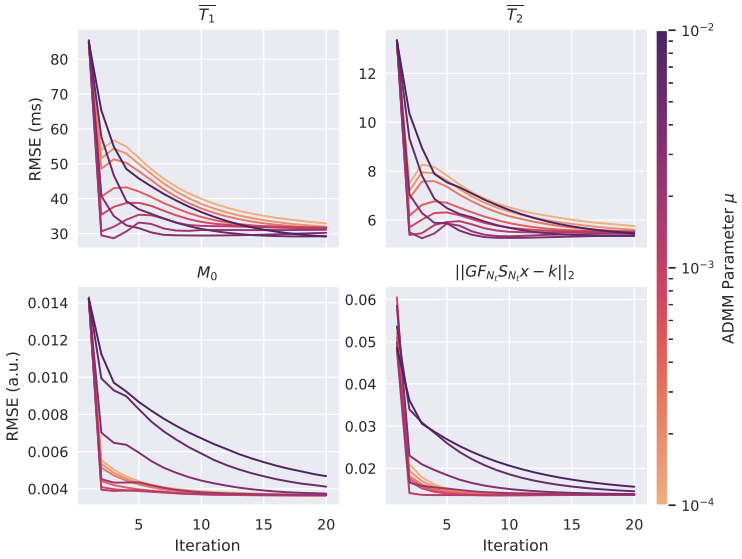

Figure S5.2: RMSE in T_1, T_2, M_0 and the residual of the fit as a function of iteration number for different values of the ADMM coupling parameter μ. The numerical BrainWeb phantom was used as ground truth. Errors were evaluated over the complete image. Geometric mean T_1 and T_2 were derived from the obtained component maps. $||GF_{N_t}S_{N_t}x-k||_2$ denotes the difference between reconstructed image series and k-space signal.

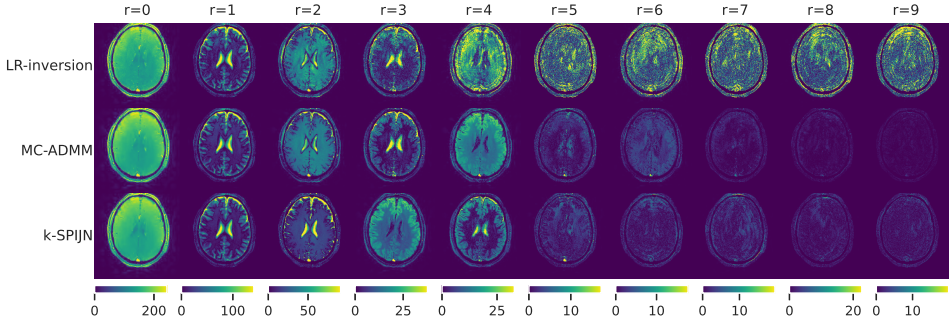

Figure S5.3: Estimated low rank images with different reconstruction methods from 1/32 undersampled data. Note that k-SPIJN uses a different set of basis signals leading to visual differences with the other 2 methods.

6

White matter changes measured by multi-component MR Fingerprinting in multiple sclerosis

Martijn. A. Nagtegaal
Ingo Hermann
Sebastian Weingärtner
Elio Martinez-Heras
Elisabet Solana
Sara Llufriu
Achim Gass
Dirk H.J. Poot
Matthias J.P. van Osch
Frans M. Vos
Jeroen de Bresser

In preparation for submission to NeuroImage

ABSTRACT

T_2-hyperintense lesions are the key imaging marker of multiple sclerosis (MS). Previous studies have shown that the white matter surrounding such lesions is often also affected by MS. Our aim was to develop a new method to visualize and quantify the extent of white matter tissue changes in MS based on relaxometry properties.

We applied a fast, multi-parametric quantitative MRI approach and used a multi-component MR Fingerprinting (MC-MRF) analysis. We assessed the differences in the MRF component representing prolonged T_2^* relaxation time between patients with MS and controls and studied the relation between this components volume and structural white matter damage identified on FLAIR MRI scans in patients with MS.

A total of 48 MS patients and 12 healthy controls were scanned with FLAIR and EPI-MRF MRI scans. MRF scans were analyzed with a joint-sparsity multi-component analysis to obtain magnetization fraction maps of different T_1, T_2^* components, representing tissues such as myelin water, white matter, gray matter and cerebrospinal fluid. In the MS patients, an additional component was identified with increased transverse relaxation times compared to the white matter, likely representing changes in free water content. Patients with MS had a higher volume of the long-T_2^* component in the white matter of the brain compared to healthy controls (B (95 %-CI) = 0.004 (0.0006-0.008), p=0.02). Furthermore, this MRF component had a moderate correlation (correlation coefficient R 0.47) with visible structural white matter changes on the FLAIR scans. Also, the component was found to be more extended in 73 % of MS patients than visible on the FLAIR scans.

Our MRF acquisition and analysis identified more white matter tissue changes in MS patients compared to controls. These tissue changes were more extensive compared to visually detectable white matter damage on FLAIR scans. This may indicate that the disease burden of MS is underestimated using only conventional clinical MRI scans.

6.1. INTRODUCTION

MULTIPLE Sclerosis (MS) is a demyelinating disease of the central nervous system. A key imaging marker of MS are T_2-hyperintense lesions, that appear mainly in the brain's white matter and are particularly visible in T_2-weighted and T_2-Fluid-attenuated inversion recovery (FLAIR) MR images [167, 168]. So-called 'dirty appearing white matter' (DAWM) is another structural abnormality of MS that can often be distinguished in the white matter surrounding the T_2-hyperintense lesions. DAWM is defined as areas of white matter that are mildly hyperintense on T_2 compared to the (surrounding) normal appearing white matter [169, 170]. However, these structural brain abnormalities by themselves are not able to fully capture the extent of white matter damage caused by MS [171, 172].

The white matter that does not show structural brain abnormalities (i.e. T_2-hyperintense lesions and/or DAWM) is traditionally regarded as normal appearing white matter. Within visually normal appearing white matter previous studies showed decreases in magnetization transfer, $R_1 (= 1/T_1)$ and $R_2^* (= 1/T_2^*)$ in MS patients compared to healthy controls, indicating that there are more subtle changes in the white matter in MS than visible on structural MRI scans [173]. Diffusion based metrics were also demonstrated to be sensitive to changes in the normal appearing white matter [174, 175]. Previous studies in MS patients have shown an increased mean diffusivity, decreased fractional anisotropy and reduced restricted signal fraction in normal appearing white matter compared to controls [176]. Sodium MRI suggested increasing axonal damage in both focal MS lesions and in normal-appearing brain tissue[177]. Limitations of these previously used methods to study changes in the normal appearing white matter in MS is that the exact extent and severity of the white matter burden is difficult to capture quantitatively and visually at the same time.

Previous studies also used advanced quantitative relaxometry MRI methods to assess the underlying microstructural changes that are present in T_2-hyperintense lesions and DAWM. Such studies found that parameters including the $T_1, T_2, T_{1\rho}$ decay constants and water content, all reflected changes within T_2-hyperintense lesions and DAWM compared to the normal appearing white matter [170]. However, these approaches require thresholds to differentiate between normal and abnormal tissue and are mostly hampered by lengthy acquisition times. MR Fingerprinting (MRF) when used with a multi-component model facilitates fast, multi-parametric, quantitative measurements sensitive to micro-structural changes to overcome these challenges [12].

In standard MRF methods the signal from every voxel in the image is matched to a signal dictionary calculated from specific combinations of relaxation times and possibly other parameters. However, such a single component model implies a drastic simplification of the complex structure of biological tissue as it does not take multi-component effects and partial voluming into account[178]. Alternatively, the measured MRF signal can be modeled as a linear combination of simulated signals, allowing for Multi component (MC)-MRF estimation, in which several components each with its individual characteristic relaxation times and magnetization fractions represent the signal in each voxel [24, 25, 36]. To aid solving this inverse problem, a joint sparsity regularization using the SPIJN algorithm was proposed, limiting the number of components (tissues) found across the brain [75]. For example, in healthy individuals MC-MRF has led to the iden-

tification of myelin water components that have relatively short relaxation times [164, 179, 180].

We hypothesized that novel quantitative MC-MRF methods are able to visualize and quantify the extent of white matter damage caused by MS, not only in visible T_2-hyperintense lesions, but also in the normal appearing white matter. Therefore, to investigate this hypothesis we performed MC-MRF to visualize and quantify the extent of white matter tissue changes in MS. We evaluated our MC-MRF approach by assessing differences between patients with MS and controls and studied the relationship between MRF features and structural white matter damage visible on FLAIR MRI images of patients with MS.

6.2. METHODS

THE image processing steps described in this section are visualized in the flow diagram in Figure 6.1.

6.2.1. DATASET

Data was acquired at 2 sites, on 3 T scanners (Magnetom Skyra and Magnetom Prisma respectively, Siemens Healthineers, Erlangen, Germany). At the first site (Medical Faculty Mannheim) 12 healthy volunteers and 18 patients with MS were scanned and at the second site (Hospital clinical Barcelona) 32 patients with MS were scanned. Previously these data were used to analyze relaxation times in T_2-hyperintense lesions as obtained from single component MRF approach [183]. This bicenter study was approved by the local institutional review board at both sites (2019-711N, HCB2012/7965), and written, informed consent was obtained from all participants prior to scanning.

An MRF-EPI sequence [11, 184] was applied with in-plane spatial resolution of 1 mm × 1 mm, slice thickness of 2 mm, bandwidth 998 Hz/px, GRAPPA factor 3, partial Fourier 5/8, fat suppression, variable flip angle (34° – 86°), TE (21-81.5 ms), TR (3530-6570 ms) and approximately 3 global inversion pulses per minute, resulting in varying inversion times during the acquisition. At site 2 simultaneous multislice imaging was used with an acceleration factor of 3. The acquisition time for site 1 was 4 minutes and 23 seconds and 1 minute and 52 seconds at site 2, at both sites covering 60 slices. T_2-FLAIR and T_2-weighted images were acquired using the same spatial resolution.

6.2.2. MRF RECONSTRUCTION AND IMAGE PROCESSING

MRF PROCESSING

Dictionaries were generated per slice using MATLAB (The MathWorks; Natick, MA, USA) consisting of 131,580 entries with T_1 (30-4000 ms) in 5 % steps, T_2 (5-3000 ms) in 5 % steps, and flip angle efficiency B_1^+ (0.65-1.35) in steps of 0.05.

Magnitude data of the MRF acquisition was denoised using Marchenko-Pastur Principle Component Analysis (MP-PCA) denoising [181]. Denoising was performed per slice and across time-frames in square patches of 7 voxels radius. Regular, single-component matching was performed on the denoised data to obtain M_0, T_1, T_2^* and effective B_1^+ maps.

Subsequently, a joint sparsity, multi-component analysis was performed using the

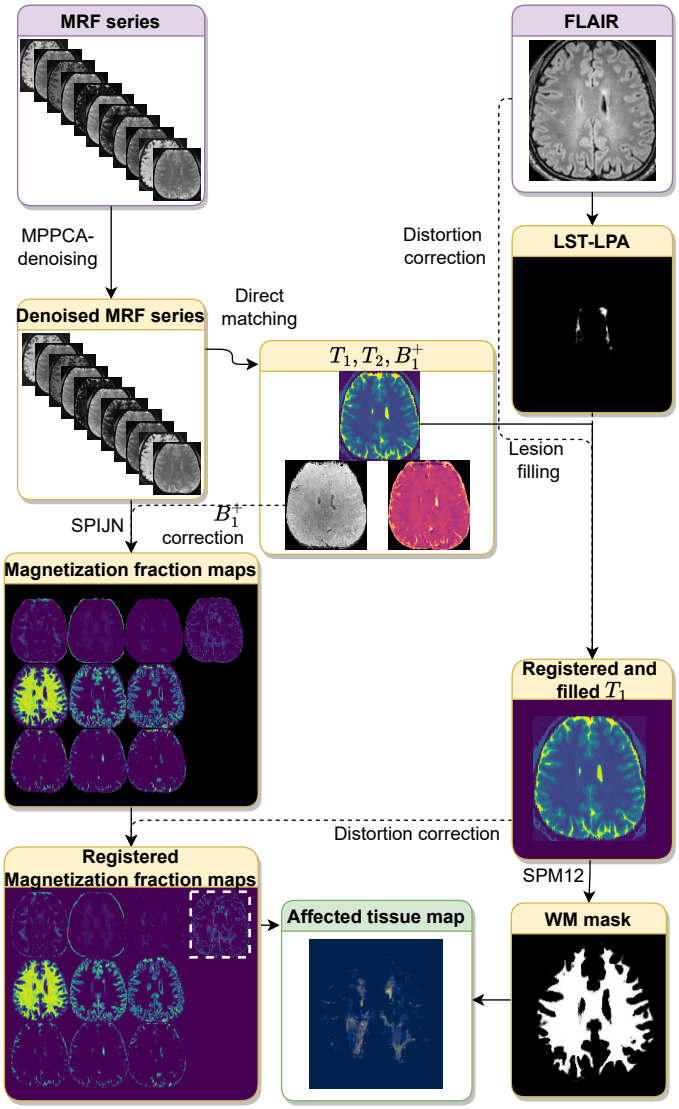

Figure 6.1: Flow diagram visualizing the proposed image processing steps. Marchenko-Pastur Principle Component Analysis (MP-PCA) denoising [181] was used to denoise the MRF images. Lesion Segmentation Toolbox version 2.0.15 [182] from which the Lesion Prediction Algorithm (LST-LPA) was used to obtain a lesion probability map for lesion filling. SPM12 [88, 89] was used to obtain white matter (WM) masks. The Sparsity promoting iterative joint NNLS (SPIJN) algorithm [75] was used to obtain Multi-component MRF magnetization fraction maps.

Sparsity Promoting Iterative Joint Non-negative least square (SPIJN) algorithm [75], in which the previously estimated B_1^+ map was used as fixed parameter. A normalized regularization $\lambda = 11$ (see [75]) was used for the MC-MRF analysis. In a pre-processing step

the M_0 map was thresholded (relative M_0>5 %) and the largest connected region was identified to be analyzed, namely the region containing the brain. This threshold (and also the ones used later) as well as regularization parameters were chosen based on 5 randomly selected datasets across sites.

The MRF-magnitude data was rigidly registered to the T_2-weighted data followed by a restricted, nonlinear registration along the phase-encode direction of the magnitude data to the T_2-weighted data using ANTs [185, 186]. This was done to correct for susceptibility artifacts.

CONVENTIONAL SEGMENTATION

T_2-hyperintense lesion segmentations were obtained using the lesion prediction algorithm from the Lesion Segmentation Toolbox version 2.0.15 (LPA-LST) [182]. Masks were obtained by applying a threshold of 0.5. Lesion filling was performed on the T_1 maps using the lesion segmentation toolbox. White matter, gray matter and cerebrospinal fluid segmentations were obtained from the lesion-filled T_1 maps using Statistical Parametric Mapping version 12 (SPM12) [88, 89].

Distortion corrected T_1 maps were registered to the MNI152 template and corresponding atlas (ICBM 2009a Nonlinear Symmetric 1 mm × 1 mm × 1 mm template) [90, 91, 187] to obtain segmentations of the frontal, occipital, parietal and temporal lobes.

MRF POSTPROCESSING

Obtained relaxation times and magnetization fractions maps from MC-MRF from the randomly selected set of five subjects were visually inspected first. The obtained magnetization fraction maps were compared to structural FLAIR images and relaxation times were compared to literature values for related tissues [55, 188]. A priori, myelin water, gray matter, white matter and cerebrospinal fluid components were expected and potentially components related to lesions. When multiple clusters were identified close to each other, k-means clustering of the log-scaled values was performed and mean and standard deviation of the relaxation times per cluster were obtained.

As further described in Section 6.3.2, visual inspection revealed components with prolonged T_2^* relaxation times compared to white matter and gray matter. Therefore, these components were further analyzed and for subjects in whom multiple component with longer T_2^* were identified, all MC-MRF components with relaxation times of 500 ms< T_1 < 2500 ms and 500 ms < T_2^* < 2500 ms were combined into a single magnetization fraction map.

Our aim was to study white matter changes in MS, therefore further analysis focused on these long-T_2^* MRF-component maps in the white matter. Non-white matter regions in the long-T_2^* MRF-component maps were masked based on the SPM12 white matter segmentation. Volumes of the long-T_2^* MRF-component maps were calculated for the different white matter regions, per hemisphere and for the complete white matter. Volumes were normalized between 0 and 1 with respect to the total white matter volume of the considered region. Magnetization fractions more than 15 % were considered as severe damage and therefore potentially lesion related voxels.

6.2.3. DIFFERENCES IN MC-MRF BETWEEN PATIENTS WITH MS AND CONTROLS

STATISTICAL ANALYSIS

All statistical tests were performed using the Statsmodels and Pingouin packages (0.5.2) [189] in Python 3.8. p-values less than 0.05 were considered statistically significant.

Least squares linear regression analyses corrected for age and sex were performed to assess the difference in estimated normalized long-T_2^* MRF-component volumes between patients with MS and controls. These analyses were performed for the total white matter volume, as well as for the white matter volume per brain lobe (frontal, occipital, parietal and temporal lobes, both left and right). Subsequently, the difference between patients with MS and controls in the volumes was assessed excluding the T_2-hyperintense lesions. For these analyses, the obtained LPA-LST lesion probability maps (thresholded at 50 %) were used to mask T_2-hyperintense lesions from the long-T_2^* MRF-component map and normalized volumes were calculated for the different white matter regions.

6.2.4. RELATION BETWEEN MC-MRF AND STRUCTURAL WHITE MATTER CHANGES ON FLAIR MRI IN PATIENTS WITH MS

VISUAL SCORING

The T_2-weighted and T_2-FLAIR scans white matter regions were evaluated by an expert neuroradiologist (JB) on a 0-5 scale reflecting the amount of structural white matter changes; this expert assessed the combined DAWM and T_2-hyperintense lesions and DAWM by itself. DAWM was defined as an uniform area of subtle signal intensity increase on T_2-FLAIR compared to the signal intensity of the normal appearing white matter [190]. The following visual volume scores were applied:

0. No structural changes
1. 0 % to 10 % abnormal white matter of total WM
2. 10 % to 25 % abnormal white matter of total WM
3. 25 % to 50 % abnormal white matter of total WM
4. 50 % to 75 % abnormal white matter of total WM
5. 75 % or more abnormal white matter of total WM

This scoring was performed per white matter region (frontal, parietal, occipital and temporal), and per hemisphere, resulting in a maximum score of 40 points. This non-linear score was used to increase sensitivity to small areas of affected tissue. Scores were summed to provide scores for the left and right hemisphere and the complete brain.

VISUAL SIMILARITY SCORING

A second similarity scoring was performed comparing the long-T_2^* MRF-component maps to the extent of structural white matter changes on the FLAIR images (i.e. T_2-hyperintense lesions and DAWM). The following scores were applied:

0. Less extensive involvement
1. Similar involvement

Table 6.1: Demographic and clinical characteristics of the scanned MS patients summarized as age, disease and the Expanded Disability Status Scale (EDSS).

	MS Patients		Healthy controls	
	Mean	Range	Mean	Range
Age (years)	41.4	23-73	27	22-43
Disease duration (years)	9.2	0.2-33	n.a.	n.a.
EDSS	2.2	0-6	n.a.	n.a.

2. More extensive involvement

For each white matter region a score was obtained for all structural white matter changes and another score for only T_2-hyperintense lesions.

STATISTICAL ANALYSIS

A Spearman pairwise correlation test was performed to test for correlations between estimated normalized volumes and the visual volume scoring within the patient group. Tests were performed for the whole white matter and also per white matter region for each hemisphere. From the tests correlation coefficients, p-values and 95 % confidence intervals were obtained.

6.3. RESULTS

6.3.1. DATASET

At the first site 12 healthy volunteers (9 male, 3 female, mean 26 years (range 22-30 years)) and 18 patients (7 male, 11 female, 39 years (23-73 years)) with MS were scanned. At the second site 30 patients (10 male, 42 years (26-62 years)) with MS were scanned. In Table 6.1 characteristics of the scanned subjects are summarized.

6.3.2. MC-MRF ANALYSIS

Examples of the obtained FLAIR images and estimated relaxation times and magnetization fraction maps from the MC-MRF are shown in Figure 6.2 for a single MS patient. In Figure 6.2 it can be observed that components 1 to 3 contain short relaxation times ($T_1 < 500$ ms) and mainly present white matter and deep gray matter regions. Such components seem related to myelin water. Component 4 is the main signal component in white matter regions. This component was estimated in all participants, as shown in Figure 6.3; the means (and standard deviations) of the relaxivities were $T_1 = 970 \pm 79$ ms and $T_2^* = 54 \pm 4.2$ ms. Components 5 (having reduced T_2^* value) and 6 as shown in Figure 6.2 relate to cortical gray matter and deep gray matter regions. Over all participants component 5 had $T_2^* \leq 46$ ms; on average $T_1 = 1197 \pm 81$ ms and $T_2^* = 35 \pm 3.3$ ms. The other gray matter component (6) showed more variation in estimated relaxation times: $T_1 = 1494 \pm 182$ ms and $T_2^* = 57 \pm 5.2$ ms. Component 7 as shown in Figure 6.2 corresponds to increased signal of the T_2-hyperintense lesions as well as in other white matter areas on the FLAIR scan and is the component of our interest with long T_2^*. Components 8 to 11 all have the maximum T_1 relaxation time of around 4000 ms and correspond to cerebrospinal fluid regions. In most cases (89 %) 3 components were identified with

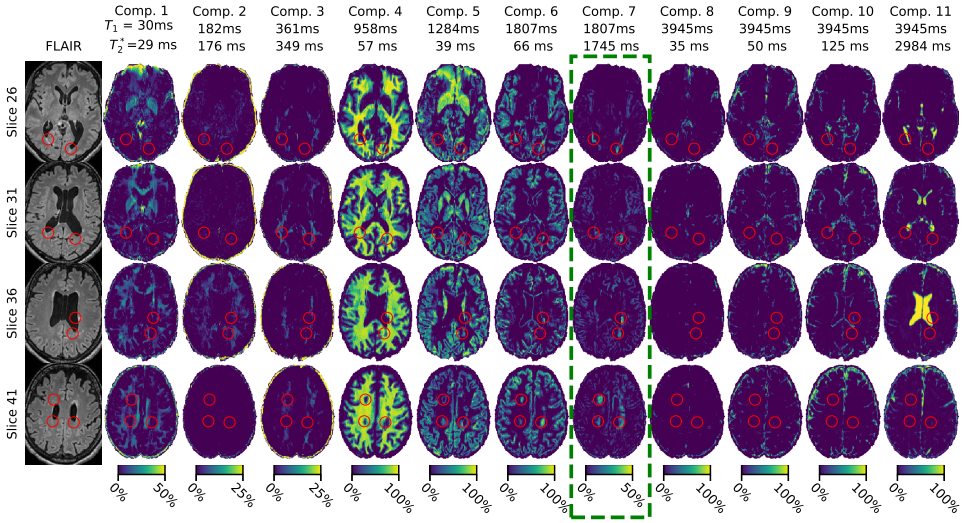

Figure 6.2: FLAIR images and obtained MC-MRF component maps a for a selection of slices of a representative MS patient. Estimated relaxation times are shown above each column. Note that color ranges differ per component for visualization purposes. Components are ordered by T_1 relaxation time. Shown images are registered to correct for susceptibility distortion. The green box indicates the component of interest. The red circles indicate white matter damage as visible in component 7. Component 2 shows a sharp increase in signal in slice 36 compared to the other slices. This is most likely caused by the different timing of RF-pulses per slice used in the EPI-MRF sequence.

$T_2^* = 46.7 \pm 4.9$ ms, 82.9 ± 11.5 ms and 2984 ± 0 ms of which the last component always had the maximum T_2^* value in our dictionary, in Figure 6.3 these components were referred to as CSF A,B and C respectively.

One or two components with 500 ms < T_1 <2500 ms, 500 ms< T_2^* < 2500 ms were observed in all participants with varying total volume and relaxation times (mean T_1 = 1489 ± 667 ms and mean $T_2^* = 1456 \pm 652$ ms). The individual T_1 and T_2^* times were very close to each other as can also be observed in Figure 6.3a. In the healthy subjects this component was limited in the WM, whereas in patients this component corresponded to structural white matter changes as readily visible in Figure 6.2.

Figure 6.4 and Figure 6.5 show detailed examples of the long-T_2^* MRF component next to the obtained FLAIR image and LST-LPA map. Figure 6.4 shows a case in which the magnetization fraction maps show large similarity to lesions and DAWM in the FLAIR images, while Figure 6.5 shows a representative case of overestimation, c.f. the performed similarity scoring.

6.3.3. DIFFERENCES IN MC-MRF BETWEEN PATIENTS WITH MS AND CONTROLS

Figure 6.6a collates the estimated relative volumes of the MRF component for the patients with MS and controls. In Table 6.2 the mean and standard deviations and the results of the performed generalized linear regression analyses are shown. Patients with

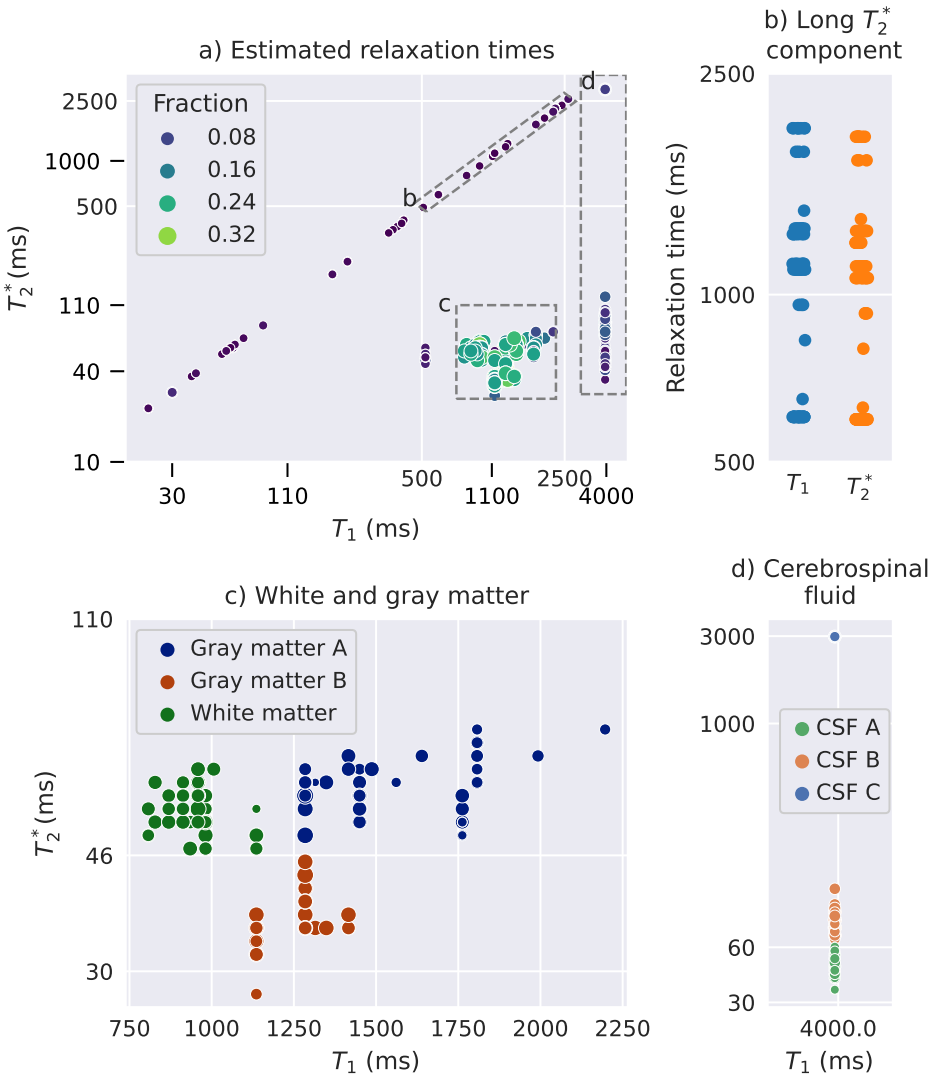

Figure 6.3: Estimated relaxation times from the MC-MRF analysis of all subjects. The size and color of the dots reflect the fraction of the component of the total volume a) Overview of all matched relaxation times; b) distribution of the components with long T_2^* relaxation times, selected as 500 ms < T_1 < 2500 ms and 500 ms< T_2^* < 2500 ms; c) close up and clustering outcome for gray and white matter components and d) close up of cerebrospinal fluid related components.

MS had a significantly higher volume of the long T_2^* component compared to controls (b=0.0044, 95 % confidence interval [0.00066 0.0081] (p=0.02)). A similar difference was observed comparing the two hemispheres separately. We also found a higher volume of the long T_2^* component in MS patients compared to controls in all individual white mat-

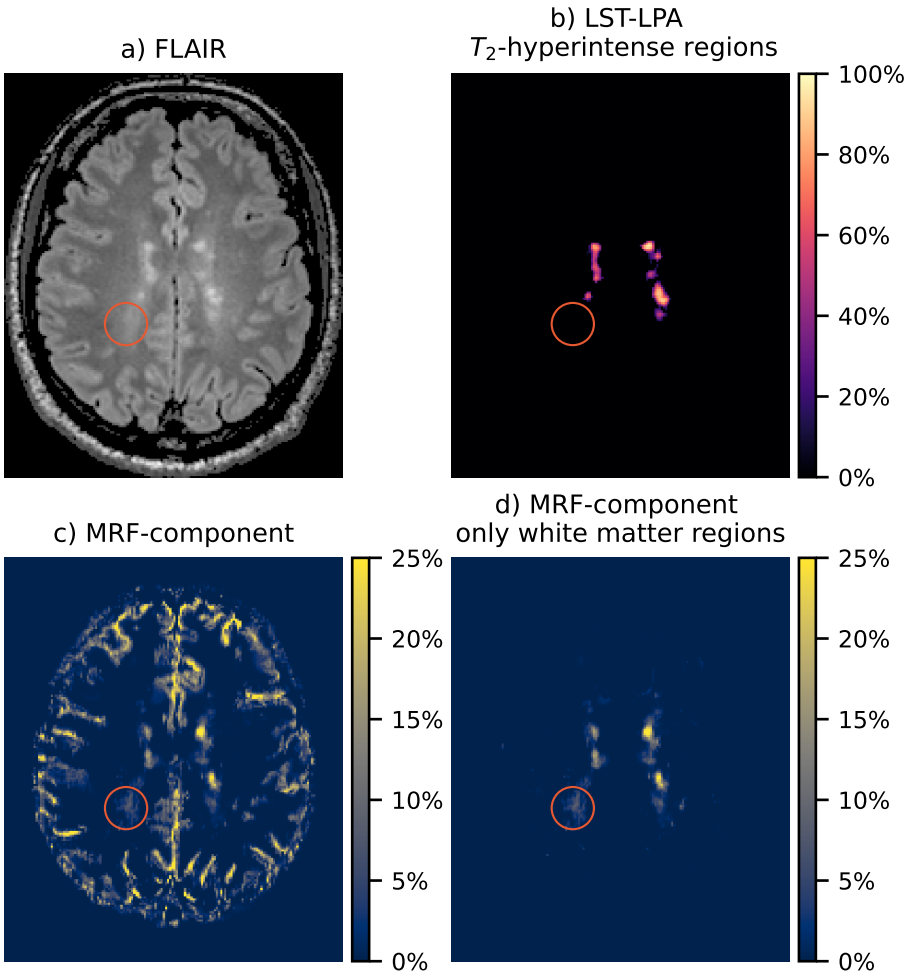

Figure 6.4: Results from a single slice of an MS patient. A region with DAWM is indicated by the red circle. a) FLAIR scan, b) estimated lesion probability map from the FLAIR scan, c) MRF component with long T_2^* before masking and d) after masking non-white matter regions.

ter regions. The largest difference (b=0.0052 [0.0019 0.0085], p=0.002) was found in the frontal lobe and the smallest difference in the temporal lobe (b=0.0039 [0.0018 0.006], p<0.001).

Additionally, Figure 6.6b and Table 6.3 show that this difference between the MS patients and healthy controls was also found when T_2-hyperintense lesions were masked and only more subtle white matter changes were considered (b=0.003, [0.00068 0.0053], p=0.012).

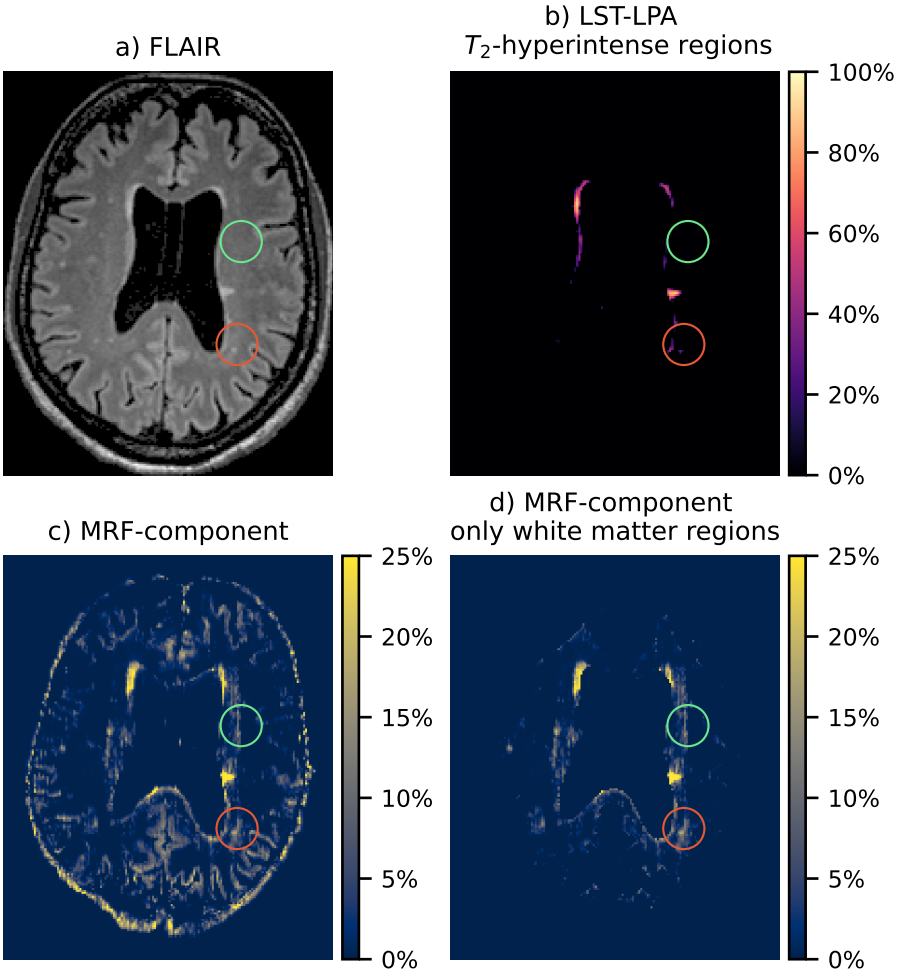

Figure 6.5: Results from a single slice of another MS patient. A region with T_2-hyperintense regions on the FLAIR scan is indicated with a red circle; a region reflecting white matter tissue changes visible only on the MRF map is indicated with a green circle. a) FLAIR scan, b) estimated lesion probability map from the FLAIR scan, c) MRF component with long T_2^* before masking and d) after masking non-white matter regions

6.3.4. RELATIONSHIP BETWEEN MC-MRF AND STRUCTURAL WHITE MATTER CHANGES ON FLAIR MRI SCANS IN PATIENTS WITH MS

Table 6.4 shows the results of the Spearman correlation of the expert neuroradiologist score for amount of white matter changes and volume of the long-T_2^* MRF component. Figure 6.7 show scatter plots of the performed scoring with linear regression estimates for the different regions. For the total white matter volume (applying summed scores) the Spearman correlation coefficent was 0.47 (95 % confidence interval: [0.22 0.66], p<0.001). All other tested correlations were significant as well (p<0.001).The cor-

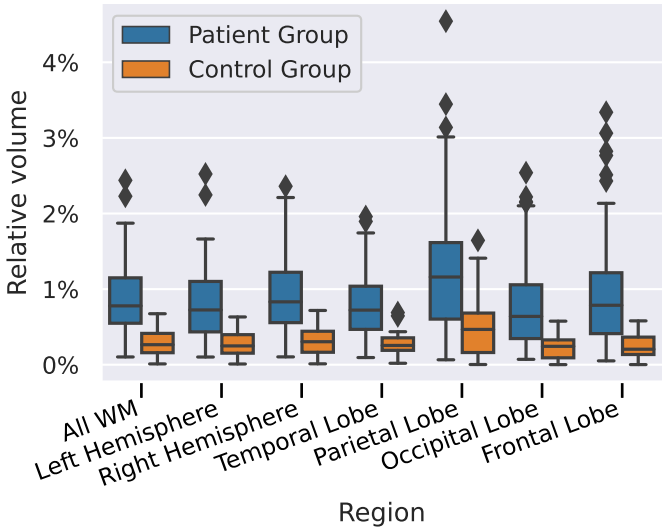

(a) Including T_2-hyperintense lesions.

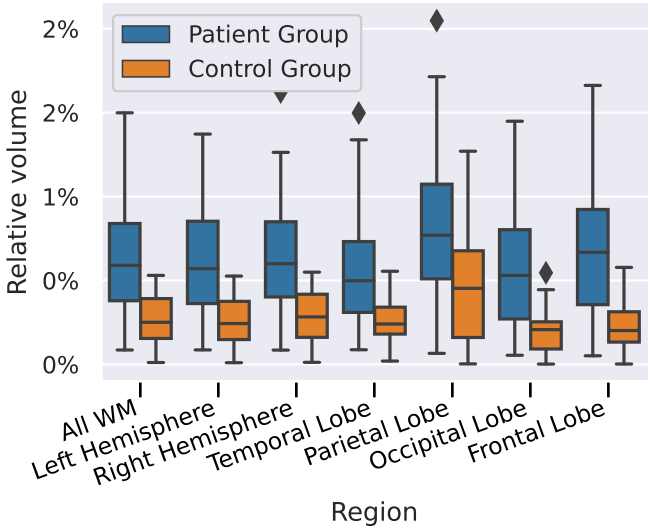

(b) After masking T_2-hyperintense lesions.

Figure 6.6: Boxplot showing the estimated relative volumes of the long-T_2^* MRF component in MS patients (blue) and controls (orange). The boxes show the quartiles of the data, the whiskers extend to the rest of the distribution, except for outliers marked with diamonds.

relation was highest in the frontal lobe and lowest in the temporal lobe. Similar correlations and p-values were obtained when the two sites was used as a co-variable in the

Table 6.2: Generalized linear regression analyses were applied to test for differences in relative volume of the long-T_2^* component between the MS patients and controls. Tests were performed for different brain regions and corrected for age and sex. A positive coefficient indicates a larger volume in the patient group. CI: confidence interval.

Brain Region	Volume in controls	Volume in patients	Regression B coefficient	95% CI	p-value
All	0.30%±0.20%	0.88%±0.53%	0.0044	[0.00066 0.0081]	0.022
Left Hemisphere	0.29%±0.19%	0.85%±0.52%	0.0043	[0.00059 0.0079]	0.024
Right Hemisphere	0.32%±0.21%	0.92%±0.56%	0.0045	[0.00065 0.0084]	0.023
Temporal Lobe	0.27%±0.17%	0.79%±0.44%	0.0039	[0.0018 0.006]	<0.001
Parietal Lobe	0.50%±0.42%	1.20%±0.79%	0.0048	[0.00092 0.0086]	0.016
Occipital Lobe	0.23%±0.15%	0.76%±0.53%	0.0049	[0.0023 0.0074]	<0.001
Frontal Lobe	0.25%±0.17%	0.92%±0.68%	0.0052	[0.0019 0.0085]	0.0023

Table 6.3: Results from the generalized linear regression analyses to test for differences in relative volume of the long-T_2^* component between the patients with MS and controls. Compared to Table 6.2 T_2-hyperintense lesions were masked after which the volumes were calculated. Comparisons were made for different regions and all were corrected for age and sex. A positive B coefficient indicates a larger volume in the patient group. CI: confidence interval.

Brain Region	Volume in controls	Volume in patients	Regression B coefficient	95 % CI	p-value
All	0.28%±0.17%	0.63%±0.33%	0.003	[0.00068 0.0053]	0.012
Left Hemisphere	0.26%±0.17%	0.62%±0.32%	0.003	[0.00071 0.0053]	0.011
Right Hemisphere	0.29%±0.18%	0.65%±0.33%	0.003	[0.00062 0.0053]	0.014
Temporal Lobe	0.25%±0.14%	0.53%±0.28%	0.0023	[0.00095 0.0037]	0.0011
Parietal Lobe	0.46%±0.34%	0.81%±0.41%	0.0026	[0.00055 0.0047]	0.014
Occipital Lobe	0.21%±0.14%	0.56%±0.32%	0.0035	[0.0019 0.005]	<0.001
Frontal Lobe	0.23%±0.15%	0.68%±0.39%	0.0039	[0.002 0.0058]	<0.001

Spearman correlation analysis as shown in Table S6.2.

When the volume of the MRF-component outside the T_2-hyperintense lesions was compared to the visual scoring significant correlations were found in the parietal (r=0.20 [0.01 0.39] p=0.04) and frontal lobe (r=0.23 [0.04 0.41] p=0.02) as shown in Table S6.1.

Figure 6.8 shows the results of the performed similarity scoring of the FLAIR images and the long-T_2^* component. For the control group almost all T_2^* component maps were scored as similar. For the patient group we observed a higher extent of the affected tissue in 73 % of the MRF scans compared to the structural white matter abnormalities on the FLAIR scans. The similarity between regions with high fractions of the (>15 %) long-T_2^* component fractions and the FLAIR images was high, as shown in Figure S6.1. A 100 % similarity in volume was observed for the healthy controls and 71 % for the patient data.

6.4. DISCUSSION

We performed a multi-component analysis on EPI-MRF data of MS patients and healthy controls and developed a suitable analysis pipeline to study white matter changes. In patients we observed an increase in volume of components with longer transverse relaxation times compared to the controls. This component correlated with

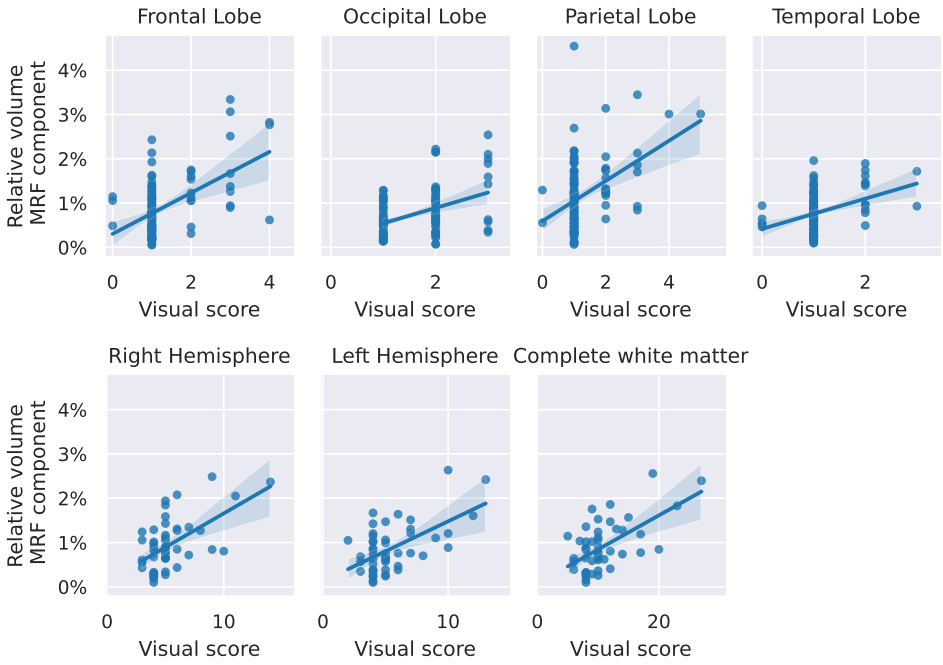

Figure 6.7: Scatter plots with linear regression estimates with 95 % confidence intervals for the visual scoring of white matter damage (x-axis) against the volume of the long-T_2^* MRF-component (y-axis). Different plots represent different anatomical regions.

Table 6.4: Spearman correlation of structural white matter changes volume scored by a neuroradiologist against long-T_2^* MRF component volume in the white matter. CI: confidence interval.

Region	Spearman correlation coefficient	95% CI	p-value
All	0.47	[0.22 0.66]	<0.001
Left Hemisphere	0.40	[0.13 0.61]	<0.001
Right Hemisphere	0.49	[0.24 0.68]	<0.001
Temporal Lobe	0.35	[0.16 0.51]	<0.001
Parietal Lobe	0.39	[0.21 0.55]	<0.001
Occipital Lobe	0.36	[0.18 0.52]	<0.001
Frontal Lobe	0.43	[0.25 0.58]	<0.001

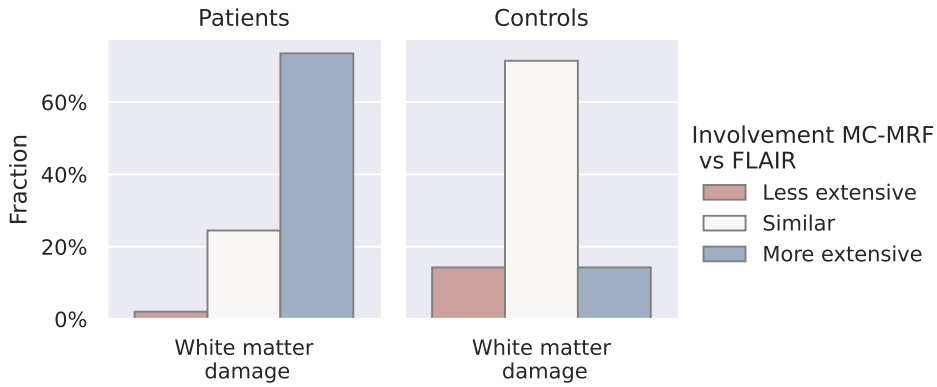

Figure 6.8: Histogram showing the visual similarity scores of the FLAIR images in comparison to the long-T_2^* MRF-component map.

white matter abnormalities as visible on T_2-FLAIR-weighted scans in MS patients, but also showed an increased involvement of the white matter compared to the FLAIR scans.

In previous studies in MS, both diffusion based measures and multi-component relaxometry were used to study microstructural white matter changes. In early diffusion studies [174, 191] it was observed that mean diffusivity was increased and the averaged fractional anisotropy was decreased in the normal appearing white matter in MS patients compared to healthy controls. In later imaging and histopathologic analyses, DAWM regions were defined in the previously perceived normal appearing white matter. These DAWM regions showed decreased fractional anisotropy on MRI and on histopathological analyses a decreased myelin density, extensive axonal loss, and chronic fibrillary gliosis was shown [190]. In more recent studies, more advanced measures such as restricted signal fraction [176] were used to study microstructural white matter changes in early MS patients. Compared to Diffusion Tensor Imaging (DTI) the employed CHARMED model separates different intra- and extracellular compartments to estimate the restricted signal fraction, an imaging parameter sensitive to the volume fraction of axons. This novel metric was obtained along with conventional DTI metrics, where a widespread

significant reduction in restricted fraction was found in normal appearing white matter in MS patients compared to controls, but no significant differences were found in conventional diffusion parameters [176]. However, conventional diffusion tensor imaging based measures lack the ability to isolate the signal contribution from different tissue compartments, thereby reducing the specificity for tissue subtypes and associated injuries or microstructural damage [192]. More recent multi-compartment diffusion MRI models, such as CHARMED, provide increased specificity, but also require long scan times (more than 15 minutes), show increased variation in parameter estimates or require high gradient hardware [192]. Multi-component MRF provides a novel approach to assess microstructural white matter changes.

Previous multi-component models have been used in MS patients based on multi-echo spin-echo sequences sensitive to T_2 effects [132, 133]. In a previous study 20 MS patients were scanned with a 48 echo multi-echo spin-echo sequence with a maximum echo time of 1.12 s. 27 out of 107 (25 %) of the T_2-hyperintense lesions showed long-T_2 signal between 200 and 800 ms in 10 out of 20 (50 %) of the MS patients. The total normal appearing white matter in MS patients yielded an average long-T_2 signal fraction of 4.2 % [132]. It was hypothesized in these studies that this long-T_2 component reflected an increase in extracellular water, similar to the microstructural damage as observed in diffusion methods, potentially related to an increase in edema. The sequence used in these studies had extremely long echo times (around one second), resulting in acquisition times of more than 6 minutes per slice (without averaging).

In our study, we were able to visualize and quantify the extent of the microstructural white matter changes by MC-MRF and showed that its volume is larger than the structural white matter abnormalities visible on FLAIR scans. These findings are in line with the previously stated hypothesis that in MS patients more brain tissue is affected than visible on structural MRI scans [133, 171, 172, 190]. Multi-component relaxometry and specifically the performed MC-MRF analysis in our study has the potential to identify water-like components (i.e. with long transverse relaxation times) that are present in the microstructure of the brain. These longer relaxation times could be caused by microstructural damage resulting in an increase in extra-cellular space reducing the interaction between hydrogen protons in these spaces. This increase in extra-cellular space is potentially due to the decrease in myelin density and axonal loss [190]. The increase in the long-T_2 component can also be caused by a form of edema, as was previously reported in patients with brain metastases based on Bayesian partial volume MC-MRF [24, 25]. In a patient with brain metastases, components with $T_2 > 100$ ms in peritumoral edema were measured [24, 25]. This component showed a similar increased T_2 relaxation time, indicating that at least parts of these areas might contain edema.

Opposed to previously proposed methods, the used EPI-MRF sequence in our study allows for full brain coverage in relatively short acquisition times of less than 6 minutes. The MRF framework allows for many readouts with relatively short time between readouts, limiting the total scan time. The obtained magnetization fraction maps selected based on their relaxation times from the MC-MRF method are easily interpretable due to the natural range between 0 and 1, where other parameters such as relaxation times or diffusivity require the choice of specific thresholds. The use of a fast multi-parametric method (which MRF facilitates) potentially allows for reduced variation in

measurements between different sites, due to the quantitative nature and correction for B_1^+ inhomogeneities.

Finally, our study has several limitations. The used EPI-MRF sequence allows for an efficient k-space coverage, but the employed gradient echoes are inherently sensitive to iron and susceptibility effects (see Figure 6.2 component 5). This could be a partial explanation for the differences we observe between brain regions. Future studies employing T_1, T_2-sensitive MRF sequences could be highly relevant in order to avoid this issue. Also, our MRF sequence used flip angle train timings that slightly vary per slice, which may induce variation in estimated tissue fractions. However, we observed that this mainly affected the myelin water like components.

The long transverse relaxation times we observed in the MC-MRF long-T_2^* component were often longer than one second, which might partly be due to measurement errors. Potentially this is caused by the reduced sensitivity to these long relaxation times of the used sequence (see Figure S6.2). In brief, we observed that the signal shapes of $T_2^* = 150\,\text{ms}$ and $T_2^* = 1\,\text{s}$ for $T_1 = 1\,\text{s}$ vary less than 1 %. Therefore the exact T_2^* estimates as obtained have a relatively large error margin compared to the values for shorter T_2^* as in for example gray and white matter. Technical improvements could therefore consist of tuning the sequence to improve sensitivity for relatively long T_2^* relaxation times. Thus, our study was performed in a small group MS patients. Our methods and results should be validated in larger groups of MS patients with variations in disease burden.

6.5. CONCLUSION

OUR MRF acquisition and proposed analysis revealed a component with long T_2^* times of which the volume correlated significantly with a score of visual changes on standard T_2-FLAIR images. These visual changes are frequently referred to as dirty-appearing white matter. Furthermore, the component's extent appeared to be larger than visually detectable white matter damage on FLAIR scans. This corroborates other evidence that the disease burden of MS could be underestimated using only conventional MRI scans.

6.6. SUPPORTING INFORMATION

Table S6.1: Spearman correlation analyses between structural white matter change volume score (excluding T_2-hyperintense lesions) by a neuroradiologist and estimated long-T_2^* MRF component volume in the white matter (without T_2-hyperintense lesions). CI: confidence interval.

Region	Spearman correlation coefficient	95% CI	p-value
Left Hemisphere	0.17	[-0.12 0.43]	0.24
Right Hemisphere	0.19	[-0.1 0.45]	0.19
Temporal Lobe	0.06	[-0.14 0.26]	0.53
Parietal Lobe	0.20	[0.01 0.39]	0.04
Occipital Lobe	0.14	[-0.06 0.33]	0.16
Frontal Lobe	0.23	[0.04 0.41]	0.02

Table S6.2: Spearman correlation analyses between structural white matter change volume score by a neuroradiologist and estimated long-T_2^* MRF component volume in the white matter when the two different sites are taken into account as co-variable. Results when T_2-hyperintense lesions where included (similar to Table 6.4) and excluded (similar to Table S6.1) are shown. CI: confidence interval.

	Region	Spearman correlation coefficient	95% CI	p-value
Including T_2-hyperintense lesions	All	0.42	[0.16 0.63]	<0.001
	Left Hemisphere	0.38	[0.11 0.6]	0.01
	Right Hemisphere	0.40	[0.13 0.61]	<0.001
	Temporal Lobe	0.33	[0.14 0.5]	<0.001
	Parietal Lobe	0.38	[0.2 0.54]	<0.001
	Occipital Lobe	0.21	[0.01 0.39]	0.04
	Frontal Lobe	0.48	[0.31 0.62]	<0.001
Excluding T_2-hyperintense lesions	All	0.08	[-0.2 0.36]	0.57
	Left Hemisphere	0.09	[-0.2 0.36]	0.56
	Right Hemisphere	0.10	[-0.19 0.37]	0.52
	Temporal Lobe	-0.05	[-0.24 0.15]	0.65
	Parietal Lobe	0.15	[-0.05 0.34]	0.15
	Occipital Lobe	-0.03	[-0.23 0.17]	0.79
	Frontal Lobe	0.34	[0.15 0.5]	<0.001

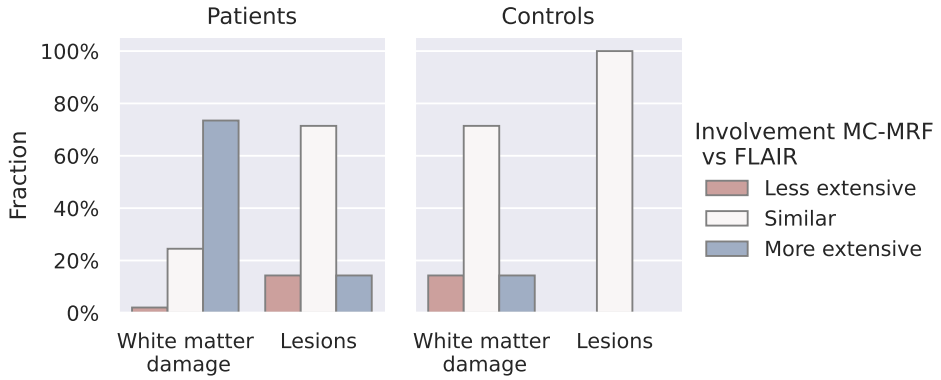

Figure S6.1: Histogram showing the visual similarity scores of the FLAIR scans compared to the long-T_2^* MRF-component map for white matter damage and T_2-hyperintense lesions.

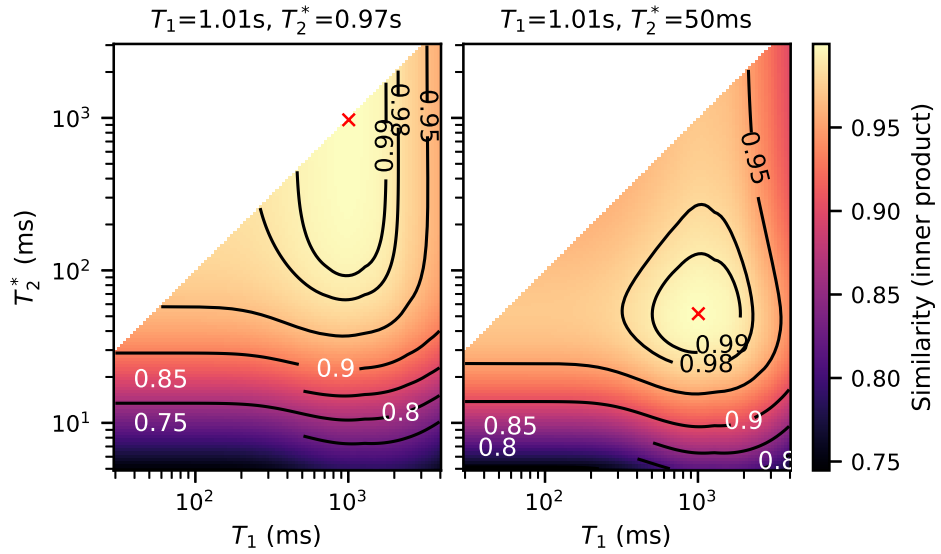

Figure S6.2: Similarity of two selected dictionary atom (red cross) and other atoms by computing the inner product. On the left $T_1 \approx T_2^* \approx 1\,\text{s}$ was used and on the right $T_1 \approx 1\,\text{s}$ and $T_2^* = 50\,\text{ms}$. A large inner product indicates that the two compared signals are very similar and as such hard to distinguish from each other. Note that a log-scaling was used for the axis. One may observe that the used MRF sequence appears to have rather low discriminative properties for longer T_2^* values.

7

Detection of small cerebral lesions using multi-component MR Fingerprinting with local joint sparsity

Martijn A. Nagtegaal
Ingo Hermann
Sebastian Weingärtner
Jeroen de Bresser
Frans M. Vos

Proc. Intl. Soc. Mag. Reson. Med. 28. ISMRM. online, 2020

ABSTRACT

We propose a novel multi-component analysis for MR fingerprinting that enables detection of small lesions, while taking partial volume effects into account. The algorithm uses a joint sparsity constraint limiting the number of components in local regions. It is evaluated in simulations and on MRF-EPI data from a patient with multiple sclerosis (MS). MS-lesions are separated from other tissues based on having increased T_2^* relaxation times. The improved sensitivity to multiple components makes it possible to detect components with long relaxation times within the lesion, possibly increasing our insight into these small pathologies.

7.1. INTRODUCTION

QUANTITATIVE MR-imaging methods, such as MR Fingerprinting (MRF) [9] and MRF-EPI [184], are used to measure tissue properties (e.g. FISP-MRF [10]: T_1, T_2; MRF-EPI [184]: T_1, T_2^*) and can therefore be used to derive standard and novel MRI-biomarkers. Common quantitative MR methods assume a single set of relaxation properties per voxel. However, this is not valid in the presence of partial volume effects as well as in tissues consisting of multiple components. Sensitivity to such multi-component effects in and around lesions can also provide more insight into disease processes.

In the brain of healthy subjects a small number of tissues is expected and multi-component MRF(MC-MRF) using (global) joint-sparsity [75] with the SPIJN algorithm, can be used to obtain a partial volume segmentation of the different components. Due to the highly correlated MRF-dictionary SPIJN is able to identify around ten tissues. However, tissue properties of small cerebral lesions can vary per lesion and occur in small regions, making the global joint sparsity less applicable. Voxel-wise methods [25, 36] without joint sparsity constraints, on the other hand, show lower noise resilience.

In this work, we develop a MC-MRF algorithm based on a joint sparsity constraint that is applied locally to be particularly sensitive to small pathologies. As a proof of principle, this method is used for automatic lesion detection in MRF-EPI data from a patient with MS.

7.2. METHOD

THE Sparsity Promoting Iterative Joint NNLS (SPIJN) algorithm [75] was extended in order to account for small structures. The resulting local-SPIJN algorithm is based on the premise that a local region only consists of a small number of components.

Hence, we solved the following minimization problem:

$$\min_{C \in \mathbb{R}_{\geq 0}^{N \times J}} \|X - DC\|_2^F \tag{7.1}$$

$$\text{s.t.} \left\| C_{R(v_j)} \right\|_r \text{ is small } \forall\, j \in \{0, \ldots, J\} \tag{7.2}$$

where X is a matrix containing the J measured signals, D the MRF-dictionary and C a matrix containing the N component weights for every voxel. $C_{R(v_j)}$ denotes the sub-matrix of C consisting of the subset R of voxels in the vicinity of voxel j. $\|\cdot\|_r$ counts the number of non-zero rows of a matrix.

We solved the problem iteratively based on the NNLS algorithm [35], with the follow-

ing iterations:

$$R = \text{diag}\left(\left(\mathbf{w}_j^{k+1}\right)^{1/2}\right), \tag{7.3a}$$

$$\tilde{D} = \begin{bmatrix} DR \\ \lambda \mathbf{1}^T \end{bmatrix}, \tag{7.3b}$$

$$\tilde{\mathbf{x}} = \begin{bmatrix} \mathbf{x}_j \\ 0 \end{bmatrix}, \tag{7.3c}$$

$$\tilde{\mathbf{c}} = \min_{c \in \mathbb{R}^N_{\geq 0}} \left\| \tilde{\mathbf{x}} - \tilde{D}\mathbf{c} \right\|_2, \tag{7.3d}$$

$$\mathbf{c}_j^{k+1} = R\tilde{\mathbf{c}}, \tag{7.3e}$$

in which λ is a sparsity regularization parameter.

Notably, weights $\mathbf{w}^{i,k+1}$ were calculated by spatial Gaussian smoothing of the previous solution c^i (row i of C) for tissue i. The standard deviation σ of the Gaussian essentially governed the locality. $\lambda = 0.8$, $\sigma = [4,4,4/2]$px= $[4,4,4]$mm (in x,y,z-direction) were used in this study.

MRF-EPI [184] was used to test the method in numerical experiments and in-vivo. A dictionary with $T_1 = 30$ ms - 4 s, $T_2^* = 5$ ms-3 s (5 % increase) and $B_1 = 0.65 - 1.35$ (0.05 stepsize) was used.

A numerical phantom of size 100×100 pixels consisting of a background tissue with $T_1 = 900$ ms, $T_2^* = 50$ ms (representing white matter) and 15 non-overlapping randomly placed dot-shaped abnormalities with log-distributed T_1, T_2^* (300 ms-2 s, 55 ms-200 ms respectively) was used to test the local-SPIJN algorithm. Transitions between background and dots were either smooth or instantaneous. Varying SNR (50,100,500) and radii (3,5,7px) were used.

Resulting partial volume segmentations B from the proposed local-SPIJN algorithm were compared to the ground truth A through the fuzzy Tanimoto coefficient [93]:

$$\text{TC}_\text{F} = \frac{\sum_i \text{MIN}(A_i, B_i)}{\sum_i \text{MAX}(A_i, B_i)}. \tag{7.4}$$

The proposed algorithm was applied to MRF-EPI data acquired from a patient with MS (resolution 1 mm × 1 mm × 2 mm, 240 × 240 × 60 voxels, acquisition time 1:52 minutes) on a 3 T scanner (Siemens, Erlangen, Germany). Components with $1.5\,\text{s} < T_1 < 2.25\,\text{s}$, $75\,\text{ms} < T_2^* < 1\,\text{s}$ were considered as potential lesions, based on increased T_2^* [193, 194]. Results are shown for 4 slices in which lesions were manually segmented by an expert radiologist on FLAIR images.

7.3. RESULTS AND DISCUSSION

SINGLE-COMPONENT MRF, SPIJN-MC-MRF and the proposed method were compared on one of the numerical phantoms as shown in Figure 7.1. Single component matching incorrectly resulted in a smooth transition in relaxation times at the borders of the structures. SPIJN-MC-MRF resulted in 2 noisy component and 7 components erroneously not confined to single lesions. The proposed method is able to detect the different lesions in isolation.

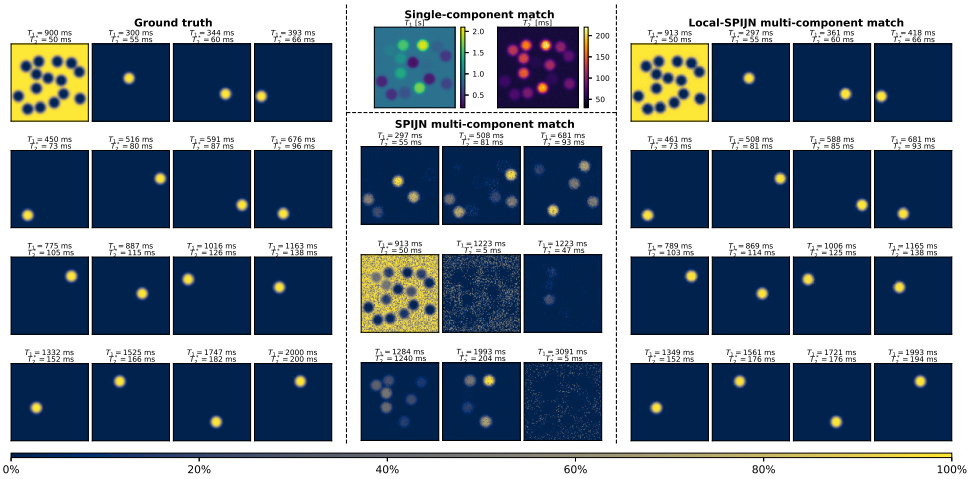

Figure 7.1: Comparison between single component matching, SPIJN-MC-MRF and the proposed method (local-SPIJN) for a numerical phantom containing 15 dot-shaped abnormalities. The simulated abnormalities have varying T_1 and T_2^* values, radius of 7 px and a smooth transition to the background, SNR=50 was used. Resulting T_1 and T_2^* times are shown for single component matching. Fraction maps are shown for the ground truth and resulting components for SPIJN and local-SPIJN MC-MRF, with their corresponding relaxation times.

Simulation results of the proposed algorithm collated in Figure 7.2, showed good agreement with the reference for $SNR \geq 100$ (error $T_1 < 1\%$, $T_2^* < 2\%$, $\mathrm{TC_f} > 0.92$). SNR=50 gave segmentations of reasonable quality ($\mathrm{TC_f} > 0.75$) [93].

Figure 7.3 shows relative differences between the $M_{0,\ 1}$ and T_2^* maps from a single component approach compared to the primary (largest) MC-MRF component. Note the small differences in the white matter (no partial volume) and increased differences around tissue boundaries, where partial volume occurs.

Figure 7.4 shows T_1 and T_2^* maps obtained from matching and signal fractions of the three components identified as lesions. Note how the detected lesions correspond to lesions as annotated in the quantitative maps. The smaller lesions had relaxation times in the range of gray matter (data not shown). To detect these lesions as well, inclusion of spatial information or other contrasts would be required.

A zoomed-in version of two slices of one lesion is shown in Figure 7.5, including the multiple components identified in the center of this lesion. The two detected extra components only occur with a lower fraction (30 %) and thus require multi-component sensitivity. The two components have long T_1 relaxation times, which could correspond to veins as more often observed in MS-lesions [167].

In this study results are shown for a single subject since the focus was on the development of the numerical methods. A topic of further research is the application to more datasets, to test the quality of the segmentations and the information contained by the smaller components in the lesions.

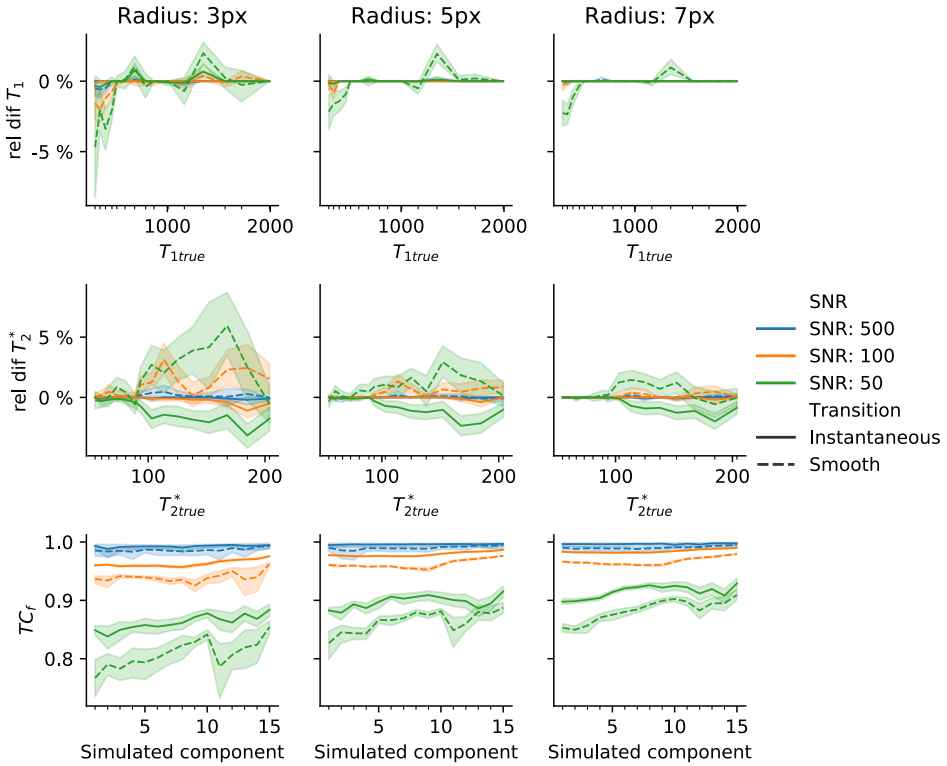

Figure 7.2: Overview of the results from the numerical simulations. 15 dots with varying T_1, T_2^* were randomly placed in an image of 100 × 100 pixels. This was repeated 50 times per radius and SNR with either smooth (dashed) or instantaneous (solid) transition to the background. The upper two rows show the relative difference between the matched and true relaxation time. The third row shows the quality of the partial volume segmentation using the fuzzy Tanimoto (TC_f) coefficient as a measure.

7.4. CONCLUSION

THE proposed local-SPIJN algorithm is able to detect small abnormalities from MRF-EPI data. This potentially improves robustness against multi-component effects around and in lesions, paving the way for better detection and deeper insights into underlying pathological changes.

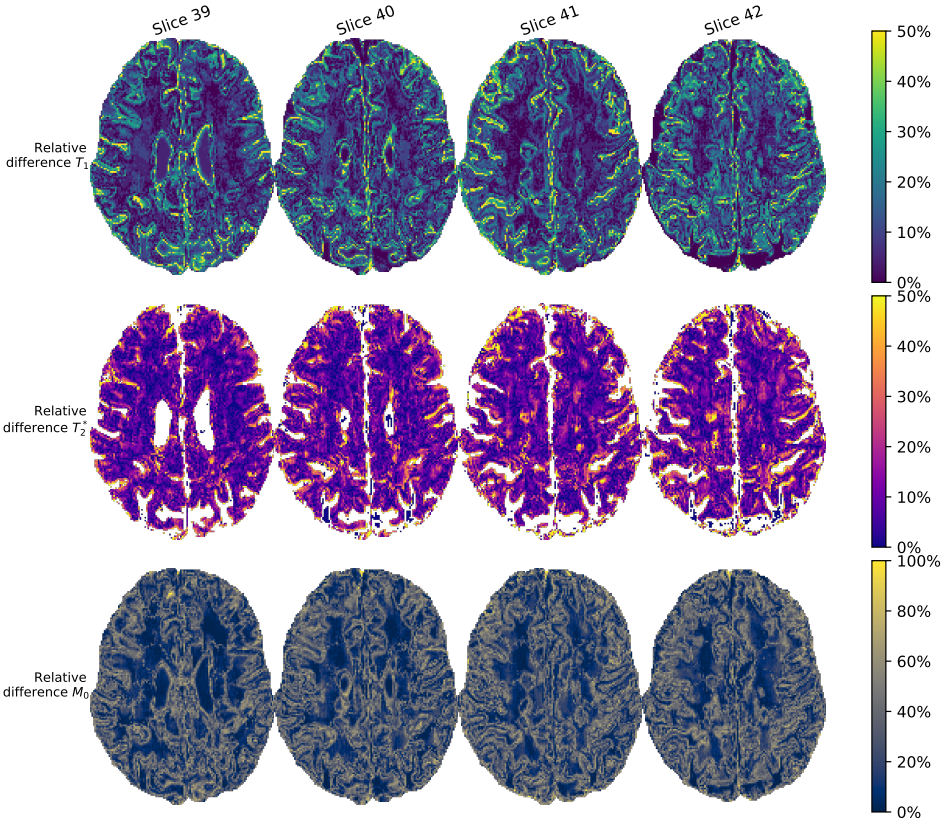

Figure 7.3: The magnitude of the relative difference between the results from the single-component matching and the primary (largest) component from the proposed multi-component matching. The values are relative to the single component outcome. High T_2^* values larger than 200 ms were masked. The maps show structural patterns around tissue boundaries, corresponding to the regions where partial volume effects occur.

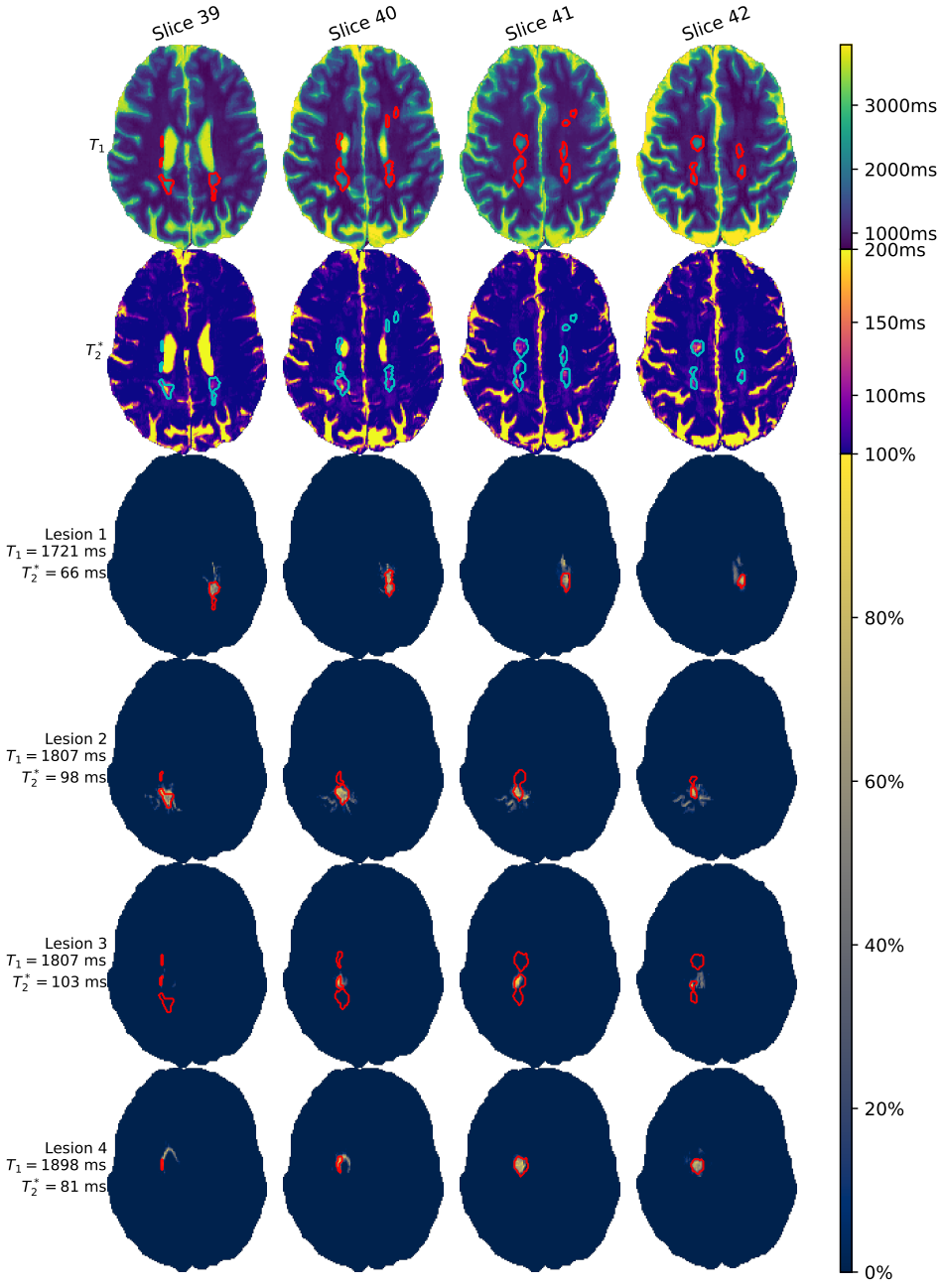

Figure 7.4: First and second row show the $_1$ and T_2^* maps as obtained with single component matching as a reference. Red and cyan contours show the lesions as annotated by a radiologist. Bottom rows show volume fractions of 3 lesion-components identified based on $_1$ and T_2^* values in the local-SPIJN multi-component match.

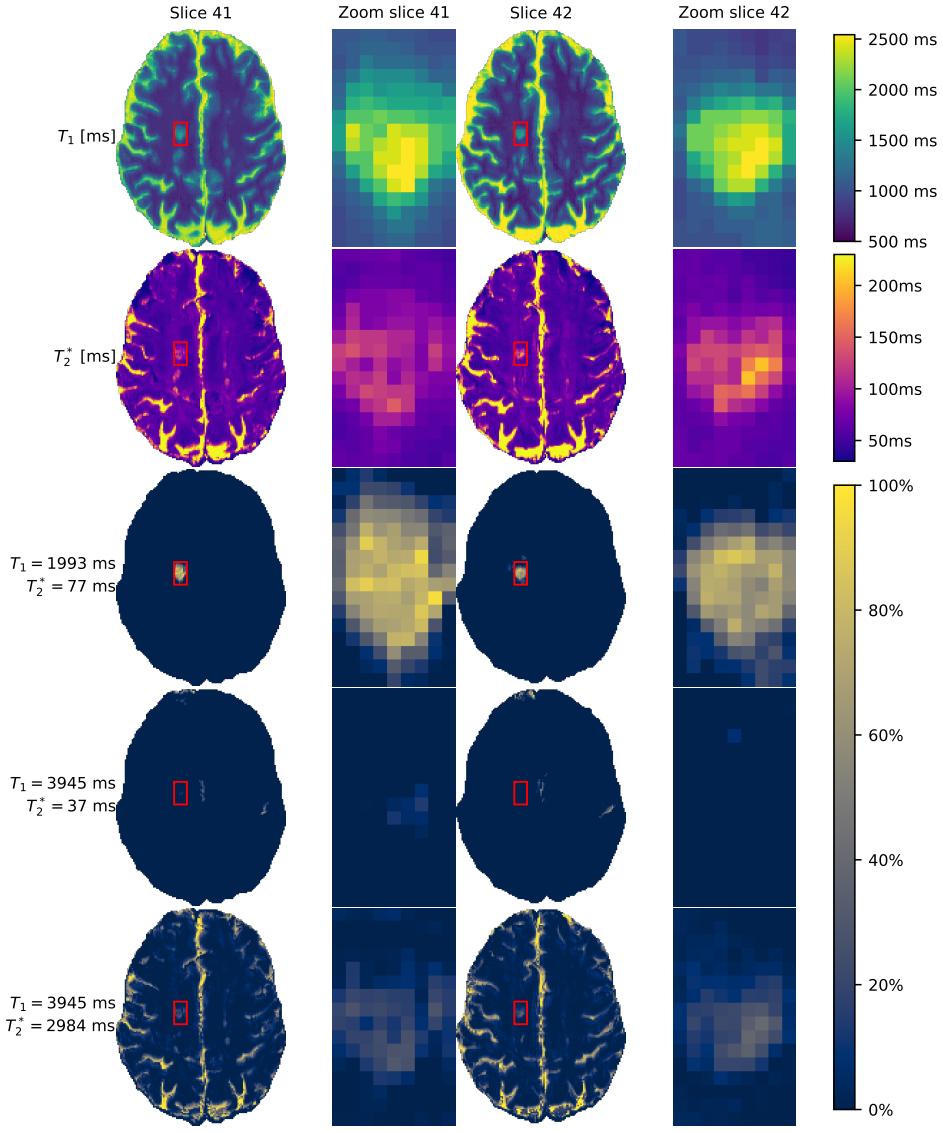

Figure 7.5: Zoomed-in versions of one of the lesions (with relaxation times $T_1 = 1993$ ms, $T_2^* = 98$ ms) with the other components present in the center of this lesion. The two upper rows show the single component T_1 and T_2^* maps, the lower three rows show the relative presence of the 3 components.

8

MITIGATING UNDERSAMPLING ERRORS IN MR FINGERPRINTING BY SEQUENCE OPTIMIZATION

David Heesterbeek
Kirsten Koolstra
Matthias J.P. van Osch
Martin B. van Gijzen
Frans M. Vos
Martijn A. Nagtegaal

Magnetic Resonance in Medicine. online version (2023) ISSN: 1522-2594
DOI: 10.1002/mrm.29554

ABSTRACT

Purpose: To develop a method for Magnetic Resonance Fingerprinting (MRF) sequence optimization that takes both the applied undersampling pattern and a realistic reference map into account.

Methods: A predictive model for the undersampling error leveraging on perturbation theory was exploited to optimize the MRF flip angle sequence for improved robustness against undersampling artifacts. In this framework parameter maps from a previously acquired MRF scan were used as reference. Sequences were optimized for different sequence lengths, smoothness constraints and undersampling factors. Numerical simulations and in vivo measurements in eight healthy subjects were performed to assess the effect of the performed optimization. The optimized MRF sequences were compared to a conventionally shaped flip angle pattern and an optimized pattern based on the Cramér-Rao lower bound (CRB).

Results: Numerical simulations and in vivo results demonstrate that the undersampling errors can be suppressed by flip angle optimization. Analysis of the in vivo results show that a sequence optimized for improved robustness against undersampling with a flip angle train of length 400 yielded significantly lower median absolute errors in T_1: 5.6 % ± 2.9 % and T_2: 7.9 % ± 2.3 % compared to the conventional (T_1: 8.0 % ± 1.9 %, T_2: 14.5 % ± 2.6 %) and CRB based (T_1: 21.6 % ± 4.1 %, T_2: 31.4 % ± 4.4 %) sequences.

Conclusion: The proposed method is able to optimize the MRF flip angle pattern such that significant mitigation of the artifacts from strong k-space undersampling in MRF is achieved.

8.1. INTRODUCTION

MAGNETIC Resonance Fingerprinting (MRF) samples the MR signal in a transient-state while varying acquisition parameters are applied [9]. After each excitation pulse an undersampled k-space read-out is acquired and reconstructed by zero-filling, even though this results in severe aliasing artifacts. Tissue parameters are generally estimated using inner product matching of the measured signal to a precalculated dictionary (e.g. yielding the longitudinal relaxation time T_1, transverse relaxation time T_2 and magnitude of the steady state magnetization ρ or M_0).

Sequence optimization has been performed to increase the accuracy of the parameter maps and to further reduce the scan time [12]. Most previous methods for sequence optimization modeled the errors in the MRF signal as independent, zero-mean stochastic noise [26–29, 195]. However, these approaches neglected spatial correlations between voxels introduced by the undersampling. For shorter acquisition times, either due to high undersampling factor and/or low number of time indices, the undersampling error can have a large effect on the accuracy and the image quality of the parameter maps [196].

In recent work, Jordan et al. [30] proposed an MRF-sequence optimization scheme that explicitly models undersampling effects as well as spatial variations of the signal phase, potentially caused by spatial variations in the B_0 and B_1 field. To reduce the computational complexity, a reference image was separated into white matter, gray matter and CSF fractions using three reference T_1, T_2 combinations. For each tissue type undersampling artifacts were precalculated per time point using the respective fraction maps. During iterations of the optimization scheme only the transverse magnetization of the three tissue types was recalculated and used as weighting per time point to obtain time-frame images. Based on these simplified reference maps, error estimates could be obtained, thereby allowing an iterative optimization procedure to reduce undersampling errors.

In this paper we aim to develop a new MRF optimization method to mitigate undersampling artifacts that applies a more sophisticated spatial reference map. While doing so, our focus will be on the flip angle train. To overcome the issue of high computational complexity we use a recently proposed model relying on perturbation theory, to predict the interplay between a specific MRF acquisition scheme and the undersampling artifacts in the tissue parameter maps [196]. Our method does not require the calculation of extensive MRF-dictionaries, includes the spatially varying signal phase in the model and allows to use any reference parameter map as target for the optimization. The predictive model and optimized sequences will be validated by means of simulations and in vivo brain scans. We hypothesize that optimization of the flip angle train can significantly reduce the undersampling errors in the reconstructed parameter maps.

8.2. THEORY

TO provide the necessary background for the performed optimization and context to the presented results, the MRF-undersampling model proposed by Stolk and Sbrizzi [196] is briefly described. We will use this model for sequence optimization in Section 8.3. Essentially, the model gives an analytical expression for the estimated quantitative

parameter maps $\boldsymbol{\theta}^*$ resulting from an MRF experiment:

$$\boldsymbol{\theta}^* \approx \boldsymbol{\theta} + \text{PSFE}(\boldsymbol{\theta}) + \mathscr{E}_1(\boldsymbol{\alpha}) + \mathscr{E}_2(\boldsymbol{\theta};\boldsymbol{\alpha}), \tag{8.1}$$

in which $\boldsymbol{\theta} \in \mathbb{R}^{N_\theta \times N_I \times N_I}$ are the N_θ reference tissue parameter maps of $N_I \times N_I$ voxels; $\boldsymbol{\alpha}$ represents the flip angle pattern and PSFE is the point spread function error that depends on the k-space sampling pattern, but is independent of the flip angle pattern (only minimized by adjusting the undersampling scheme). Importantly, $\mathscr{E}_1(\boldsymbol{\alpha})$ and $\mathscr{E}_2(\boldsymbol{\theta};\boldsymbol{\alpha})$ are error terms that do depend on the flip angle pattern and can therefor be minimized by appropriately adjusting the flip angles. In further equations the dependence on $\boldsymbol{\alpha}$ has been omitted for ease of notation.

The (to be estimated) parameters of our focus are:

$$\boldsymbol{\theta}^{(*)}(\vec{x}) = \left(T_1^{(*)}(\vec{x})\,, T_2^{(*)}(\vec{x}), \text{Re}\left(\rho^{(*)}(\vec{x})\right), \text{Im}\left(\rho^{(*)}(\vec{x})\right)\right)^T$$

such that the number of parameters $N_\theta = 4$. Notice that the steady state magnetization $\rho^{(*)} \in \mathbb{C}^{N_I \times N_I}$ contains the (estimated) spatially varying, signal phase.

The rest of this section contains an overview of the key steps in the model derivation from Stolk and Sbrizzi [196] The undersampled time-series images from an MRF scan are written as a convolution of the transverse magnetization at time TE of the readout with a Point Spread Function (PSF) that depends on the k-space sampling scheme:

$$I_j(\vec{x}|\boldsymbol{\theta}) = \sum_{\vec{y}\in G} P_j(\vec{x}-\vec{y}) m_j(\boldsymbol{\theta}(\vec{y})), \tag{8.2}$$

in which $I_j(\vec{x}|\boldsymbol{\theta}) \in \mathbb{C}^{N_I \times N_I}$ is the undersampled time-series image at time index j; G is the spatial domain; $P_j \in \mathbb{C}^{N_I+2\lfloor N_I/2\rfloor \times N_I+2\lfloor N_I/2\rfloor}$ is the PSF for time index j that models the effect of undersampling; $\boldsymbol{m}(\boldsymbol{\theta}) \in \mathbb{C}^{N_J}$ is the transverse magnetization over time determined by reference parameters $\boldsymbol{\theta}$ and $m_j(\boldsymbol{\theta})$ the magnetization at time index j.

Observe that (8.2) partitions the description of the undersampled images in a spatial component (the PSF) that depends on the k-space sampling pattern, and a temporal component (the transverse magnetization) that depends on the flip angle pattern. Only the temporal component needs to be updated when optimizing for the acquisition parameters. This proves to be useful for obtaining feasible calculation times.

MRF parameter estimation can be conceived as the voxel-wise least-square minimization based on N_J time-series images $\boldsymbol{I} \in \mathbb{C}^{N_J \times N_I \times N_I}$:

$$\boldsymbol{\theta}^*(\vec{x}) = \underset{\tilde{\boldsymbol{\theta}}\in\mathbb{R}^{N_\theta}}{\arg\min} \left\| \boldsymbol{I}(\vec{x}|\boldsymbol{\theta}) - \boldsymbol{m}(\tilde{\boldsymbol{\theta}}) \right\|^2, \tag{8.3}$$

in which $\boldsymbol{I}(\vec{x}|\boldsymbol{\theta}) \in \mathbb{C}^{N_J}$ denotes the observed signal in a voxel at location $\vec{x}$, which depends on $\boldsymbol{\theta}$ in all voxels due to the applied PSF.

The estimate $\boldsymbol{\theta}^*$ is a stationary point of the objective function (8.3), such that:

$$\text{Re}\left(\left(\boldsymbol{m}(\tilde{\boldsymbol{\theta}}) - \boldsymbol{I}(\vec{x}|\boldsymbol{\theta})\right), \frac{\partial}{\partial\theta_p}\boldsymbol{m}(\tilde{\boldsymbol{\theta}})\right)\Big|_{\tilde{\boldsymbol{\theta}}=\boldsymbol{\theta}^*(\vec{x})} = 0, \tag{8.4}$$

for all $\vec{x}$ in the spatial domain G and each $p \in \{1,2,..,N_\theta\}$.
From (8.2) and (8.4) it can be deduced that:

$$\begin{aligned} 0 = \mathrm{Re}\Big(& \sum_{j=1}^{N_J} m_j(\boldsymbol{\theta}^*(\vec{x}))\overline{\mathscr{D} m_{j;p}(\boldsymbol{\theta}^*(\vec{x}))} \\ & - \sum_{j=1}^{N_J} \sum_{\vec{y}\in G} P_j(\vec{x}-\vec{y}) m_j(\boldsymbol{\theta}(\vec{y}))\overline{\mathscr{D} m_{j;p}(\boldsymbol{\theta}^*(\vec{x}))}\Big), \end{aligned} \tag{8.5}$$

in which $\overline{\mathscr{D}\boldsymbol{m}}$ is the complex conjugate of the Jacobian matrix of the magnetization vector $\boldsymbol{m}$.

Since (8.5) cannot be rewritten in a closed form expression for $\boldsymbol{\theta}^*$, a perturbation theoretic expansion is initially performed which is subsequently linearized. It is assumed that the range of tissue parameter values is small such that the magnetization can be considered linear with respect to the tissue parameters, allowing for the expansion. Defining $\boldsymbol{\eta} = (T_1, T_2)$, the parameters of $\boldsymbol{\theta}$ and $\boldsymbol{\theta}^*$ are expanded through:

$$\begin{aligned} \boldsymbol{\eta}^{(*)}(\vec{x}) &= \boldsymbol{\eta}_0 + \boldsymbol{\eta}_1^{(*)}(\vec{x}), \\ \rho^{(*)}(\vec{x}) &= \rho_0^{(*)}(\vec{x})\big(1 + \rho_1^{(*)}(\vec{x})\big), \end{aligned} \tag{8.6}$$

in which $\boldsymbol{\eta}_0$ are the assumed spatially constant values that we set to the mean T_1 and T_2 value of the reference map; $\boldsymbol{\eta}_1^{(*)}(\vec{x})$ and $\rho_1^{(*)}(\vec{x})$ are (estimated) contrast terms (i.e. offsets with respect to constants) and ρ_0 is a binary mask for zero-signal areas. Due to the linearity of $\rho^{(*)}$ in the magnetization function we can write:

$$\boldsymbol{m}(\boldsymbol{\theta}^{(*)}(\vec{x})) = \rho_0^{(*)}(\vec{x})\boldsymbol{m}(\boldsymbol{\theta}_0 + \boldsymbol{\theta}_1^{(*)}(\vec{x})), \tag{8.7}$$

in which

$$\rho_0^*(\cdot) = \frac{1}{N_J}\sum_{j=1}^{N_J} P_j(\cdot) * \rho_0(\cdot) \tag{8.8}$$

and

$$\begin{aligned} \boldsymbol{\theta}_0 + \boldsymbol{\theta}_1^{(*)}(\vec{x}) = & \Big(\boldsymbol{\eta}_0, 1, 0\Big)^T + \\ & \Big(\boldsymbol{\eta}_1^{(*)}(\vec{x}), \mathrm{Re}\big(\rho_1^{(*)}(\vec{x})\big\}, \mathrm{Im}\big\{\rho_1^{(*)}(\vec{x})\big)\Big)^T. \end{aligned} \tag{8.9}$$

Note that because of the binary mask $\boldsymbol{\theta}^{(*)}(\vec{x}) \neq \boldsymbol{\theta}_0 + \boldsymbol{\theta}_1^{(*)}(\vec{x})$.

The perturbation equations (8.6) and (8.9) facilitate extraction of an explicit expression for $\boldsymbol{\theta}^*(\vec{x})$. This is done by substituting the perturbation theoretic expansions and performing a first order Taylor expansion of the two terms in (8.5) around $\boldsymbol{\theta}_0$. For in-

stance, the Taylor expansion of the first term in (8.5) yields:

$$
\begin{aligned}
&m_j(\boldsymbol{\theta}^*(\vec{x}))\overline{\mathscr{D}m_{j;p}(\boldsymbol{\theta}^*(\vec{x}))} = \\
&|\rho_0^*(\vec{x})|^2 \cdot m_j(\boldsymbol{\theta}_0+\boldsymbol{\theta}_1^*(\vec{x}))\overline{\mathscr{D}m_{j;p}(\boldsymbol{\theta}_0+\boldsymbol{\theta}_1^*(\vec{x}))} \approx \\
&|\rho_0^*(\vec{x})|^2 \cdot \\
&\Big(m_j(\boldsymbol{\theta}_0)\overline{\mathscr{D}m_{j;p}(\boldsymbol{\theta}_0)} + \sum_{q=1}^{N_\theta} \mathscr{D}m_{j;q}(\boldsymbol{\theta}_0)\overline{\mathscr{D}m_{j;p}(\boldsymbol{\theta}_0)}\theta_{1,q}^*(\vec{x}) \\
&+ \sum_{q=1}^{N_\theta} m_j(\boldsymbol{\theta}_0)\overline{\mathscr{D}^2 m_{j;p,q}(\boldsymbol{\theta}_0)}\theta_{1,q}^*(\vec{x})\Big).
\end{aligned}
\tag{8.10}
$$

Based on these Taylor expansions an *explicit* expression for $\boldsymbol{\theta}_1^*(\vec{x})$ can be obtained, that can be rewritten into the form presented in equation (8.1). For the error terms $\mathscr{E}_1$ and $\mathscr{E}_2$ this results in:

$$
\begin{aligned}
\mathscr{E}_{1;p}(\boldsymbol{\alpha}) &= |\rho_0^*|^2 \sum_{q=1}^{N_\theta} \mathrm{Re}(N)_{p,q}^{-1}\mathrm{Re}\left(\overline{\rho_0^*}S_{\mathrm{resid;q}}^{(1,0)} * \rho_0\right), \\
\mathscr{E}_{2;p}(\boldsymbol{\theta},\boldsymbol{\alpha}) &= |\rho_0^*|^2 \sum_{q=1}^{N_\theta} \mathrm{Re}(N)_{p,q}^{-1}\mathrm{Re}\left(\overline{\rho_0^*}\sum_{r=1}^{N_\theta} S_{\mathrm{resid;q,r}}^{(1,1)} * (\rho_0\theta_{1;r})\right),
\end{aligned}
\tag{8.11}
$$

for $p \in \{1,2,..,N_\theta\}$. Here the following definitions have been used:

$$
\begin{aligned}
N_{p,q} &= \sum_{j=1}^{N_J} \overline{\mathscr{D}M_{j;p}(\boldsymbol{\theta}_0)}\mathscr{D}M_{j;q}(\boldsymbol{\theta}_0), \\
S_{\mathrm{resid;q}}^{(1,0)} &= \sum_{j=1}^{N_J}\left(P_j - \frac{1}{N_J}\sum_{i=1}^{N_J} P_i\right)\overline{\mathscr{D}M_{j;q}(\boldsymbol{\theta}_0)}M_j(\boldsymbol{\theta}_0), \\
S_{\mathrm{resid;q,r}}^{(1,1)} &= \sum_{j=1}^{N_J}\left(P_j - \frac{1}{N_J}\sum_{i=1}^{N_J} P_i\right)\overline{\mathscr{D}M_{j;q}(\boldsymbol{\theta}_0)}\mathscr{D}M_{j;r}(\boldsymbol{\theta}_0).
\end{aligned}
\tag{8.12}
$$

Note that N is also known as the Fisher information matrix. A more detailed derivation of (8.1) can be found in e.g. [101, 196] Using this approach, an expression is found for the predicted parameters (given certain reference parameter values). We will use this expression to mitigate the undersampling dependent error terms.

One may observe that the derived expression for $\boldsymbol{\theta}_1^*$ only depends on $\boldsymbol{m}(\boldsymbol{\theta}_0)$ and the first and second order derivatives of $\boldsymbol{m}$ in $\boldsymbol{\theta}_0$. Next to the use of precomputed PSFs (See (8.2)), this is the second step that makes this model suitable for sequence optimization, since only $\boldsymbol{m}(\boldsymbol{\theta}_0)$ and its derivatives are required instead of the computation of a large dictionary.

8.3. METHODS

METHODS were implemented in Python. The full implementation of the proposed optimization scheme, used reference maps and optimized sequences can be found at https://github.com/imphys/MRF_undersampling_optimization [197]. Results were visualized with Python libraries Matplotlib [198] and Seaborn [199].

8.3.1. SEQUENCE OPTIMIZATION

MRF sequences were optimized for a gradient spoiled SSFP acquisition [10] with a fixed repetition time (TR) of 15 ms. The Extended Phase Graph (EPG) formalism [112] was used to simulate the MRF signals $\boldsymbol{m}(\boldsymbol{\theta})$ over time. Using this approach the derivatives with respect to the tissue parameters can be calculated analytically through differentiation of the relaxation matrix and the term representing the recovery towards thermal equilibrium. All MRF scans used the same constant density, spiral k-space trajectory with an effective undersampling factor of 1/32. Incremental steps of 360°/32 rotation were applied between readouts and starting angles were equally distributed across sequence repetitions.

The cost function for this optimization problem was based on the relative errors $r_{\{1,2\},i}$ predicted by the model:

$$r_{\{1,2\},i} = \frac{T^{\text{und}}_{\{1,2\},i} - T^{\text{ref}}_{\{1,2\},i}}{T^{\text{ref}}_{\{1,2\},i}}, \tag{8.13}$$

for voxel i where $T^{\text{und}}_{\{1,2\},i}$ denotes the (undersampled) predictions resulting from (8.1) and $T^{\text{ref}}_{\{1,2\},i}$ is the reference value. The Root-Mean-Square (RMS) of the relative errors of non-masked voxels was used as a measure for the optimization performance:

$$\text{RMS}_{T_{\{1,2\}}} = \sqrt{\frac{1}{N_{\text{vox}}} \sum_{i=1}^{N_{\text{vox}}} r^2_{\{1,2\},i}}, \tag{8.14}$$

in which N_{vox} is the number of non-masked voxels. The mask used to calculate the RMS error strictly removed the zero-signal voxels (air) surrounding the head. Optimizations for in vivo data were based on previously acquired parameter maps from a single, fully sampled brain slice masked by thresholding the proton density map (see Figure 8.1).

Different optimization schemes were considered. Mathematically this design problem was posed as:

$$\begin{aligned} \min_{\{\alpha_j\}_{j=1}^{N_J}} \quad & \text{Cost function} \\ \text{s.t.} \quad (1): \quad & \text{LB} \le \alpha_1 \le 180^\circ \\ & \text{LB} \le \alpha_j \le 60^\circ \qquad \forall\ j \in \{2,3,..,N_J\} \\ (2): \quad & |\alpha_{j+1} - \alpha_j| \le 1^\circ \quad \forall\ j \in \{2,3,...,N_J - 1\}, \end{aligned} \tag{8.15}$$

in which the cost function is dependent on the relative errors while LB is a to be defined Lower Bound, as presented in Table 8.1. The (six) performed optimizations were variations on the first optimization option *OptA*, with $\frac{1}{2}\left(\text{RMS}_{T_1} + \text{RMS}_{T_2}\right)$ as cost function, using 400 flip angles, a 1/32 undersampling factor, a 10° lower bound and a smoothness constraint. We performed the variations (See Table 8.1) to study the effects of the applied constraints. The first constraint was introduced to restrict the solution space and limit power deposition. The second constraint, on the flip angle difference, promotes a smooth evolution of the transverse magnetization. These constraints were similar to

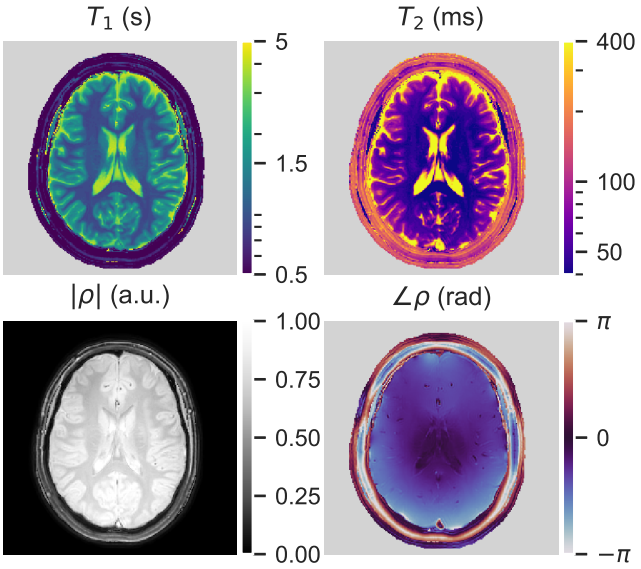

Figure 8.1: Maps of T_1, T_2 and ρ that were used as reference in sequence optimizations for the in-vivo data. Maps were estimated from a previously performed fully sampled 3 T inversion recovery gradient spoiled SSFP MRF acquisition.

[26] A conventionally shaped MRF sequence (See Figure 8.4) was used as initialization in all optimizations.

We solved the optimization problem (8.15) using Sequential Least-Square Quadratic Programming (SLSQP) [200]. This algorithm reformulates the problem by applying a quadratic approximation to the cost function at the current solution. The resulting constrained, quadratic optimization problem is solved based on a linearization of the constraints. Since the problem is non-convex, global convergence is not guaranteed and the algorithm can get stuck in a poor local minimum. However, in initial experiments we did not observe this behavior.

A multi-processor implementation with 8 CPUs (Intel E5-2683 CPU) was used to compute the different gradient steps in the SLSQP algorithm. This resulted in calculation times of approximately 32 hours per complete sequence optimization during which 400 parameters were optimized.

Our optimized sequences were compared to a state-of-the-art optimization method based on the Cramér-Rao lower bound (CRB) [26]. The CRB is a theoretical lower bound on the variance of any unbiased estimator of parameters assuming stochastic noise. The normalized CRB for a single tissue voxel was calculated as $\text{nCRB}(\theta_p) = \sqrt{\frac{\rho^2 \text{CRB}(\theta_p)}{\theta_p^2 \sigma^2}}$ for tissue parameter θ_p, where ρ is the steady state magnetization and σ^2 is the variance of the stochastic noise. Using the SLSQP solver, a sequence with minimal nCRB for an a priori defined set of tissues was obtained. Two single tissue signals with representative values for white and gray matter in the brain were chosen for the optimization, i.e.

Table 8.1: Settings for the optimizations as performed in this study.

Name	Cost function	Sequence length (N_J) i.e. #optimization parameters	Undersampling factor	Readouts	Lower Bound constraint ①	Smoothness constraint ②
Optimization A (*OptA*)	$\frac{1}{2}(\mathrm{RMS}_{T_1} + \mathrm{RMS}_{T_2})$	400	1/32	400	10°	✓
Optimization B (*OptB*)	$\frac{1}{2}(\mathrm{RMS}_{T_1} + \mathrm{RMS}_{T_2})$	400	3/32	1200	10°	✓
Optimization C (*OptC*)	$\frac{1}{2}(\mathrm{RMS}_{T_1} + \mathrm{RMS}_{T_2})$	200	2/32	400	10°	✓
Optimization D (*OptD*)	$\frac{1}{2}(\mathrm{RMS}_{T_1} + \mathrm{RMS}_{T_2})$	400	1/32	400	0°	✓
Optimization E (*OptE*)	$\frac{1}{2}(\mathrm{RMS}_{T_1} + \mathrm{RMS}_{T_2})$	400	1/32	400	10°	×
Optimization F (*OptF*)	RMS_{T_2}	400	1/32	400	10°	✓

$(T_1, T_2) = (700\,\mathrm{ms}, 60\,\mathrm{ms}), (1100\,\mathrm{ms}, 100\,\mathrm{ms})$ from [26], while the constraints of *OptA* (See Table 8.1) were used. The normalized CRB values were also calculated for the optimized sequences as previously proposed (*OptA-F*). For this purpose, 1000 T_1 and T_2 combinations were randomly drawn from the reference maps as shown in Figure 8.1.

8.3.2. NUMERICAL EXPERIMENTS

A numerical checkerboard phantom was used for validation of the error model and our optimization strategy. Furthermore, it was used to study the effect of spatial variations in the signal phase, which was modeled as a time-wise constant complex phase term, while applying a conventionally shaped FA-pattern (See Figure 8.4). The MRF-undersampling model proposed by Stolk and Sbrizzi [196] was validated by comparison to brute force simulations. They consisted of EPG simulations, subsequently Fourier transformation, undersampling and then inverse (non uniform) Fourier transformed image formation, after which parameter estimates were obtained via dictionary matching. The efficacy of our optimization strategy was tested using the numerical phantom as reference map and with constraints as for *OptA* (See Table 8.1).

8.3.3. IN VIVO EXPERIMENTS

In vivo brain scans were acquired on a 3 T Philips Ingenia (Philips, Best, The Netherlands) from 8 healthy subjects to compare the performance of the different MRF sequences. This study was approved by the local medical ethics committee and from all volunteers informed consent was obtained prior to image acquisition. Subjects were instructed to move as little as possible during the entire scan session.

In each subject, the conventional sequence (*Conv*), *OptA*, and the CRB optimized sequence were all acquired with the undersampling factors 1/32, 3/32 and 32/32 (fully sampled). These fully sampled acquisitions essentially resulted in three reference maps for each subject. Sequence *OptB* was acquired with an undersampling factor of 3/32, *OptC* with 2/32 and *OptD-F* with 1/32. A delay time of 6 s was used between repetitions of the same flip angle patterns. Two slices were acquired with a 2 cm slice gap of which the lower slice was positioned to intersect the ventricles, similar to Figure 8.1. The field of view was 224 mm × 224 mm mm^2 with a resolution of 1 mm × 1 mm and 5 mm slice

thickness.

A dictionary was calculated for each flip angle pattern with T_1 values ranging from 150 ms to 5 s and T_2 values from 30 ms to 1 s both applying a step size of 3 %. Dictionary matching was performed to obtain ρ, T_1 and T_2 estimates. To minimize errors due to slight motion, the fully sampled reference scans and undersampled scans were rigidly registered based on the T_1 maps using the mutual information metric [201]. After registration, voxel-wise relative error maps $\mathbf{r}_{1,2}$ (8.13) were computed for each undersampled acquisition based on the three different fully sampled reference series. From the parameter maps brain tissue was segmented, using a signal intensity threshold to exclude regions outside the skull and a $T_1 > 1.6$ s threshold to exclude CSF to prevent unpredictable errors due to flow phenomena. From the masked relative error maps, the median absolute (relative) error was calculated:

$$\mathrm{MAE}_{\{1,2\}} = \mathrm{median}(|\mathbf{r}_{\{1,2\}}|). \tag{8.16}$$

This was found to be a more robust error measure compared to the RMSE which is sensitive to outliers. Note that the mask applied to calculate the MAE and generate the figures in the Results is different from the one applied to calculate the RMSE used for the cost function calculation: the latter merely serves to remove zero-signal voxels.

For each undersampled scan and parameter map, three MAE values were computed corresponding to the three different fully sampled sequences. Presented results were based on the reference scan for which the MAE was minimal. MAE values were compared between sequences with an equal number of readouts (i.e. flip angle train length × number of repeats). A Wilcoxon signed-rank test was performed to compare MAE values of the conventionally shaped flip angle pattern, CRB optimized and undersampling optimized sequences. A P-value < 0.05 was considered to indicate a significant difference.

8

8.4. RESULTS

8.4.1. NUMERICAL EXPERIMENTS

To validate the used error model and test the dependency on spatial variations in signal phase, the relative errors predicted by the model were compared to brute force validation simulations, as shown in Figure 8.2. Notice that the model predictions closely resemble the maps from the simulations; additionally an increasing error with larger 'phase deformation' (left to right) can be observed. The T_1 error maps showed a similar outcome (see Supporting Information, Figure S8.1).

Error maps for T_2 estimation, reflecting the terms from (8.1) before and after optimization are shown in Figure 8.3. Observe that the individual $\mathscr{E}_1$ and $\mathscr{E}_2$ error terms are effectively minimized and that the remaining total relative error is dominated by the PSF error (as the latter error can be mitigated only by the use of a different undersampling scheme). Also, note that the $\mathscr{E}_1$ error before optimization does not show the spatial checkerboard-like variation, which is visible in the $\mathscr{E}_2$ error (See (8.1)).

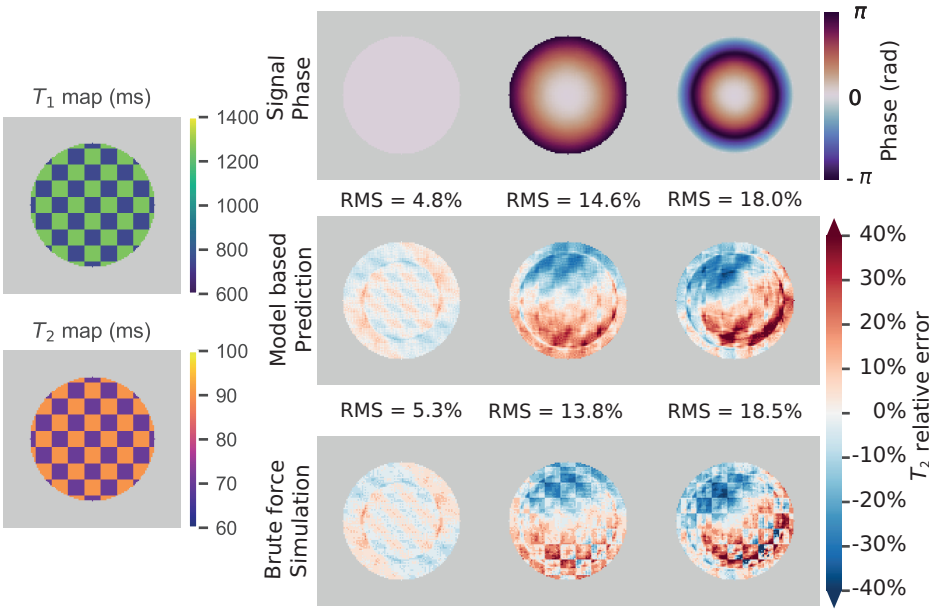

Figure 8.2: Comparison of relative errors in T_2 value predicted by the model (center row) and those obtained in brute force simulation (bottom row) for different signal phase distortions (top row). The numerical phantom with the checkerboard pattern is shown in the left column.

8.4.2. OPTIMIZATION RESULTS

Figure 8.4 shows the conventional flip angle train, the flip angle train resulting from CRB optimization and those obtained after optimization of each sequence option with our approach using in vivo reference maps (See Figure 8.1). All optimized sequences begin with a 180° pulse, although this was a free parameter in the optimization. After the initial 180° pulse, each optimized sequence starts with the smallest flip angle (0° or 10°). Subsequently, they exhibit a gradual increase in flip angle (albeit varying across the sequences), except for *OptE*.

Distributions of nCRB values, per definition without taking into account undersampling artifacts, for the different flip angle trains are shown in Figure 8.5. These were computed for a selection of 1000 T_1 and T_2 values sampled from the reference brain (see Supporting Information, Figure S8.2 for the distribution of these values). The CRB optimized flip angle pattern had the lowest combined mean nCRB (nCRB-T_1 = 1.37 ± 0.16, nCRB-T_2 = 1.69 ± 0.19). However, mean nCRBs of both patterns *OptA* (nCRB-T_1 = 1.40 ± 0.14, nCRB-T_2 = 1.83 ± 0.23) and *OptB* (nCRB-T_1 = 1.38 ± 0.13, nCRB-T_2 = 1.82 ± 0.22) were very similar.

8.4.3. IN VIVO EXPERIMENTS

Figure 8.6 shows the relative error maps for one subject for sequences with 400 readouts (see Supporting Information, Figure S8.3 for two other subjects). Specifically notice that the spatial correlations present with the *Conv* and CRB optimized sequence are miti-

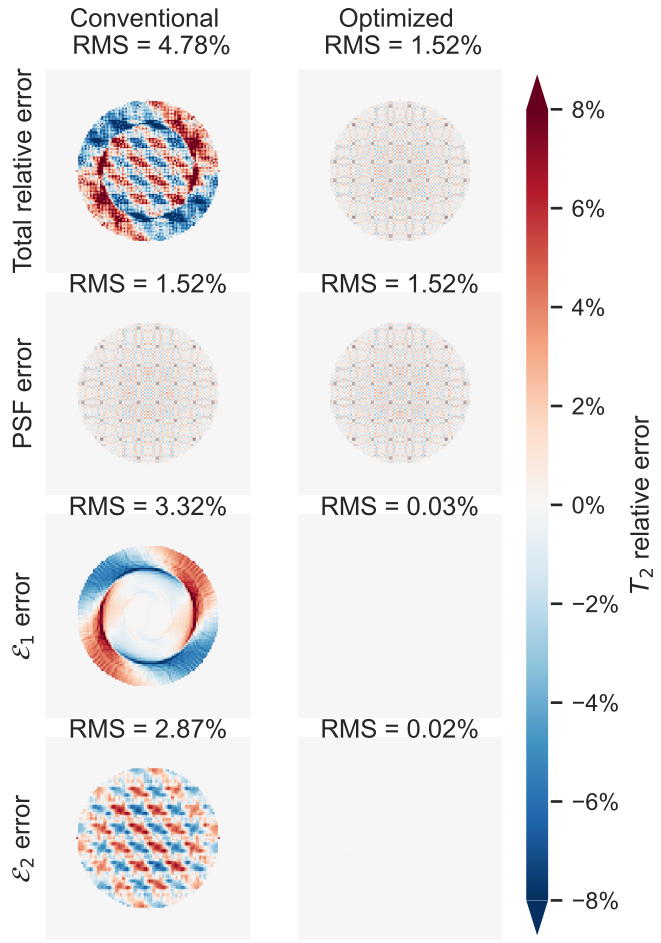

Figure 8.3: Total T_2 undersampling error estimation (upper row) subdivided into the components c.f. (8.1) for the numerical checkerboard phantom with a conventional and optimized flip angle pattern (left and right column respectively); the signal phase was kept spatially constant (left column in Figure 8.2).

gated in *OptA* and *OptD* (both regarding T_1 and T_2), and *OptC* (only for T_1). Notably, the CRB optimized pattern shows an increased error compared to all other sequences. Furthermore, the error maps for the *Conv* and CRB optimized sequence show an asymmetric distribution along the slice. We observed in simulations that these asymmetries rotate with the starting angle of the spiral undersampling pattern, suggesting that this pattern is responsible for the asymmetric distribution.

Figure 8.7 shows the relative error maps for the same subject for acquisitions with 1200 readouts. Observe that the error maps show less variation for 1200 readouts than for 400 readouts, both visually and in terms of the median absolute error.

In Figure 8.8 the model-based error predictions and error maps derived from in vivo acquisitions are depicted. The figure shows results using the sequences *Conv, OptA*

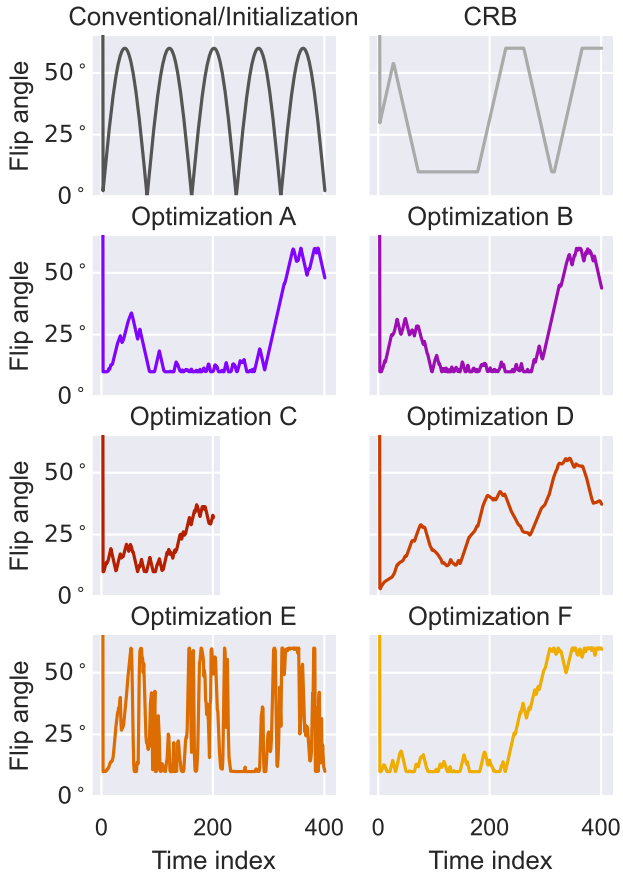

Figure 8.4: Conventional FA train, CRB optimized FA train and FA trains optimized for different MRF sequence options based on the proposed approach. The different constraints used for Optimization A to Optimization F are specified in Table 8.1.

and *CRB*. Observe that for *Conv* and *CRB*, measured and model-based error maps show strong visual similarities and the MAE values are in agreement. However, for *OptA* the undersampling artifacts are mitigated to such an extend that other error sources become dominant in the in vivo scans resulting in a model underestimation of the MAE.

Figure 8.9 shows box plots of MAE values based on the scans of 8 healthy volunteers. The differences between sequences were tested with the Wilcoxon test. The CRB optimized sequence differed significantly ($P < 10^{-3}$) from all other sequences, although this difference was smaller for 1200 readouts. For 400 readouts, the error in sequence *OptA* (MAE-T_1 = 5.6 % ± 2.87 % and MAE-T_2 = 7.9 % ± 2.31 %) was significantly smaller than the conventional (MAE-T_1 = 8.0 % ± 1.92 %, MAE-T_2 = 14.5 % ± 2.65 %) and CRB optimized (MAE-T_1 = 21.6 % ± 4.14 %, MAE-T_2 = 31.4 % ± 4.41 %) sequences.

The differences visually observed in Figure 8.6, 8.7 are confirmed in the median ab-

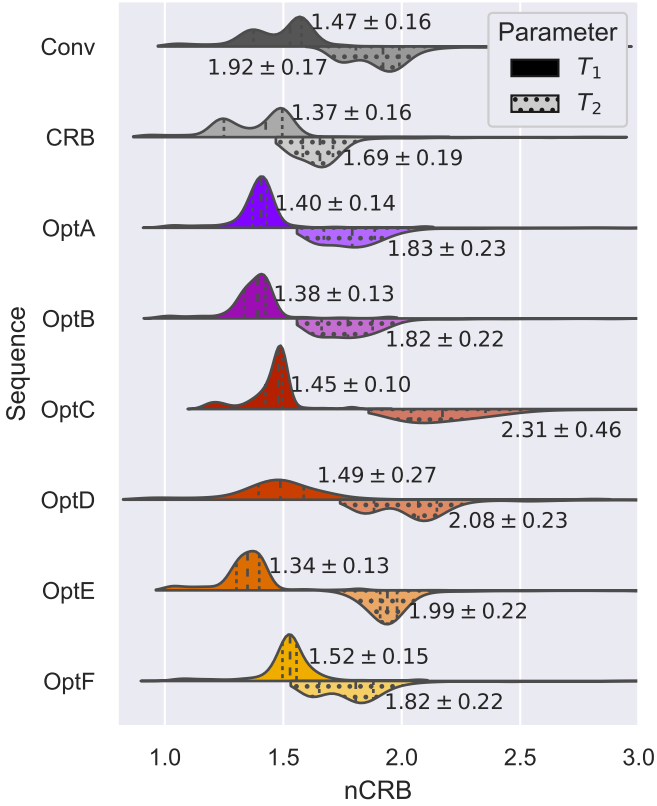

Figure 8.5: Violin plots of normalized Cramér-Rao lower bounds of T_1 and T_2 values (top and bottom of each line, respectively) for the optimized MRF trains shown in Figure 8.4. Normalized CRB values were computed for a selection of 1000 T_1 and T_2 values sampled from the reference brain in Figure 8.1. Values next to each distribution are the mean value and standard deviation.

solute error distributions in Figure 8.9. MAE values were generally smaller for the optimized sequences *OptA*-*OptD* compared to the conventional sequences. The increased number of readouts (1200) resulted in a decrease in MAE for all sequences, but the significant difference between *Conv* and *OptA* in T_2 remained. The set of optimization constraints (See Table 8.1) clearly affected the estimated MAE values. Sequence *OptE* (no smoothness constraint) yielded an increased error compared to *OptA* and no significant improvement compared to the *Conv* sequence. *OptF* was not optimized for T_1 and the effect of this can be seen in an increase in T_1-MAE compared to the *Conv* sequence, while the T_2-MAE is significantly smaller.

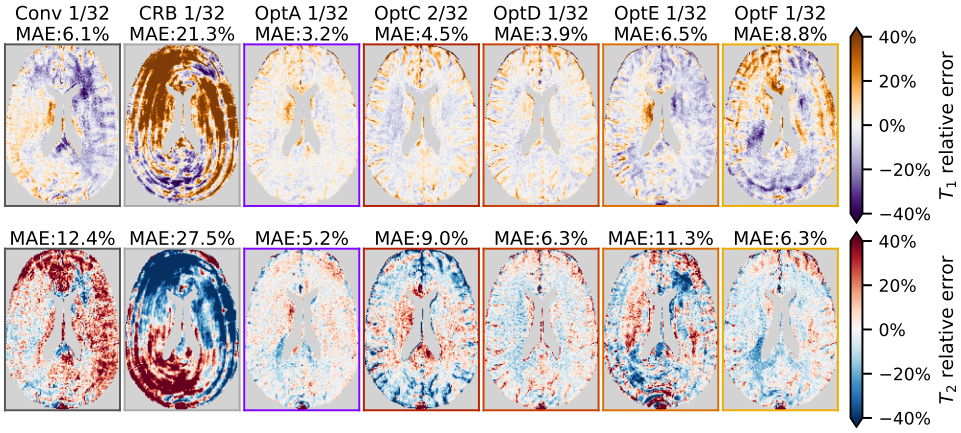

Figure 8.6: In vivo relative error maps for T_1 (top) and T_2 (bottom) in one subject, applying the different flip angle trains with 400 readouts. Above each map the corresponding Median Absolute Error (MAE) is indicated. Notice that the optimized sequences show reduced errors compared to the conventionally shaped and CRB pattern. Observe that *OptF* was not optimized for T_1 which results in large errors in the T_1 map. The colors of the box edges correspond to the colors used in Figures 8.4 and 8.5 and reflect the different sequences.

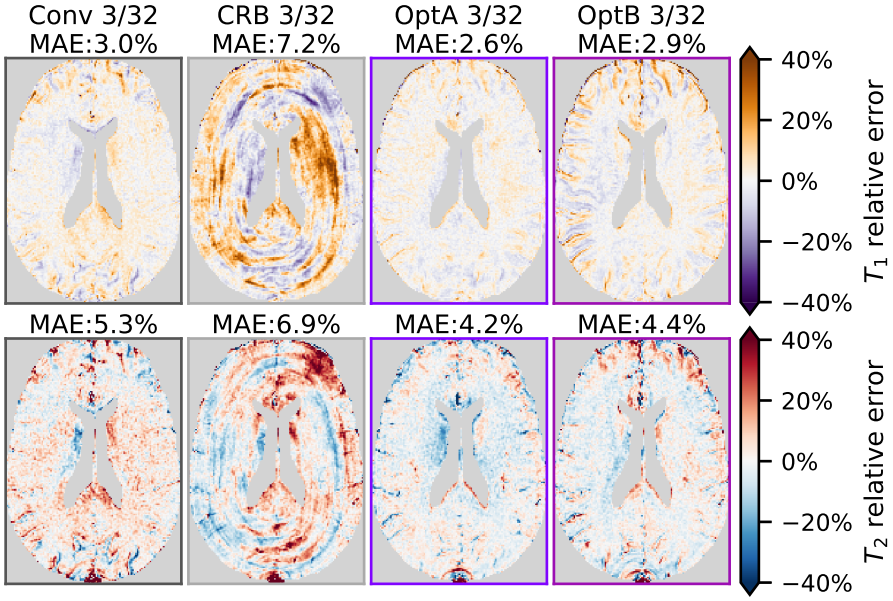

Figure 8.7: In vivo relative error maps for T_1 (top) and T_2 (bottom) in one subject, applying the different optimized flip angle trains with 1200 readouts. Above each map the corresponding Median Absolute Error (MAE) is indicated. The colors of the box edges correspond to the colors used in Figures 8.4 and 8.5 and reflect the different sequences.

8.5. DISCUSSION

We proposed an optimization scheme that mitigates the undersampling error in MRF by adjusting the flip angle train. The proposed optimization applied previ-

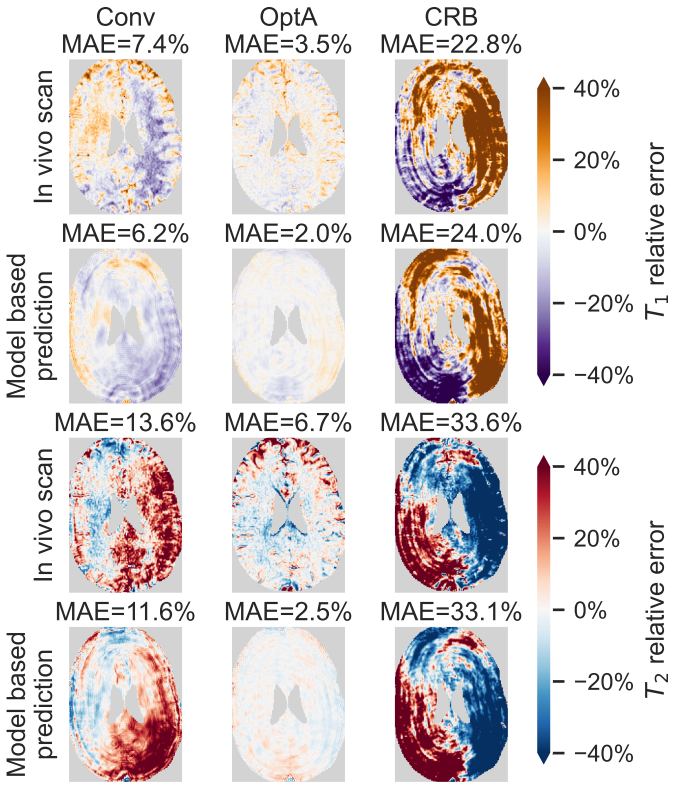

Figure 8.8: Relative error maps measured in vivo (first and third row) and model predictions (second and fourth row) for a healthy subject regarding estimation of T_1 (top two rows) and T_2 (bottom two rows) parameters for different sequences (across columns). The Median Absolute Error (MAE) was computed for the non-masked regions.

ously acquired parameter maps as the reference for optimization. This is the main difference with the work by Jordan et al. [30] where a numerical, discretized phantom was used, opposed to the flexibility of the here presented framework. We studied the effect of different optimization constraints and performed in vivo experiments to verify the effectiveness of our approach.

Initial numerical experiments (See Figure 8.2, 8.3) demonstrated the effect of the signal phase on the undersampling error and how the adopted undersampling model [196] can be exploited to predict and minimize this error. The ability to correctly predict the MAE and relative error maps was further validated in in vivo scans for different sequences (Figure 8.8). The predicted and observed error maps were most similar when undersampling artifacts are the dominant source of error (sequences *Conv*, *CRB*). After the optimization, others error sources, such as thermal noise or misregistration, become dominant so that the error predictions do not match the in vivo results anymore (c.f. sequence *OptA*).

The in vivo experiments concerned optimizations based on a single in vivo refer-

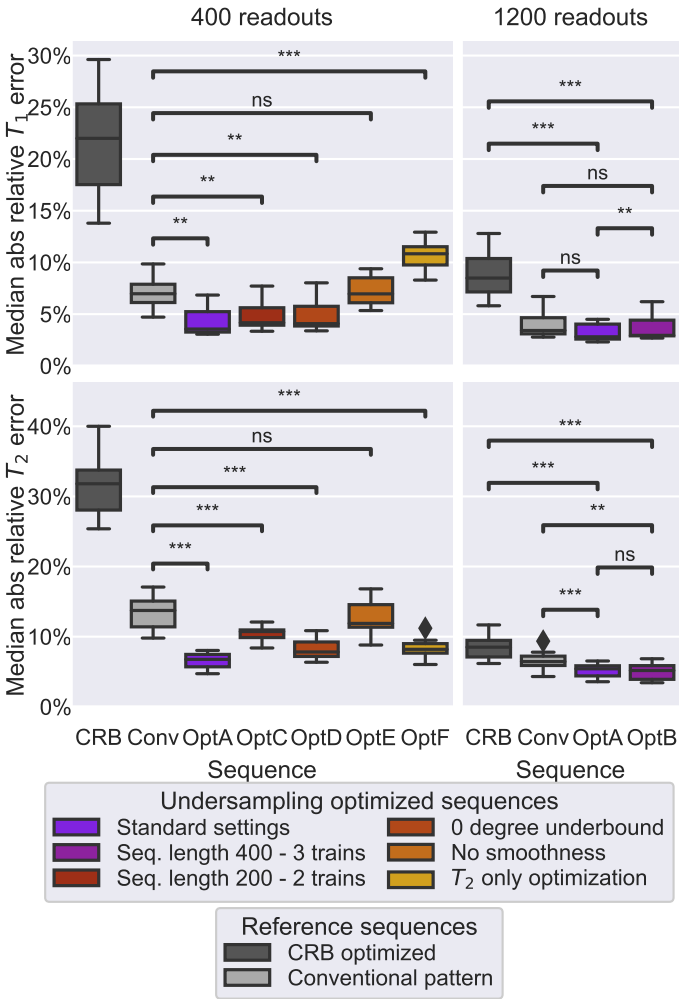

Figure 8.9: Comparison between reference sequences (gray) and sequences optimized for undersampling regarding the median absolute relative T_1 and T_2 error in scans of 8 healthy subjects. Almost all sequences optimized for undersampling differ significantly from the reference sequences for the shortest scan time (400 readouts). A Wilcoxon signed-rank test was used to compare the distribution of MAE-values. The annotations point out noteworthy comparisons: ns indicates non-significance; *: $0.01 < P \leq 0.05$; **: $0.001 < P \leq 0.01$; ***: $10^{-4} < P \leq 0.001$; ****: $P < 10^{-4}$.

ence map (See Figure 8.1) while a range of constraints was applied (See Table 8.1). The optimization showed to be effective for different parts of the brain (See Figure 8.9, Supporting Information, Figure S8.3), indicating that it is robust to differences between regions of interest. We only optimized and evaluated our method for T_1 and T_2 since we considered these parameters the most relevant for clinical use. The settings as used for *OptA* were chosen similar to [26] Although the CRB pattern and the sequence options A-F show similarities (e.g. low FAs around index 150 and peak at the end), taking the un-

dersampling into account in the optimization had a significant effect on the error (See Figure 8.9). The poor performance of the CRB optimized sequence points out that optimization for such a presumed fully sampled signal is not always effective when undersampling is used in the acquisition. The settings for *OptA* were used as a starting point for the sequence variations *OptB* to *OptF*.

Sequence *OptB* was designed with three repeats of the same flip angle train, resulting in 1200 readouts. The resulting flip angle pattern only showed small differences with *OptA*. Also, the differences in mean absolute error in the in vivo experiments were not significant. Based on this we conclude that an increased number of repetitions does not need to be taken into account in the flip angle pattern optimization.

In sequence *OptC* the sequence length was reduced to 200 flip angles and this sequence was repeated twice after a repetition delay of 6 s. As such two inversion pulses are applied, potentially enhancing T_1 sensitivity. The computed nCRBs (Figure 8.5) and in vivo errors (Figure 8.7 and Figure 8.9) show that the shorter sequence length mainly affected the T_2 estimation: the nCRB increased and the T_2-MAE was significantly higher compared to *OptA*. Therefore, a longer flip angle train with less repetition (and less inversion pulses) would be preferred over a shorter sequence to improve T_2 accuracy and avoid the need of a repetition delay time of several seconds.

The lower bound of 10° was reduced to 0° for sequence *OptD* resulting in a flip angle pattern that started at 0° after the inversion pulse. The optimized sequence showed a step wise increasing pattern, which is seemingly smoother than the other patterns. Compared to *OptA* an increased T_2-nCRB was found (See Figure 8.5). The T_2-MAE of *OptD* showed a small increase in error compared to *OptA*, although the difference was not significant. As such both options seem viable.

Sequence *OptE* did not include a smoothness constraint, resulting in stronger variations. While reducing a potential bias, leaving out a constraint comes with an increased risk of getting trapped in a poor local minimum during optimization or overfitting. Another potential source of error is the increased sensitivity to B_1^+ inhomogeneities that is associated with a rapidly varying flip angle train [202]. This may explain the higher MAE (See Figure 8.9) compared to other undersampling optimized sequences and the insignificant difference with the conventional approach.

Only optimizing for T_2 as for *OptF* yielded a high T_1-nCRB and low T_2-nCRB (See Figure 8.5). Simultaneously, *OptF* performed worse for T_1 than the conventional sequence, but T_2 estimations were similar to *OptA*. This indicates that the sequence improved compared to the initialization, but was not able to achieve extra T_2 sensitivity compared to combined optimization. The optimized flip angle pattern (Figure 8.4) shows a clear difference compared to *OptA* in the first 200 time points where all pulses stay low (< 20°). We hypothesize that this difference reduces the T_1 encoding and makes the sequence less appropriate for T_1 estimation.

Based on the performed experiments it may be concluded that the smoothness constraint leads to lower errors; furthermore, a longer sequence is preferred over a shorter sequence with multiple repetitions and inversion pulses (for the here considered combination of 200 and 400 flip angle pulses). The effects of reducing the lower bound on the flip angle were minimal.

The used solver (SLSQP) is prone to find different local minima, but in initial exper-

iments we found that different initializations led to slightly different flip angle patterns with very similar cost. Potentially different optimization schemes could be applied, e.g. simplicial homology global optimization [203], to find a global optimum with respect to a certain reference map or multiple reference maps, but this would be at the cost of increased computation time. We do not consider such optimizations necessary since we do not expect the global minimum to significantly outperform the solutions we found.

A limitation of our approach is that optimizations did not include TR to reduce computation time. By exploiting the use of GPUs and restricting the number of free parameters, e.g using b-spline representations [204], computation time can be further reduced to the order of minutes. This could allow for co-optimization of TR, and potentially further enhance the undersampling robustness of the sequence.

Computation times are also affected by the initialization choice. In particular, initialization close to the optimum will yield a reduction in computation time. A very short computation time might facilitate estimation of the optimized MRF sequences in real time. Thus, optimization could be performed based on selected scan settings, time constraints and specific geometry immediately before an actual scan.

Another limitation is that only 2D acquisitions and one specific undersampling trajectory were considered. The method can be extended to 3D acquisitions in a straightforward manner, although this would, again, lead to computational challenges. The optimization method can also be easily adapted to other k-space trajectories (e.g. radial or variable density spirals), where we expect that these optimizations are especially beneficial with high undersampling factors. A more complicated extension of the proposed model could be the co-optimization of the undersampling trajectory and MRF flip angle train. For such co-optimization, deep learning methods, such as supervised learning, can be of use. For example, a supervised learning framework has been proposed to design MR sequences including RF pulses and gradients for weighted images [205].

Our paper focused on zero-filled nuFFT reconstructions and did not employ low rank reconstruction [61, 148]. The use of the latter could lead to similar improvements in image quality, at the cost of increased reconstruction times. When using improved reconstructions, CRB optimized patterns may still be very effective as was shown previously [26, 27]. Whether the combination of the proposed optimized sequences and more advanced reconstruction schemes can lead to further improvements or mitigates the optimization effects is another subject for further study.

8.6. CONCLUSION

An optimization framework for MRF sequences taking the undersampling pattern into account was proposed and successfully validated in simulations and brain scans in healthy volunteers. The optimized flip angle patterns can mitigate the artifacts from strong undersampling in MRF. In in vivo experiments, the relative errors resulting from our optimized sequences are significantly smaller compared to standard sequence designs. The proposed framework and resulting optimized MRF sequences could be applied in further use of MRF and may reduce the need for improved reconstructions.

8.7. SUPPORTING INFORMATION

The full implementation of the proposed optimization scheme, used reference maps and optimized sequences can be found at https://github.com/imphys/MRF_undersampling_optimization [197].

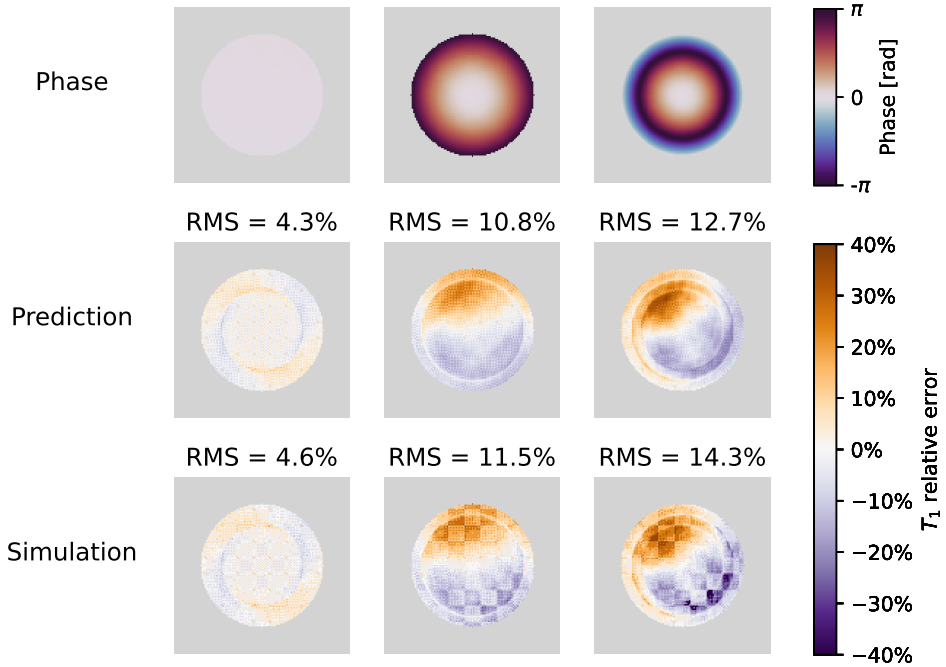

Figure S8.1: Comparison of relative errors in T_1 value predicted by the model (center row) and those obtained in brute force simulation (bottom row) for different signal phase distortions (top row).

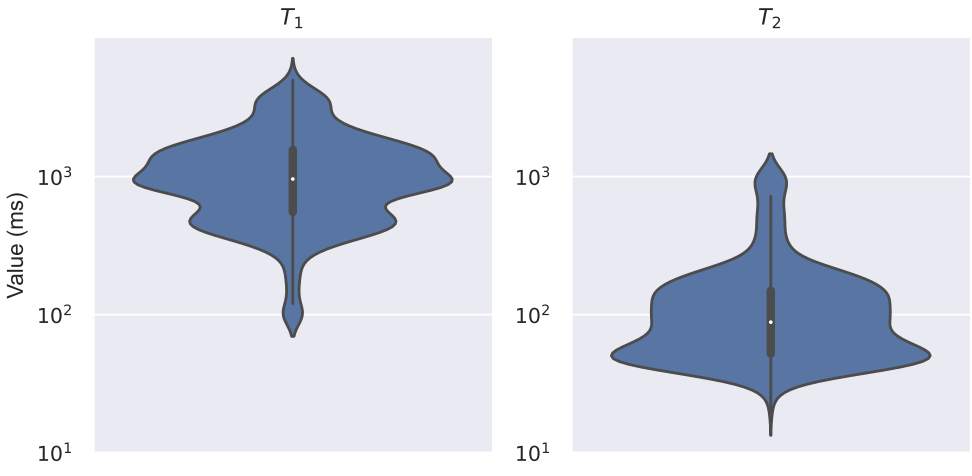

Figure S8.2: Violin plots showing the distribution of T_1 and T_2 values in the (random) selection used for the CRB calculations.

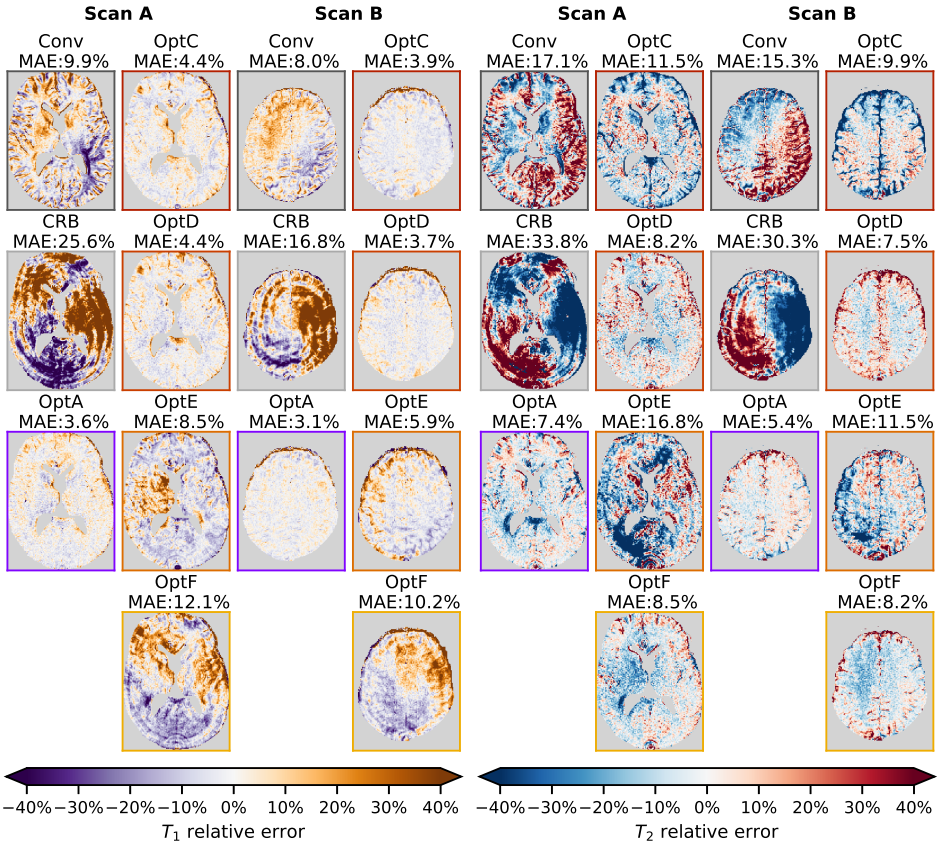

Figure S8.3: In vivo relative error maps for T_1 (left) and T_2 (right) in two different subjects (A,B) applying the different flip angle trains with 400 readouts. Above each map the corresponding Median Absolute Error (MAE) is indicated.

9

Through-plane Motion in Magnetic Resonance Fingerprinting: Simulations and Phantom Experiments

Martijn A. Nagtegaal
Charles McGrath
Christian Günthner
Manuel Baumann

Proc. Intl. Soc. Mag. Reson. Med. 30 (2020). ISMRM. London, 2020

ABSTRACT

Motion can not always be avoided in MR protocols and can therefore cause spatial, blurry artifacts or under- or overestimation in the parameter maps. In plane motion can often be corrected with improved reconstruction methods, but through plane motion in 2D acquisitions is more difficult to compensate. Actually, the primary direction of organ motion for transversal acquisitions in the abdominal region is through-plane. The compensation of such motion is especially challenging for MR Fingerprinting (MRF) because, in general, no information about the spin history of incoming tissue is known. In the present work, we show how to include through-plane motion into the EPG-based signal simulation of MRF and present motion-corrected T_1 and T_2 mapping for a phantom experiment with simplified, one-dimensional through-plane motion.

9.1. INTRODUCTION

MOTION correction for MR Fingerprinting [9] has been applied mostly to (rigid) in-plane motion [32]. A general intrinsic robustness of MRF to through-plane motion has been observed [31], however, the authors also note that simply excluding motion-effected intervals from MRF matching yield strong bias, especially in T_2, depending on the temporal distribution of the motion pattern. Therefore, in this study a method is proposed to simulate through-plane motion effects in EPG simulations for MRF with the goal of improving parameter estimation in cases of such motion by matching against a motion-augmented dictionary.

9.2. METHODS

SIMULATIONS

A slice profile-corrected extended phase graph (EPG) algorithm [112, 206] was implemented as illustrated in Figure 9.1. Slice profiles were obtained using the hard-pulse approximation. To simulate through-plane motion, the EPG-states were moved in the slice direction(z-direction) by a discrete number of steps before each RF-pulse. This enables the simulation of arbitrary motion patterns across time. Simulations were performed with a single T_1 and T_2-combination, assuming homogeneity in the z-direction.

Dictionaries for different motion patterns (see last row in Figure 9.5) were calculated for values of $T_1 = 200 - 1800\,\text{ms}$, $T_2 = 30 - 500\,\text{ms}$ (5 % steps) and $B_1^+ = 90\,\% - 110\,\%$ (1 %-point steps). The RF-shape was discretized in 400 steps. Calculations were performed in Python with Numba JIT compiling to reduce computation time [207]. Simulations on a standard desktop PC took approximately 12 s per dictionary atom.

ACQUISITIONS

MRF acquisitions were performed on a 3 T Philips Achieva MRI (Philips, Best, The Netherlands). Sequence input files were adapted to include an extra parameter to adjust slice positioning for each RF pulse during the sequence separately. A spoiled-SSFP MRF-sequence was used [10]. All scans were performed on the EuroSpin phantom (see Figure 9.2 for reference T_1, T_2 maps), such that movement took place along the direction of the vials, guaranteeing that equal T_1 and T_2 was entering and leaving the slice. All scans

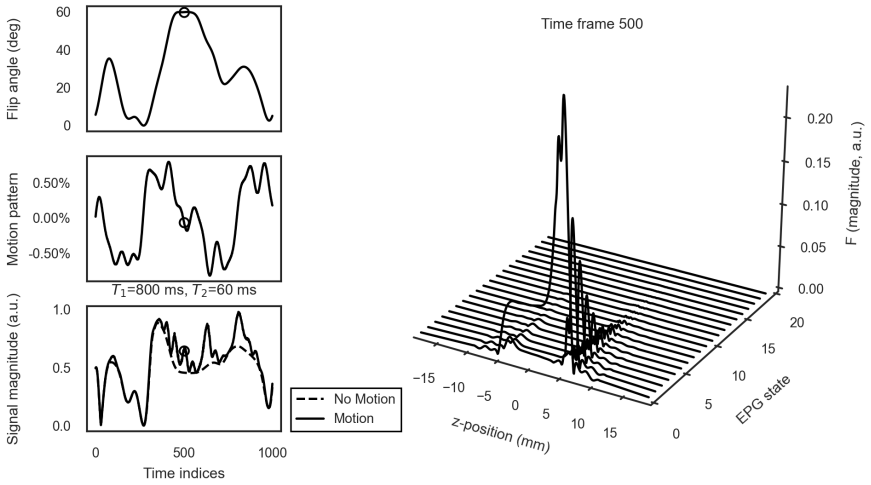

Figure 9.1: (For animation see digital version) Left: MRF flip angle train of length 1000 (top) with a prescribed motion pattern in z-direction (middle) and its effect on a single signal trajectory (bottom). Right: EPG state at varying time points.

were preceded by an adiabatic, non slice-selective inversion pulse.

The following scans were performed:

1. Fully-sampled Cartesian acquisition, sequence length 500 (interpolated version of Figure 9.1) [29]
   (a) Without motion;
   (b) Step-like motion at index no. 250.
2. Undersampled constant-density spiral acquisition (sampling: 1/32), sequence length 1000 (see Figure 9.1) (see Figure 9.4 for motion patterns)
   (a) Without motion;
   (b) Step-like motion at index no. 500;
   (c) Sinusoidal motion with maximum relative amplitude of 80 %;
   (d) Smooth, random-like motion with maximum relative amplitude of 80 %.

A sequence of length 1000 instead of 500 was used for the undersampled data to increase the number of data points. Using several repetitions of the acquisition was considered less realistic, since most motion does not repeat itself with the same period as the flip angle train.

Dictionary matching was performed on the measured data with corrected and uncorrected dictionaries. B_1^+ estimates were obtained by matching Cartesian motion data (1b) to the complete dictionary. B_1^+ was fixed in the remaining matches.

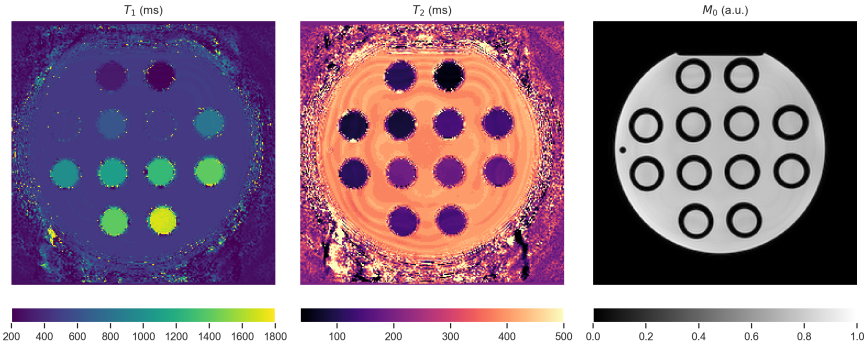

Figure 9.2: Reference T_1, T_2 and M_0 maps from a fully sampled, Cartesian MRF scan for the EuroSpin phantom.

9.3. RESULTS AND DISCUSSION

COMPARISON between simulation and fully sampled Cartesian measurements (Figure 9.3a-b) shows that the effects of through-plane motion can be simulated accurately. Motion leads to strong signal variations, caused by unperturbed longitudinal magnetization entering the slice.

We observed that B_1^+ effects show a strong influence on the effect of sudden motion (see Figure 9.3c), resulting in a B_1^+-dependent phase drift in the transient oscillations. Correction to motion effects could be applied effectively for fully sampled data (see Figure 9.4 and T_2-errors were minimized. In undersampled spiral acquisitions motion resulted in a T_2-overestimation (Figure 9.5), as has been observed before in literature. Errors were more pronounced for longer T_2-times(see Figure 9.2 for comparison). This T_2-error was decreased for sinusoidal and random-like motion by matching with a corrected dictionary. Correction for step-like motion resulted in an increased, spatially heterogeneous error in both T_1 and T_2. We hypothesize that this is caused by the sudden peak in signal and interplay with undersampling artifacts [196], possibly reduced by the use of improved reconstruction methods [61], with an SVD-compression from the corrected dictionary.

The motion simulation makes the simplifying assumption that only the F_0 configuration state is leading to signal (spoiling condition). However, motion also leads to spatial asymmetries in the magnetization response (Figure 9.1), allowing higher-order states to contribute to the signal. This may lead to additional off-resonance dependency of the signal, which was not accounted for here [208].

A limitation of the proposed work is the assumption that the same T_1,T_2-properties leave and enter the slice. However T_2-errors as introduced by motion are often larger than the differences between neighboring tissues, making this simplification justifiable.

Here, we restricted the analysis to motion on the order of the slice thickness. However, motion in free-breathing abdominal imaging can be multiples thereof. One approach is the use of prospective slice-tracking. Our results can be viewed as add-on motion correction accounting for residual relative motion.

In our experiments, the motion pattern was known beforehand, which is in reality not the case. However, estimation of through-plane motion, e.g. through correlation

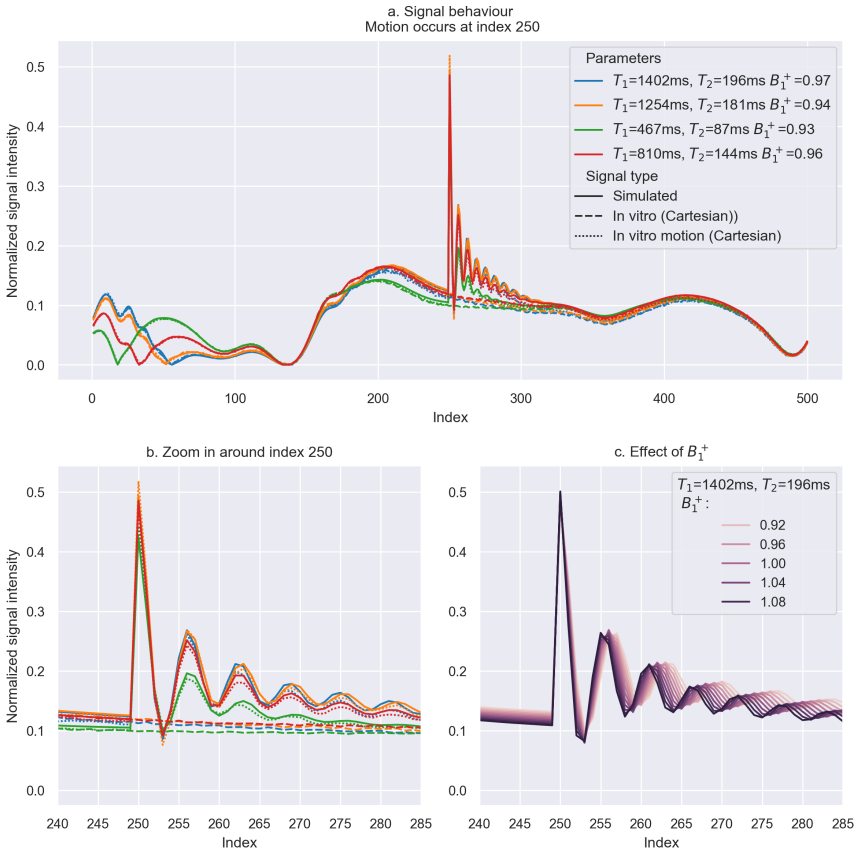

Figure 9.3: Top (a): Effect of motion occurring at index no. 250 for four different T_1/T_2 combinations using a sequence of length 500 [29] (see Figure 9.1) and a fully-sampled Cartesian acquisition. Bottom: Zoomed motion-effected region (left, b) and the effect of varying B_1^+ on the simulated signal trajectories with motion (right c).

with the signal from a respiratory bellow or camera-based tracking system may be possible allowing to augment the dictionary after the scan.

9.4. CONCLUSION

We have shown a method to include through-plane motion into the EPG simulation that leads to improved T_2 results when matching against a motion-augmented MRF dictionary in the absence of additional undersampling effects.

ACKNOWLEDGMENTS

The authors want to thank Kay Nehrke, Gastao Cruz for fruitful discussion and Peter Koken for supplying the base MR Fingerprinting patch. This work originated from the

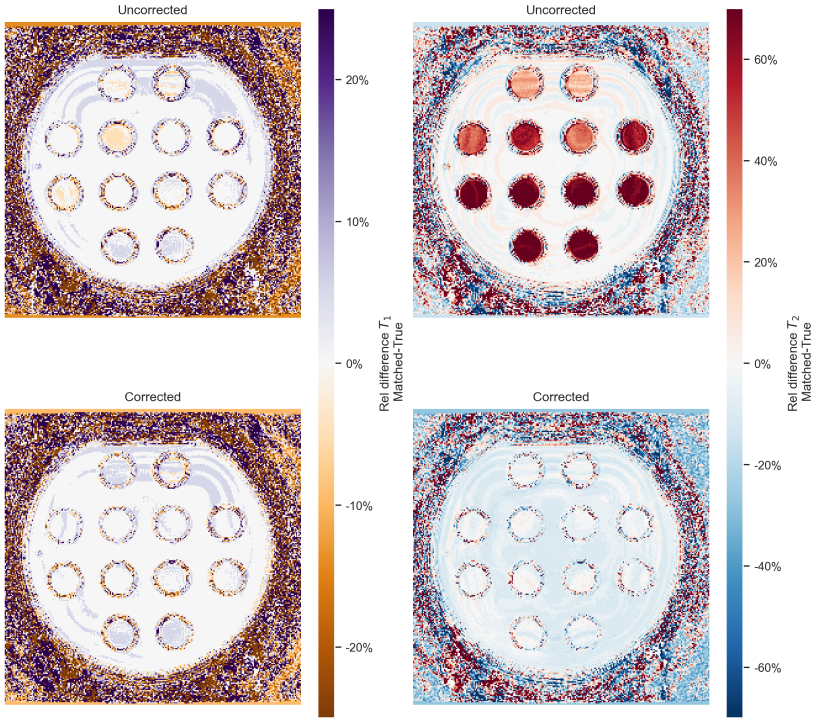

Figure 9.4: Left: Relative difference in T_1 for dictionary matching consisting of (un-)corrected signal trajectories with respect to the ground truth. Right: The respective relative difference in T_2. Controlled motion occurred at the middle of a Cartesian fully-sampled acquisition (as in Figure 9.3).

3rd MR Fingerprinting Workshop at Philips Research Hamburg.

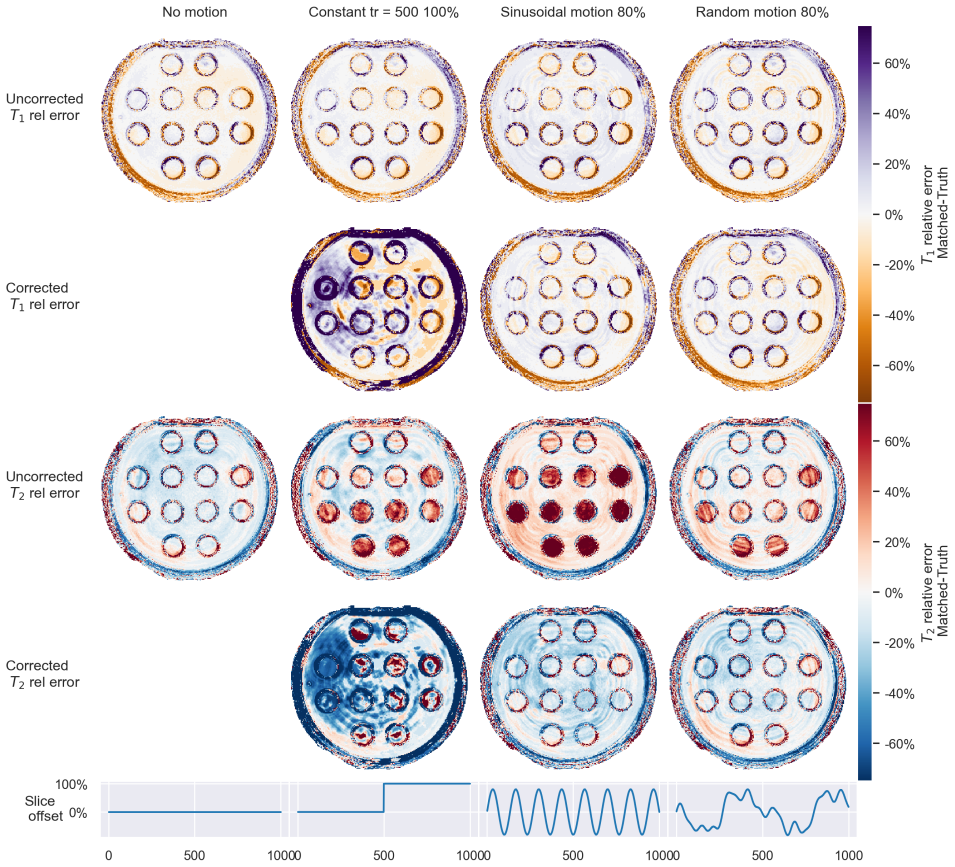

Figure 9.5: Comparison of relative errors in T_1 and T_2 for three different motion patterns (lower row) and single-spiral acquisitions with undersampling factor 32. Matching was performed with dictionaries uncorrected and corrected for the through-plane motion. A sequence of length 1000 was used to increase information contained in the data, were repeated spiral with same motion was considered less realistic.

10

DISCUSSION AND CONCLUSION

10.1. RESEARCH OVERVIEW

THE goal of this thesis was to obtain additional information from acquired signals, reduce parameter estimation errors and limit scan time for quantitative MRI. In particular, it focused on multi-component and multi-parametric estimations based on MR fingerprinting techniques.

In Chapter 2 we introduced a joint sparsity constraint in a multi-component MRF framework. The regularization thus imposed acted on the full image domain instead of taking a more common voxelwise approach. It showed to be very effective in stabilizing the multi-component problem, making it easier to interpret the obtained results by highly reducing the number of non-zero component maps.

As shown in Chapter 3 the proposed SPIJN algorithm from Chapter 2 yielded highly reproducible signal fraction maps for white matter, gray matter and CSF. Furthermore, smaller details were observable compared to maps obtained with conventional, T_1 based approaches, especially in regions with extensive partial volume effects (e.g. the peripheral CSF). Simultaneously, however, we found increased coefficients of variation of the SPIJN-MRF total volume estimations compared to the estimations from standard methods, c.q. from FSL and SPM12.

In Chapter 4 we combined an initial, single component parameter estimation of the B_1^+ field with the multi-component SPIJN approach. This enabled to obtain myelin water fraction (MWF) maps with improved noise robustness and reduced reconstruction time compared to the standard MATLAB NNLS method [114] (minutes versus hours).

To further enhance the acquisition time and reduce noise sensitivity of multi-component estimations we proposed the MC-ADMM and k-SPIJN reconstruction methods in Chapter 5. These methods performed multi-component estimations directly from k-space data. In effect, improved stability of the estimation was especially observed in the myelin water component maps.

In Chapter 6 we applied the proposed multi-component MRF analysis in a clinical cohort of MS patients and healthy controls. We observed a statically significant volume increase of a component with prolonged T_2^* values in the patients compared to the

healthy controls. This volume also correlated significantly with a visual score of damaged white matter regions and therefore may allow quantification of the extent of white matter damage. We also found that it facilitated increased sensitivity to damaged white matter compared to FLAIR scans.

In Chapter 7 we adapted the SPIJN algorithm to be more sensitive to local tissue structures, including abnormalities. This was done by only considering a local, Gaussian weighted region around each voxel, at the cost of an extra tune-able parameter, namely the width of this Gaussian. In EPI-MRF scans of MS patients it enabled to identify distinct tissue components related to lesions.

Subsequently, in Chapter 8 we proposed a method to optimize MRF sequences given a realistic reference map. It optimized the applied flip-angle train given certain acquisition settings such as the FOV, undersampling factor etc. The optimized sequences yielded markedly less undersampling artifacts than those obtained with conventional sequences.

In Chapter 9 we modified the simulations as used for MRF dictionary calculations to simulate the effect of different types of motion during MRF acquisition. The motion changes the spin history of the protons and results in an altered effective signal. In phantom experiments we observed that measurements and simulations were in line. We found that T_2 estimations were more affected by motion than T_1 estimations, which we partly attribute to the use of a non-slice selective inversion pulse.

10.2. RELATIONSHIP TO CURRENT DEVELOPMENTS

IN the course of this thesis project other developments took place in the field of multi-component and multi-parameter quantitative MRI. These developments are in part directly related to work as described in this thesis, but also relevant from a broader perspective as they may open alternative research alleys.

To regularize the multi-component estimation problem we introduced a joint-sparsity regularization in Chapter 2. Since its introduction the method has been adopted in several other works [79, 164]. In particular, SPIJN-MRF was applied in [79] for myelin water fraction mapping in developing children to identify a range of relaxation times per tissue type. In [164] the SPIJN algorithm was combined with an MRF sequence using an increased number of inversion pulses to make the sequence more sensitive to the myelin water component. Recently, Golbabaee and Poon [209] proposed a new algorithm for multi-component MRF based on a SGB-Lasso technique, estimating a small number of components over the full brain, which is comparable to our approach. The latter reference is not employing a dictionary approach, but a neural network. The resulting SPIJN magnetization fraction maps were distinctly different from ours, potentially due to the used regularization. The MC-MRF maps obtained with their method, do show similarities to the results we previously obtained. In recent work for T_2^* based MWF estimation [210], a similar joint-sparsity constraint was introduced resulting in similar improvements in estimated myelin water mapping as we observed in Chapter 4.

In Chapter 4 we translated the methods developed for MRF to MWF-T_2-relaxometry. While we estimated a B_1^+ map from single component matching, [211] applied a B_1^+ map acquired by a conventional method for correction. This has been proposed before in MRF and signifies the overlap between different quantitative MRI approaches. Espe-

cially for MWI based on T_2-relaxometry some further improvements can be observed that may help to enable clinical usability. An example is the use of compressed sensing in these methods [212] and the use of deep learning for faster computation times [138] and/or more accurate image reconstruction. Compressed sensing will allow for reduced acquisition times, at the mere expense of (slightly) increased computation times for image reconstruction and is already widely used. Alternatively, deep learning image reconstruction can also enable reduced acquisition times, but bears the risk of overtraining and/or a lack of training data. To further facilitate clinical use, a reduction of the acquisition time could be found in the use of more efficient spiral trajectories and the use of enhanced reconstruction methods, see e.g. Chapter 5.

Recently a MWF atlas [92] based on MESE-MWF mapping was made available and this can be considered as an important step towards more clinical adaptation, since it offers well documented reference values. Neither for single-component nor for multi-component MRF such an atlas is currently available.

It is known that single-component MRF allows for reproducible and repeatable estimations of T_1 and T_2 relaxation times [82]. Its main strength lies in the high repeatability it offers for longitudinal studies, enabling the identification of relatively small tissue changes over time. Additionally, it offers advantages for the identification of relatively small signal changes, compared to the signal from healthy tissue. In such cases an increased sensitivity over weighted images is to be expected [213]. Still, true clinical adaptation remains uncertain while relaxometry changes only give an indirect measure of tissue alterations and require additional imaging time.

Multi-component MRF provides a more sophisticated way to obtain information about tissue structures. Particularly, it facilitates sub-voxel segmentation of different tissues by obtaining magnetization fractions of each such tissue type. What is more, as demonstrated in Chapter 7 a local-SPIJN multi-component model allows for identification of white matter lesions in MS patients. Recently [23, 24, 213] it was found that partial volume segmentations from MRF imaging based on k-means clustering also allows for identification of lesions in epilepsy patients and different tissue types in brain tumors. The methods from Chapter 7 and the referred papers yield increased numbers of identified components, which makes the outcomes hard to compare to standard multi-component approaches and therefore difficult to verify. Also, the sensitivity to parameters in the algorithms, such as number of k-means clusters or neighborhood size, increases, which makes the methods less stable. To improve generalizability in follow-up research, the sensitivity to used regularization and estimation settings is of importance in future studies.

Some limitations remain regarding the used multi-component model and the choice of specific MRF sequences. While applying a non-negative, linear combination of dictionary atoms no magnetization transfer between components was taken into account by me. It has already been shown, however, that ignoring magnetization transfer effects can lead to potential biases [214] in MC-DESPOT estimations. It is, fortunately, possible to include this in the MRF signal model [215] and effectively define an inverse problem. However, this inverse problem contains more free parameters than in the non-exchange case and will constitute a numerically challenging problem, both with respect to stability and computation time. As a solution Hilbert et al. [216] created a large dictionary

consisting of a subset of these free parameters in a two-pool model, allowing to estimate the fractional pool-size while adopting fixed, previously reported relaxation times for the semi-solid pool. Also, in recent work Assländer et al. [217] were able to estimate the transverse relaxation time of the semi-solid pool. In the latter work sequences were optimized for this purpose based on the Cramér Rao lower bound and parameters were estimated voxel-wise using a neural network [218] to partly overcome the ill-posedness of the estimation problem.

We have seen that most of the different sequences used in Chapters 2, 3 and 5 enabled distinction of myelin water from white matter. A future direction could be the development of MRF sequences that are more sensitive to the shorter relaxation times of myelin water (perhaps by using more inversion pulses [164]), less influenced by magnetization transfer effects than others, or for which a potential bias can be estimated.

Whether future myelin water imaging methods will make use of T_2-MESE based sequences or T_1-T_2 sensitive MRF sequences will depend both on practical issues such as scan time, and proceeding future insight into potential differences between the sequence types and their accuracy and precision. With respect to scan time MRF currently has marked advantages, but the long line of work on MESE sequences, makes it currently a more established candidate.

10.3. FUTURE DIRECTIONS

In my view the main added value of a new quantitative MRI method should be in measuring novel tissue properties and/or enabling clinical adaptation. As such, the concept of estimating the B_1^+ field using a single component estimation, as proposed in Chapter 4, combined with a joint sparsity constraint, can be regarded as more valuable than the achieved, mere reduction in computation time.

Recent work in MRF looked into the possibility to combine MRF $T_1 - T_2$ estimations and diffusion measurements [219]. Such new measurement approaches can allow for improved estimations of tissue parameters, just as the combination of MRF with ASL [73] or allow for correction of potential confounding factors. For diffusion-MRF multi-component models will be relevant for estimations in and around the myelin. In MRF-ASL methods partial volume effects can also be confounding factors, that are sometimes taken into account [220].

In Chapter 3 studying the reproducibility of MC-MRF in healthy, experienced volunteers, motion artifacts were identified in 10 of 40 scans. Although only a relatively small number of slices was affected by this, a full brain volume analysis could not be done, because of the corrupted results in a some slices. Therefore, I think that improved robustness to motion is of more interest for clinical practice than an improved noise robustness. By providing a model including the effects of different motion patterns, as in Chapter 9, more insight into the effects of through-plane motion can be obtained. However, this will not enable full compensation to motion, since in-plane motion will need to be corrected for as well. I expect that for clinical applications of MRF encompassing full brain coverage, motion correction methods will be required. Such correction based on (self-)navigators (e.g. [86]) with retrospective correction for 3D acquisitions is a first possibility. However, this will result in increased computation complexity and a slight increase in acquisition time. A second option could be a 2D acquisition with on-the-

fly detection of motion corrupted slices enabling a new acquisition of the specific slices when necessary.

In Chapter 6 we made a step towards potential clinical use of a multi-component MRF protocol. Particularly we observed that a distinct MRF component could be related to white matter damage. As such, this may provide a way to quantify tissue changes with improved sensitivity compared to contrast weighted scans. In previous MESE T_2 based work [132] components with prolonged T_2 were observed as well, but this did not lead to clinical application. Potentially the combination of improved acquisition and reconstruction techniques will enable further insight into white matter damage as signified by appearance of white matter T_2-hyperintensities or dirty appearing white matter. For true practical assessment of damaged white matter tissue a better biophysical understanding of my results and validation in MRF sequences sensitive to T_2 instead of T_2^* are essential.

Although important progress was made in MRF technology since its proposal, I believe several further steps are needed to support clinical use. A remaining hurdle is in the translation from proposals of advanced techniques in papers to use in follow-up studies. In publications these advanced methods show their potential to aid clinical interpretation, but only few of the published papers on MRF include a thorough description of the proposed methods by publishing the developed code. Practicing open science by publishing code, sharing protocols where possible and publishing FAIR (Findable, Accessible, Interoperable, Reusable) data will help the adoption and enable improvement of proposed methods. For the manuscripts included in this thesis I have made code available whenever possible. More important and probably more problematic is the difficulty that lies in sharing the exact details of programmed MR sequences, especially between different vendors, resulting in challenges regarding both reproducibility and transparency. Especially the workload that comes with attempting to reproduce the current state-of-the-art pulse sequences in my opinion hinders further development. Fortunately, I currently see a movement in research, aiming to improve this, e.g. by the development of open pulse programming frameworks [221–223] and the use of vendor-independent sequences for quantitative MRI [224].

On a critical note, MRF has not shown to be the "killer" application that makes it commercially interesting for vendors and scientifically attractive for (clinical) research sites to invest (more) time and resources. Recent examples of successful technological introductions adopted by clinicians are compressed sensing and diffusion weighted imaging. Compressed sensing [225] showed to be an efficient way to reduce scan time, while maintaining image quality and is currently becoming standard on clinical MR systems. Likewise, diffusion weighted imaging has shown to be a important source of information to study the brain, e.g. it enables the detection of lesions in stroke patients [226]. For the compressed sensing example reduced scan time proved a game changing property, while for diffusion weighted image the uniqueness of obtained information was pivotal.

MRF enables the acquisition of highly reproducible quantitative maps at low scan times. Counter-intuitively, MRF might have a big impact on qualitative imaging when it is used to create synthetic weighted images, allowing for more flexibility in the obtained contrasts and reducing scan time since only one acquisition is required. Such synthetic,

weighted images could neatly fit in the clinical workflow, but requires that the quality is as good as or better than currently used FLAIR, T_1- and T_2-weighted images. The obtained quantitative maps could also be used for volumetric measurements, potentially reducing inter-scanner variation due to the quantitative nature of the used maps. However, T_1 and T_2 are rather general magnetization properties. I therefore expect that clinical, pivotal applications of MRF are not to be found solely in T_1 and T_2 maps, but will require a more direct measure of (pathological) changes within tissues as I touched upon in Chapter 6.

10.4. CONCLUSION

THROUGH the research described in this thesis I have created methods with which more information from MR images can be obtained than is visible at first sight, as I demonstrated with the myelin water maps and in visualizing affected white matter regions. I especially worked on multi-component models, providing a brighter glimpse of the complex structure that the brain is. My sincere hope is that the developed methods further expand the versatility of quantitative MRI and will spark new developments and applications of MRF and other MR techniques.

BIBLIOGRAPHY

[1] Lorenzo Pini et al. “Brain atrophy in Alzheimers Disease and aging”. In: *Ageing Research Reviews* 30 (Sept. 2016), pp. 25–48. ISSN: 15681637. DOI: 10.1016/j.arr.2016.01.002.

[2] Sean Deoni. “Chapter 1 - Biophysical and Physiological Principles of T1 and T2”. In: *Advances in Magnetic Resonance Technology and Applications*. Ed. by Nicole Seiberlich et al. Vol. 1. Quantitative Magnetic Resonance Imaging. Academic Press, Jan. 1, 2020, pp. 3–17. DOI: 10.1016/B978-0-12-817057-1.00003-2.

[3] Hai-Ling Margaret Cheng et al. “Practical medical applications of quantitative MR relaxometry”. In: *Journal of Magnetic Resonance Imaging* 36.4 (2012), pp. 805–824. ISSN: 1522-2586. DOI: 10.1002/jmri.23718.

[4] Sara Dastmalchian et al. “Radiomic analysis of magnetic resonance fingerprinting in adult brain tumors”. In: *European Journal of Nuclear Medicine and Molecular Imaging* (Sept. 26, 2020). ISSN: 1619-7089. DOI: 10.1007/s00259-020-05037-w.

[5] Robert W. Brown et al., eds. *Magnetic Resonance Imaging: Physical Principles and Sequence Design*. Chichester, UK: John Wiley & Sons Ltd, Apr. 22, 2014. ISBN: 978-1-118-63395-3. DOI: 10.1002/9781118633953.

[6] Mark A. Griswold et al. “Generalized autocalibrating partially parallel acquisitions (GRAPPA)”. In: *Magnetic Resonance in Medicine* 47.6 (2002), pp. 1202–1210. ISSN: 1522-2594. DOI: 10.1002/mrm.10171.

[7] Klaas P. Pruessmann et al. “SENSE: Sensitivity encoding for fast MRI”. In: *Magnetic Resonance in Medicine* 42.5 (1999), pp. 952–962. ISSN: 1522-2594. DOI: 10.1002/(SICI)1522-2594(199911)42:5<952::AID-MRM16>3.0.CO;2-S.

[8] Sean C.L. Deoni. “High-resolution T1 mapping of the brain at 3T with driven equilibrium single pulse observation of T1 with high-speed incorporation of RF field inhomogeneities (DESPOT1-HIFI)”. In: *Journal of Magnetic Resonance Imaging* 26.4 (2007), pp. 1106–1111. ISSN: 1522-2586. DOI: 10.1002/jmri.21130.

[9] Dan Ma et al. “Magnetic resonance fingerprinting”. In: *Nature* 495.7440 (Mar. 2013), pp. 187–192. ISSN: 0028-0836, 1476-4687. DOI: 10.1038/nature11971.

[10] Yun Jiang et al. “MR fingerprinting using fast imaging with steady state precession (FISP) with spiral readout”. In: *Magnetic Resonance in Medicine* 74.6 (2015), pp. 1621–1631. ISSN: 1522-2594. DOI: 10.1002/mrm.25559.

[11] Benedikt Rieger et al. “Magnetic resonance fingerprinting using echo-planar imaging: Joint quantification of T1 and relaxation times”. In: *Magnetic Resonance in Medicine* 78.5 (2017), pp. 1724–1733. ISSN: 1522-2594. DOI: 10.1002/mrm.26561.

[12] Debra F. McGivney et al. “Magnetic resonance fingerprinting review part 2: Technique and directions”. In: *Journal of Magnetic Resonance Imaging* 51.4 (2020), pp. 993–1007. ISSN: 1522-2586. DOI: 10.1002/jmri.26877.

[13] Bhairav Bipin Mehta et al. “Magnetic resonance fingerprinting: a technical review”. In: *Magnetic Resonance in Medicine* (Sept. 14, 2018). ISSN: 07403194. DOI: 10.1002/mrm.27403.

[14] Mark Jenkinson et al. “FSL”. In: *NeuroImage*. 20 YEARS OF fMRI 62.2 (Aug. 15, 2012), pp. 782–790. ISSN: 1053-8119. DOI: 10.1016/j.neuroimage.2011.09.015.

[15] John Ashburner. “A fast diffeomorphic image registration algorithm”. In: *NeuroImage* 38.1 (Oct. 15, 2007), pp. 95–113. ISSN: 1053-8119. DOI: 10.1016/j.neuroimage.2007.07.007.

[16] Eva Alonso-Ortiz, Ives R. Levesque, and G. Bruce Pike. “MRI-based myelin water imaging: A technical review”. In: *Magnetic Resonance in Medicine* 73.1 (Jan. 1, 2015), pp. 70–81. ISSN: 1522-2594. DOI: 10.1002/mrm.25198.

[17] Mark D. Does. “Inferring brain tissue composition and microstructure via MR relaxometry”. In: *NeuroImage* (Dec. 2017). ISSN: 10538119. DOI: 10.1016/j.neuroimage.2017.12.087.

[18] Kenneth P. Whittall et al. “In vivo measurement of T2 distributions and water contents in normal human brain”. In: *Magnetic Resonance in Medicine* 37.1 (1997), pp. 34–43. ISSN: 1522-2594. DOI: 10.1002/mrm.1910370107.

[19] Alex Mackay et al. “In vivo visualization of myelin water in brain by magnetic resonance”. In: *Magnetic Resonance in Medicine* 31 (June 1994), pp. 673–677. DOI: 10.1002/mrm.1910310614.

[20] Kathryn L. West et al. “Myelin volume fraction imaging with MRI”. In: *NeuroImage*. Microstructural Imaging 182 (Nov. 15, 2018), pp. 511–521. ISSN: 1053-8119. DOI: 10.1016/j.neuroimage.2016.12.067.

[21] Gian Franco Piredda et al. “Probing myelin content of the human brain with MRI: A review”. In: *Magnetic Resonance in Medicine* 85.2 (2021), pp. 627–652. ISSN: 1522-2594. DOI: 10.1002/mrm.28509.

[22] Sean C. L. Deoni et al. “Gleaning multicomponent T1 and T2 information from steady-state imaging data”. In: *Magnetic Resonance in Medicine* 60.6 (Dec. 1, 2008), pp. 1372–1387. ISSN: 1522-2594. DOI: 10.1002/mrm.21704.

[23] Dan Ma et al. “Development of high-resolution 3D MR fingerprinting for detection and characterization of epileptic lesions”. In: *Journal of Magnetic Resonance Imaging* 49.5 (2019), pp. 1333–1346. ISSN: 1522-2586. DOI: 10.1002/jmri.26319.

[24] Anagha Deshmane et al. “Partial volume mapping using magnetic resonance fingerprinting”. In: *NMR in Biomedicine* 32.5 (May 2019), e4082. ISSN: 0952-3480, 1099-1492. DOI: 10.1002/nbm.4082.

[25] Debra McGivney et al. “Bayesian estimation of multicomponent relaxation parameters in magnetic resonance fingerprinting: Bayesian MRF”. In: *Magnetic Resonance in Medicine* (Nov. 20, 2017). ISSN: 07403194. DOI: 10.1002/mrm.27017.

[26] B. Zhao et al. “Optimal Experiment Design for Magnetic Resonance Fingerprinting: Cramér-Rao Bound Meets Spin Dynamics”. In: *IEEE Transactions on Medical Imaging* 38.3 (Mar. 2019), pp. 844–861. ISSN: 0278-0062. DOI: 10.1109/TMI.2018.2873704.

[27] Jakob Assländer et al. “Optimized quantification of spin relaxation times in the hybrid state”. In: *Magnetic Resonance in Medicine* 82.4 (2019), pp. 1385–1397. ISSN: 1522-2594. DOI: 10.1002/mrm.27819.

[28] Ouri Cohen and Matthew S. Rosen. “Algorithm comparison for schedule optimization in MR fingerprinting”. In: *Magnetic Resonance Imaging* 41 (Sept. 1, 2017), pp. 15–21. ISSN: 0730-725X. DOI: 10.1016/j.mri.2017.02.010.

[29] K. Sommer et al. “Towards predicting the encoding capability of MR fingerprinting sequences”. In: *Magnetic Resonance Imaging* 41 (Sept. 1, 2017), pp. 7–14. ISSN: 0730-725X. DOI: 10.1016/j.mri.2017.06.015.

[30] Stephen P. Jordan et al. “Automated design of pulse sequences for magnetic resonance fingerprinting using physics-inspired optimization”. In: *Proceedings of the National Academy of Sciences* 118.40 (Oct. 5, 2021), e2020516118. DOI: 10.1073/pnas.2020516118.

[31] Zidan Yu et al. “Exploring the sensitivity of magnetic resonance fingerprinting to motion”. In: *Magnetic Resonance Imaging* 54 (Dec. 1, 2018), pp. 241–248. ISSN: 0730-725X. DOI: 10.1016/j.mri.2018.09.002.

[32] Gastão Cruz et al. “Rigid motion-corrected magnetic resonance fingerprinting”. In: *Magnetic Resonance in Medicine* 81.2 (2019), pp. 947–961. ISSN: 1522-2594. DOI: 10.1002/mrm.27448.

[33] Jussi Tohka. “Partial volume effect modeling for segmentation and tissue classification of brain magnetic resonance images: A review”. In: *World Journal of Radiology* 6.11 (Nov. 28, 2014), pp. 855–864. ISSN: 1949-8470. DOI: 10.4329/wjr.v6.i11.855.

[34] Kenneth P Whittall and Alexander L MacKay. “Quantitative interpretation of NMR relaxation data”. In: *Journal of Magnetic Resonance* 84.1 (Aug. 1989), pp. 134–152. ISSN: 00222364. DOI: 10.1016/0022-2364(89)90011-5.

[35] Charles L. Lawson and Richard J. Hanson. *Solving least squares problems*. SIAM, 1974. 337 pp. ISBN: 978-0-89871-356-5.

[36] Sunli Tang et al. “Multicompartment magnetic resonance fingerprinting”. In: *Inverse Problems* 34.9 (Sept. 1, 2018), p. 094005. ISSN: 0266-5611, 1361-6420. DOI: 10.1088/1361-6420/aad1c3.

[37] Roberto Duarte et al. “Greedy Approximate Projection for Magnetic Resonance Fingerprinting with Partial Volumes”. In: *arXiv:1807.06912 [eess]* (July 18, 2018). DOI: 10.48550/arXiv.1807.06912.

[38] Daeun Kim et al. “Relaxation-Relaxation Correlation Spectroscopic Imaging (RR-CSI): Leveraging the Blessings of Dimensionality to Map In Vivo Microstructure”. In: *arXiv:1806.05752 [eess]* (June 14, 2018). DOI: 10.48550/arXiv.1806.05752.

[39] Dosik Hwang and Yiping P. Du. “Improved myelin water quantification using spatially regularized non-negative least squares algorithm”. In: *Journal of Magnetic Resonance Imaging* 30.1 (June 25, 2009), pp. 203–208. ISSN: 1522-2586. DOI: 10.1002/jmri.21783.

[40] Dushyant Kumar et al. “Noise robust spatially regularized myelin water fraction mapping with the intrinsic B1-error correction based on the linearized version of the extended phase graph model”. In: *Journal of Magnetic Resonance Imaging* 43.4 (Apr. 1, 2016), pp. 800–817. ISSN: 1522-2586. DOI: 10.1002/jmri.25078.

[41] Dushyant Kumar et al. “Using 3D spatial correlations to improve the noise robustness of multi component analysis of 3D multi echo quantitative T2 relaxometry data”. In: *NeuroImage* 178 (Dec. 5, 2018), pp. 583–601. ISSN: 10538119. DOI: 10.1016/j.neuroimage.2018.05.026.

[42] Daeun Kim and Justin P. Haldar. “Greedy algorithms for nonnegativity-constrained simultaneous sparse recovery”. In: *Signal Processing* 125 (Aug. 1, 2016), pp. 274–289. ISSN: 0165-1684. DOI: 10.1016/j.sigpro.2016.01.021.

[43] D. F. McGivney et al. “SVD Compression for Magnetic Resonance Fingerprinting in the Time Domain”. In: *IEEE Transactions on Medical Imaging* 33.12 (Dec. 2014), pp. 2311–2322. ISSN: 0278-0062. DOI: 10.1109/TMI.2014.2337321.

[44] Y. C. Pati, R. Rezaiifar, and P. S. Krishnaprasad. “Orthogonal matching pursuit: recursive function approximation with applications to wavelet decomposition”. In: *Proceedings of 27th Asilomar Conference on Signals, Systems and Computers*. Proceedings of 27th Asilomar Conference on Signals, Systems and Computers. Nov. 1993, 40–44 vol.1. DOI: 10.1109/ACSSC.1993.342465.

[45] Simon Foucart and David Koslicki. “Sparse Recovery by Means of Nonnegative Least Squares”. In: *IEEE Signal Processing Letters* 21.4 (Apr. 2014), pp. 498–502. ISSN: 1070-9908, 1558-2361. DOI: 10.1109/LSP.2014.2307064.

[46] M.F. Duarte et al. “Distributed Compressed Sensing of Jointly Sparse Signals”. In: *Proceedings of the 2005 Asilomar Conference on Signals, Systems, and Computers*. IEEE, 2005, pp. 1537–1541. ISBN: 978-1-4244-0131-4. DOI: 10.1109/ACSSC.2005.1600024.

[47] S.F. Cotter et al. “Sparse solutions to linear inverse problems with multiple measurement vectors”. In: *IEEE Transactions on Signal Processing* 53.7 (July 2005), pp. 2477–2488. ISSN: 1053-587X. DOI: 10.1109/TSP.2005.849172.

[48] Joel A. Tropp, Anna C. Gilbert, and Martin J. Strauss. “Algorithms for simultaneous sparse approximation. Part I: Greedy pursuit”. In: *Signal Processing* 86.3 (Mar. 2006), pp. 572–588. ISSN: 01651684. DOI: 10.1016/j.sigpro.2005.05.030.

[49] Joel A. Tropp. “Algorithms for simultaneous sparse approximation. Part II: Convex relaxation”. In: *Signal Processing* 86.3 (Mar. 2006), pp. 589–602. ISSN: 01651684. DOI: 10.1016/j.sigpro.2005.05.031.

[50] J. D. Blanchard et al. “Greedy Algorithms for Joint Sparse Recovery”. In: *IEEE Transactions on Signal Processing* 62.7 (Apr. 2014), pp. 1694–1704. ISSN: 1053-587X. DOI: 10.1109/TSP.2014.2301980.

[51] Marcel Warntjes et al. “Modeling the Presence of Myelin and Edema in the Brain Based on Multi-Parametric Quantitative MRI”. In: *Frontiers in Neurology* 7 (2016). ISSN: 1664-2295. DOI: 10.3389/fneur.2016.00016.

[52] P.A. Hasgall et al. *ITIS Database for thermal and electromagnetic parameters of biological tissues*. May 4, 2018. URL: https://itis.swiss/virtual-population/tissue-properties/.

[53] J Hennig. “Multiecho imaging sequences with low refocusing flip angles”. In: *Journal of Magnetic Resonance* 78.3 (July 1988), pp. 397–407. ISSN: 00222364. DOI: 10.1016/0022-2364(88)90128-X.

[54] Anagha Deshmane et al. “Tissue Mapping in Brain Tumors with Partial Volume Magnetic Resonance Fingerprinting (PV-MRF)”. In: *Proc. Intl. Soc. Mag. Reson. Med. 23*. 2015, p. 0071.

[55] Jorge Zavala Bojorquez et al. “What are normal relaxation times of tissues at 3 T?” In: *Magnetic Resonance Imaging* 35 (Jan. 2017), pp. 69–80. ISSN: 0730725X. DOI: 10.1016/j.mri.2016.08.021.

[56] Debra McGivney et al. “Segmentation of Brain Tissues using a Bayesian Estimation of Multicomponent Relaxation Values in Magnetic Resonance Fingerprinting”. In: *Proc. Intl. Soc. Mag. Reson. Med. 26*. Paris, 2018, p. 1022.

[57] Jing Zhang et al. “Comparison of myelin water fraction from multiecho T2 decay curve and steady-state methods”. In: *Magnetic Resonance in Medicine* 73.1 (Jan. 1, 2015), pp. 223–232. ISSN: 1522-2594. DOI: 10.1002/mrm.25125.

[58] M. Davies et al. “A Compressed Sensing Framework for Magnetic Resonance Fingerprinting”. In: *SIAM Journal on Imaging Sciences* 7.4 (Jan. 1, 2014), pp. 2623–2656. DOI: 10.1137/130947246.

[59] Eric Y. Pierre et al. “Multiscale reconstruction for MR fingerprinting”. In: *Magnetic Resonance in Medicine* 75.6 (2016), pp. 2481–2492. ISSN: 1522-2594. DOI: 10.1002/mrm.25776.

[60] Mariya Doneva et al. “Matrix completion-based reconstruction for undersampled magnetic resonance fingerprinting data”. In: *Magnetic Resonance Imaging* 41 (Sept. 2017), pp. 41–52. ISSN: 0730725X. DOI: 10.1016/j.mri.2017.02.007.

[61] Jakob Assländer et al. “Low rank alternating direction method of multipliers reconstruction for MR fingerprinting: Low Rank ADMM Reconstruction”. In: *Magnetic Resonance in Medicine* 79.1 (Jan. 2018), pp. 83–96. ISSN: 07403194. DOI: 10.1002/mrm.26639.

[62] C. Badve et al. “MR Fingerprinting of Adult Brain Tumors: Initial Experience”. In: *American Journal of Neuroradiology* 38.3 (Mar. 1, 2017), pp. 492–499. ISSN: 0195-6108, 1936-959X. DOI: 10.3174/ajnr.A5035.

[63] J. B. M. Warntjes et al. “Rapid magnetic resonance quantification on the brain: Optimization for clinical usage”. In: *Magnetic Resonance in Medicine* 60.2 (2008), pp. 320–329. ISSN: 1522-2594. DOI: https://doi.org/10.1002/mrm.21635.

[64] Laura Nunez-Gonzalez et al. “Accuracy and repeatability of QRAPMASTER and MRF-vFA”. In: *Magnetic Resonance Imaging* 83 (Nov. 1, 2021), pp. 196–207. ISSN: 0730-725X. DOI: 10.1016/j.mri.2021.09.004.

[65] Yong Chen et al. “MR Fingerprinting for Rapid Quantitative Abdominal Imaging”. In: *Radiology* 279.1 (Apr. 1, 2016), pp. 278–286. ISSN: 0033-8419. DOI: 10.1148/radiol.2016152037.

[66] Kyeong Hwa Ryu et al. “Initial clinical experience of synthetic MRI as a routine neuroimaging protocol in daily practice: A single-center study”. In: *Journal of Neuroradiology*. 47e Congrès de la Société française de neuroradiologie 47.2 (Mar. 1, 2020), pp. 151–160. ISSN: 0150-9861. DOI: 10.1016/j.neurad.2019.03.002.

[67] Antonio Giorgio and Nicola De Stefano. “Clinical use of brain volumetry”. In: *Journal of Magnetic Resonance Imaging* 37.1 (2013), pp. 1–14. ISSN: 1522-2586. DOI: 10.1002/jmri.23671.

[68] David E. Ross. “Review of longitudinal studies of MRI brain volumetry in patients with traumatic brain injury”. In: *Brain Injury* 25.13 (Dec. 1, 2011), pp. 1271–1278. ISSN: 0269-9052. DOI: 10.3109/02699052.2011.624568.

[69] Rutger Heinen et al. “Robustness of Automated Methods for Brain Volume Measurements across Different MRI Field Strengths”. In: *PloS One* 11.10 (2016), e0165719. ISSN: 1932-6203. DOI: 10.1371/journal.pone.0165719.

[70] Jeroen de Bresser et al. “A comparison of MR based segmentation methods for measuring brain atrophy progression”. In: *NeuroImage* 54.2 (Jan. 2011), pp. 760–768. ISSN: 10538119. DOI: 10.1016/j.neuroimage.2010.09.060.

[71] Roberto Duarte et al. “Greedy approximate projection for magnetic resonance fingerprinting with partial volumes”. In: *Inverse Problems* 36.3 (Feb. 12, 2020), p. 035015. ISSN: 0266-5611. DOI: 10.1088/1361-6420/ab356d.

[72] O. Jaubert et al. “Free-running cardiac magnetic resonance fingerprinting: Joint T1/T2 map and Cine imaging”. In: *Magnetic Resonance Imaging* 68 (May 1, 2020), pp. 173–182. ISSN: 0730-725X. DOI: 10.1016/j.mri.2020.02.005.

[73] Pan Su et al. “Multiparametric estimation of brain hemodynamics with MR fingerprinting ASL”. In: *Magnetic Resonance in Medicine* 78.5 (2017), pp. 1812–1823. ISSN: 1522-2594. DOI: 10.1002/mrm.26587.

[74] Daeun Kim et al. “Multidimensional correlation spectroscopic imaging of exponential decays: From theoretical principles to in vivo human applications”. In: *NMR in Biomedicine* 33.12 (2020), e4244. ISSN: 1099-1492. DOI: 10.1002/nbm.4244.

[75] Martijn A. Nagtegaal et al. “Fast multi-component analysis using a joint sparsity constraint for MR fingerprinting”. In: *Magnetic Resonance in Medicine* 83.2 (2020), pp. 521–534. ISSN: 1522-2594. DOI: 10.1002/mrm.27947.

[76] C Laule et al. “Myelin water imaging in multiple sclerosis: quantitative correlations with histopathology”. In: *Multiple Sclerosis Journal* 12.6 (Nov. 2006), pp. 747–753. ISSN: 1352-4585, 1477-0970. DOI: 10.1177/1352458506070928.

[77] Cornelia Laule et al. “Myelin water imaging of multiple sclerosis at 7ăT: Correlations with histopathology”. In: *NeuroImage* 40.4 (May 1, 2008), pp. 1575–1580. ISSN: 1053-8119. DOI: 10.1016/j.neuroimage.2007.12.008.

[78] Shannon Kolind et al. “Brain and cord myelin water imaging: a progressive multiple sclerosis biomarker”. In: *NeuroImage. Clinical* 9 (2015), pp. 574–580. ISSN: 2213-1582. DOI: 10.1016/j.nicl.2015.10.002.

[79] Matteo Cencini et al. “Myelin Water Fraction Mapping in developing children using Magnetic Resonance Fingerprinting”. In: *Proc. Intl. Soc. Mag. Reson. Med. 29*. ISMRM. Vol. 29. ISMRM, 2021, p. 0165.

[80] Yong Chen et al. “MR fingerprinting enables quantitative measures of brain tissue relaxation times and myelin water fraction in the first five years of life”. In: *NeuroImage* 186 (Feb. 1, 2019), pp. 782–793. ISSN: 1053-8119. DOI: 10.1016/j.neuroimage.2018.11.038.

[81] B. Aubert-Broche et al. “Twenty New Digital Brain Phantoms for Creation of Validation Image Data Bases”. In: *IEEE Transactions on Medical Imaging* 25.11 (Nov. 2006), pp. 1410–1416. ISSN: 0278-0062. DOI: 10.1109/TMI.2006.883453.

[82] Gregor Körzdörfer et al. “Reproducibility and Repeatability of MR Fingerprinting Relaxometry in the Human Brain”. In: *Radiology* (June 18, 2019), p. 182360. ISSN: 0033-8419. DOI: 10.1148/radiol.2019182360.

[83] Guido Buonincontri et al. “Multi-site repeatability and reproducibility of MR fingerprinting of the healthy brain at 1.5 and 3.0T”. In: *NeuroImage* 195 (July 15, 2019), pp. 362–372. ISSN: 1053-8119. DOI: 10.1016/j.neuroimage.2019.03.047.

[84] Matthias Weigel. “Extended phase graphs: Dephasing, RF pulses, and echoes - pure and simple”. In: *Journal of Magnetic Resonance Imaging* 41.2 (2015), pp. 266–295. ISSN: 1522-2586. DOI: 10.1002/jmri.24619.

[85] Bhairav Bipin Mehta et al. “Image reconstruction algorithm for motion insensitive MR Fingerprinting (MRF): MORF”. In: *Magnetic Resonance in Medicine* 80.6 (2018), pp. 2485–2500. ISSN: 1522-2594. DOI: 10.1002/mrm.27227.

[86] Jan W. Kurzawski et al. “Retrospective rigid motion correction of three-dimensional magnetic resonance fingerprinting of the human brain”. In: *Magnetic Resonance in Medicine* 84.5 (2020), pp. 2606–2615. ISSN: 1522-2594. DOI: 10.1002/mrm.28301.

[87] Y. Zhang, M. Brady, and S. Smith. “Segmentation of brain MR images through a hidden Markov random field model and the expectation-maximization algorithm”. In: *IEEE Transactions on Medical Imaging* 20.1 (Jan. 2001), pp. 45–57. ISSN: 0278-0062. DOI: 10.1109/42.906424.

[88] John Ashburner and Karl J. Friston. “Unified segmentation”. In: *NeuroImage* 26.3 (July 1, 2005), pp. 839–851. ISSN: 1053-8119. DOI: 10.1016/j.neuroimage.2005.02.018.

[89] *SPM - Statistical Parametric Mapping*. URL: https://www.fil.ion.ucl.ac.uk/spm/ (visited on 10/13/2019).

[90] Vs Fonov et al. “Unbiased nonlinear average age-appropriate brain templates from birth to adulthood”. In: *NeuroImage* 47 (July 2009), S102. ISSN: 10538119. DOI: 10.1016/S1053-8119(09)70884-5.

[91] Vladimir Fonov et al. “Unbiased average age-appropriate atlases for pediatric studies”. In: *NeuroImage* 54.1 (Jan. 2011), pp. 313–327. ISSN: 10538119. DOI: 10.1016/j.neuroimage.2010.07.033.

[92] Adam V. Dvorak et al. “An atlas for human brain myelin content throughout the adult life span”. In: *Scientific Reports* 11.1 (Jan. 11, 2021), pp. 1–13. ISSN: 2045-2322. DOI: 10.1038/s41598-020-79540-3.

[93] W. R. Crum, O. Camara, and D. L. G. Hill. “Generalized Overlap Measures for Evaluation and Validation in Medical Image Analysis”. In: *IEEE Transactions on Medical Imaging* 25.11 (Nov. 2006), pp. 1451–1461. ISSN: 0278-0062. DOI: 10.1109/TMI.2006.880587.

[94] Greg J. Stanisz et al. “T1, T2 relaxation and magnetization transfer in tissue at 3T”. In: *Magnetic Resonance in Medicine* 54.3 (Sept. 2005), pp. 507–512. ISSN: 0740-3194, 1522-2594. DOI: 10.1002/mrm.20605.

[95] Mustapha Bouhrara and Richard G. Spencer. “Rapid simultaneous high-resolution mapping of myelin water fraction and relaxation times in human brain using BMC-mcDESPOT”. In: *NeuroImage* 147 (Feb. 15, 2017), pp. 800–811. ISSN: 1053-8119. DOI: 10.1016/j.neuroimage.2016.09.064.

[96] Eva Alonso-Ortiz, Ives R. Levesque, and G. Bruce Pike. “Multi-gradient-echo myelin water fraction imaging: Comparison to the multi-echo-spin-echo technique”. In: *Magnetic Resonance in Medicine* 79.3 (2018), pp. 1439–1446. ISSN: 1522-2594. DOI: 10.1002/mrm.26809.

[97] Adam V. Dvorak et al. “Comparison of multi echo T 2 relaxation and steady state approaches for myelin imaging in the central nervous system”. In: *Scientific Reports* 11.1 (Jan. 14, 2021), pp. 1–12. ISSN: 2045-2322. DOI: 10.1038/s41598-020-80585-7.

[98] Dana L. Tudorascu et al. “Reproducibility and Bias in Healthy Brain Segmentation: Comparison of Two Popular Neuroimaging Platforms”. In: *Frontiers in Neuroscience* 10 (2016), p. 503. ISSN: 1662-453X. DOI: 10.3389/fnins.2016.00503.

[99] Frederick Klauschen et al. “Evaluation of automated brain MR image segmentation and volumetry methods”. In: *Human Brain Mapping* 30.4 (2009), pp. 1310–1327. ISSN: 1097-0193. DOI: 10.1002/hbm.20599.

[100] Kenneth O. Johnson, Ryan K. Robison, and James G. Pipe. “Rigid Body Motion Compensation for Spiral Projection Imaging”. In: *IEEE Transactions on Medical Imaging* 30.3 (Mar. 2011), pp. 655–665. ISSN: 1558-254X. DOI: 10.1109/TMI.2010.2091146.

[101] David G. J. Heesterbeek. “Sequence optimisation for Magnetic Resonance Fingerprinting”. mastersthesis. Delft, The Netherlands: Delft University of Technology, Oct. 2021.

[102] J.A. Fessler et al. “Toeplitz-based iterative image reconstruction for MRI with correction for magnetic field inhomogeneity”. In: *IEEE Transactions on Signal Processing* 53.9 (Sept. 2005), pp. 3393–3402. ISSN: 1941-0476. DOI: 10.1109/TSP.2005.853152.

[103] Jianqing Fan and Runze Li. “Variable Selection via Nonconcave Penalized Likelihood and its Oracle Properties”. In: *Journal of the American Statistical Association* 96.456 (Dec. 2001), pp. 1348–1360. ISSN: 0162-1459, 1537-274X. DOI: 10.1198/016214501753382273.

[104] C. Laule et al. “Water content and myelin water fraction in multiple sclerosis”. In: *Journal of Neurology* 251.3 (Mar. 1, 2004), pp. 284–293. ISSN: 0340-5354, 1432-1459. DOI: 10.1007/s00415-004-0306-6.

[105] Tobias Djamsched Faizy et al. “Heterogeneity of Multiple Sclerosis Lesions in Multislice Myelin Water Imaging”. In: *PLOS ONE* 11.3 (Mar. 18, 2016), e0151496. ISSN: 1932-6203. DOI: 10.1371/journal.pone.0151496.

[106] Alex L. MacKay and Cornelia Laule. “Magnetic Resonance of Myelin Water: An in vivo Marker for Myelin”. In: *Brain Plasticity* 2.1 (Dec. 21, 2016). Ed. by Bernard Zalc, pp. 71–91. ISSN: 22136304, 22136312. DOI: 10.3233/BPL-160033.

[107] Colin S. Poon and R. Mark Henkelman. “Practical T2 quantitation for clinical applications”. In: *Journal of Magnetic Resonance Imaging* 2.5 (1992), pp. 541–553. ISSN: 1522-2586. DOI: 10.1002/jmri.1880020512.

[108] Ives R. Levesque, Charmaine L. L. Chia, and G. Bruce Pike. “Reproducibility of in vivo magnetic resonance imagingbased measurement of myelin water”. In: *Journal of Magnetic Resonance Imaging* 32.1 (2010), pp. 60–68. ISSN: 1522-2586. DOI: 10.1002/jmri.22170.

[109] Sandra M. Meyers et al. “Multicenter measurements of myelin water fraction and geometric mean T2: Intra- and intersite reproducibility”. In: *Journal of Magnetic Resonance Imaging* 38.6 (2013), pp. 1445–1453. ISSN: 1522-2586. DOI: 10.1002/jmri.24106.

[110] Thomas Prasloski et al. “Rapid whole cerebrum myelin water imaging using a 3D GRASE sequence”. In: *NeuroImage* 63.1 (Oct. 15, 2012), pp. 533–539. ISSN: 1053-8119. DOI: 10.1016/j.neuroimage.2012.06.064.

[111] Gerhard S. Drenthen et al. “Applicability and reproducibility of 2D multi-slice GRASE myelin water fraction with varying acquisition acceleration”. In: *NeuroImage* 195 (June 4, 2019), pp. 333–339. ISSN: 1053-8119. DOI: 10.1016/j.neuroimage.2019.04.011.

[112] Jürgen Hennig. “Echoeshow to generate, recognize, use or avoid them in MR-imaging sequences. Part I: Fundamental and not so fundamental properties of spin echoes”. In: *Concepts in Magnetic Resonance* 3.3 (1991), pp. 125–143. ISSN: 1099-0534. DOI: 10.1002/cmr.1820030302.

[113] Simon J. Graham, Peter L. Stanchev, and Michael J. Bronskill. “Criteria for analysis of multicomponent tissue T2 relaxation data”. In: *Magnetic Resonance in Medicine* 35.3 (Mar. 1996), pp. 370–378. ISSN: 07403194. DOI: 10.1002/mrm.1910350315.

[114] Thomas Prasloski et al. “Applications of stimulated echo correction to multi-component T2 analysis”. In: *Magnetic Resonance in Medicine* 67.6 (June 2012), pp. 1803–1814. ISSN: 07403194. DOI: 10.1002/mrm.23157.

[115] Youngjin Yoo et al. “Fast computation of myelin maps from MRI T2 relaxation data using multicore CPU and graphics card parallelization”. In: *Journal of Magnetic Resonance Imaging* 41.3 (2015), pp. 700–707. ISSN: 1522-2586. DOI: 10.1002/jmri.24604.

[116] Lisa Eunyoung Lee et al. “Inter-Vendor Reproducibility of Myelin Water Imaging Using a 3D Gradient and Spin Echo Sequence”. In: *Frontiers in Neuroscience* 12 (2018). ISSN: 1662-453X. DOI: 10.3389/fnins.2018.00854.

[117] Gerhard S. Drenthen et al. “A new analysis approach for T2 relaxometry myelin water quantification: Orthogonal Matching Pursuit”. In: *Magnetic Resonance in Medicine* 81.5 (2019), pp. 3292–3303. ISSN: 1522-2594. DOI: 10.1002/mrm.27600.

[118] Greg J. Stanisz and R. Mark Henkelman. “Diffusional anisotropy of T2 components in bovine optic nerve”. In: *Magnetic Resonance in Medicine* 40.3 (1998), pp. 405–410. ISSN: 1522-2594. DOI: 10.1002/mrm.1910400310.

[119] Ashish Raj et al. “Multi-Compartment T2 Relaxometry Using a Spatially Constrained Multi-Gaussian Model”. In: *PLoS ONE* 9.6 (June 4, 2014). Ed. by Friedemann Paul, e98391. ISSN: 1932-6203. DOI: 10.1371/journal.pone.0098391.

[120] Christian EL Hajj et al. “Multi-Exponential Relaxation Times Maps Reconstruction and Unsupervised Classification in Magnitude Magnetic Resonance Imaging”. In: *2019 27th European Signal Processing Conference (EUSIPCO)*. 2019 27th European Signal Processing Conference (EUSIPCO). Sept. 2019, pp. 1–5. DOI: 10.23919/EUSIPCO.2019.8902817.

[121] Alireza Akhondi-Asl et al. “T2-Relaxometry for Myelin Water Fraction Extraction Using Wald Distribution and Extended Phase Graph”. In: *Medical Image Computing and Computer-Assisted Intervention MICCAI 2014*. Ed. by Polina Golland et al. Springer International Publishing, 2014, pp. 145–152. ISBN: 978-3-319-10443-0.

[122] Marcus Björk et al. “A multicomponent T2 relaxometry algorithm for myelin water imaging of the brain”. In: *Magnetic Resonance in Medicine* 75.1 (Jan. 1, 2016), pp. 390–402. ISSN: 0740-3194. DOI: 10.1002/mrm.25583.

[123] Petre Stoica and Prabhu Babu. “Parameter estimation of exponential signals: A system identification approach”. In: *Digital Signal Processing* 23.5 (Sept. 1, 2013), pp. 1565–1577. ISSN: 1051-2004. DOI: 10.1016/j.dsp.2013.05.003.

[124] M. Yaghoobi, D. Wu, and M. E. Davies. “Fast Non-Negative Orthogonal Matching Pursuit”. In: *IEEE Signal Processing Letters* 22.9 (Sept. 2015), pp. 1229–1233. DOI: 10.1109/LSP.2015.2393637.

[125] Thi Thanh Nguyen et al. “An optimized version of non-negative OMP”. In: *XXVIe Colloque GRETSI Traitement du Signal des Images*. Juan-les-Pins, France, 2017, p. 5. DOI: <hal-01585253>.

[126] Mark D. Does et al. “Evaluation of principal component analysis image denoising on multi-exponential MRI relaxometry”. In: *Magnetic Resonance in Medicine* 81.6 (2019), pp. 3503–3514. ISSN: 1522-2594. DOI: 10.1002/mrm.27658.

[127] Mariya Doneva et al. “Compressed sensing reconstruction for magnetic resonance parameter mapping”. In: *Magnetic Resonance in Medicine* 64.4 (Oct. 1, 2010), pp. 1114–1120. ISSN: 1522-2594. DOI: 10.1002/mrm.22483.

[128] Wen Li, Mark Griswold, and Xin Yu. “Fast cardiac T1 mapping in mice using a model-based compressed sensing method”. In: *Magnetic Resonance in Medicine* 68.4 (2012), pp. 1127–1134. ISSN: 1522-2594. DOI: 10.1002/mrm.23323.

[129] José P. Marques et al. “MP2RAGE, a self bias-field corrected sequence for improved segmentation and T1-mapping at high field”. In: *NeuroImage* 49.2 (Jan. 15, 2010), pp. 1271–1281. ISSN: 1053-8119. DOI: 10.1016/j.neuroimage.2009.10.002.

[130] Joëlle K. Barral et al. “A robust methodology for in vivo T1 mapping”. In: *Magnetic Resonance in Medicine* 64.4 (2010), pp. 1057–1067. ISSN: 1522-2594. DOI: 10.1002/mrm.22497.

[131] Noam BenEliezer, Daniel K. Sodickson, and Kai Tobias Block. “Rapid and accurate T2 mapping from multispin-echo data using Bloch-simulation-based reconstruction”. In: *Magnetic Resonance in Medicine* 73.2 (Feb. 1, 2015), pp. 809–817. ISSN: 1522-2594. DOI: 10.1002/mrm.25156.

[132] Cornelia Laule et al. “MR evidence of long T2 water in pathological white matter”. In: *Journal of Magnetic Resonance Imaging* 26.4 (2007), pp. 1117–1121. ISSN: 1522-2586. DOI: 10.1002/jmri.21132.

[133] C. Laule et al. “Long T2 water in multiple sclerosis: What else can we learn from multi-echo T2 relaxation?” In: *Journal of Neurology* 254.11 (Nov. 1, 2007), pp. 1579–1587. ISSN: 1432-1459. DOI: 10.1007/s00415-007-0595-7.

[134] Vanessa Wiggermann et al. “Non-negative least squares fitting of multi-exponential T2 decay data: Are we able to accurately measure the fraction of myelin water?” In: *Proc. Intl. Soc. Mag. Reson. Med. 27*. Annual meeting of the ISMRM. Vol. 27. Montreal, Canada, 2019, p. 4402.

[135] Ming Yuan and Yi Lin. “Model selection and estimation in regression with grouped variables”. In: *Journal of the Royal Statistical Society: Series B (Statistical Methodology)* 68.1 (2006), pp. 49–67. ISSN: 1467-9868. DOI: 10.1111/j.1467-9868.2005.00532.x.

[136] D. Wipf and S. Nagarajan. “Iterative Reweighted {ℓ_1} and {ℓ_2} Methods for Finding Sparse Solutions”. In: *IEEE Journal of Selected Topics in Signal Processing* 4.2 (Apr. 2010), pp. 317–329. ISSN: 1932-4553. DOI: 10.1109/JSTSP.2010.2042413.

[137] Jieun Lee et al. “Artificial neural network for myelin water imaging”. In: *Magnetic Resonance in Medicine* 83.5 (2020), pp. 1875–1883. ISSN: 1522-2594. DOI: 10.1002/mrm.28038.

[138] Hanwen Liu et al. “Myelin water imaging data analysis in less than one minute”. In: *NeuroImage* (Jan. 21, 2020), p. 116551. ISSN: 1053-8119. DOI: 10.1016/j.neuroimage.2020.116551.

[139] Joonmi Oh et al. “Measurement of in vivo multi-component T2 relaxation times for brain tissue using multi-slice T2 prep at 1.5 and 3 T”. In: *Magnetic Resonance Imaging* 24 (Jan. 2006), pp. 33–43. DOI: 10.1016/j.mri.2005.10.016.

[140] Yiping P. Du et al. “Fast multislice mapping of the myelin water fraction using multicompartment analysis of T decay at 3T: A preliminary postmortem study”. In: *Magnetic Resonance in Medicine* 58.5 (2007), pp. 865–870. ISSN: 1522-2594. DOI: 10.1002/mrm.21409.

[141] Xiaozhi Cao et al. “Robust sliding-window reconstruction for Accelerating the acquisition of MR fingerprinting”. In: *Magnetic Resonance in Medicine* 78.4 (2017), pp. 1579–1588. ISSN: 1522-2594. DOI: 10.1002/mrm.26521.

[142] Gastao Cruz et al. “Accelerated magnetic resonance fingerprinting using soft-weighted key-hole (MRF-SOHO)”. In: *PLOS ONE* 13.8 (Aug. 9, 2018), e0201808. ISSN: 1932-6203. DOI: 10.1371/journal.pone.0201808.

[143] Jonathan I. Tamir et al. “T2 shuffling: Sharp, multicontrast, volumetric fast spin-echo imaging”. In: *Magnetic Resonance in Medicine* 77.1 (2017), pp. 180–195. ISSN: 1522-2594. DOI: https://doi.org/10.1002/mrm.26102.

[144] Gastão Lima da Cruz et al. “Sparsity and locally low rank regularization for MR fingerprinting”. In: *Magnetic Resonance in Medicine* 81.6 (2019), pp. 3530–3543. ISSN: 1522-2594. DOI: 10.1002/mrm.27665.

[145] Tao Zhang, John M. Pauly, and Ives R. Levesque. “Accelerating parameter mapping with a locally low rank constraint”. In: *Magnetic Resonance in Medicine* 73.2 (2015), pp. 655–661. ISSN: 1522-2594. DOI: 10.1002/mrm.25161.

[146] Aurélien Bustin et al. “High-dimensionality undersampled patch-based reconstruction (HD-PROST) for accelerated multi-contrast MRI”. In: *Magnetic Resonance in Medicine* 81.6 (2019), pp. 3705–3719. ISSN: 1522-2594. DOI: 10.1002/mrm.27694.

[147] Bo Zhao et al. “Improved magnetic resonance fingerprinting reconstruction with low-rank and subspace modeling”. In: *Magnetic Resonance in Medicine* 79.2 (2018), pp. 933–942. ISSN: 1522-2594. DOI: 10.1002/mrm.26701.

[148] B. Zhao et al. “Maximum Likelihood Reconstruction for Magnetic Resonance Fingerprinting”. In: *IEEE Transactions on Medical Imaging* 35.8 (Aug. 2016), pp. 1812–1823. ISSN: 0278-0062. DOI: 10.1109/TMI.2016.2531640.

[149] Stephen Boyd et al. “Distributed Optimization and Statistical Learning via the Alternating Direction Method of Multipliers”. In: *Foundations and Trendső in Machine Learning* 3.1 (Jan. 1, 2011), pp. 1–122. ISSN: 1935-8237. DOI: 10.1561/2200000016.

[150] Antonin Chambolle and Thomas Pock. “A First-Order Primal-Dual Algorithm for Convex Problems withăApplications to Imaging”. In: *Journal of Mathematical Imaging and Vision* 40.1 (May 1, 2011), pp. 120–145. ISSN: 1573-7683. DOI: 10.1007/s10851-010-0251-1.

[151] Frank Ong, Martin Uecker, and Michael Lustig. “Accelerating Non-Cartesian MRI Reconstruction Convergence Using k-Space Preconditioning”. In: *IEEE Transactions on Medical Imaging* 39.5 (May 2020), pp. 1646–1654. ISSN: 1558-254X. DOI: 10.1109/TMI.2019.2954121.

[152] Frank Ong and Michael Lustig. “SigPy: a python package for high performance iterative reconstruction”. In: *Proceedings of the International Society of Magnetic Resonance in Medicine, Montréal, QC* 4819 (2019).

[153] Karsten Sommer et al. “Determination of the Optimum Pattern Length of MRF Sequences”. In: *Proc. Intl. Soc. Mag. Reson. Med. 25*. ISMRM. Vol. 25. Honolulu, USA: ISMRM, 2017, p. 1491.

[154] D. L. Collins et al. “Design and construction of a realistic digital brain phantom”. In: *IEEE Transactions on Medical Imaging* 17.3 (June 1998), pp. 463–468. ISSN: 0278-0062. DOI: 10.1109/42.712135.

[155] Martin Buehrer et al. “Array compression for MRI with large coil arrays”. In: *Magnetic Resonance in Medicine* 57.6 (2007), pp. 1131–1139. ISSN: 1522-2594. DOI: 10.1002/mrm.21237.

[156] Martin Uecker et al. “ESPIRiTan eigenvalue approach to autocalibrating parallel MRI: Where SENSE meets GRAPPA”. In: *Magnetic Resonance in Medicine* 71.3 (2014), pp. 990–1001. ISSN: 1522-2594. DOI: 10.1002/mrm.24751.

[157] Mark H. Van Benthem and Michael R. Keenan. “Fast algorithm for the solution of large-scale non-negativity-constrained least squares problems”. In: *Journal of Chemometrics* 18.10 (2004), pp. 441–450. ISSN: 1099-128X. DOI: 10.1002/cem.889.

[158] Yuancheng Luo and Ramani Duraiswami. “Efficient Parallel Nonnegative Least Squares on Multicore Architectures”. In: *SIAM Journal on Scientific Computing* 33.5 (Jan. 1, 2011), pp. 2848–2863. ISSN: 1064-8275. DOI: 10.1137/100799083.

[159] Martijn. A. Nagtegaal et al. “Detection of small cerebral lesions using multi-component MR Fingerprinting with local joint sparsity”. In: *Proc. Intl. Soc. Mag. Reson. Med. 28 (2020)*. ISMRM. Vol. 28. online, 2020, p. 1828.

[160] Christopher C. Cline et al. “AIR-MRF: Accelerated iterative reconstruction for magnetic resonance fingerprinting”. In: *Magnetic Resonance Imaging* 41 (Sept. 1, 2017), pp. 29–40. ISSN: 0730-725X. DOI: 10.1016/j.mri.2017.07.007.

[161] Peter Börnert et al. “Improvements in spiral MR imaging”. In: *Magnetic Resonance Materials in Physics, Biology and Medicine* 9.1 (Oct. 1, 1999), pp. 29–41. ISSN: 1352-8661. DOI: 10.1007/BF02634590.

[162] Ronal Coronado et al. “A Spatial Off-Resonance Correction in Spirals for Magnetic Resonance Fingerprinting”. In: *IEEE Transactions on Medical Imaging* 40.12 (Dec. 2021), pp. 3832–3842. ISSN: 1558-254X. DOI: 10.1109/TMI.2021.3100293.

[163] Kirsten Koolstra et al. “Waterfat separation in spiral magnetic resonance fingerprinting for high temporal resolution tissue relaxation time quantification in muscle”. In: *Magnetic Resonance in Medicine* 84.2 (2020), pp. 646–662. ISSN: 1522-2594. DOI: 10.1002/mrm.28143.

[164] Di Cui, Edward S. Hui, and Peng Cao. “A multi-inversion-recovery magnetic resonance fingerprinting for multi-compartment water mapping”. In: *Magnetic Resonance Imaging* 81 (Sept. 1, 2021), pp. 82–87. ISSN: 0730-725X. DOI: 10.1016/j.mri.2021.06.005.

[165] David G.J. Heesterbeek et al. “Sequence optimisation mitigating undersampling errors in Magnetic Resonance Fingerprinting”. In: *Proc. Intl. Soc. Mag. Reson. Med. 30 (2022)*. ISMRM. Vol. 30. London: ISMRM, May 2022, p. 0561.

[166] Martijn Nagtegaal and Emiel Hartsema. *Multi-component MRF reconstruction*. 2022. DOI: 10.4121/19434689.V1.

[167] Massimo Filippi et al. “MRI criteria for the diagnosis of multiple sclerosis: MAGNIMS consensus guidelines”. In: *The Lancet Neurology* 15.3 (Mar. 1, 2016), pp. 292–303. ISSN: 1474-4422. DOI: 10.1016/S1474-4422(15)00393-2.

[168] Wardlaw Joanna M., Valdés Hernández Maria C., and MuñozManiega Susana. “What are White Matter Hyperintensities Made of?” In: *Journal of the American Heart Association* 4.6 (2015), e001140. DOI: 10.1161/JAHA.114.001140.

[169] Cornelia Laule et al. “Diffusely Abnormal White Matter in Multiple Sclerosis: Further Histologic Studies Provide Evidence for a Primary Lipid Abnormality With Neurodegeneration”. In: *Journal of Neuropathology & Experimental Neurology* 72.1 (Jan. 1, 2013), pp. 42–52. ISSN: 0022-3069. DOI: 10.1097/NEN.0b013e31827bced3.

[170] James Cairns et al. “Diffusely abnormal white matter in multiple sclerosis”. In: *Journal of Neuroimaging* 32.1 (2022), pp. 5–16. ISSN: 1552-6569. DOI: 10.1111/jon.12945.

[171] Natalia M. Moll et al. “Multiple sclerosis normal-appearing white matter: Pathologyimaging correlations”. In: *Annals of Neurology* 70.5 (2011), pp. 764–773. ISSN: 1531-8249. DOI: 10.1002/ana.22521.

[172] Massimo Filippi et al. “Association between pathological and MRI findings in multiple sclerosis”. In: *The Lancet Neurology* 18.2 (Feb. 1, 2019), pp. 198–210. ISSN: 1474-4422. DOI: 10.1016/S1474-4422(18)30451-4.

[173] Emilie Lommers et al. “Multiparameter MRI quantification of microstructural tissue alterations in multiple sclerosis”. In: *NeuroImage: Clinical* 23 (Jan. 1, 2019), p. 101879. ISSN: 2213-1582. DOI: 10.1016/j.nicl.2019.101879.

[174] D. J. Werring et al. “Diffusion tensor imaging of lesions and normal-appearing white matter in multiple sclerosis”. In: *Neurology* 52.8 (May 1, 1999), pp. 1626–1626. ISSN: 0028-3878, 1526-632X. DOI: 10.1212/WNL.52.8.1626.

[175] Rajikha Raja, Gary Rosenberg, and Arvind Caprihan. “Review of diffusion MRI studies in chronic white matter diseases”. In: *Neuroscience Letters* 694 (Feb. 16, 2019), pp. 198–207. ISSN: 0304-3940. DOI: 10.1016/j.neulet.2018.12.007.

[176] Silvia De Santis et al. “Evidence of early microstructural white matter abnormalities in multiple sclerosis from multi-shell diffusion MRI”. In: *NeuroImage: Clinical* 22 (Jan. 1, 2019), p. 101699. ISSN: 2213-1582. DOI: 10.1016/j.nicl.2019.101699.

[177] Claudia E. Weber et al. “Diffusely appearing white matter in multiple sclerosis: Insights from sodium (23Na) MRI”. In: *Multiple Sclerosis and Related Disorders* 49 (Apr. 1, 2021), p. 102752. ISSN: 2211-0348. DOI: 10.1016/j.msard.2021.102752.

[178] Kenneth P. Whittall, Alex L. MacKay, and David K.B. Li. “Are mono-exponential fits to a few echoes sufficient to determine T2 relaxation for in vivo human brain?” In: *Magnetic Resonance in Medicine* 41.6 (June 1999), pp. 1255–1257. ISSN: 0740-3194, 1522-2594. DOI: 10.1002/(SICI)1522-2594(199906)41:6<1255::AID-MRM23>3.0.CO;2-I.

[179] Martijn Nagtegaal et al. “Multicomponent MR fingerprinting reconstruction using joint-sparsity and low-rank constraints”. In: *Magnetic Resonance in Medicine* n/a (n/a 2022). ISSN: 1522-2594. DOI: 10.1002/mrm.29442.

[180] Matteo Cencini et al. “Magnetic resonance fingerprinting with dictionary-based fat and water separation (DBFW MRF): A multi-component approach”. In: *Magnetic Resonance in Medicine* 81.5 (2019), pp. 3032–3045. ISSN: 1522-2594. DOI: 10.1002/mrm.27628.

[181] Jelle Veraart et al. “Denoising of diffusion MRI using random matrix theory”. In: *NeuroImage* 142 (Nov. 15, 2016), pp. 394–406. ISSN: 1053-8119. DOI: 10.1016/j.neuroimage.2016.08.016.

[182] Paul Schmidt. “Bayesian inference for structured additive regression models for large-scale problems with applications to medical imaging”. PhD thesis. Ludwig-Maximilians-Universität München, 2017. DOI: 10.5282/EDOC.20373.

[183] Ingo Hermann et al. “Accelerated white matter lesion analysis based on simultaneous T1 and T2* quantification using magnetic resonance fingerprinting and deep learning”. In: *Magnetic Resonance in Medicine* 86.1 (2021), pp. 471–486. ISSN: 1522-2594. DOI: 10.1002/mrm.28688.

[184] Benedikt Rieger et al. “Time efficient whole-brain coverage with MR Fingerprinting using slice-interleaved echo-planar-imaging”. In: *Scientific Reports* 8.1 (Apr. 27, 2018), p. 6667. ISSN: 2045-2322. DOI: 10.1038/s41598-018-24920-z.

[185] Brian B Avants, Nick Tustison, and Gang Song. “Advanced normalization tools (ANTS)”. In: *Insight j* 2.365 (2009), pp. 1–35.

[186] Arno Klein et al. “Evaluation of 14 nonlinear deformation algorithms applied to human brain MRI registration”. In: *NeuroImage* 46.3 (July 2009), pp. 786–802. ISSN: 10538119. DOI: 10.1016/j.neuroimage.2008.12.037.

[187] D. Louis Collins et al. “ANIMAL+INSECT: Improved Cortical Structure Segmentation”. In: *Information Processing in Medical Imaging*. Ed. by Attila Kuba, Martin áamal, and Andrew Todd-Pokropek. Red. by Gerhard Goos, Juris Hartmanis, and Jan van Leeuwen. Vol. 1613. Berlin, Heidelberg: Springer Berlin Heidelberg, 1999, pp. 210–223. DOI: 10.1007/3-540-48714-X_16.

[188] L. Nunez-Gonzalez et al. “Accuracy and repeatability of joint sparsity multi-component estimation in MR Fingerprinting”. In: *NeuroImage* 263 (Nov. 1, 2022), p. 119638. ISSN: 1053-8119. DOI: 10.1016/j.neuroimage.2022.119638.

[189] Raphael Vallat. “Pingouin: statistics in Python”. In: *Journal of Open Source Software* 3.31 (Nov. 19, 2018), p. 1026. ISSN: 2475-9066. DOI: 10.21105/joss.01026.

[190] Alexandra Seewann et al. “Diffusely Abnormal White Matter in Chronic Multiple Sclerosis: Imaging and Histopathologic Analysis”. In: *Archives of Neurology* 66.5 (May 11, 2009), pp. 601–609. ISSN: 0003-9942. DOI: 10.1001/archneurol.2009.57.

[191] M. Filippi et al. “Diffusion tensor magnetic resonance imaging in multiple sclerosis”. In: *Neurology* 56.3 (Feb. 13, 2001), pp. 304–311. ISSN: 0028-3878, 1526-632X. DOI: 10.1212/WNL.56.3.304.

[192] D.A. Lakhani et al. “Advanced Multicompartment Diffusion MRI Models and Their Application in Multiple Sclerosis”. In: *American Journal of Neuroradiology* 41.5 (May 2020), pp. 751–757. ISSN: 0195-6108, 1936-959X. DOI: 10.3174/ajnr.A6484.

[193] J. P. Mostert et al. “T2 lesions and rate of progression of disability in multiple sclerosis”. In: *European Journal of Neurology* 17.12 (2010), pp. 1471–1475. ISSN: 1468-1331. DOI: 10.1111/j.1468-1331.2010.03093.x.

[194] R. Dobson and G. Giovannoni. “Multiple sclerosis a review”. In: *European Journal of Neurology* 26.1 (2019), pp. 27–40. ISSN: 1468-1331. DOI: 10.1111/ene.13819.

[195] David Leitão et al. “Efficiency analysis for quantitative MRI of T1 and T2 relaxometry methods”. In: *Physics in Medicine & Biology* 66.15 (July 2021), 15NT02. ISSN: 0031-9155. DOI: 10.1088/1361-6560/ac101f.

[196] Christiaan C Stolk and Alessandro Sbrizzi. “Understanding the Combined Effect of k-Space Undersampling and Transient States Excitation in MR Fingerprinting Reconstructions”. In: *IEEE Transactions on Medical Imaging* 38.10 (Oct. 2019), pp. 2445–2455. ISSN: 1558-254X. DOI: 10.1109/TMI.2019.2900585.

[197] David G. J. Heesterbeek and Martijn A. Nagtegaal. *MRF undersampling optimization: Software and code for the publication: Mitigating undersampling errors in Magnetic Resonance Fingerprinting by sequence optimization*. 2022. DOI: 10.4121/20101127.V2.

[198] John D. Hunter. “Matplotlib: A 2D Graphics Environment”. In: *Computing in Science Engineering* 9.3 (May 2007), pp. 90–95. ISSN: 1558-366X. DOI: 10.1109/MCSE.2007.55.

[199] Michael L. Waskom. “seaborn: statistical data visualization”. In: *Journal of Open Source Software* 6.60 (Apr. 6, 2021), p. 3021. ISSN: 2475-9066. DOI: 10.21105/joss.03021.

[200] Dieter Kraft. “A software package for sequential quadratic programming”. In: *DFVLR Obersfaffeuhofen, Germany* (1988).

[201] Eleftherios Garyfallidis et al. “Dipy, a library for the analysis of diffusion MRI data”. In: *Frontiers in Neuroinformatics* 8 (Feb. 21, 2014). ISSN: 1662-5196. DOI: 10.3389/fninf.2014.00008.

[202] Guido Buonincontri and Stephen J. Sawiak. “MR fingerprinting with simultaneous B1 estimation”. In: *Magnetic Resonance in Medicine* 76.4 (2016), pp. 1127–1135. ISSN: 1522-2594. DOI: 10.1002/mrm.26009.

[203] Stefan C. Endres, Carl Sandrock, and Walter W. Focke. “A simplicial homology algorithm for Lipschitz optimisation”. In: *Journal of Global Optimization* 72.2 (Oct. 1, 2018), pp. 181–217. ISSN: 1573-2916. DOI: 10.1007/s10898-018-0645-y.

[204] Evan Scope Crafts et al. “An efficient approach to optimal experimental design for magnetic resonance fingerprinting with B-splines”. In: *Magnetic Resonance in Medicine* 88.1 (2022), pp. 239–253. ISSN: 1522-2594. DOI: 10.1002/mrm.29212.

[205] A. Loktyushin et al. “MRzero - Automated discovery of MRI sequences using supervised learning”. In: *Magnetic Resonance in Medicine* 86.2 (2021), pp. 709–724. ISSN: 1522-2594. DOI: 10.1002/mrm.28727.

[206] Shaihan J. Malik et al. “Spatially resolved extended phase graphs: Modeling and design of multipulse sequences with parallel transmission”. In: *Magnetic Resonance in Medicine* 68.5 (2012), pp. 1481–1494. ISSN: 1522-2594. DOI: 10.1002/mrm.24153.

[207] Siu Kwan Lam, Antoine Pitrou, and Stanley Seibert. “Numba: a LLVM-based Python JIT compiler”. In: *Proceedings of the Second Workshop on the LLVM Compiler Infrastructure in HPC*. LLVM ’15. New York, NY, USA: Association for Computing Machinery, Nov. 15, 2015, pp. 1–6. ISBN: 978-1-4503-4005-2. DOI: 10.1145/2833157.2833162.

[208] Christian Guenthner et al. “A unifying view on extended phase graphs and Bloch simulations for quantitative MRI”. In: *Scientific Reports* 11.1 (Oct. 28, 2021), pp. 1–19. ISSN: 2045-2322. DOI: 10.1038/s41598-021-00233-6.

[209] Mohammad Golbabaee and Clarice Poon. “An off-the-grid approach to multi-compartment magnetic resonance fingerprinting”. In: *Inverse Problems* 38.8 (June 2022), p. 085002. ISSN: 0266-5611. DOI: 10.1088/1361-6420/ac70da.

[210] Quan Chen, Huajun She, and Yiping P. Du. “Improved quantification of myelin water fraction using joint sparsity of T2* distribution”. In: *Journal of Magnetic Resonance Imaging* 52.1 (2020), pp. 146–158. ISSN: 1522-2586. DOI: 10.1002/jmri.27013.

[211] Nima Mehdizadeh and Alan H. Wilman. “Myelin water fraction mapping from multiple echo spin echoes and an independent B1+ map”. In: *Magnetic Resonance in Medicine* 88.3 (Sept. 2022), pp. 1380–1390. ISSN: 1522-2594. DOI: 10.1002/mrm.29286.

[212] Adam V. Dvorak et al. “Multi-spin echo T2 relaxation imaging with compressed sensing (METRICS) for rapid myelin water imaging”. In: *Magnetic Resonance in Medicine* 84.3 (2020), pp. 1264–1279. ISSN: 1522-2594. DOI: 10.1002/mrm.28199.

[213] Congyu Liao et al. “Detection of Lesions in Mesial Temporal Lobe Epilepsy by Using MR Fingerprinting”. In: *Radiology* 288.3 (June 19, 2018), pp. 804–812. ISSN: 0033-8419. DOI: 10.1148/radiol.2018172131.

[214] Daniel J. West et al. “Inherent and unpredictable bias in multi-component DESPOT myelin water fraction estimation”. In: *NeuroImage* 195 (July 15, 2019), pp. 78–88. ISSN: 1053-8119. DOI: 10.1016/j.neuroimage.2019.03.049.

[215] Shaihan J. Malik, Rui Pedro A. G. Teixeira, and Joseph V. Hajnal. “Extended phase graph formalism for systems with magnetization transfer and exchange”. In: *Magnetic Resonance in Medicine* 80.2 (2018), pp. 767–779. ISSN: 1522-2594. DOI: 10.1002/mrm.27040.

[216] Tom Hilbert et al. “Magnetization transfer in magnetic resonance fingerprinting”. In: *Magnetic Resonance in Medicine* 84.1 (2020), pp. 128–141. ISSN: 1522-2594. DOI: 10.1002/mrm.28096.

[217] Jakob Assländer et al. *Rapid quantitative magnetization transfer imaging: utilizing the hybrid state and the generalized Bloch model*. July 17, 2022. DOI: 10.48550/arXiv.2207.08259.

[218] Xiaoxia Zhang et al. “CramérRao bound-informed training of neural networks for quantitative MRI”. In: *Magnetic Resonance in Medicine* n/a (n/a 2022). ISSN: 1522-2594. DOI: 10.1002/mrm.29206.

[219] Maryam Afzali et al. “MR Fingerprinting with b-Tensor Encoding for Simultaneous Quantification of Relaxation and Diffusion in a Single Scan”. In: *Magnetic Resonance in Medicine* (June 17, 2022). ISSN: 1522-2594. DOI: 10.1002/mrm.29352.

[220] Pan Su et al. “MR fingerprinting ASL: Sequence characterization and comparison with dynamic susceptibility contrast (DSC) MRI”. In: *NMR in Biomedicine* 33.1 (2020), e4202. ISSN: 1099-1492. DOI: 10.1002/nbm.4202.

[221] Jon-Fredrik Nielsen and Douglas C. Noll. “TOPPE: A framework for rapid prototyping of MR pulse sequences”. In: *Magnetic Resonance in Medicine* 79.6 (2018), pp. 3128–3134. ISSN: 1522-2594. DOI: 10.1002/mrm.26990.

[222] Kelvin J. Layton et al. “Pulseq: A rapid and hardware-independent pulse sequence prototyping framework”. In: *Magnetic Resonance in Medicine* 77.4 (2017), pp. 1544–1552. ISSN: 1522-2594. DOI: 10.1002/mrm.26235.

[223] Cristoffer Cordes et al. “Portable and platform-independent MR pulse sequence programs”. In: *Magnetic Resonance in Medicine* 83.4 (2020), pp. 1277–1290. ISSN: 1522-2594. DOI: 10.1002/mrm.28020.

[224] Agah Karakuzu et al. “Vendor-neutral sequences and fully transparent workflows improve inter-vendor reproducibility of quantitative MRI”. In: *Magnetic Resonance in Medicine* 88.3 (2022), pp. 1212–1228. ISSN: 1522-2594. DOI: 10.1002/mrm.29292.

[225] Michael Lustig, David Donoho, and John M. Pauly. “Sparse MRI: The application of compressed sensing for rapid MR imaging”. In: *Magnetic Resonance in Medicine* 58.6 (2007), pp. 1182–1195. ISSN: 1522-2594. DOI: 10.1002/mrm.21391.

[226] K.J. van Everdingen et al. “Diffusion-Weighted Magnetic Resonance Imaging in Acute Stroke”. In: *Stroke* 29.9 (Sept. 1998), pp. 1783–1790. DOI: 10.1161/01.STR.29.9.1783.

ACKNOWLEDGEMENTS

AFTER years of education and research finishing my PhD journey with this PhD thesis can be seen as a last step. This journey sometimes felt like a stroll with friends, sometimes like a tough interval training or a beautiful race on a sunny day, but almost never felt lonely. I would like to take the opportunity here to thank everyone who was supporting from the side, handing out drinks and cookies, who was walking or running along or who was just there when I needed them.

First of all I want to thank my supervisory committee who supported me to follow my interests during these 4 years of research and was there to ask the right questions. Some people were shocked when I told them I had four supervisors, but I considered myself lucky with the mix of experts to receive advice from. Frans, as promotor you fulfilled the role of coach, trainer and mentor. It always felt like your first priority was my development during my PhD research. I really appreciate how you gave me the opportunity to develop myself during these years and how you supported our research in these year. Thijs, in this list of people you are the first who literally ran along with me. I am very happy that you welcomed me from the start to partly work in Leiden in the Gorter group and that you were there on the side to reflect on all my questions and provide me with slightly different insights every time. Dirk, with you as one of my co-promotors I knew that no detail would go unnoticed and that I could always come to you with any question I had. I really appreciate how you always made time for me and how you were immediately up-to-date with what I was trying to do. Jeroen, you were definitely not a fellow runner in this analogy and I don't know which sport would reflect the differences between a physicist or mathematician and a radiologist well enough, but I think these differences are what made it so valuable to have you on my team. You were always able to ask new and different questions and keep my eyes on the (clinical) problems we were trying to solve, this is a lesson that will stay with me. But not only the fact that you are a radiologist made you a great fit, but also your everlasting optimism and positive energy when I was slightly done with the questions we wanted to answer.

The start of my PhD research was perhaps already on a snowy day in February 2018 when I visited Philips Hamburg for the first time, for an interview for my M.Sc. thesis project. I especially want to thank Mariya here who supported me for 8 months during this project that formed the start of this PhD thesis. If 5 (co-) promotors would have been an option, you should have been there. I really appreciate how you supervised me on a daily basis during this project. I am still surprised how much we got done during these 8 months and how I benefit from that to this day. I also want to thank Thomas, Peter, Jakob and Burkhard here who helped my during this project and also later on. It is great to have people with so many years of experience to reach out to. During this project I also got to know Malte, a great person and a friend I hope to keep even when, perhaps, one of us is not attending MRI conferences anymore. Related to that I want to thank the people I met during the MRF workshops, Gastao, Olivier, Christian, Charles, Oscar, Manuel and many

others, for the great introduction into the MRI community and the shared experiences and struggles.

There are some people who ran most kilometers together with me during these four years. First of all I want to thank Kirsten here who was already working on MRF in Leiden and was happy to answer every technical or practical question I had and who made sure that the LUMC felt like a warm place. Laura, thanks to our collaboration there was always something to work on during the Covid days of working from home and I really appreciate how we took the time to learn from each other. Chih-Hsien, although we did not directly work on the same projects in these four years, the shared experience and meetings really helped me to reflect on what I was doing and I enjoyed having you around. Perhaps the closest collaborations was with the students I supervised. Corné, supervising you was a special experience during strict Covid times and as the cliché requires you were way taller than I thought when I met you in person 4 months after your project ended. It is a pleasure to still see you in person in Leiden. Together with Jasper I learned how to manage a project when not everything goes according to plan, but in the end we can look back on a nice project. Maaike, our project was a different experience again and it was very nice to see how much you gained confidence and learned during this project. Sven it is great to currently supervise you and to puzzle with you. Emiel, it was a pleasure that you reached out to Frans and me to do a MSc project. We always enjoyed your progress meetings with GANTT charts and Forze stories and I admire your down-to-earth way of working. It is great to see that you went to Philips to continue on what you learned with us. David, you are probably the person with whom I had the most scientific discussions in the last years and in each of them we gained new insights. I consider myself lucky that we could work together and I hope we stay in touch!

Next to that I want to thank everyone within ImPhys for their presence and support in these 4 years (with the risk of forgetting people). Jos, Leon, Peter and Christiaan, as my "old" QI friends you were there for coffee breaks and all kinds of discussion. Henry, Ronald, Angela and Annelies, talking about coffee and other support, I very much appreciate how you keep the whole group running. Sebastian, Sjoerd, Bernd, Lucas, Jeroen, David, although you were not directly involved in my research, some more experienced opinions were always appreciated. Agis, Djalma and Chih-Hsien, I enjoyed your company in the office, although all the homeworking didn't always help. Sharing surprises, frustrations and stories was always a pleasure! Joao, Chiara, Paulina, Masja and Ayda, it was great to see you starting in the new lab and hear what you were working on. Ingo, I especially appreciate our visit to ESMRMB when every colormap was critically evaluated. Dion, Fabian, Jack, Boudewine, Moein, Rik, Baptiste, Alina, Changchung, Yidong, Xiufeng, not necessary our shared interest in Medical Imaging or the shared hallway but the shared interest in each other, especially during lunches, made me feel like part of a group with you.

During my research I was lucky enough to also be part of the C.J. Gorter MRI Center, something I appreciated very much with the extra group of MRI researchers I got to know and the extra seminars to attend. Lena, Kevin, Aashley, thanks for sharing an office with me the last months with a ridiculous paper output and great support! Bart, Emiel, Ingmar, Ernst, Bea, Jasmin, Tom, Daniëlle, Lydiane, Sophie, Merlijn, Leonie, Thijs, Yiming, Javad, Manon, Emma, Ellen, Whitney, Matthieu, Ballász, Michael, Donnie, Rosanne,

Wyger, Reijer, Suzanne, Lisa, Myriam, Chloé, Eche, Barbara, Wouter, Paul, Joe, thanks for the coffees, lunches, ISMRM visits, moral support and the welcoming surrounding! Thijs, Andrew, Hermien, Jan-Willem, Louise, Peter and Itamar, you brought together a great group of researchers with an extraordinary group feeling.

The extra activities I could start during my PhD also added something extra to this. Everyone involved in the FPC, UPC, Hoe?Zo! Show, ISMRM Benelux 2021, ISMRM Benelux Pubquiz, thanks for the opportunity to work with you!

Luckily there are also non-research related things in life, that somehow also help in doing research. I want to thank everyone from *De Lekkere Lopers*, first of all trainers Han and Bram, but also running friends Timo, Andy, Elias, Maikel, Philip, Michiel, Leon, Noah ,Jan, Marco, Jolijn, Daan, PC and everyone else. Bestuur VI and Bestuur 83, it is great to be still in touch with you after these years and see how everyone develops. Miles, Simon, Jacco, Aranka, Robert, Tom and Jorrit, I consider myself lucky with friends like you, always in for a serious chat, a game or a discussion about doing a PhD and other steps in life. I could write long stories about each one of you, but perhaps there are better places for that.

Ook mijn schoonfamilie, Ed, Sjanie, Merel en Renske, ik ben al weer lang onderdeel van jullie gezin en daar ben ik heel blij mee. Bedankt voor de interesse en de warme omgeving die jullie altijd bieden aan Esther en mij. Alle familie, ooms, tantes, neven en nichten zijn ook een warm bad waar ik altijd op terug kan vallen en waarin oprechte interesse altijd naar voren komt.

Rens, we kennen elkaar door en door en soms verschillen we, maar als het er op aan komt ben je er altijd voor me. Ik weet niet wat we beide doen over tien jaar, maar dat we altijd op elkaar terug kunnen vallen weet ik zeker. Papa en Mama, jullie hebben me vanaf het begin altijd aangemoedigd om mijn interesses achterna te gaan en niet snel op te geven. Met, onder andere, abonnementen op de Kijk (en Donald Duck), bezoekjes aan musea, een gezonde dosis doorzettingsvermogen en heel veel vertrouwen , hebben jullie me gemaakt tot wie ik nu ben. Discipline gaat hand in hand met ontspanning en je ontwikkelen en doen wat je leuk vindt en goed kan, is wat me hier gebracht heeft op de laatste pagina van mijn proefschrift. Heel erg bedankt.

Esther, zonder jou was dit proefschrift niet geworden wat het nu is, maar was ik ook niet geweest wie ik nu ben. Samen kunnen we zo veel. Ik hou van jou!

CURRICULUM VITÆ

Martijn Arie Nagtegaal

December 14 1993 Born in Alphen aan den Rijn, The Netherlands.

EDUCATION

2006–2012 Secondary School
Het Groene Hart Lyceum
Alphen aan den Rijn, The Netherlands

2012–2015 Bachelor of Science in Applied Physics (*Cum laude*)
Bachelor of Science of Applied Mathematics (*Cum laude*)
Delft University of Technology
Delft, The Netherlands

2016–2018 Master of Science in Scientific Computing
Berlin University of Technology
Berlin, Germany

2016–2018 Master of Science in Applied Mathematics (*Cum laude*)
Delft University of Technology
Delft, The Netherlands
Thesis: Sparsity promoting algorithms for multi-component magnetic resonance parameter mapping
Supervisor: Dr. M. Doneva (*Philips Research, Hamburg*)
Prof. dr. R. Nabben (*Berlin University of Technology*)

2019–2023 Ph.D. in Applied Physics
Delft University of Technology
Delft, The Netherlands
Thesis: Estimation of multiple components and parameters for quantitative MRI
Promotors: Dr. F. M. Vos
Delft University of Technology
Prof. dr. ir. M. J. P. van Osch
Leiden University Medical Center
Co-promotors: Dr. J. H. J. M. de Bresser
Leiden University Medical Center
Dr. ir. D. H. J. Poot
Erasmus MC

List of Publications

Journal Publications

1. **Martijn. A. Nagtegaal**, Ingo Hermann, Sebastian Weingärtner, Elio Mirtinez-Heras, Elisabet Solana, Sara Llufriu, Achim Gass, Dirk H.J. Poot, Matthias J.P. van Osch, Frans M. Vos, Jeroen de Bresser. "White matter changes measured by multi-component MR Fingerprinting in multiple sclerosis ". *In preparation for submission to NeuroImage.* **Chapter 6 of this thesis.**

2. David G.J. Heesterbeek, Kirsten Koolstra, Matthias J.P. van Osch, Martin B. van Gijzen, Frans M. Vos, **Martijn A. Nagtegaal**. "Mitigating undersampling errors in MR Fingerprinting by sequence optimization". In: Magnetic Resonance in Medicine *Online available* ISSN: 1522-2594. doi: 10.1002/mrm.29554. **Chapter 8 of this thesis.**

3. **Martijn A. Nagtegaal**[1], Emiel Hartsema[1], Kirsten Koolstra, and Frans Vos. "Multicomponent MR fingerprinting reconstruction using joint-sparsity and low-rank constraints". In: Magnetic Resonance in Medicine 89.1 (2023). ISSN: 1522-2594. doi: 10.1002/mrm.29442 **Chapter 5 of this thesis.**

4. Laura Nunez-Gonzalez[1], **Martijn A. Nagtegaal**[1], Dirk H. J. Poot, Jeroen de Bresser, Matthias J. P. van Osch, Juan A. Hernandez- Tamames, and Frans M. Vos. "Accuracy and repeatability of joint sparsity multi-component estimation in MR Fingerprinting". In: NeuroImage 263 (Nov. 1, 2022), p. 119638. ISSN: 1053-8119. doi: 10.1016/j. neuroimage.2022.119638. **Chapter 3 of this thesis.**

5. Ingo Hermann, Eloy Martínez-Heras, Benedikt Rieger, Ralf Schmidt, Alena-Kathrin Golla, Jia-Sheng Hong, Wei-Kai Lee, Wu Yu-Te, **Martijn A. Nagtegaal**, Elisabeth Solana, Sara Llufriu, Achim Gass, Lothar R. Schad, Sebastian Weingärtner, and Frank G. Zöllner. "Accelerated white matter lesion analysis based on simultaneous T_1 and T_2^* quantification using magnetic resonance fingerprinting and deep learning". In: Magnetic Resonance in Medicine 86.1 (2021), pp. 471486. ISSN: 1522-2594. doi: 10.1002/mrm.28688.

6. **Martijn A. Nagtegaal**, Peter Koken, Thomas Amthor, Jeroen de Bresser, Burkhard Mädler, Frans Vos, and Mariya Doneva. "Myelin water imaging from multi-echo T2 MR relaxometry data using a joint sparsity constraint". In: *NeuroImage* 219 (Oct. 1, 2020), p. 117014. ISSN: 1053-8119. doi: 10.1016/j. neuroimage.2020.117014. **Chapter 4 of this thesis.**

7. **Martijn A. Nagtegaal**, Peter Koken, Thomas Amthor, and Mariya Doneva. "Fast multi-component analysis using a joint sparsity constraint for MR fingerprinting". In: *Magnetic Resonance in Medicine* 83.2 (2020), pp. 521534. ISSN: 1522-2594. doi: 10.1002/mrm.27947. **Chapter 2 of this thesis.**

8. **Martijn. A. Nagtegaal** and Miriam Blaauboer. "Implementation of a quantum private query using single- photon transistors". In: *Journal of Physics B: Atomic, Molecular and Optical Physics* 52.4 (Jan. 2019), p. 045501. ISSN: 0953-4075. doi: 10.1088/1361-6455/aafbc0

[1] Authors contributed equally

CONFERENCE CONTRIBUTIONS

1. **Martijn A. Nagtegaal**, Ingo Hermann, Sebastian Weingärtner, Elio Mirtinez-Heras, Elisabet Solana, Sara Llufriu, Achim Gass, Dirk H.J. Poot, Matthias J.P. van Osch, Frans M. Vos, Jeroen de Bresser. "White matter changes measured by multi-component MR Fingerprinting in multiple sclerosis ".
    - ISMRM, Toronto, June 2023, Power Pitch.
    - ISMRM Benelux, Brussels, March 2023. Oral presentation.

2. **Martijn A. Nagtegaal**, Simon Konstandin, Nicolas Gross-Weege, Volkmar Schulz, Matthias Günther, Matthias J.P. van Osch. "Vendor neutral pulse programming: Running gamma-STAR sequences on Philips Hardware". ISMRM, Toronto June 2023. Poster presentation.

3. **Martijn A. Nagtegaal**[1], Emiel Hartsema[1], Kirsten Koolstra, and Frans M. Vos. "Joint sparsity multi-component MRF reconstruction - directly from k-space to component maps".
    - In: Proc. Intl. Soc. Mag. Reson. Med. 30 (2022). ISMRM. London, May 2022. p. 2514. Poster presentation. *Magna Cum Laude Merit Award*
    - ISMRM Benelux. Maastricht, April 2022. Oral presentation by Emiel Hartsema

4. David G.J. Heesterbeek, Martin van Gijzen, Frans M. Vos, and **Martijn A. Nagtegaal**. "Sequence optimisation mitigating undersampling errors in Magnetic Resonance Fingerprinting". In: Proc. Intl. Soc. Mag. Reson. Med. 30. ISMRM. London, May 2022, p. 0561. Power pitch. *Magna Cum Laude Merit Award*

5. **Martijn A. Nagtegaal**, Charles McGrath, Christian Gunther, and Manuel Baumann. "Through-plane Motion in Magnetic Resonance Fingerprinting: Simulations and Phantom Experiments". In: Proc. Intl. Soc. Mag. Reson. Med. 30. ISMRM. London, May 2022. p. 2519. Poster presentation. **Chapter 9 of this thesis.**

6. **Martijn A. Nagtegaal**[1], Laura Nunez-Gonzalez[1], Dirk H. J. Poot, Jeroen de Bresser, Matthias J.P. Osch, Hernandez Tamanes, and Frans M. Vos. "Accuracy and repeatability of joint sparsity multi-component estimations in MR Fingerprinting".
    - In: Proc. Intl. Soc. Mag. Reson. Med. 30. ISMRM. London May 2022. p. 2599. Poster presentation.
    - ISMRM Benelux. Maastricht, April 2022. Oral presentation.

7. **Martijn A. Nagtegaal**, Laura Nunez-Gonzalez, Dirk H.J. Poot, Matthias J.P. Osch, Jeroen de Bresser, Juan A. Hernandez Tamanes, and Frans M. Vos. "Estimating tissue volume fractions and proton density in multi-component MRF". In: Proc. Intl. Soc. Mag. Reson. Med. 29. ISMRM. online, May 2021, p. 1543. Poster presentation.

8. David G.J. Heesterbeek, Frans Vos, Martin van Gijzen, and **Martjn A. Nagtegaal**. "Sequence Optimisation for Multi-Component Analysis in Magnetic Resonance Fingerprinting". In: Proc. Intl. Soc. Mag. Reson. Med. 29. ISMRM. online, May 2021, p. 1561. Poster presentation.

9. **Martijn. A. Nagtegaal**, Ingo Hermann, Sebastian D. Weingärtner, Jeroen de Bresser, and Frans M. Vos. "Detection of small cerebral lesions using multi-component MR Fingerprinting with local joint sparsity". In: Proc. Intl. Soc. Mag. Reson. Med. 28. ISMRM. online, 2020, p. 1828. Poster presentation. *Magna Cum Laude Merit Award* **Chapter 7 of this thesis.**

10. **Martijn A. Nagtegaal**, Thomas Amthor, Peter Koken, and Mariya Doneva. "MR Fingerprinting multi- component analysis using a fast joint sparsity algorithm". In: Proc. Intl. Soc. Mag. Reson. Med. 27. ISMRM. Montreal, Canada, May 13, 2019, p. 1106. Oral presentation. *Magna Cum Laude Merit Award*

11. **Martijn A. Nagtegaal**, Burkhard Mädler, Thomas Amthor, Peter Koken, and Mariya Doneva. "A fast, joint sparsity constrained algorithm for improved myelin water fraction mapping". In: Proc. Intl. Soc. Mag. Reson. Med. 27. ISMRM. Montreal, Canada, May 13, 2019, p. 4401. Poster presentation.

12. **Martijn A. Nagtegaal**, Thomas Amthor, Peter Koken, and Mariya Doneva. "The need of a varying flip angle in multi-component analysis with IR-bSSFP sequences." In: Proc. Intl. Soc. Mag. Reson. Med. 27. ISMRM. Montreal, Canada, May 13, 2019, p. 4522. Poster presentation.

SUPERVISED STUDENT PROJECTS

BACHELOR THESES

1. Corné Haasjes. "Effects of B_1^+ corrections on MRF and QTI feature maps". *TU Delft* Applied Physics. April 2020 - July 2021. Grade 8.5

2. Maaike Smit. "Precision of myelin water fraction estimations for slice-wise varying MR Fingerprinting". 2021. *TU Delft* Applied Physics. April 2021 - August 2021. Grade 7.5.

3. Jasper van der Gronde. "B-Spline parameterized sequence optimization for undersampled Magnetic Resonance Fingerprinting". September 2021 - July 2022. *TU Delft* Applied Physics. Grade 7.

MASTER THESES

1. David G.J. Heesterbeek. "Sequence optimisation for Magnetic Resonance Fingerprinting". September 2020-September 2021. *TU Delft* Applied Physics and Applied Mathematics. Grade 9.

2. Emiel Hartsema. "Joint sparse multi-component MR Fngerprinting reconstruction by iterative rank decay". October 2020 - July 2021. *TU Delft* Applied Physics. Grade 8.5.

3. Sven Kwinkelenberg. *In preparation.* "Magnetization transfer in the context of multi-component MR Fingerprinting". September 2022 - 2023. *TU Delft* Applied Physics